Kinetics of Radical Reactions of Tropospheric Importance

A thesis submitted in partial fulfilment of
the requirements of the degree of D.Phil.

by

Paul S. Monks

Christ Church
Oxford

Michaelmas 1991

Acknowledgements

Not that I had any reason for hating school. Strange as it may seem to my readers, I was not unpopular there. I was a modest good-humoured boy. It was Oxford that made me insufferable.

Max Beerbohm, 1872-1956,
More. Going back to School

In my time in Oxford, I have had the somewhat dubious privilege of working with many people. I now have the opportunity to thank them.

My moral mentor and supervisor, Dr. R.P. Wayne whose *wisdom* in all matters is unsurpassed and his wife Brenda, whom I give my special thanks.

To the seemingly "ubiquitous" and omnipresent Wayne group. In particular George, partner in every conceivable crime and master of British Telecom. The all seeing and never commenting Saint Carlos whose patience with us thickies is beyond belief. Pete for his never ending ability to make my apparatus work when I couldn't. Gerhard aka Gerzza and Doug without whose wit, charm and help I would not have been able to survive.

Dave and Will "The Boyz" for making me into their laboratory technician, Annie for the can of peaches, Paula for having a huge sense of humour and the biology lessons, Andy for being Scottish and Amy for well, being a secretary.

I must also thank the many other members of the Wayne group past and present who have made my life what it is (*sic*).

The NERC for giving me a studentship and an acronym I never could get right.

And finally, but not least, my parents for there never ending love and support and my brother Jonathan for teaching me "ow real people speak".

Abstract

KINETICS OF RADICAL REACTIONS OF TROPOSPHERIC IMPORTANCE

by

Paul S. Monks

Christ Church

Michaelmas 1991

submitted for the degree of D.Phil.

The object of the research described in this thesis is to provide, by means of laboratory experiments, data required to understand the atmospheric chemistry of the nitrate radical, from both a mechanistic and kinetic point of view.

The low pressure discharge-flow kinetic technique coupled detection of the NO_3 radical by optical absorption was used to measure the temperature-dependent rate coefficients for the reaction of NO_3 with 1-butene, 1-chloro-1-butene, 2-chloro-2-butene, 3-chloro-1-butene, 1-chloro-2-butene, 2-chloro-2-butene, 1-chloromethylpropene, 3-chloromethylpropene, 3-bromo-1-butene, 4-bromo-1-butene and 2-bromo-2-butene. The atmospheric implications for the reaction of NO_3 with these compounds are discussed.

In order to understand the patterns of reactivity towards NO_3 exhibited by these compounds, a number of approaches were adopted. First, a non-quantitative approach employing the simple ideas of inductive and mesomeric effects. Secondly the observed reactivity of NO_3 towards these compounds was discussed, quantitatively, in terms of the relative energies of the interacting orbitals. This quantitative analysis required an extensive set of molecular orbital calculations were undertaken at various levels of sophistication. A good correlation was found, for compounds not containing vinylic halogen atoms, between -E(HOMO) and the measured rate constant; the data were used also to calculate "group-reactivity factors". In an extension to this work a new empirical correlation is presented that takes account of the contribution, in terms of the atomic orbital coefficients, of vinylic halogen atoms to the observed rate constant. To provide support for these calculations, work was undertaken using photoelectron spectroscopy to characterise experimentally the individual molecular orbitals. A correlation between the inverse of the molecular polarisability and the activation energy of the reaction is also described.

Complementary work was undertaken in a unconventional flash-photolysis system to look at the kinetics of the reaction

$$NO_3 + NO_3 \rightarrow 2\ NO_2 + O_2$$

over a pressure range of 2 to 100 Torr in helium. The measured rate coefficient was found to be pressure independent and to have a value of $(2.2 \pm 1.0) \times 10^{-16}$ cm^3 $molecule^{-1}$ s^{-1}.

The experimental work on the nitrate radical was extended to look at the laser-induced fluorescence (LIF) spectrum and at the quenching of the excited state of the nitrate radical.

Preface

This thesis has been prepared such that each of the chapters are self-contained; i.e. the description of the apparatus used is in the same chapter as the results obtained from them. Reactions, equations and tables are numbered from the start of each chapter. The only exception to this are the references. As the whole thesis encompasses NO_3 chemistry and many of the references are common to all the chapters they have been brought together and listed in alphabetical order at the end of the thesis.

The units used in the text are the ones commonly used in gas kinetic studies rather than S.I. units; e.g. molecule cm^{-3} rather than mole m^{-3}. Other common gas-phase kinetic nomenclature is also used; e.g. $[X]_0$ denotes the initial concentration of a reactant. Similarly, many of the molecules described are given their common names in preference to the systematic ones; e.g. tetramethylethylene is used in preference 2,3-dimethylbut-2-ene.

Table of Contents

Chapter 1: Introduction

1.1 The terrestrial atmosphere 3
1.2 Chemistry in the troposphere 8
1.3 The nitrate radical 14

Chapter 2: The kinetics of the reaction of the nitrate radical with a series of halobutenes and 1-butene

2.1 Introduction 24
2.2 Kinetic measurements using the discharge-flow technique 26
2.3 Experimental details 32
2.3.1 Apparatus 32
2.3.2 Production of NO_3 34
2.3.3 Detection of NO_3 36
2.3.4 Absolute concentrations of NO_3 39
2.3.5 Calibration of flows 44
2.3.6 Materials 48
2.4 The reaction of NO_3 with 1-butene 49
2.4.1 Results 49
2.5 The reaction of NO_3 with a series of halobutenes 55
2.5.1 The treatment of experimental data 55
2.5.2 Results 58
2.6 Discussion 68
2.7 Atmospheric implications 81
2.8 Conclusions 82

Chapter 3: Patterns of reactivity in the reactions of NO_3

3.1 Introduction 84
3.2 Experimental 86
3.2.1 Semi-empirical methods 86
3.2.2 Photoelectron spectroscopy 90
3.3 Variation of the activation energies for the addition reactions of NO_3 92
3.4 Rationalisation of the reactivity of NO_3 towards alkenes using a frontier orbital approach
3.4.1 Frontier orbital approach 99
3.4.2 Correlations 109
3.5 Group reactivity factors 111
3.6 Photoelectron spectroscopy of the halobutene compounds 115
3.6.1 Photoelectron spectroscopy 115
3.6.2 Results and Discussion 117
3.6.3 Conclusions from the PE spectra of the halobutenes 128
3.7 Comparisons and Conclusions 130

Chapter 4: The NO_3 self-reaction

4.1 Introduction 139
4.2 Flash Photolysis 141
4.3 A comparison of flow tube and flash photolysis kinetic techniques 142
4.4 Apparatus 145
4.4.1 The reaction cell and gas-handling manifolds 145
4.4.2 Production of NO_3 147
4.4.3 Detection of NO_3 149
4.4.4 Signal processing and recording of data 150
4.5 Results I 153
4.5.1 Simple considerations 154
4.6 Simulation and fitting of a photolysis build-up and decay; Mechanistic considerations 159
4.6.1 Kinetic modelling of the build-up/photolysis phase of the reaction
4.6.2 Possible production of NO_3 from photolysis of HNO_3 162
4.6.3 Products of the reaction NO_3 + F; FO_x chemistry 167
4.6.4 The effect of $[NO_2]_0$ on the NO_3 build-up profile 171
4.6.5 The modulated steady-state 173
4.6.6 Products of the NO_3 + NO_3 reaction 176
4.6.7 The outcome 182
4.7 Development of a kinetic model, for quantitative fitting of the NO_3 decays
4.7.1 Fitting procedures 184
4.7.2 A re-appraisal of the L-M method *vs* FACSIMILE for non-linear fitting of the experimental data 186
4.7.3 Kinetic fitting to a more complex scheme 191
4.8 Results II 195
4.9 Discussion 197
4.9.1 Comparison and trends 197
4.9.2 Pressure dependence of the NO_3 + NO_3 reaction ? 199
4.10 Conclusions 201

Chapter 5: The laser-induced fluorescence of NO_3

5.1 Introduction 202
5.2 Laser-induced fluorescence 204
5.2.1 Laser-induced fluorescence of NO_3 207
5.3 Experimental 211
5.3.1 The laser system 211
5.3.2 The reaction cell 213
5.3.3 LIF collection optics 213
5.3.4 Signal processing and recording 214
5.4 Results 215
5.4.1 Detection of NO_3 219
5.4.2 Lifetime of emission decays for excited NO_3 223
5.5 Comparison of methods used for detection of NO_3 in kinetic studies 230
5.6 Conclusions 234

Appendix I: The photoelectron spectra of the halobutenes 235

Appendix II: The FORTRAN program for converting Flash-Photolysis traces 244

References 251

Chapter 1

Introduction

"All things by immortal power,
near or far, hiddenly, to each
other linked are"

Francis Thompson, 1897

The Earth and its environment are changing on an unprecedented scale. The Earth, as far as we know, is an unique planet, where a thin blanket of air, a thinner film of water, and the thinnest veneer of soil sustain an everchanging web of life. Man, of all the diverse species on the planet, has the power to change irrevocably the very environment that supports life.

Realisation of this has come slowly. In the case of the atmosphere, as early as the 12th century Moses Maimonides (1135-1204) noted the first urban air pollution. With the change from wood burning to coal burning and the onset of the industrial revolution, urban air pollution got worse. In 1952, there were 4000 fatalities ascribed to the London 'pea-soupers' (Wilkins,1954). After the 'smog' endemics of the 40's and 50's, there came another realisation of the global impact man was having on the atmosphere, with the discovery of the so-called 'Ozone-hole' (Farman *et al.*, 1985). Previously unprecedented action was taken with summit meetings and ministerial conferences which led to the signing of the Montreal Protocol.

Central to the understanding of the atmosphere is our scientific knowledge of global and regional processes, and the ability of science to predict the future behaviour of the Earth system. This work is in some part a small contribution to our understanding of how one atmospherically important species behaves with respect to reaction with both itself and organic compounds.

1.1 The terrestrial atmosphere

The atmosphere (Greek 'atmos'='vapour' + 'sphiara'='ball') is the gaseous envelope that surrounds a heavenly body. The terrestrial atmosphere is principally composed of nitrogen (*ca.* 78%) and oxygen (*ca.* 21%) but the trace species (<1%) (Holland, 1978) can exert a profound effect on the physical structure of the atmosphere. On the basis of the temperature altitude profile the Earth's atmosphere can be divided into several distinct regions (See figure 1.1).

The region nearest to the surface of the earth is called the troposphere (0-15km) (Greek 'tropos' = 'turning'). In practice the troposphere is divided into two regions. Between the surface and some 0.5 to 2km by day, less by night, there is a region of highly turbulent mixing, the boundary layer (Seinfeld, 1986). The turbulent mixing is caused by the increased friction of air movements with the surface and can serve locally (i.e. geographically) to concentrate anthropogenic or biogenic emissions (artificial or natural). Above the boundary layer lies the so called free troposphere, where atmospheric circulation is unimpeded, but not unaffected, by the surface. As a consequence of the temperature decreasing with altitude in the troposphere (*ca.* 6.5K km^{-1}), the vertical convective mixing for species emitted from the surface is relatively fast at about a week, in comparison to about a year for horizontal mixing in an entire hemisphere (Seinfeld, 1986). Only species with relatively long atmospheric lifetimes (i.e. stable and non-reactive gases), e.g. CH_4 or N_2O, display homogenous distribution within a hemisphere, whereas species with shorter atmospheric lifetimes display variations between different airmasses dependent on regional, meteorological or geographical factors. This fact can be used to establish the source(s) of emission (Schwartz, 1989).

Essentially all the water vapour, clouds and precipitation in the earth's atmosphere are found in the troposphere; as a result, removal of pollutants by precipitation scavenging can be an important loss process (see §1.2).

The dependency of temperature on altitude in the terrestrial atmosphere can be used to define the location of different regions of the atmosphere (See figure 1.1). The boundary layer between the troposphere and the stratosphere is indicated by a temperature gradient inversion, the cooler airmass of the stratosphere 'sitting' on top of the turbulent airmass of the troposphere. This temperature inversion (i.e. change in sign of the temperature gradient) delineates the two regions. This inversion layer is called the tropopause. The temperature at the tropopause is *ca.* 210K; this fact accounts for the relative dryness of the stratosphere, $[H_2O] \approx$ 2-3ppm, in comparison with the troposphere, where the $[H_2O]$ typically several parts per thousand. The actual height of the tropopause is determined by latitude and meteorological and seasonal factors (W.M.O., 1985). An important consideration in atmospheric chemistry is the dynamical transfer of chemical constituents in both directions across the tropopause. Relatively little is known about the mechanisms of Stratospheric-Tropospheric (Strat-Trop) exchange (Wayne, 1991). One mechanism known to occur at mid to high latitudes is tropopause folding (Campbell, 1986). Thin (~1km) laminar intrusions of stratospheric air enter the troposphere for up to 1000km parallel to the jet stream and become mixed with turbulent tropospheric air. This sort of mixing takes place predominantly along the tropics because of the powerful convection current generated by solar heating. Transport between the two regions is in the order of 22-44% of the total mass of stratospheric air each year (Campbell, 1986). A comprehensive review of the dynamics and meteorology that leads to Strat-Trop exchange is given by the W.M.O. (1985).

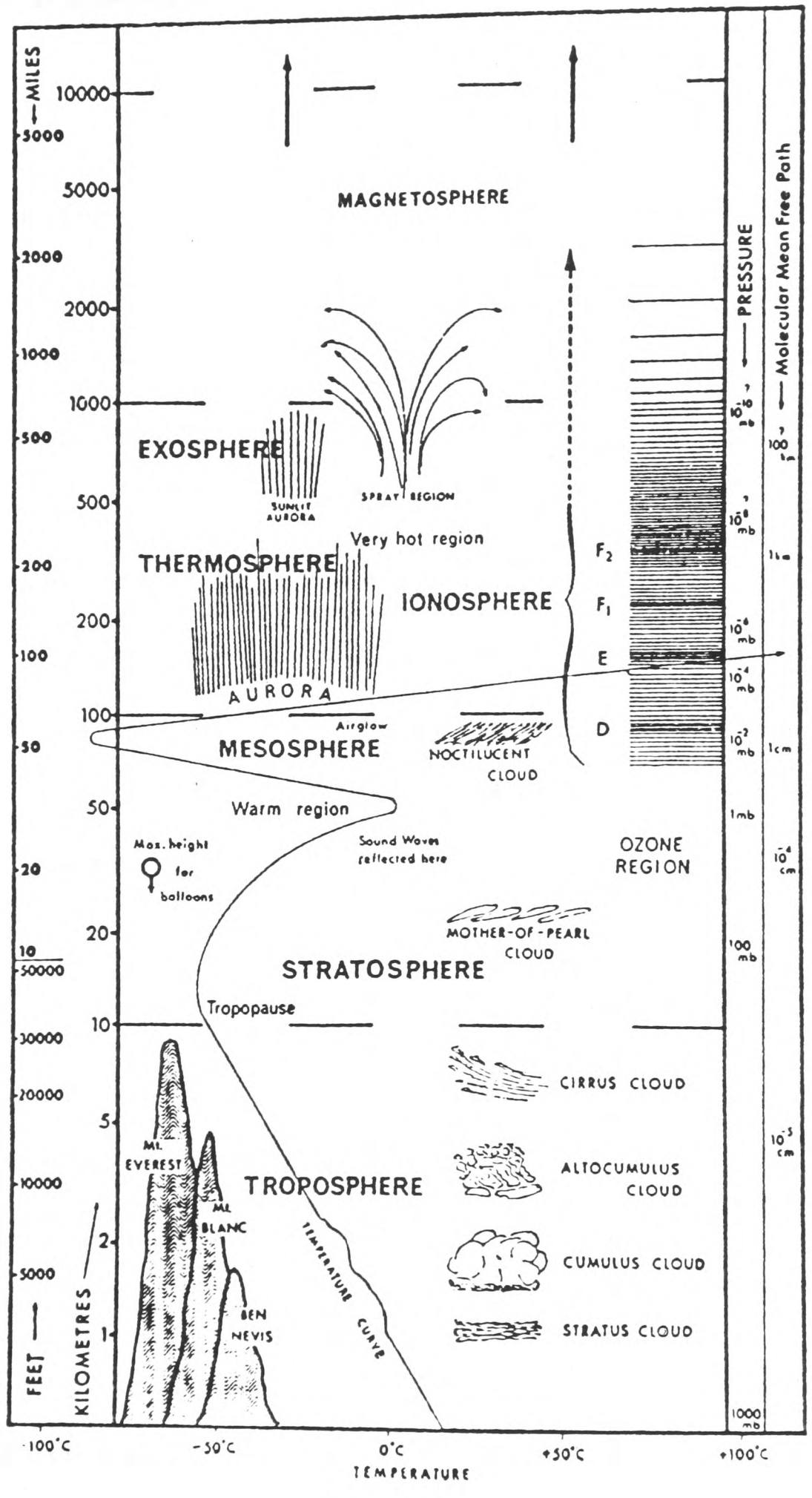

Figure 1.1 A schematic representation of the atmosphere

Coupled to the change in temperature with altitude is the change of pressure with altitude in the troposphere. A good approximation for this change is

$$p = p_o \exp\left(\frac{-mgz}{kT}\right) \qquad (1.1)$$

where p is the pressure, p_0 is the pressure at a reference altitude (often sea level), z the altitude, m the relative molecular mass (~0.2x32(O_2)+0.8x28(N_2) = 28.8), g the acceleration due to gravity and k the Boltzmann constant. The quantity (kT/mg) is described as the scale height for a particular temperature and mass, i.e. the vertical distance corresponding to a pressure drop by a factor $1/e$ compared to the reference altitude. For the terrestrial atmosphere the scale height, H_s, varies between 6km at T~210K to 8.5km at T~290K. The rapid decrease in pressure with height means that 80-90% of the mass of the atmosphere is located below the tropopause (*ca.* 15km). The range of temperature and pressure in the troposphere dictates the chemistry that occurs, especially where the chemistry is characterised by rate constants with large positive temperature dependencies (Campbell, 1986).

Above the tropopause lies the stratosphere (15-50km) (Greek 'stratos'='layered'). The air mass in this region is stratified and vertical transport takes considerably longer than in the troposphere. An important feature of the stratosphere is the presence of the trace species Ozone. Ozone is formed by the action of ultra-violet (UV) radiation on oxygen.

$$O_2 + h\nu \longrightarrow O + O \qquad (1.2)$$

$\lambda < 242.4$nm (Ogawa, 1971)

$$O + O_2 + M \longrightarrow O_3 + M \qquad (1.3)$$

Several factors contribute to the importance of the presence of Ozone in the stratosphere. Perhaps the most important is the relationship between the absorption spectrum and the

protection of living organisms. At $\lambda < 230$nm, O_2 filters out solar ultra-violet but at $\lambda >$ 230nm (especially 230-290nm) Ozone is the only chemical species in the stratosphere capable of attenuating the potentially harmful effects of the Sun's radiation (Coyle *et al.*, 1982). The reason for the gradual increase in temperature to about 270K at the stratopause is the direct result of heating by absorption of solar uv radiation in the so-called Ozone layer. Circulation patterns in the stratosphere are almost exclusively horizontal (Houghton, 1986) and have the net effect of transporting heat from low to high latitudes. As the pressure in the stratosphere is lower than that in the troposphere, the change in pressure with height can critically influence the chemistry of reactions whose rates are dependent on pressure.

Above the stratopause at altitudes between 50 and 85km lies the mesosphere. The temperature decreases at a rate of about 3.75K km^{-1} (Wayne, 1991) until it reaches a minimum around 175K making these the coldest temperatures in the atmosphere. Pressures in this region are extremely low at about 0.1 Torr.

The chemistry in this region is characterised by complex ion-ion and ion-molecule interactions, the region above 100km often being referred to as the ionosphere (Kelley, 1989). Above the mesosphere, at altitudes greater than about 85km, lies the thermosphere. The atmosphere is so thin, i.e. the pressure is so low, that molecular collisions between gaseous species become very infrequent. Molecular densities are in the order of 10^{13} molecule cm^{-3} compared to $2.5x10^{19}$ molecule cm^{-3} (Seinfeld, 1986) at sea level. One consequence of this is that energy may not be equilibrated between the various degrees of freedom (i.e. vibrational, rotational and translational modes), so that the concept of temperature in this region is misleading. The temperatures in this region are driven by the absorption of extreme

uv solar radiation of $\lambda < 110$nm. At such short wavelengths most gaseous molecules are photoionised. Temperatures can be as high as 1100K by day and 880K by night (Wayne, 1991) but this is a reflection of the "thinness" of the atmosphere. Maximum temperatures also depend on solar photon flux which in turn is dependent on solar activity.

The chemistry of the stratosphere, mesosphere and thermosphere is of little relevance to the work presented in this thesis and will not be discussed further.

1.2 Chemistry in the troposphere

As 90% of the total mass of the atmosphere resides in the troposphere, the bulk of the minor trace gas burden is found there. The surface of the Earth acts as the major source for these trace gases. The type of emission falls into two broad classes, biogenic or natural and anthropogenic or man-made emission. The physical lifetime of a trace component is defined by the source-transport-sink sequence (Andreae, 1987), but chemical changes may occur on time-scales comparable with or smaller than this lifetime. The physical removal processes are normally divided into, *dry* deposition, where trace species are adsorbed irreversibly onto soil, water or plant surfaces and *wet* deposition where constituents are incorporated into precipitation elements, e.g. clouds, rain-drops and aerosols. These physical processes can also be linked to chemical processes which take place in aerosols such as fog, rain and cloud-drops (Jacob *et al.*, 1989), on surfaces (heterogenous) and gas-particulate transformation (Finlayson-Pitts and Pitts, 1986). These types of processes lead to a well known atmospheric pollution phenomenon such as "acid-rain" (Schwartz, 1989).

The homogenous gas-phase chemistry in the troposphere is dominated by the reactions of the hydroxyl radical during the daytime (Finlayson-Pitts and Pitts, 1986), despite its relatively low concentration of *ca.* 10^6 molecule cm^{-3}. The most important source of OH is the reaction of electronically excited oxygen with water

$$O(^1D) + H_2O \longrightarrow 2\ OH \qquad (1.4)$$

$O(^1D)$ is generated by photolysis of ozone by radiation in the near ultra-violet

$$O_3 + h\nu \longrightarrow O(^1D) + O_2(^1\Delta_g) \qquad (1.5)$$

λ~310nm (DeMore *et al.*, 1990)

Other sources include the photolysis of HONO (Stockwell and Calvert, 1978) and indirectly the photolysis of HCHO (DeMore *et al.*, 1990). The ozone required for $O(^1D)$ production can be of stratospheric origin or produced *via* photolysis of NO_2

$$NO_2 + h\nu \longrightarrow O + NO \qquad (1.6)$$

$\lambda \leq 400nm$ (DeMore *et al.*, 1990)

$$O + O_2 + M \longrightarrow O_3 + M \qquad (1.3)$$

(Chapman, 1930)

The sinks for the OH radical in the troposphere are dependent on the composition of the ambient air mass, which in turn relies on the geographical region, i.e. rural, urban, coastal etc., over which the air is situated.

The remote rural region is the simplest case that illustrates the action of OH chemistry on trace species. This type of area has low hydrocarbon concentrations with perhaps the exception of CH_4, CFCs and natural hydrocarbons such as terpenes. The two main reactions of the OH radical in the unpolluted troposphere are with carbon monoxide and methane.

$$OH + CO \longrightarrow CO_2 + H \qquad (1.7)$$

$$OH + CH_4 \longrightarrow CH_3 + H_2O \quad (1.8)$$

Methane is the simplest and most abundant hydrocarbon in the earth's atmosphere (Stauffer *et al.*, 1985; Rinsland *et al.*, 1985). Reaction 1.8 is the start of the important oxidation pathway of methane (Ravishankara, 1988) (See figure 1.2) and is illustrative of the chemical degradation pathways prevalent in the tropospheric breakdown of volatile organic compounds (V.O.C.). The next step in the oxidation scheme is the formation of HO_2 and CH_3O_2

$$H + O_2 + M \longrightarrow HO_2 + M \quad (1.9)$$

$$CH_3 + O_2 \longrightarrow CH_3O_2 \quad (1.10)$$

In tropospheric regions where there are relatively few trace species, both HO_2 and CH_3O_2 can react to produce peroxides

$$HO_2 + HO_2 \longrightarrow H_2O_2 + O_2 \quad (1.11)$$

$$CH_3O_2 + HO_2 \longrightarrow CH_3OOH + O_2 \quad (1.12)$$

Further reactions with OH, or photolysis, of these peroxides can lead to the regeneration of radical species which can subsequently re-enter the reaction chain (1.7-1.12). Another atmospheric fate of these peroxide compounds is 'rain-out' as they are highly soluble in cloud-droplets.

One key issue in the understanding of atmospheric chemistry is the way in which tropospheric ozone is produced. The only known way of producing ozone in the troposphere is from the photolysis of NO_2 (reactions 1.6 and 1.3). Table 1.1 shows the reaction cycle for the catalytic production of ozone; analogous cycles exist for reaction chains involving RO_2 (e.g. CH_3O_2), and in all cases, NO_x must be present. In this context, NO_x refers to the sum of NO and NO_2, where as NO_y means 'odd-nitrogen', defined as the sum of NO_x and oxidised N species that represent sources or sinks of NO_x e.g. N_2O_5, HNO_3 and NO_3.

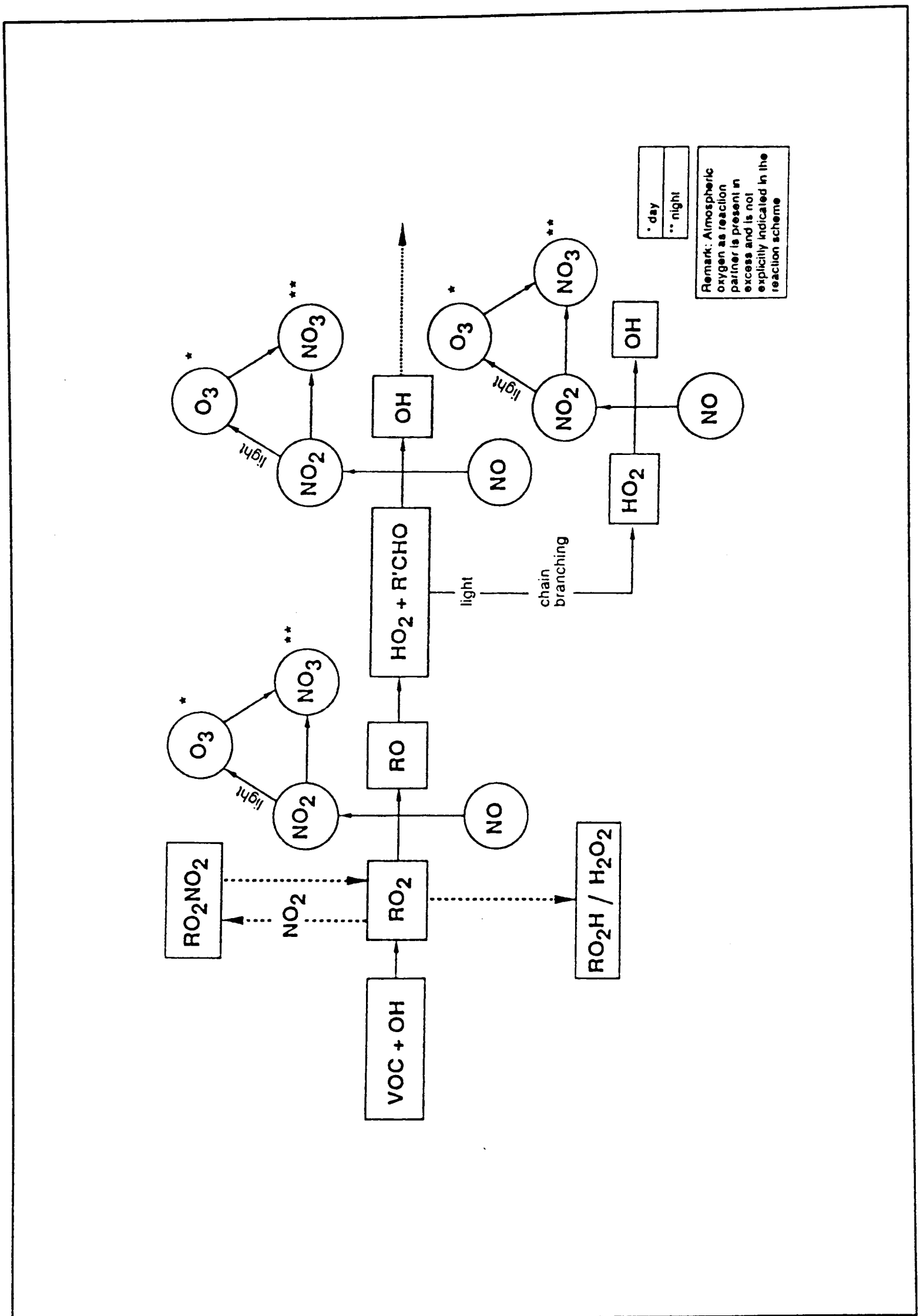

Figure 1.2 - The atmospheric oxidation cycle for volatile organic compounds as initiated by reaction with the OH radical.

Table 1.1 - A reaction cycle to produce tropospheric ozone

$$NO_2 + h\nu \longrightarrow NO + O \qquad (1.6)$$
$$O + O_2 + M \longrightarrow O_3 + M \qquad (1.3)$$
$$OH + CO \longrightarrow CO_2 + H \qquad (1.7)$$
$$H + O_2 + M \longrightarrow HO_2 + M \qquad (1.9)$$
$$HO_2 + NO \longrightarrow OH + NO_2$$

$$CO + 2\,O_2 + h\nu \longrightarrow CO_2 + O_3$$

Below a critical value of the ratio $[NO]/[O_3]$, ozone loss instead of production can occur *via* the sequence shown in Table 1.2.

Table 1.2 - A loss cycle for O_3 in the troposphere

$$HO_2 + O_3 \longrightarrow OH + 2\,O_2$$
$$CO + OH \longrightarrow H + CO_2 \qquad (1.7)$$
$$H + O_2 + M \longrightarrow HO_2 + M \qquad (1.9)$$

$$CO + O_3 \longrightarrow CO_2 + O_2$$

The tropospheric abundance of ozone is obviously critical in determining the oxidising capacity of the troposphere (Graedel and Crutzen, 1989). This is because ozone is not only an oxidising agent itself but is also the primary source of OH. Further factors determining the rate of formation of ozone, as implied in tables 1.1 and 1.2, are the concentrations of NO_x and the peroxy radical derivatives of CO and CH_4 (as well as other hydrocarbons). Until recently, measurements of NO_x in remote rural regions have been thought to be representative of the "natural" troposphere. However, this is not wholly true; NO_x can be transported over long distances (Singh *et al.*, 1986) in the form of peroxyacetylnitrate (PAN; $CH_3CO.O_2NO_2$) formed by the reaction pathway

$$CH_3CHO + OH \longrightarrow CH_3CO + H_2O \quad (1.13)$$

$$CH_3CO + O_2 \longrightarrow CH_3CO.O_2 \quad (1.14)$$

$$CH_3CO.O_2 + NO_2 \rightleftharpoons CH_3CO.O_2NO_2 \quad (1.15)$$

The thermal equilibrium (1.15) between PAN and its pre-cursers, as shown in equation (1.15), is shifted to the right hand side at lower temperatures. This means at higher altitudes (i.e. lower temperatures) in the troposphere PAN is relatively stable, but if PAN is transported to warmer regions (nearer to the Earth's surface), possibly over large distances and to regions remote from the local (polluted) source, it can dissociate releasing NO_x, i.e. it can act as a reservoir for long range transport of NO_x.

For the majority of organic compounds emitted into the troposphere, reaction by day with the OH radical is the major chemical loss process (Atkinson, 1986)

$$RH + OH \longrightarrow R + H_2O \quad (1.16)$$

where R is an organic species. However, reaction 1.16 may only be a minor loss process for OH (Atkinson, 1989) in comparison with reactions 1.9 and 1.10. The tropospheric fates of a large number of organic compounds have been recently reviewed (Atkinson, 1990).

There is another form of tropospheric oxidising chemistry which takes place, in contrast to OH chemistry, at night. It involves the nitrate radical, the subject of this thesis, and is discussed in detail in §1.3.

1.3 The nitrate radical

The nitrate radical, NO_3, was probably one of the first transient species to be detected by absorption spectroscopy, over 100 years ago by Hautefeuille and Chappuis (1881, 1882a,b). In both the stratosphere and the troposphere, NO_3 is formed by the reaction

$$NO_2 + O_3 \longrightarrow NO_3 + O_2 \qquad (1.17)$$

$$k_{1.17}(298K) = 1.9x10^{-17}\ cm^3\ molecule^{-1}\ s^{-1}\ \text{(DeMore } \textit{et al.}\text{, 1990)}$$

The NO_3 production reaction (1.17) is relatively slow and this goes some way to explaining why NO_3 chemistry is more prevalent in the polluted urban environment, where concentrations of both pre-cursor species tend to be larger than in rural regions. Reaction (1.17) is followed by the reaction

$$NO_2 + NO_3 + M \rightleftharpoons N_2O_5 + M \qquad (1.18)$$

The dinitrogen pentoxide produced in this reaction can act as a reservoir species. Dissociation of N_2O_5 can apparently be an additional source of NO_3, but as N_2O_5 is formed solely *via* reaction 1.18, the ultimate concentration of N_2O_5 is dependent on the occurrence of reaction 1.17. An atmospheric fate of N_2O_5 is the irreversible heterogenous conversion in the presence of water to yield nitric acid

$$N_2O_5 + H_2O \longrightarrow 2\ HNO_3 \qquad (1.19)$$

thus contributing to atmospheric acidification. The implications of reaction (1.19) in the production of NO_3 in regions with relatively low or high humidities, e.g. deserts or marine environments, has been discussed by Russell *et al.* (1986), who showed that in geographical regions with high humidity, production of NO_3 was impaired by loss *via* reactions (1.18) and (1.19).

As a consequence of the chemistry outlined in reactions (1.17) and (1.18), the atmospheric oxidation potential of NO_3 is limited by the availability of O_3 and related to the abundance of NO_2, the atmospheric mixing ratio of which is variable in the troposphere, ranging from ~5ppt to 100ppb (Wayne *et al.*, 1991). Estimated production rates of NO_3 in the boundary layer are *ca.* $6x10^6$ molecule cm^{-3} s^{-1}. The importance of N_2O_5 as a source, or conversely a sink, for NO_3 will depend on temperature, pressure and meteorological factors (Russell *et al.*, 1986).

In the daytime, NO_3 is rapidly photolysed

$$NO_3 + h\nu \longrightarrow NO_2 + O \qquad (1.20a)$$

$$\longrightarrow NO + O_2 \qquad (1.20b)$$

at wavelengths less than 630nm (Magnotta and Johnson, 1980). The combined photolysis rate of channels (1.20a,b) leads to an estimated natural lifetime due to photolysis of *ca.* 5s during the daytime. The relative contributions of various reactions to the production of NO_3 by reactions other than (1.17) have been discussed by Zellner and Weibrig (1991). As well as the photolytic destruction (1.20a,b) of NO_3, there are reactions such as

$$NO + NO_3 \longrightarrow NO_2 + NO_2 \qquad (1.21)$$

$$k_{1.21}(298K)=2.8x10^{-11}\ cm^3\ molecule^{-1}\ s^{-1}\ \text{(DeMore } et\ al.\text{, 1990)}$$

that account for further chemical removal of the nitrate radical. The diurnal variation of nitrogen-oxide species at mid-latitudes has been measured (Logan, 1983) and the concentration of NO_3 drops to less than 1ppt during the day (see figure 1.3).

At night, when the photolysis of both NO_2 (1.6) and NO_3 ceases, the production of NO_3 can proceed *via* reaction 1.17, if the $[O_3]$ and $[NO_2]$ are large enough. Nitrogen oxide, produced

from daytime photolysis of NO_2 (1.6), is converted back to nitrogen dioxide *via* the reaction

$$NO + O_3 \longrightarrow NO_2 + O_2 \qquad (1.22)$$

$k_{1.22}(298K)=1.8x10^{-14}$ cm^3 $molecule^{-1}$ s^{-1} (DeMore *et al.*, 1990)

In the dark, clean atmosphere the ultimate concentration of NO_3 is controlled by reactions 1.17 and 1.18. The stationary-state concentration of the nitrate radical ($[NO_3]_{ss}$) is given by

$$[NO_3]_{ss} = \frac{k_{1.17}[O_3]}{k_{1.18}[M]} \qquad (1.23)$$

At T=293K, $[O_3] = 1.25x10^{12}$ molecule cm^{-3} and a pressure of 1013mb, $[NO_3]_{ss} \approx 2.7x10^7$ molecule cm^{-3}. The time taken to achieve this stationary state can be up to 2 hours in the presence of *ca.* 40ppt of NO_2 (Wayne *et al.*, 1991).

There are further loss processes to be considered in the dark, clean troposphere. The first is the possibility of heterogenous loss of NO_3

$$NO_3 + H_2O(\ell) \longrightarrow \text{Products} \qquad (1.24)$$

The nitrate radical does not react with water itself (1.24) but will react with dissolved anions (Dogliotti and Hayon, 1967),

$$NO_3(g) + Cl^-(\ell) \longrightarrow NO_3^-(\ell) + Cl(g) \qquad (1.25)$$

This heterogenous loss to, anions present in, water surfaces is in accordance with field measurements (e.g. Platt *et al.*, 1984). A possible second loss process is the unimolecular decomposition of NO_3. Johnston, Cantrell and Calvert (1986) reported evidence from both laboratory and field studies in support of the existence of this loss process but there is still a discrepancy between the upper limits for this process from both types of studies and the relative contribution in the atmosphere (Russell *et al.*, 1986).

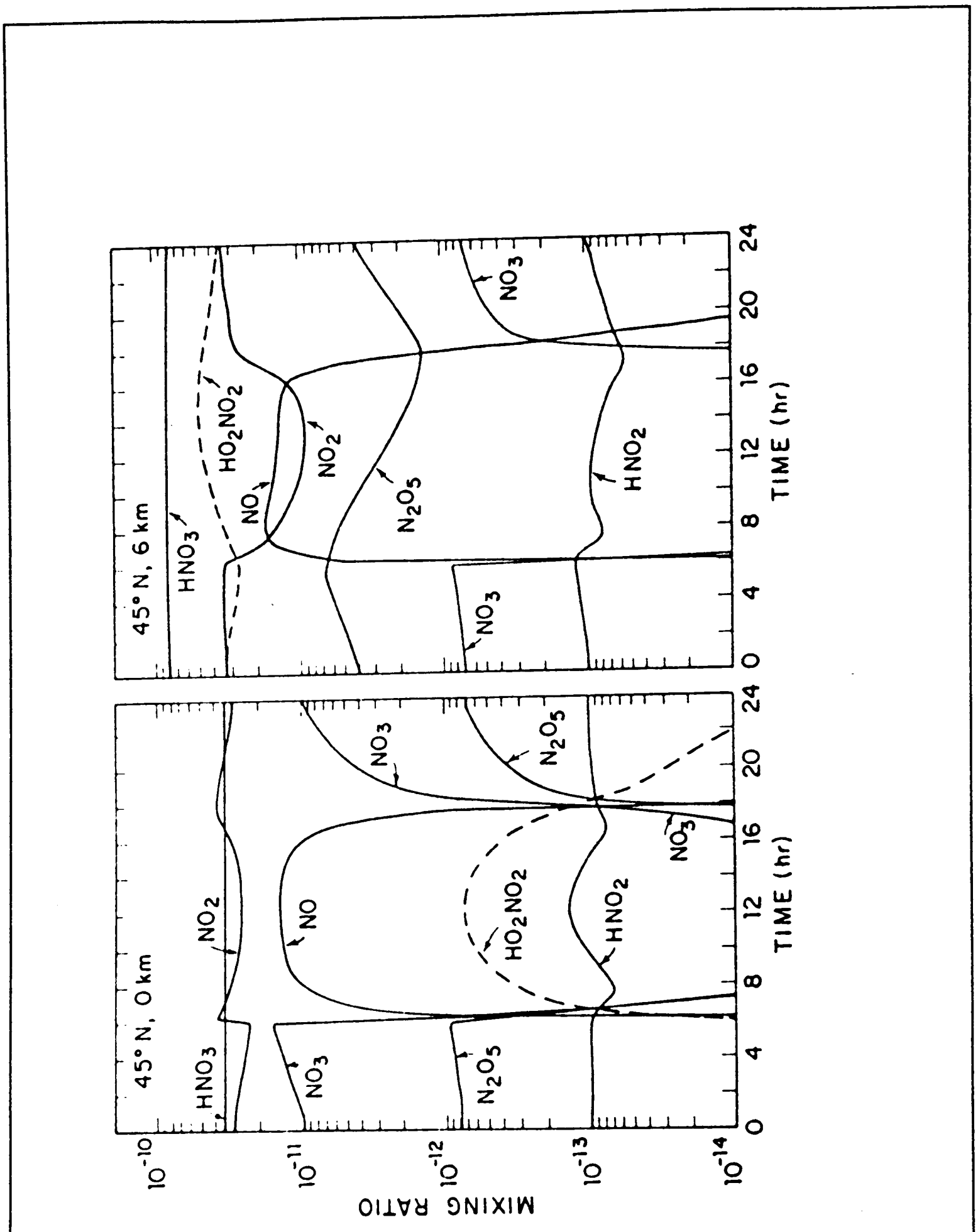

Figure 1.3 The diurnal variation in the [NO_3] and other nitrogen oxides at mid-latitudes (Logan, 1978)

The nitrate radical was first detected in the night-time stratosphere by Noxon *et al.* (1978). This was followed by the confirmation of the presence of NO_3 in the troposphere by Platt *et al.* (1980). The role of NO_3 scavenging by both aqueous media and organic compounds has been described by Perner *et al.* (1991). As an air parcel containing terpenes passed through the atmospheric observation area, there was a simultaneous drop in the observed $[NO_3]$. This discovery of tropospheric scavenging of NO_3 at night highlights the role of the nitrate radical as an active participant in the free-radical chemistry of the troposphere. Though the OH radical is the most important agent of attack on organic species, NO_3 will usually be the most important oxidising species in the troposphere at night. The reactions of NO_3 with organic compounds can be broken down into two classes of reactions, based on the form of the initial step. The first class are the hydrogen abstraction processes of the type

$$NO_3 + RH \longrightarrow HNO_3 + R \qquad (1.26)$$

The second class are addition processes to unsaturated double bonds of the type

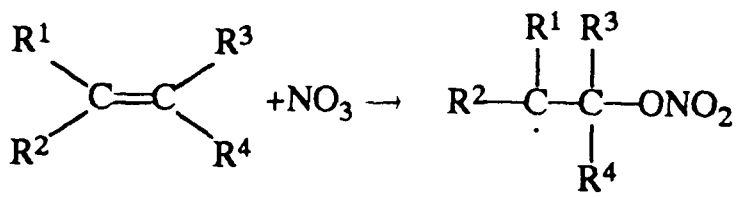

(1.27)

The products of reaction (1.26) are HNO_3 (which can contribute to atmospheric acidification) and a radical. This radical in the presence of oxygen is likely to form a peroxy radical (RO_2). If RH is an aldehyde, the acyl radical products of reaction (1.26) could yield acylperoxy radicals($R.CO.O_2$), a potential source of peroxyacylnitrates. The adduct formed in reaction (1.27) can either eliminate NO_2 to yield an epoxide or, in the presence of oxygen and NO_2, form a nitrate (Wangberg *et al.*, 1990) (See figure 1.4). The behaviour of NO_3 in the troposphere is summarised in figure 1.5.

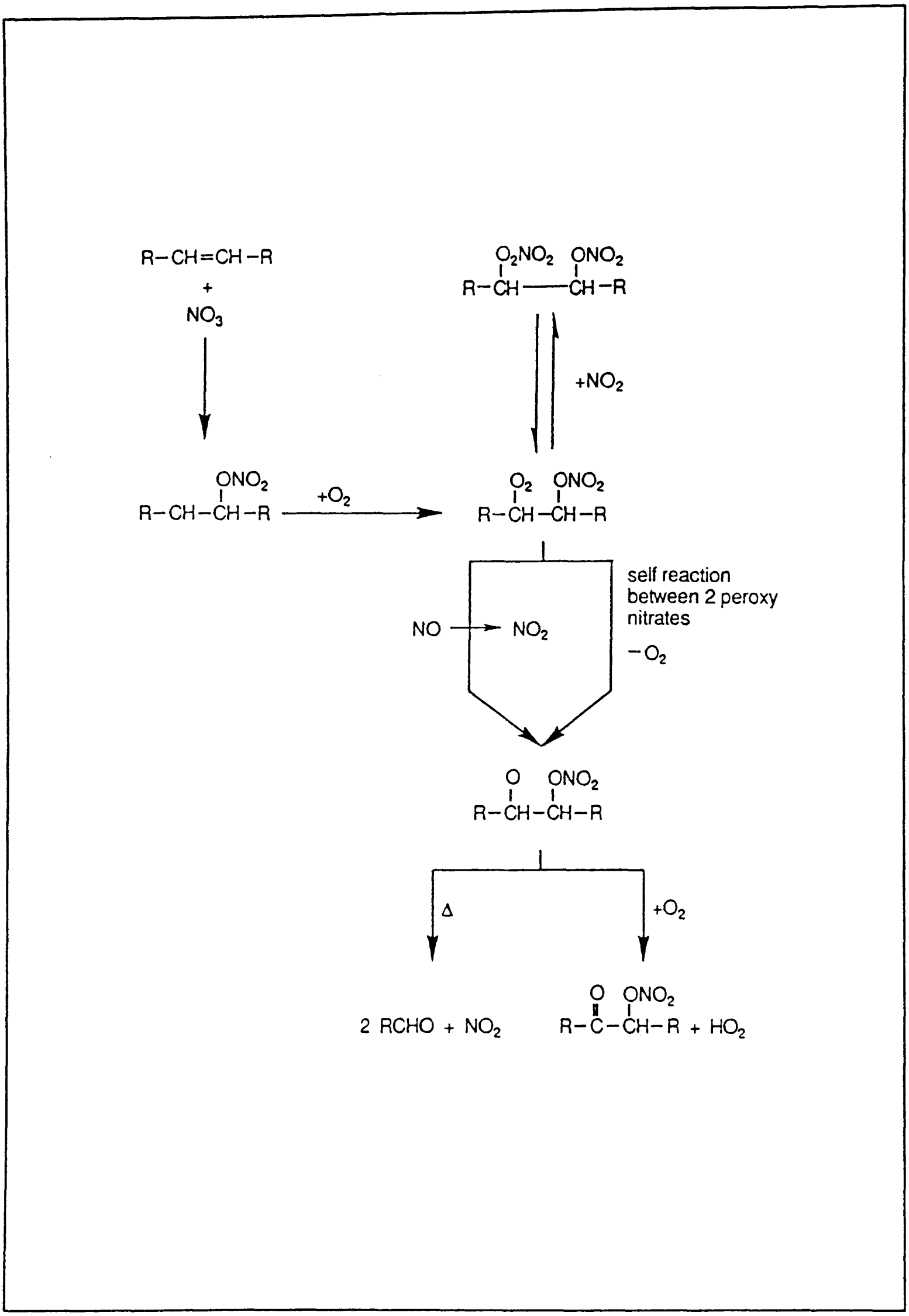

Figure 1.4 The volatile organic compound oxidation chain for the reaction of NO_3 with an alkene.

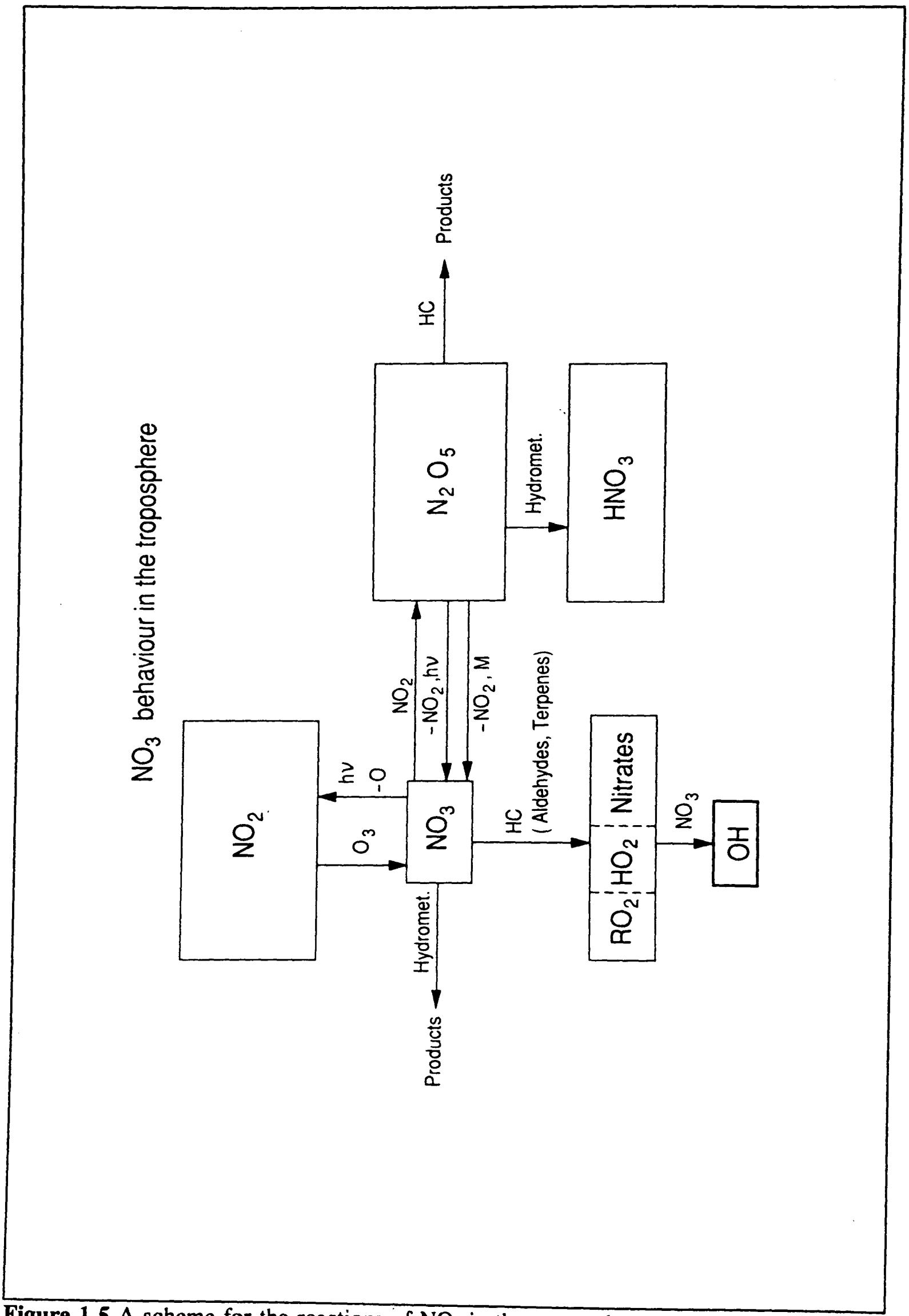

Figure 1.5 A scheme for the reactions of NO_3 in the troposphere

For some compounds e.g. dimethylsulphide (DMS) (Cox, 1990), phenols, cresols (Carter, 1990) and terpenes (Wayne *et al.*, 1991) the reaction with NO_3 is a more important atmospheric loss process than reaction with OH. DMS is the most abundant of all biogenic-sulphur compounds, being produced by phytoplankton in oceanic surface waters (Andreae, 1987). Depending on the availability of NO_x species in coastal regions (Prospero and Savoie, 1989), the reaction of NO_3 with DMS could contribute significantly to the formation of HNO_3 in such areas. The reaction can either be an addition (1.28a) or an abstraction process

$$NO_3 + CH_3SCH_3 \longrightarrow CH_3SONO_2 + CH_3 \quad (1.28a)$$

$$\longrightarrow CH_3SCH_2 + HNO_3 \quad (1.28b)$$

Jensen *et al.* (1991) have tentatively concluded that reaction (1.28b) is the more dominant product channel.

One particularly extreme form of atmospheric pollution, which causes eye irritation, plant damage and visibility degradation is *Photochemical* or *Los Angeles Smog* (Finlayson-Pitts and Pitts, 1985). The smog is formed by the action of photochemically produced oxidants such as O_3, NO_2 and peroxyacylnitrates (PAN) on mixtures of NO_x and hydrocarbons (Leighton, 1961). The chemistry taking place implicitly involves the action of OH on hydrocarbons to produce peroxy radicals, which subsequently drives the NO to NO_2 conversion (see figure 1.2) (Finlayson and Pitts, 1977). It is the PAN produced as a by-product (1.13-1.15) (Finlayson, Pitts and Winer, 1977) of the photochemical oxidation cycle which is of the most harm to man (Wayne, 1991). The implication in photochemical smog production is that the peroxy-chemistry is driven by the photolytic production of the precursors by sunlight. There is a recent suggestion by Platt *et al.* (1990), that an analogous cycle could be driven at night-time by NO_3. Night-time concentrations of RO_2 of up to 1.2×10^{10} molecule$\cdot$cm^{-3} have been

measured (Micelcic *et al.*, 1985). The rate limiting step in the reaction scheme presented is the formation of RO_2 and RO radicals, by the reaction of NO_3 with an organic compound. Rapid consecutive reactions lead to RO_2 radicals which are lost either by self-reaction or by reaction with NO_3. In subsequent steps, HO_2 radicals are produced, which can be partly converted to OH via the reaction

$$HO_2 + NO_3 \longrightarrow OH + NO_2 + O_2 \qquad 80\% \qquad (1.29a)$$

$$\longrightarrow HNO_3 + O_2 \qquad 20\% \qquad (1.29b)$$

The mechanism presented by Platt *et al.* (1990), is itself tentative due to the uncertainties in a number of the rate constants.

In conclusion, the involvement of NO_3 in tropospheric chemistry has six significant consequences:

i) At night, the radical controls the 'odd-nitrogen' budget in the atmosphere *via* reaction 1.18;

ii) It contributes to night-time atmospheric acidification by production of HNO_3, either from hydrolysis of N_2O_5 (1.19) or as product from a hydrogen abstraction process (1.25);

iii) Primary organic pollutants, as well as natural compounds, can be oxidised and removed during the night;

iv) Free radicals produced by the reaction of NO_3 with an organic compound, which probably undergo rapid conversion to HO_2 and RO_2, can participate in further (NO_3 initiated) oxidation chain reactions;

v) Toxic and noxious compounds, e.g. peroxyacetylnitrates, as well as other nitrate and

oxidised compounds, may be formed;

vi) Products of the reaction of NO_3 with certain classes of compounds can act as temporary reservoirs for NO_x in the atmosphere; these compounds can subsequently be transported over long distances.

The following chapters describe work performed to investigate the chemistry of the nitrate radical, mainly of relevance to tropospheric chemistry.

Chapter 2

The reaction of NO_3 with a series of halo-butenes and 1-butene

2.1 Introduction

The urban troposphere contains a wide range of organic compounds. In a recent survey of ambient air masses of U.S. cities, more than 100 different hydrocarbons were identified (Seila and Lonnemann, 1988). The oxidation of these compounds by OH during the day and NO_3 at night in both the polluted and unpolluted troposphere has been outlined in Chapter 1. Although most saturated organic compounds react in the gas phase faster with OH than with NO_3, there are two factors to take into consideration when comparing tropospheric loss rates for certain classes of organic compounds, e.g. alkenes. The first is that the range of rate constants for the reaction of alkenes with NO_3 extends from $2x10^{-16}$ cm^3 $molecule^{-1}$ s^{-1} for ethene (40,000 times smaller than that for reaction with OH) to $2x10^{-11}$ cm^3 $molecule^{-1}$ s^{-1} for α-terpinene (similar to that for reaction with OH). The second factor is the average concentration of NO_3, which by night is about 1000 times larger than the average daytime concentration of OH. Reaction with NO_3 is therefore the major oxidation route for many unsaturated species, making a knowledge of the reactivity patterns exhibited by NO_3 a key issue for a better understanding of tropospheric chemistry (Wayne *et al.*, 1991) (§2.7).

In this chapter we present a study of the reaction of NO_3 with a series of halo-butenes and the parent unsubstituted compounds. The data are presented in two sections; the first covers the reaction of NO_3 and 1-butene (§2.4) studied under pseudo-first order conditions. The second section (§2.5) considers the reactions of NO_3 with a series of halo-substituted 1-butenes and 2-butenes. The kinetic data were obtained using the discharge-flow technique coupled to optical-absorption detection of NO_3. A brief outline of the discharge-flow technique is given in §2.2. A simple argument is presented (§2.6) in order to explain the

observed reactivity of these compounds in terms of substituent effects. A more thorough rationale of the kinetic data for these reactions in terms of patterns of reactivity is given in Chapter 3.

2.2 Kinetic measurements using the discharge flow technique

The flow tube kinetic method has evolved from the early discharge tube studies of Wood (1905) (Dieke, 1956) and Bonhoeffer (1924). R.W. Wood applied the method mainly to spectroscopic problems and he could be said to be the "father" of resonance fluorescence (Wood and Mohler, 1918). The first kinetic measurements using a flow tube were made in the late 1920s by Smallwood (1929) on the rate of recombination of H. At about the same time a group of chemists working under Bonhoeffer (1924) began making kinetic measurements in a discharge-flow system. The important step in their work was the invention of a gauge for measuring partial pressures of gases in discharged mixtures, the Wrede-Hartreck gauge (Hartreck, 1928; Wrede, 1929). In the late 1950s and early 1960s, the discharge-flow technique began to take-off as the major source of thermal rate data. In 1958, Kaufman (1958) demonstrated the first titration reactions using the air-afterglow system. This breakthrough provided a clean quantitative method of preparing labile species. The development of discharge flow as an important technique in gas-phase kinetics had become possible with major developments in instrumentation namely, mass spectrometry (Hipple and Stevenson, 1943) and electron paramagnetic resonance (Beringer and Castle, 1949), and their application to the detection of radicals and stable species under flow conditions. With the advent of this technology coupled to the discharge-flow technique there was an explosion in the number and type of kinetic systems that could be studied with increased sensitivity and

therefore accuracy.

There are many variants of the discharge-flow technique, but they can all be described as a '*pump - probe*' type of experiment. In conventional discharge-flow experiments the pump phase involves electrodeless discharge, photolytic or thermal generation of the reactive species. The time delay between the '*pump*' and '*probe*' is given by the flow time between the mixing and detection regions. The versatility of the probe phase (i.e. detection) of a discharge-flow experiment is discussed in §4.3.

The basic precept of the discharge-flow technique is that for anything moving at a constant velocity, the distance travelled is proportional to time. Thus, since species can be generated separately and brought together, the measurement between the point of mixing of the species and detection allows the time that gases have been in contact to be calculated. By varying either the point of injection or that of detection the time evolution in the concentration of a radical or stable species can be established, i.e. in any fixed distance from the point of mixing the concentrations of reactants are invariant with respect to time. This premise only holds, if the flowdynamics satisfy certain criteria:

i) the gas flow is laminar (i.e. non-turbulent);

ii) the flow velocity ($\bar{v}$) of the gases are constant along the reaction vessel (i.e. tube);

iii) there are no radial concentration gradients.

The discharge-flow apparatus used in this work is shown in figure 2.1. It is illustrative of a typical discharge-flow apparatus. A carrier-gas, M, in our case He, enters the flow tube through a side-arm at the back of the flow tube. As the carrier gas constitutes the major component (*ca.* 95%) of the flow, it defines the physical properties of the gas-stream.

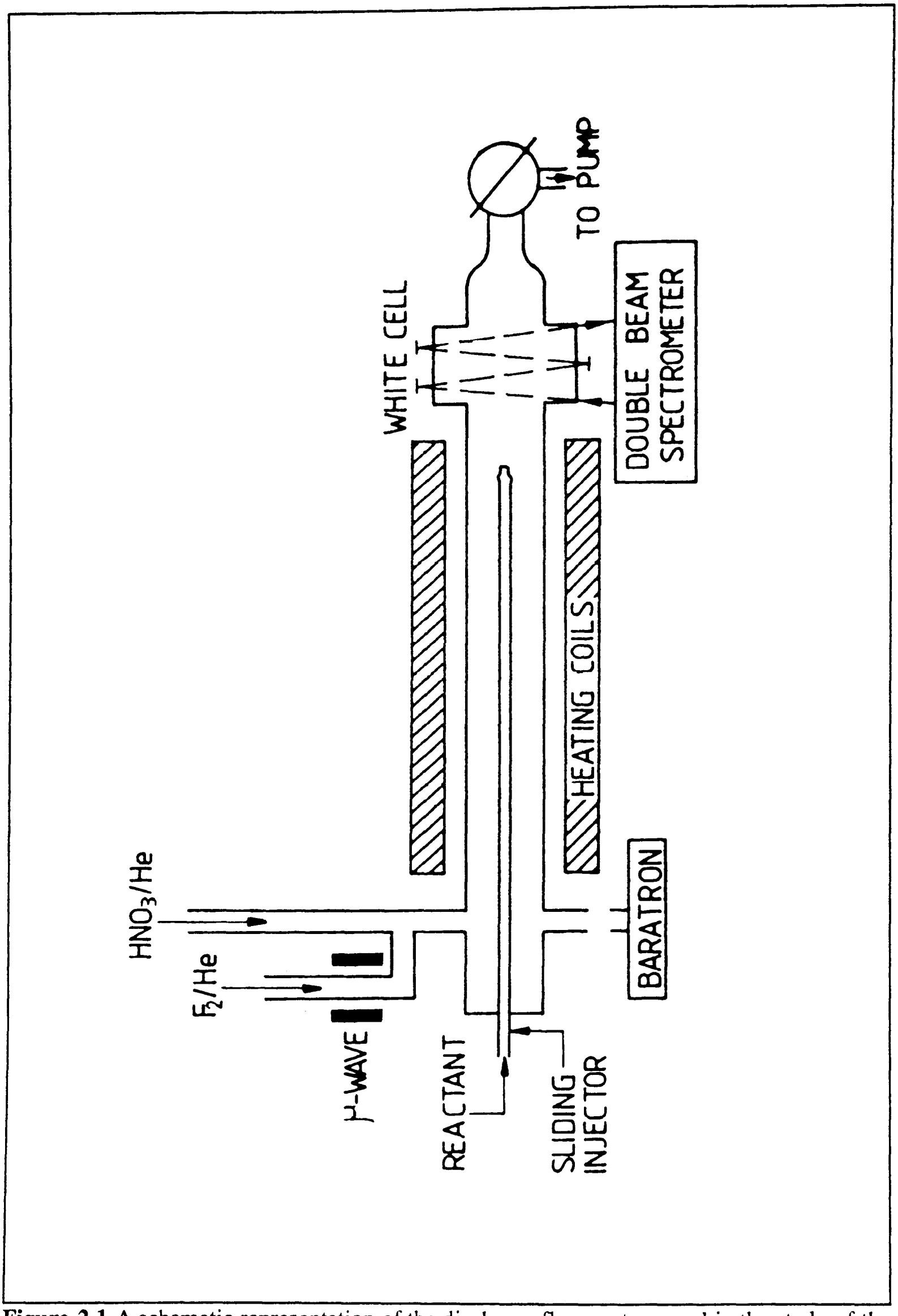

Figure 2.1 A schematic representation of the discharge flow system used in the study of the reactions of NO_3.

Helium is a good carrier gas because of its chemical inertness, high thermal conductivity so that it can act as a heat bath maintaining the reactants at the same temperature as the wall, it has excellent diffusional coefficients, it is monoatomic and so largely unaffected by microwave discharge and can serve as a (poor) third-body in termolecular reactions.

The type of flow that develops in a tube of circular cross-section (radius=R), is characterised by the Reynolds number (R_e) (Kay and Nedderman, 1985). The Reynolds number is a dimensionless ratio which is dependent on the physical parameters of the carrier gas

$$R_e = \frac{2R \times \bar{v} \times \rho}{\eta} \qquad (2.1)$$

where the flow velocity, $\bar{v}$, the viscosity of the gas, the density of the gas, η. If the Reynolds number is <2000, the flow is said to be laminar or streamline; when conditions are such that R_e >2000 there is the possibility of turbulent flow. Flow tubes are typically operated under conditions where $R_e < 100$. In this work $\bar{v}$ ranged from about 200 to 1100 cm s^{-1} (see equation 2.2) giving $2<R_e<10$ [for He, $\eta=1.96\times10^{-5}$ kg m^{-1} s^{-1} and $\rho=4.3\times10^{-4}$ kg m^{-3} at a pressure of 2 Torr (Matheson Company Inc., 1971)] such that streamlined flow can be assumed at all times. If the pressure becomes too low, the mean free path, λ, of the molecules in the carrier gas becomes comparable with the diameter of the flow tube and the flow is described as "slip-flow" ($0.02<\lambda<1.3R$).

The flow speed, or linear flow velocity, $\bar{v}$, can be calculated, providing the flow rates of all the gases, F (i.e. Σf_i), flow tube pressure, P_T, temperature, T, and cross-sectional area, A, are known

$$\bar{v} = \frac{F \times T}{P_T \times A \times \phi} \qquad (2.2)$$

where ϕ is a constant relating the quantities which depends on the units of the variables in equation 2.2. If A is in cm^2, P_T in Torr, F in molecule s^{-1}, T in K and $\bar{v}$ in cm s^{-1} then ϕ is 9.658×10^{18} molecule cm^{-3} $Torr^{-1}$ K. All the parameters required to calculate $\bar{v}$ can be determined experimentally.

The linear flow velocity can be used as a measure of contact time if 'plug-flow' is occurring. It occurs when all the gases within the flow tube are moving with a constant average velocity, i.e. the velocity profile is uniform over the radial cross-section. This is obviously not the case in laminar flow because viscous drag at the walls will cause the velocity profile to be parabolic. The parabolic Poiseille velocity distribution is described as

$$v_r = 2v_{r=0}\left(1 - \frac{r^2}{R^2}\right) \qquad (2.3)$$

where R is the radius of the tube and r is the co-ordinate distance from the centre of the tube, making $v_{r=0}$, the velocity of the gas at the centre of the tube (*c.f.* plug flow where $v_r = v_{r=0}$ =constant). However, a uniform radial concentration will exist if the diffusional dispersion of species within the tube is sufficiently fast that the concentration profile is invariant with r. This rapid diffusion of species generally occurs at total pressures of less than 5 Torr (depending on RMM)[i], so that at these low pressures the assumption of plug-flow is valid.

Flow tubes are normally operated at pressures and concentrations which simultaneously make the experiment possible and minimise the number of corrections to the observed rate constant because of diffusion of the reactive species. There are two possible types of diffusion that

[i] RMM - Relative Molecular Mass

can take place in a flow tube, namely

i) radial diffusion - concentration gradients across the flow tube;

ii) axial diffusion - net diffusive flux along the axis of the tube.

The experimental conditions that are likely to make radial concentration gradients more significant are

a) a radical of large relative molecular mass;

b) a high pressure in the flow tube (as $D \propto 1/P$);

c) large heterogenous losses of the radical at the wall.

The first two factors serve to limit the rate of diffusion and prevent radial concentration gradients being eliminated. The third factor serves to enhance the radial concentration gradient, which can be further excerbated if the flow velocities are such that the gas near the walls has a longer residence time than the faster moving reactants in the centre (*c.f.* plug-flow).

The second diffusional correction is required because a concentration gradient is set up along the tube as reaction takes place, the axial concentration gradient being greater the larger the extent of reaction. The net diffusive flux will behave in accordance with Fick's first law.

$$J = -D \frac{dc}{dz} \qquad (2.4)$$

where J is the diffusive flux (molecule cm^{-2} s^{-1}) and D is the diffusion coefficient (cm^2 s^{-1}) (Merrero and Mason, 1972). Axial diffusion will be important under conditions where

a) the radical is of low relative molecular mass;

b) the total pressure in the flow tube is low;

c) the homogenous reaction of interest is fast.

Accurate diffusional correction factors, taking account of both radial and axial diffusion, can be obtained by solving the continuity equation (Judeikis, 1980). For most purposes several approximate formulations suffice. For example, under typical conditions when wall losses are small and diffusion is rapid compared with the rate of reaction, (k) the (pseudo-)first-order decay of the minority constituent can be calculated from the phenomenological rate coefficient (k_{exp}) by (Keyser, 1984)

$$k = k_{exp}\left(1 + \frac{k_{exp}D}{\bar{\nu}^2} + \frac{k_{exp}R^2}{48D}\right) \qquad (2.5)$$

where D is the diffusion coefficient of the radical (minority) species through the bath gas. The first term of equation 2.5 is a correction due to axial diffusion and the second a correction due to radial diffusion. Recent examples of the application of these types of corrections to flow tube studies include Abbatt and Anderson (1991) and Keyser (1991).

2.3 Experimental details

2.3.1 Apparatus

The discharge flow apparatus used in this study is represented schematically in figure 2.1

The flow tube was made from borosilicate glass (Pyrex) tubing of internal diameter 38 mm and length 120 cm. For the investigation of the reactions of NO_3, the internal surface was uncoated. The downstream end of the flow tube was connected *via* a glass screw joint (Soverel 42, J. Bibby Ltd.) to the detection region (§2.3.3). After the detection region a greased tap allowed the gases to flow from the flow tube through a glass trap, held at liquid

nitrogen temperature (T=77 K), to a pump with a large ballast volume (Edwards ES200). With helium as the bath gas, this arrangement allowed flow velocities of between 2 and 6 ms^{-1} at T=298 K. The organic reactants were introduced through a sliding injector, also made from Pyrex, of external diameter 15 mm. The tip of the injector had a spray-nozzle to ensure rapid mixing of the reactants into the carrier flow. The flow tube was sealed at the upstream end by an aluminium block bored out to the appropriate size to allow the injector to move freely. A pair of 'O'-rings set apart in grooves inside the block provided the vacuum seal around the injector, the volume in between being pumped by a rotary pump (Edwards ES50). The position of the sliding injector could be changed from between 5 to 70cm from the centre of the observation region giving contact times in the region of 16 to 200ms. Pressures inside the flow tube were measured by a capacitance manometer (MKS Baratron 170M, 10 Torr range) and were in the region of 1.5-2 Torr.

The gas handling manifold consisted of two lines, made from Pyrex with PTFE taps (Youngs Scientific Ltd.). On the first line, which was pumped *via* the flow tube, were the storage bulbs required for the reactant (2 dm^3) and fluorine mixtures (5 dm^3). Pressures within the storage bulbs were measured with glass bourdon or "spoon" gauges (Wayne,1981), which are particularly robust for the pressure measurement of corrosive gases. Low pressures within this manifold were measured using the same capacitance manometer as was employed on the flow tube. The second manifold was kept at a higher vacuum by an oil diffusion pump (Edwards EO 1A) backed by a rotary pump (Edwards ES50), the pressures being measured *via* Pirani and Penning gauges (Edwards).

Flows from the storage bulbs or gas cylinders were monitored using ball flow meters (Jencon,

RS Type) and regulated with stainless steel fine-flow meters (Nupro). A brass needle valve (Edwards) was used to regulate the main helium flow.

The flow tube was heated by an oven 1.2 m long, containing 6 longitudinal heating elements. The temperature was regulated electronically and the oven was able to provide stable temperatures between room temperature and 473 K. An extra, independently regulated heater was used for the first 20 cm upstream portion of the flow tube, ensuring an uniform temperature profile at longer contact times and the pre-heating of reactants entering the flow tube. The constant temperature region ended *ca.* 30 cm from the observation region, which was at room temperature (see figure 2.2). Four type-K British standard (Ni-Al and Ni-Cr) thermocouples were attached to the flow tube, two in the middle section and one at each end of the main heater. Each one was provided with a digital readout (PCL construction). The centre thermocouple (*ca.* 44 cm from the observation region) was attached to a thermocouple amplifier with built-in ice-point compensation and set-point mode operation. The temperature of the flow tube could be regulated to ±3 K of the set-point temperature (Canosa-Mas *et al.*, 1988).

2.3.2 Production of NO_3

A number of different methods for production of the nitrate radical (Wayne *et al.*, 1991) are available in discharge-flow based studies.

In the work presented here, NO_3 radicals were generated by the reaction

$$F + HNO_3 \longrightarrow HF + NO_3 \qquad (2.6)$$

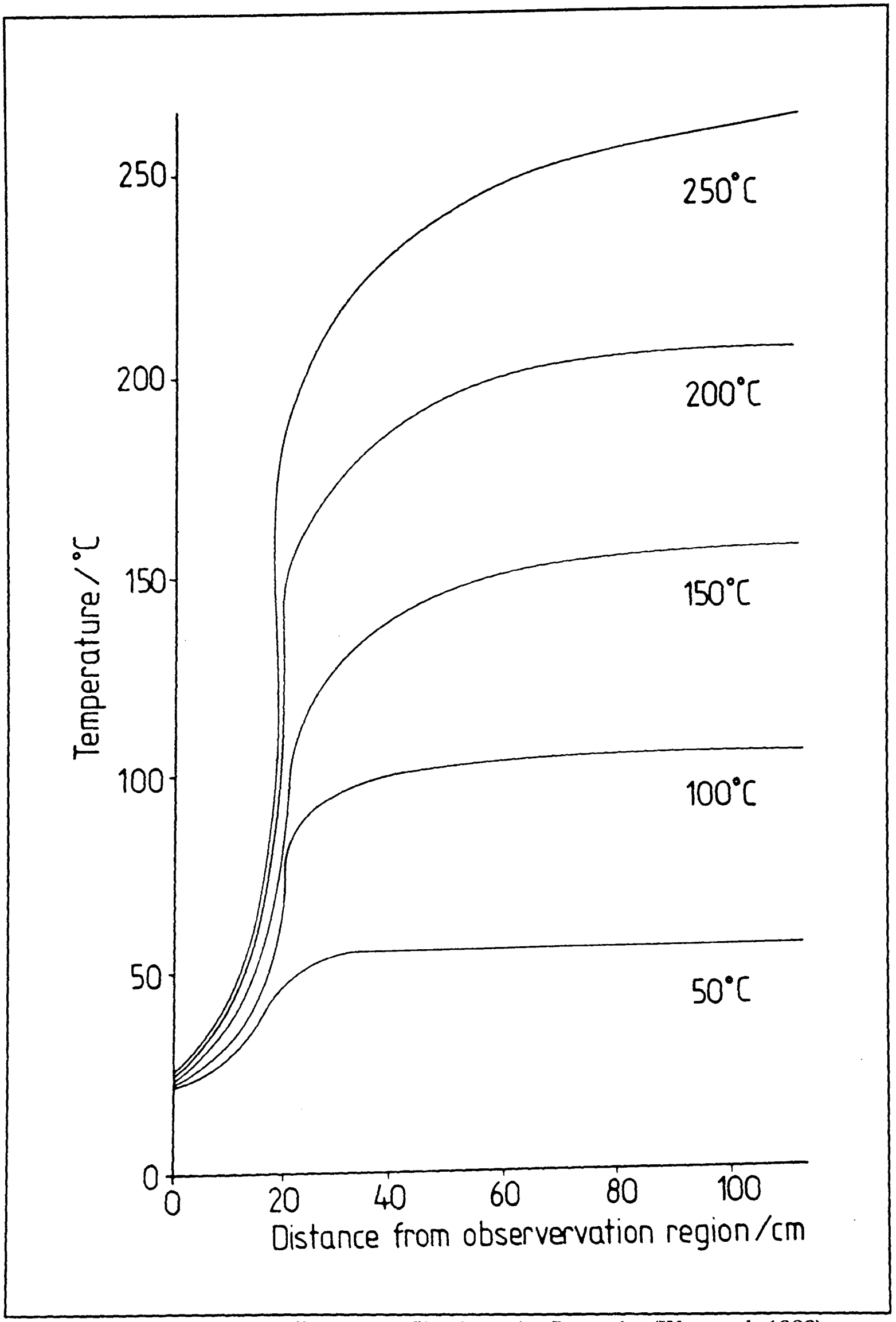

Figure 2.2 The temperature-distance profile along the flow tube (Waygood, 1988)

and admitted at the back of the flow tube. Fluorine atoms were generated by a 2450MHz microwave discharge (Power supply, E.M.S. Microtron 2000) on a mixture of *ca.* 5% fluorine in helium. Anhydrous nitric acid vapour was provided by bubbling helium through a 1:2 mixture of HNO_3 with sulphuric acid held at approximately 258 K by surrounding it with a slush bath consisting of solid CO_2 and ethylene glycol. Reaction 2.6 is rapid with a rate constant at room temperature of $(2.7\pm0.5)\times10^{-11}$ cm^3 molecule^{-1} s^{-1} (Mellouki *et al.*, 1987); it is exothermic by over 150 kJ mol^{-1}. HF, the other primary product of reaction 2.6, is relatively inert in this system, making it a particularly clean source of NO_3. The ratio of $[F]_o/[HNO_3]_o$ is critical for optimal production (Canosa-Mas *et al.*, 1987) of NO_3. If $[F]_o>[HNO_3]_o$, several secondary reactions become important

$$F + NO_3 \longrightarrow FO + NO_2 \qquad (2.7)$$

$$k_{2.7} = 3\times10^{-11} \text{ cm}^3 \text{ molecule}^{-1} \text{ s}^{-1} \text{ (Rahman } et\ al.\text{,1988)}$$

$$FO + NO_3 \longrightarrow FO_2 + NO_2 \qquad (2.8)$$

$$k_{2.8} = 1\times10^{-12} \text{ cm}^3 \text{ molecule}^{-1} \text{ s}^{-1} \text{ (Rahman } et\ al.\text{,1988)}$$

$$FO + FO \longrightarrow F + F + O_2 \qquad (2.9)$$

$$k_{2.9} = 1.5\times10^{-11} \text{ cm}^3 \text{ molecule}^{-1} \text{ s}^{-1} \quad \text{(De More } et\ al.\text{, 1990)}$$

Canosa-Mas *et al.* (1987) showed that increasing the $[F_2]$ that passed through the microwave cavity resulted in a steady build-up in $[NO_3]$ to an optimum concentration followed by a rapid fall-off as reactions 2.7-2.9 became important.

2.3.3 Detection of NO_3

Optical spectroscopy is a versatile technique for the detection of gas-phase species, since it can be specific, sensitive and non-invasive. In the case of the NO_3 radical, one electronic

transition lies conveniently in the visible region of the electromagnetic spectrum (see figure 2.3). The transitions leading to this spectrum are not unambiguously assigned. What is thought to be the 0-0 band is at λ=661.9 nm and is the most intense transition in the spectrum. The λ=623.5 nm band is the first member of the symmetric stretching vibration and has roughly ⅔ of the peak absorption of the band at λ=661.9 nm. These absorptions are fairly narrow and have the advantage of lying clear of the absorptions of other interfering species with the exception of O_3 and NO_2 (Okabe, 1971).

In the present study, NO_3 was detected by monitoring the optical absorption at λ=662 nm. The light source (quartz-halogen lamp, 100 W) and monochromator were part of a Pye dual-beam spectrophotometer (model SP700A). The monochromatic light from the sample beam channel of the spectrophotometer was reflected into the four-pass White cell (White,1942) before being reflected into the detection region of the instrument (see figure 2.4 for the optical layout). The dual-beam operation of the instrument allows the detection of smaller changes in absorption than is possible with single-beam operation. The amount of light passing through the sample channel must be the same as that passing through the reference channel when there are no absorbing species present. The correct optical balance was achieved by placing filters of differing optical density in the reference beam channel. On entrance to the sample/reference compartments, an optical chopper modulated both the sample and reference light beams. A piece of soft iron attached to the chopper blades allowed the pick-up coils to supply a 25 Hz reference signal for the boxcar. The reference for the 300 Hz signal was provided by a vane placed *ca.* 1 mm from the chopper blades which acted as a variable condenser. The modulated light beams fell onto a photomultiplier, which passed a signal to an amplifier and a dual-boxcar (Abernathy,1970), where it was de-multiplexed using the

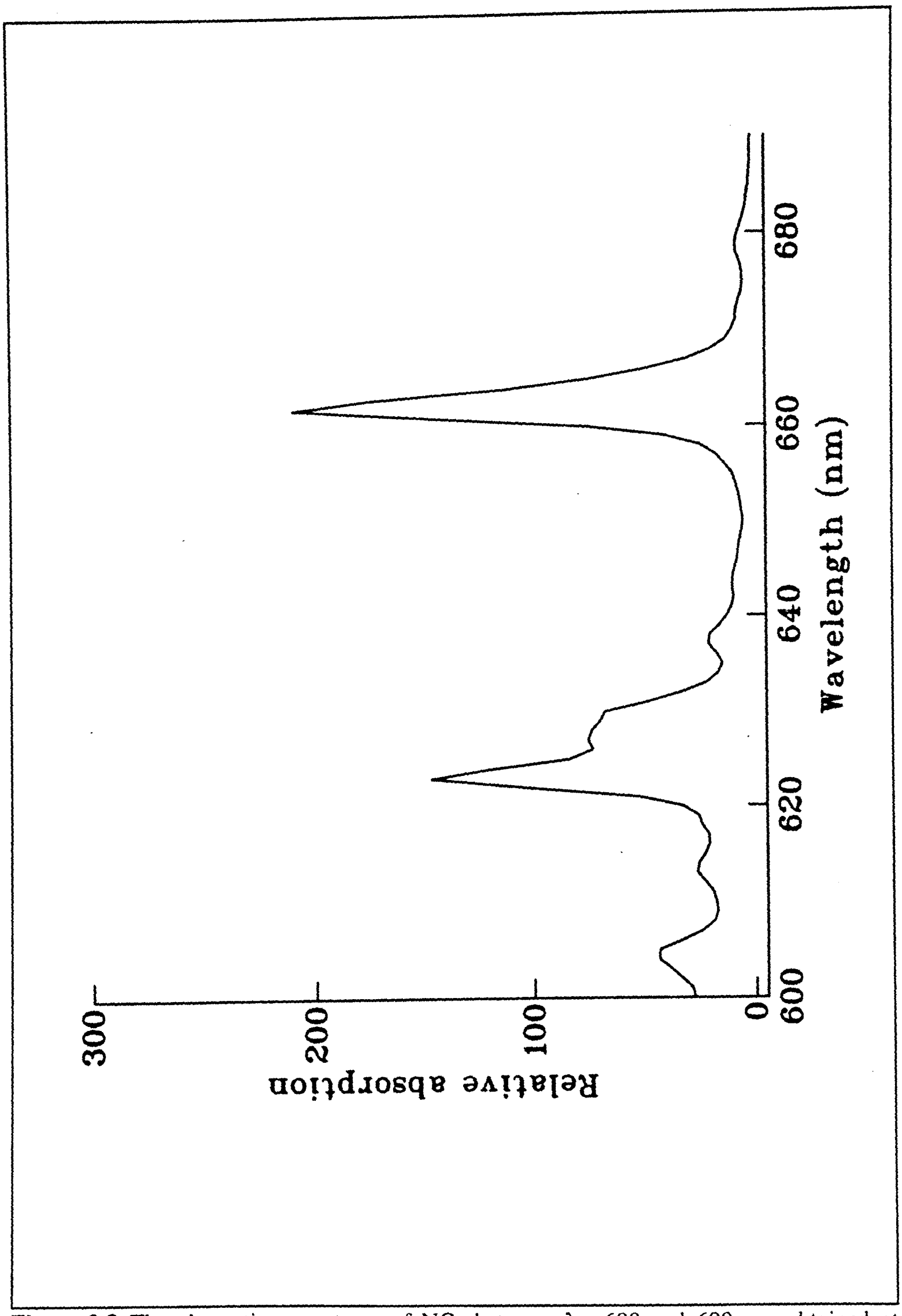

Figure 2.3 The absorption spectrum of NO_3 between λ= 600 and 690 nm obtained at T=298 K (Sander, 1986)

reference signals, then filtered. A boxcar (Rabek, 1982) provides a means of detecting repetitive signals buried in noise. The boxcar has a sample-and-hold system, the sampling time being determined by the reference signal from the chopper. The reference pulse triggers a pulse generator which can produce a square-wave pulse of given duration and delay which is used to gate or "window" the signal. The boxcar integrates the signal over this pre-defined gating period. The dual-boxcar arrangement allows the signals from both the sample and reference channels to be integrated. The output difference signals from the reference and sample boxcars were subtracted from each other to provide a signal which was proportional to the small absorptions taking place in the cell. The output signal was further amplified and filtered before being passed to the chart recorder (Goertz Servoscribe). The boxcars had integration times of *ca.* 1 s. The detection limit for NO_3, for a signal to noise ratio of 1:1 and with an integration time of *ca.* 10 s, was typically 10^{12} molecule cm^{-3}.

2.3.4 Absolute concentrations of NO_3

In optical-absorption studies there is often a need to know the absolute concentration of a atom or radical species. For NO_3 in flow-tube studies there are three reasons to know the absolute concentration:

a) to ensure pseudo-first order kinetic conditions are maintained.

b) to provide $[NO_3]$ should numerical modelling be required.

c) to test whether the optical system is performing in the correct manner.

Optical absorbances are related to concentration by the Beer-Lambert law (2.10)

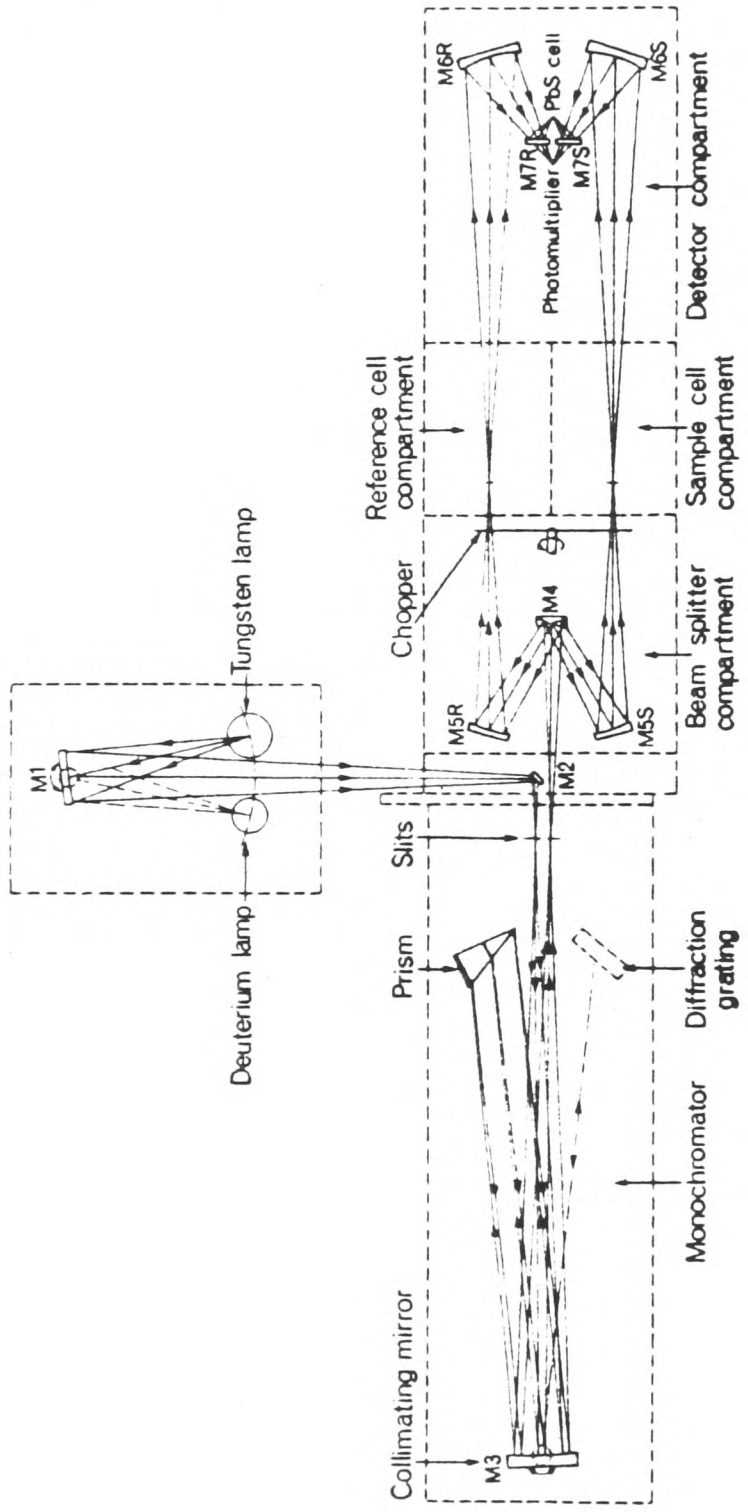

Figure 2.4 The optical layout of the SP700A spectrophotometer, the sample compartment was modified to direct the beams into a multi-pass White cell.

$$I_t = I_o \exp(-\sigma c l) \tag{2.10}$$

where I_o is the intensity of the transmitted light in the absence of any absorbing species, I_t is the intensity of transmitted light in the presence of absorbing species, σ is the absorption cross-section, c is the concentration of the absorbing species and l is the geometric path length. The relationship between I_t and I_{abs} (the amount of light absorbed), which is more useful in dual-beam operation, is given by equation (2.11)

$$I_t = I_o - I_{abs} \tag{2.11}$$

It therefore follows from equation 2.10 that

$$\ln\left(1 - \frac{I_{abs}}{I_o}\right) = -\sigma\, c\, l \tag{2.12}$$

When the amount of absorption is small, i.e. I_{abs}/I_o is small; a Taylor expansion of the logarithm and ignoring higher powers of I_{abs}/I_o leads to

$$\frac{I_{abs}}{I_o} \simeq \sigma\, c\, l \tag{2.13}$$

This equation is the more usual form of the Beer-Lambert law used in the analysis of pseudo-first-order kinetics presented later in this chapter, where I_{abs}/I_o is rarely greater than 0.02, such that the approximation made in equation 2.13 is valid.

From equation 2.10 it can be seen that if you want to determine the absolute concentration of an absorber you must first determine the absolute absorption cross-section (σ). In discharge-flow studies the methodology behind our experimental measurement of σ was first demonstrated by Kaufman (1958) while studying the air afterglow reaction, 2.14

$$O + NO \longrightarrow NO_2 + h\nu \tag{2.14}$$

he observed that the reaction

$$O + NO_2 \longrightarrow NO + O_2 \qquad (2.15)$$

was extremely fast and could be used as a gas-phase titration reaction for oxygen atoms, thus effectively measuring their concentration. The end point for reaction 2.15 was detected by the extinction of the airglow emission. A titration reaction is one that is fast, stoichiometric and provides a clean, quantitative method of preparing labile species. Titration reactions have now emerged for many atomic and radical species (Clyne, 1973).

For the determination of absolute concentrations of NO_3 the titration reaction

$$NO_3 + NO \longrightarrow NO_2 + NO_2 \qquad (2.16)$$

was used, the experimental procedure for which has been described previously (Canosa-Mas *et al.*, 1987). Though reaction 2.16 is suitably fast for a titration reaction, it is followed by secondary chemistry: the reaction

$$NO_2 + NO_3 + M \rightleftharpoons N_2O_5 + M \qquad (2.17)$$

has an influence and so numerical modelling must be used to determine the $[NO_3]$. $k_{2.17}[M]$ takes values between 8.3×10^{-14} to 1.3×10^{-13} cm^3 $molecule^{-1}$ s^{-1} for the range of [M] values used in our flow studies (Smith *et al.*, 1985).

In the titration experiment a mixture of pure NO in helium (*ca.* 5%) is added to the main flow from a fixed injector position. The injector position is chosen to be at short contact times so as to minimise the contribution of reaction 2.17. The [NO] is increased incrementally until the $[NO_3]$ has dropped to below the detection limit. The loss of NO_3 is related to [NO] by the expression

$$-\Delta[NO_3] = s\Delta[NO] \qquad (2.18)$$

where s is the stoichiometry factor representing the number of molecules of NO_3 consumed for each molecule of NO added. Practically, the stoichiometry factor takes values between 1.0 and 1.15, indicating that reaction (2.17) has a contribution to the overall reaction scheme.

An iterative procedure is then undertaken in order to calculate accurately both σ_{expt} and values of s for the experimental points. First, a good visual fit to the experimental data is obtained in a plot of absorbances versus [NO] using several different estimates of $\sigma_{expt.}$. The limit of accuracy of this method for estimation of $\sigma_{expt.}$ is about ±10%. The stoichiometry factor s 2.18 is then calculated for each experimental point or any series of arbitrary points, using numerical integration of equations 2.16 and 2.17 with $[NO_3]$ at t=0 derived from the estimate obtained from the visual fit. The resultant plot of s versus [NO] is linear. A final plot of absorbance versus s[NO] is generated which has a slope that is proportional to the experimentally derived absorption cross-section (σ_{expt}).

This iterative procedure has been computerised, the numerical integration procedure being performed by the Runge-Kutte method (Hall and Watt, 1976). The advantage of applying numerical integration to the data is that the σ_{expt} obtained from the data no longer has the implicit assumption that s=1 associated with it. In order to compare σ_{expt} with σ_{662}, an experimentally determined convolution factor is used, which is measured by scanning the monochromator through the λ=662 nm peak in order to measure the experimental line width.

The absorption cross-section, at λ=662 nm and at 298 K, derived from these experiments was 2.23×10^{-17} cm^2 $molecule^{-1}$ before convolution. The presently recommended value for σ_{662} is 2.1×10^{-17} cm^2 $molecule^{-1}$ (Sander, 1986). There is much discussion in the literature (Wayne

et al., 1991) on the temperature dependence of the absorption cross section of NO_3. Strong temperature dependences were seen by both Sander (1986) and Ravishankara and Mauldin (1986), which contradicts the temperature-invariant results of Cantrell *et al.* (1987). For the purposes of calculations presented later using NO_3 absorption cross sections, the recommendations given in Wayne *et al.* (1991) for the cross sections were followed. Other commonly used titration reactions for NO_3 include the reaction with TME (Sander, 1986) and hex-2-yne (Benter *et al.*, 1991).

2.3.5 Calibration of flow meters

In order to establish flow velocities and concentrations in a discharge flow system, it is necessary to measure flow rates accurately and reproducibly. This makes calibration of flow meters one of the most important experimental procedures when measuring rate constants by discharge flow. A 10% error in a flow calibration can create an error of a factor of two in a rate constant.

As stated earlier in §2.3.1, the type of flow meter used in the discharge-flow work was a Jencon meterate RS type (JMRS). JMRS flow meters use the viscous drag created between the flowing gas and a ball held in a vertical tapered tube as a measure of flow, the taper being wider at the top of the tube than the bottom. The position of the ball in the tube is taken as a measure of the volume flow rate of the gas.

An important experimental consideration when using flow meters is the variation of flow with 'back' pressure. As many reactants are stored in bulbs, prolonged mass flow from the bulb

A)

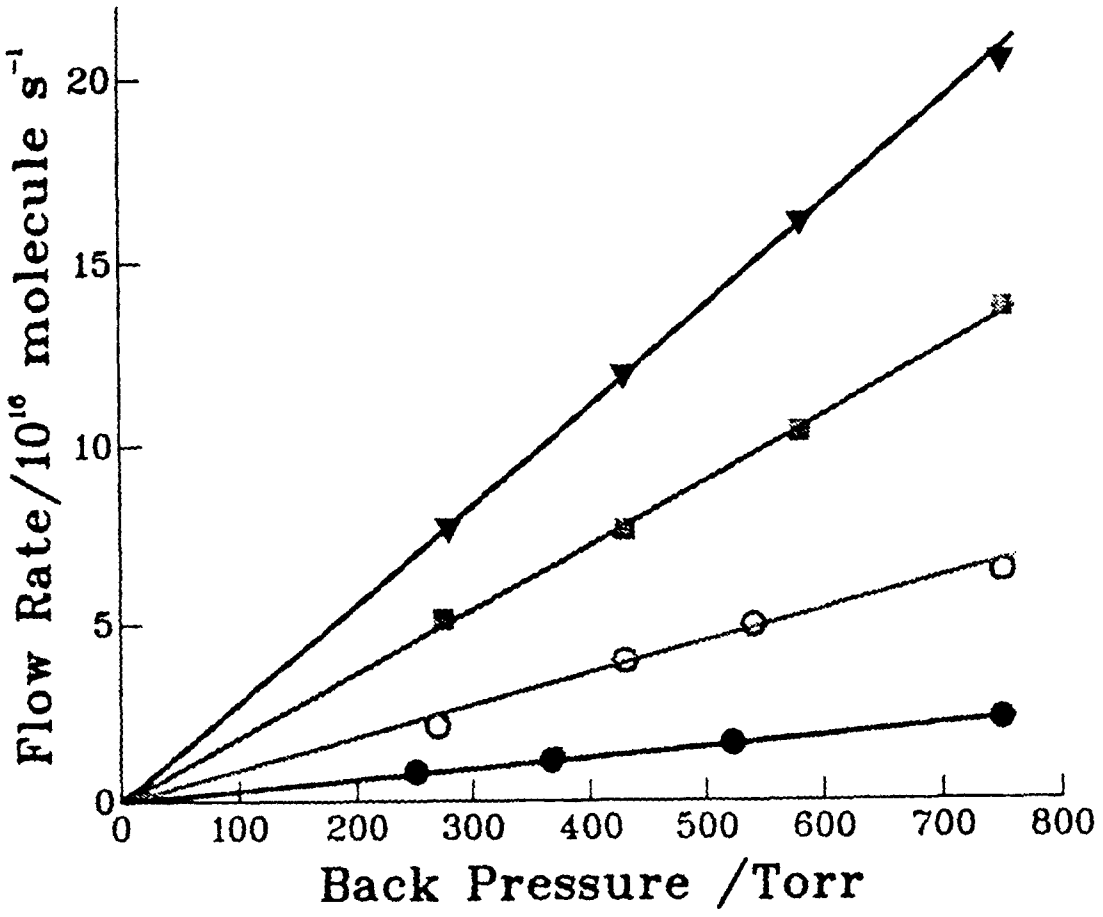

B)

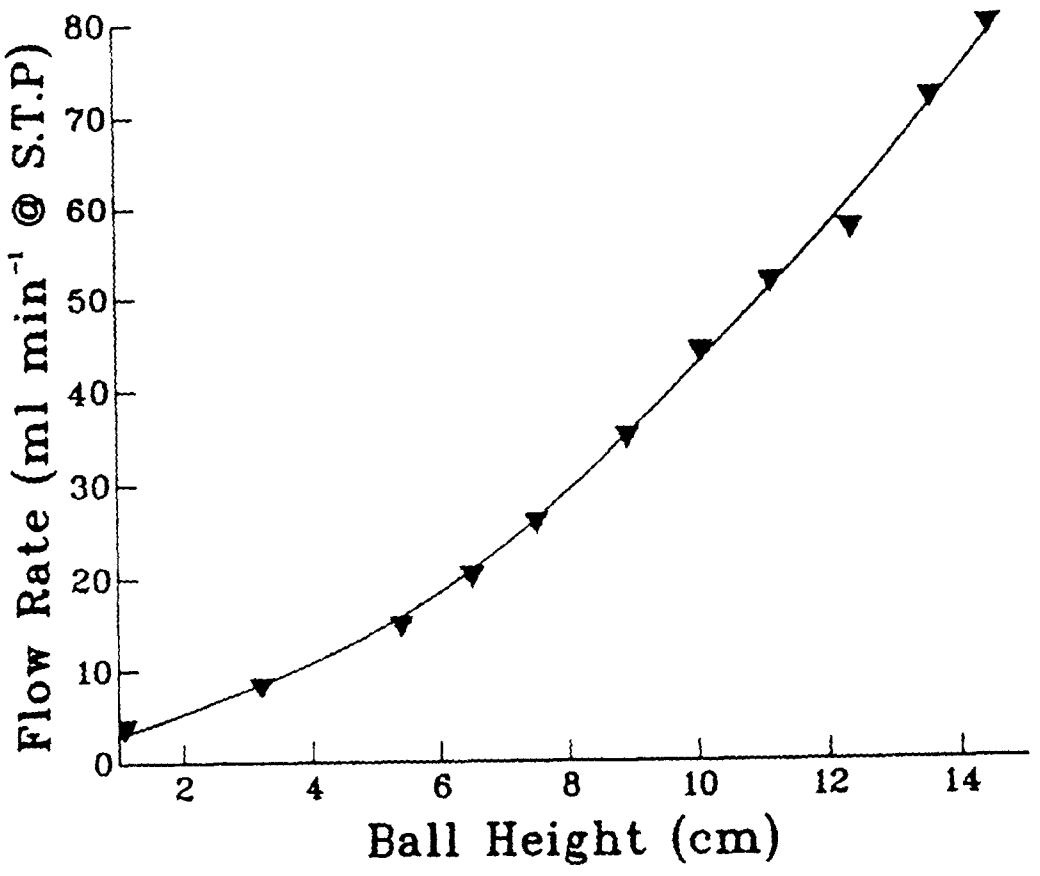

Figure 2.5 a) Variation of flow rate of helium with changing back pressure for a JMRS (RS 1). Points are taken for ball readings of ▾, 15.0; ■, 12.0; o, 8.0; ●, 4.0 (all cm). b) A typical JMRS (RS1) flow calibration for helium corrected to STP.

causes a decrease in pressure in both the bulb and at the flow meter. This makes it important to know how the reading of a flow meter responds to the changing pressure of a reactant in a bulb, this is commonly referred to as the 'back' pressure. The problem is alleviated practically if there is a constant (known) 'back' pressure e.g. by bubbling a gas through an atmospheric pressure oil bubbler.

With a JMRS flowmeter, the flow rate is proportional to pressure for a given ball reading according to the equation

$$Flow\ rate(P\ Torr) = Flow\ rate(760\ Torr)\ \frac{P}{760} \qquad (2.19)$$

which is valid so long as the 'back' pressure does not fall below *ca.* 250 Torr. Figure 2.5a shows the characteristics of flow meters with respect to a change in back pressure.

A second factor must also be considered when calibration of JMRS is undertaken. The flow rate of a gas is proportional to the viscosity (η). With a JMRS type flowmeter for two gases of viscosity η_a and η_b, for a given ball reading, the flow rates are related as

$$Flow\ rate_a = Flow\ rate_b\ \frac{\eta_b}{\eta_a} \qquad (2.20)$$

Nonetheless, it is good experimental practice to calibrate flowmeters for any gas used, and this is of particular importance for mixtures of gases which possess viscosities which are not simple linear functions of the individual viscosities of the two gases (Reid *et al.*, 1977).

Most flowmeter calibrations are conducted under the premise of flowing a known amount of gas through the flowmeter in a known time. Two methods are used:

a) Pressure drop or increase in a known volume with time. First, the volume within the apparatus which the flowmeter is to be calibrated for, is volume calibrated, by the expansion of a known pressure (P_{calib}) and volume (V_{calib}) of gas into a unknown volume (V), these volumes being related by

$$V_{calib}\left(\frac{P_{calib}}{P}-1\right) = V \tag{2.21}$$

the unknown pressure (P) being measured by a suitable pressure measurement device. The next step is to flow the gases from this calibrated volume through the flowmeter, the change in pressure due to the flow being measured by an absolute (e.g. Baratron) or differential (e.g. Validyne) pressure gauge. The pressure change (ΔP) in a known time period is recorded (in Torr s^{-1}) at several different flow meter readings (ball height, pressure difference etc.) The change in pressure with time is then converted into a flow rate by

$$\frac{\Delta P}{\Delta t} * \frac{V}{RT} = \frac{\Delta n}{\Delta t} \tag{2.22}$$

then

$$Flow\ Rate = \frac{\Delta n}{\Delta t} * \frac{760}{\bar{p}} * 60 * 22.42\times10^{3} * \frac{298}{273} \tag{2.23}$$

where the 760 / $\bar{p}$ term corrects for a change in back pressure, the other terms correct to the conditions of S.T.P., so that the flow rate is given in the units of m*l* min^{-1} at T = 298 K and 1 atmosphere. A typical calibration curve is shown in Figure 2.5b.

b) Displacement of water. A known volume of water is displaced by a flow of gas. This method is normally used for large flow rate meters such as JMRS series 2 or 3 (flow rate (He), at T=298K, < 2500 m*l* min^{-1}). The preferred form of this calibration is to draw gas

from a volume recording the time taken for a certain volume of water to replace the gas. A large reservoir of water is required so that there is effectively no change in water level during the calibration and therefore no change in effective back pressure. A calculation similar to the one in equation 2.21 is performed.

2.3.6 Materials

Helium (B.O.C., commercial grade) was passed through an Oxisorb cartridge (Messer-Griesheim) to remove traces of oxygen and a cold trap (T=77K) and a molecular sieve trap (T=263 K) to remove any traces of water. A silicone oil bubbler maintained the back pressure of helium at atmospheric pressure. Diluted fluorine (B.O.C., 5% in He) was used as supplied. Anhydrous gaseous HNO_3 in an He carrier was produced by bubbling helium through a 2:1 mixture of H_2SO_4 (Fisons, 98%) and HNO_3 (B.D.H.; AristaR, *ca.* 70%) maintained at approximately 238 K by an ethylene glycol/solid CO_2 slush bath. Nitric oxide (B.O.C., purity>99%) was purified by trap-to-trap distillation to remove NO_2.

The organic reactants used were 1-butene (99%), 1-chloro-1-butene (Wiley, 99%, equal mixtures of both the cis- and trans-isomers), 2-chloro-1-butene (Wiley, 98%), 3-chloro-1-butene (Aldrich, 99+%), 2-chloro-2-butene (Aldrich, 99+%, equal mixture of both the cis- and trans-isomers), 3-chloromethylpropene (T.C.I., 99%), 1-chloromethylpropene (T.C.I., 99%), 3-bromo-1-butene (Aldrich, 98%), 4-bromo-1-butene (Aldrich, 99%) and 2-bromo-2-butene (Aldrich, 98%). All reactants were purified by fractional distillation under reduced pressure by successive trap-to-trap distillation. With all compounds except 2-chloro-1-butene, no detectable impurities could be found with conventional FID and TCD gas-chromatography.

Because of the low vapour pressure of the reactants (*ca.* 130 Torr at room temperature), mixtures in purified helium were prepared with special care to avoid condensation of the reactants in the storage bulb. In the case of 2-chloro-1-butene the impurity was identified as 1,1-dichloro-1-butene by GC-MS, and was removed by vacuum distillation under reduced pressure.

2.4 The reaction of NO_3 with 1-butene

2.4.1 Experimental Results

The concentrations of 1-butene were sufficient for a pseudo-first-order analysis to be valid (i.e. [1-butene]>>[NO_3]). At elevated temperatures, the observation region was not at the same temperature as the flow tube region: however, the downstream temperature profile has no relevance for the analysis of the data under pseudo-first-order conditions (Westenberg and DeHas, 1967).

The concentrations of NO_3 were determined as a function of the distance from the tip of the injector to the detection region. The observed [NO_3] decays were plotted as logarithms of the ratio of absorption in the absence and presence of reactant against time. Figure 2.6 shows a typical plot for the reaction of NO_3 with 1-butene. Such plots were linear and the slopes yield the phenomenological first-order rate constant, k_{obs}, for the loss of NO_3 in the presence of reactant; within error, the intercepts were zero. The slope of a plot of k_{obs} versus [1-butene] yielded a second-order bimolecular rate constant for the reaction

$$CH_3CH_2CH{=}CH_2 + NO_3 \rightarrow \text{Products} \qquad (2.24)$$

Examples of second-order plots are shown in figure 2.7, for three temperatures. At room

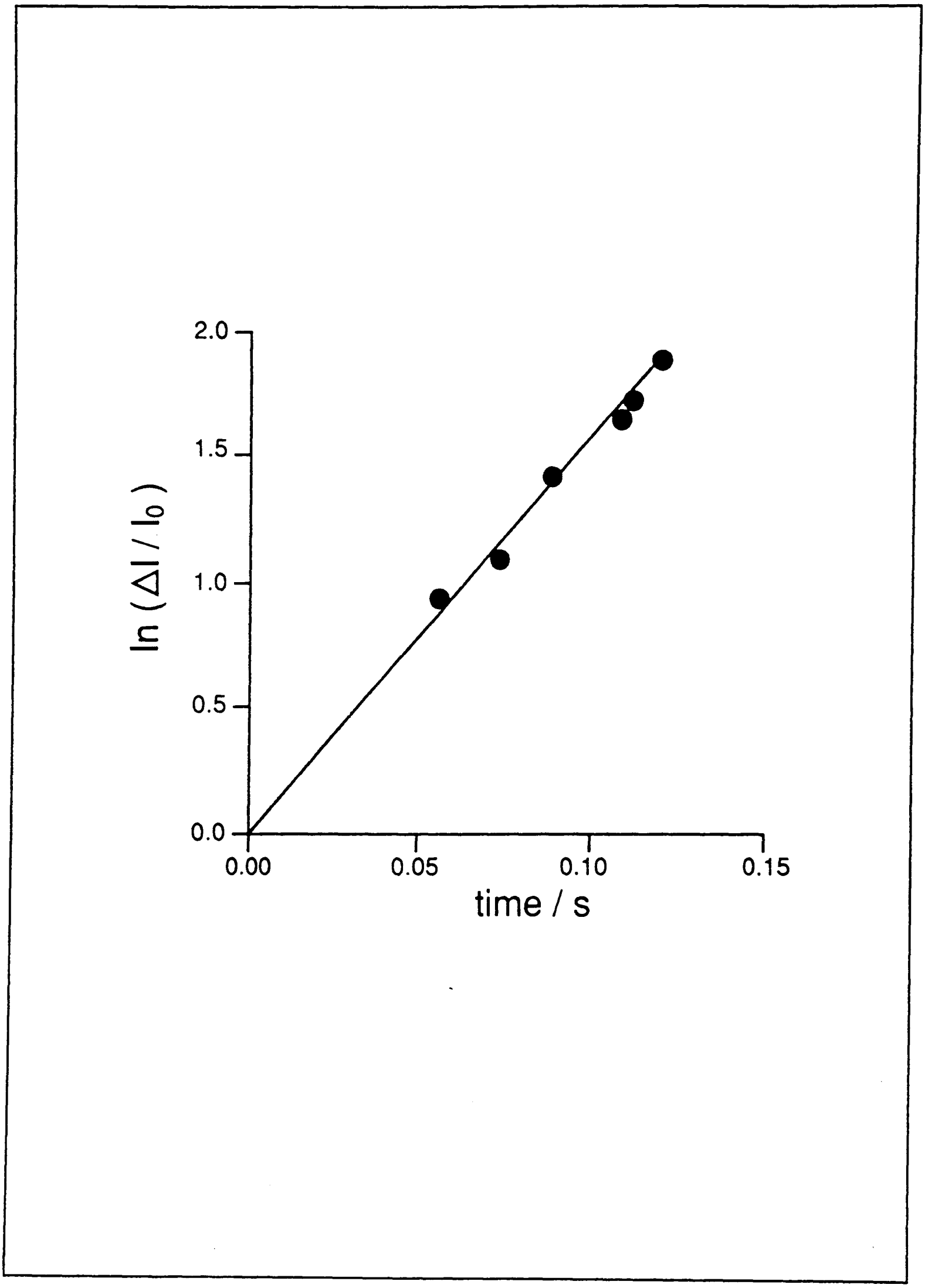

Figure 2.6 An example first order plot for the reaction of 1-butene with NO_3; I°_a is the intensity of absorption in the absence of reactant; I^{t}_a is the intensity of absorption in the presence of reactant at contact time t.

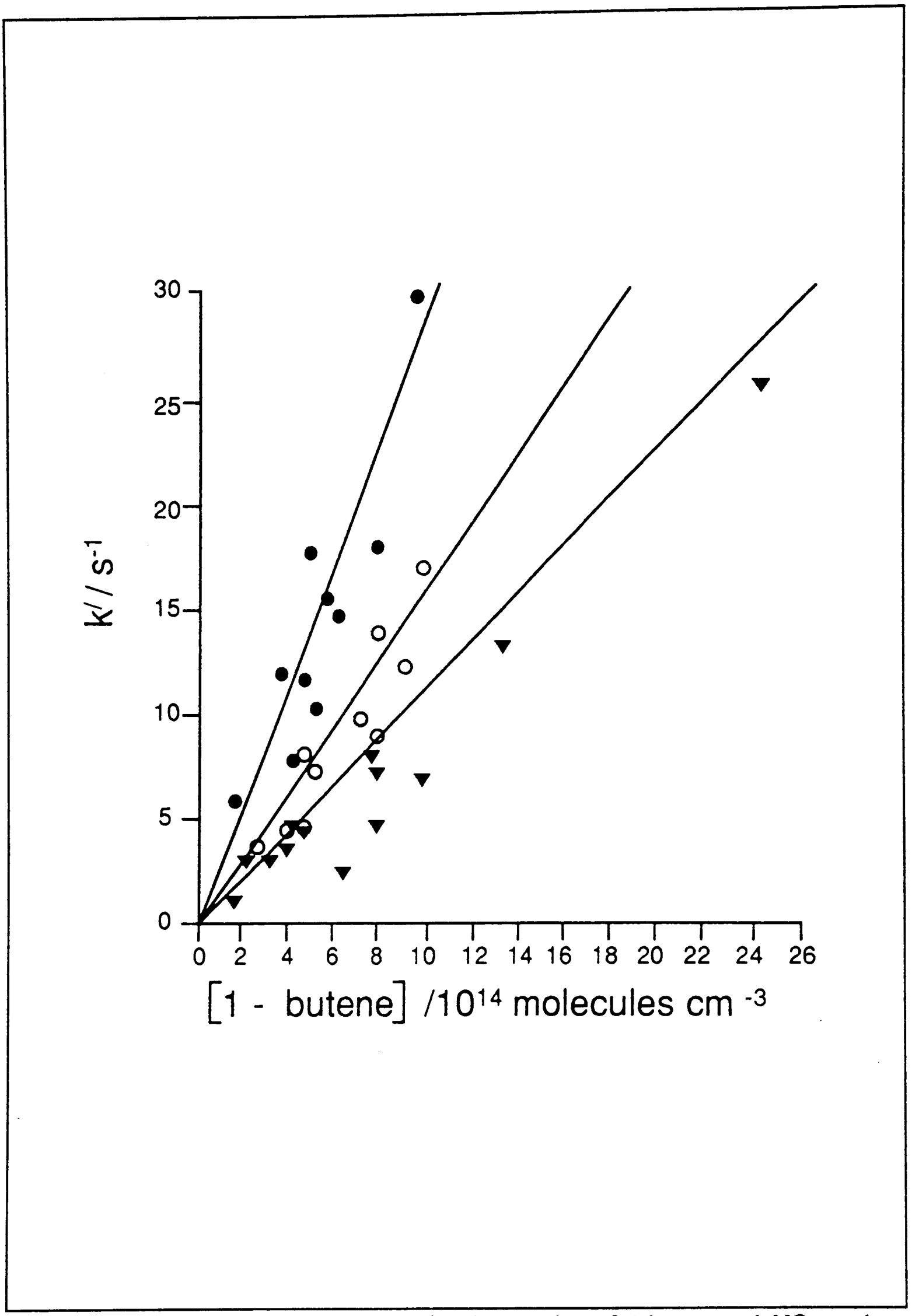

Figure 2.7 Example second order plots for the reaction of 1-butene and NO_3 at three different temperatures; ▾, T=298 K; ○, T=323 K; ●, T=423 K.

temperature the mean second-order rate constant from the pseudo-first-order measurements is $(1.1\pm0.2)\times10^{-14}$ cm^3 molecule^{-1} s^{-1} (95% confidence limits).

Experiments were performed at a series of different temperatures up to 473K. The data were fitted to the Arrhenius expression

$$\ln k_{2.24} = \ln A - \frac{E_a}{RT} \qquad (2.25)$$

Figure 2.8 shows the Arrhenius plot for the reaction of NO_3 with 1-butene (the error bars on the points are 2σ). A linear least-squares analysis of the data yields an activation energy of (7.8 ± 1.2)kJ mol^{-1} and a pre-exponential factor of about 2.5×10^{-11} cm^3 molecule^{-1} s^{-1} (the long extrapolation to the y-axis needed to obtain the pre-exponential factor makes an error analysis of little value). The detailed results are shown in Table 2.1. It is worth noting that the Arrhenius plot shown in figure 2.8 is a good straight line, unlike the one for propene (Canosa-Mas *et al.*, 1991). In the case of the reaction of NO_3 with propene, the authors ascribed the observed curvature in the Arrhenius plot at higher temperatures to competition between allylic hydrogen abstraction and the NO_3-double bond addition process. There is no evidence in these results for a significant contribution to the global rate constant even at the highest temperatures of an allylic hydrogen abstraction process. This conclusion is in agreement with the experiments of Kleinermanns and Luntz (1982) which suggest that the abstraction of an allylic hydrogen by $O(^3P)$ is more difficult in the case of 1-butene than propene.

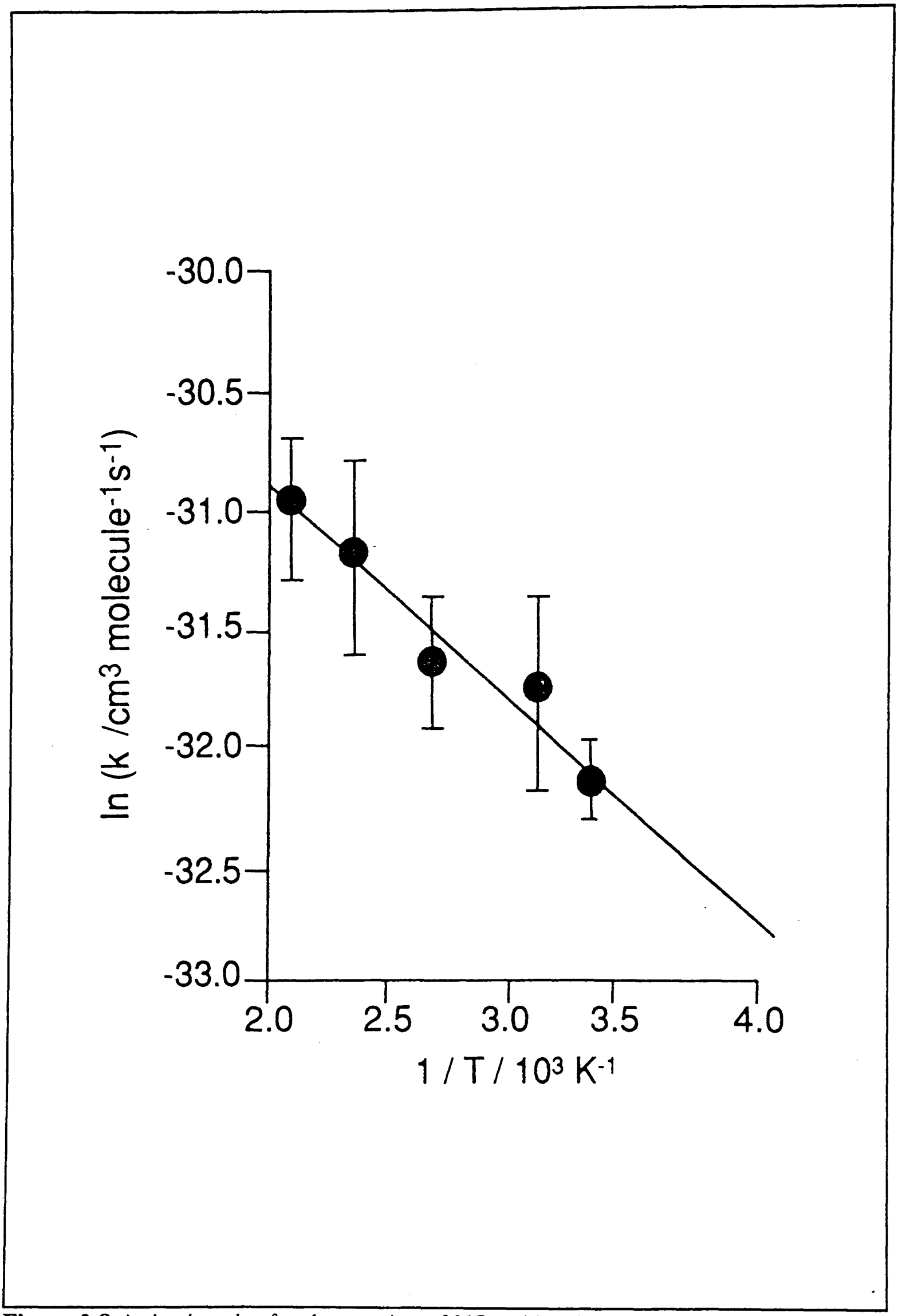

Figure 2.8 Arrhenius plot for the reaction of NO_3 with 1-butene

Table 2.1 - The rate constants for the reaction of 1-butene with the NO_3 radical

T K	P(Total) Torr	$10^{-14}[NO_3]$ molecules cm^{-3}	$10^{-14}[X]_o$ molecules cm^{-3}	$10^{14}k$ cm^3 $molecule^{-1}s^{-1}$
299	1.07-2.18	<0.51	1.94-24.1	1.1±0.2
323	1.31-1.36	<0.43	2.66-9.85	1.6±0.5
373	1.34-1.89	<0.39	2.99-8.01	1.8±0.4
423	1.27-1.40	<0.37	1.91-9.39	2.9±1.0
473	1.36-1.45	<0.32	1.80-6.50	3.6±0.8

[X] is the [reactant]; The error limits quoted are 2σ.

At the pressures and temperatures used in our experiments, the adduct formed in reaction (2.24) will decompose to give the epoxide and NO_2 (Dlugokcenky and Howard, 1989). The latter species could go on to react with NO_3 in the reaction

$$NO_3 + NO_2 + M \rightleftharpoons N_2O_5 + M \qquad (2.17)$$

$k_{2.17}=5.7x10^{-14}$ cm^3 $molecule^{-1}$ s^{-1} (P=2 Torr, M=He) (Smith *et al.*, 1985)

leading to the measured k_{obs} being greater than the true value of $k_{2.24}$. However, modelling studies indicate that the additional loss of NO_3 resulting from the participation of this reaction was less than 1% for the concentrations and contact times of these experiments. The results are discussed in detail in §2.6

2.5 The reaction of NO_3 with a series of halobutenes

2.5.1 The treatment of experimental data

The reactions studied in this work can be represented by the equation

$$C_4H_7X + NO_3 \longrightarrow \text{products} \qquad (2.26)$$

$$X = Cl \text{ or } Br \text{ on } C_1 \text{ to } C_4$$

Because the halobutenes have relatively low vapour pressures, the concentration of excess reagent was less than ten times greater than $[NO_3]$, and a second-order kinetic analysis was used. For the room temperature data, the experimentally measured contact times and concentrations were fitted, using a non-linear least squares routine, to a standard second-order rate equation (e.g. Laidler, 1987)

$$[NO_3]_m = \frac{([NO_3]_i - [X]_i)\ \exp\{k_{2.26}t([NO_3]_i - [X]_i)\}}{(\exp\{k_{2.26}t([NO_3]_i - [X]_i)\} - ([X]_i/[NO_3]_i))} \qquad (2.27)$$

$[NO_3]_m$ = measured concentration of NO_3 at observation region
$[NO_3]_i$ = initial concentration of NO_3
$[X]_i$ = initial concentration of the reactant
t = contact time

Both $[NO_3]_i$ and $k_{2.26}$ were varied. The value of $[NO_3]_i$ that gave the best fit was little different from the measured NO_3 concentration without reactant, and $k_{2.26}$ was not sensitive to a change in this value. The validity of the fitting procedure was checked independently using the FACSIMILE program (Chance *et al.*, 1977) and both methods gave consistent results for $k_{2.26}$ to within ±2%. An example fit is shown in figure 2.9.

The analysis of the data obtained at elevated temperatures was made more complicated because of the impracticality of heating the observation region. Direct measurement of the

temperature of the flow tube showed that it dropped very rapidly outside the heated zone (see § 2.3.1). Under pseudo-first-order conditions, the measured rate constant is characteristic of the heated region (Westenberg and De Haas, 1967), but under second-order conditions, the situation is not so simple. Two methods were used to calculate the rate constants at temperatures above ambient. The first employed the second-order rate equation integrated without limits (0→∞),

$$[NO_3]_m = \frac{[X]_i - [NO_3]_i}{\exp\{([X]_i - [NO_3]_i)\ (k_{2.26}(T)t + C)\} - 1} \qquad (2.28)$$

with the rate constant at high temperature, $k_{2.26}(T)$, and the constant of integration, C, floated as parameters to fit the observed data. The integration constant was used as a parameter to allow for the change in contact time and concentrations between the flow tube (at high temperature) and the detection cell (at room temperature). Equation (2.28) was tested using simulated data typical of our experimental conditions - temperature profiles in the flow tube have been measured previously (Canosa-Mas *et al.*, 1991). Three activation energies of reaction (0, 15 and 30 $kJmol^{-1}$) were tried, and using a step-ladder approach (Canosa-Mas *et al.*, 1991), $[NO_3]$ *vs.* time profiles were calculated. Analysis of the simulated data, using a non-linear least-squares method applied to equation (2.28), was found to give the high temperature value of $k_{2.26}$ used in the simulation. A typical fit is shown in Figure 2.9.

In the second method, it was assumed that the temperature dropped instantaneously to ambient outside the heated zone, as illustrated in Figure 2.10. The standard second-order equations were then applied to the two temperature regimes. In the room-temperature region, $[NO_3]$ and time are related by the expression:

A)

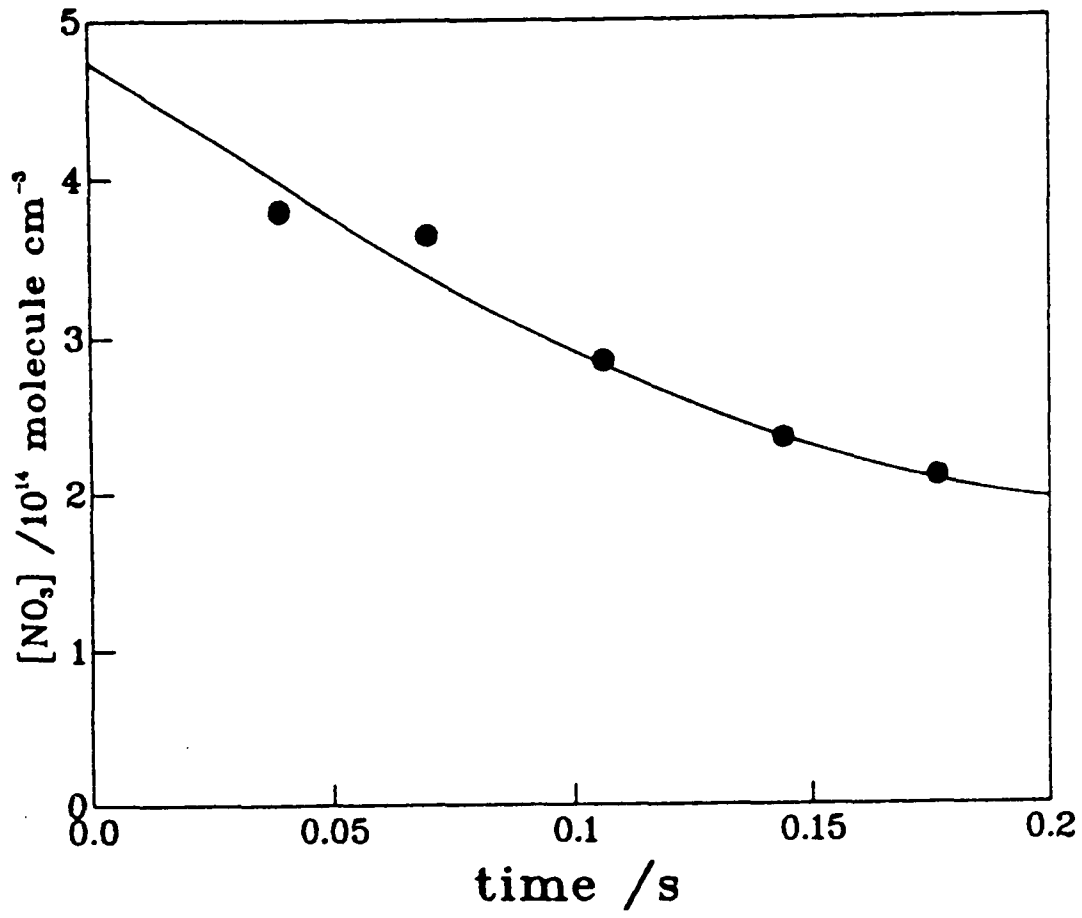

B)

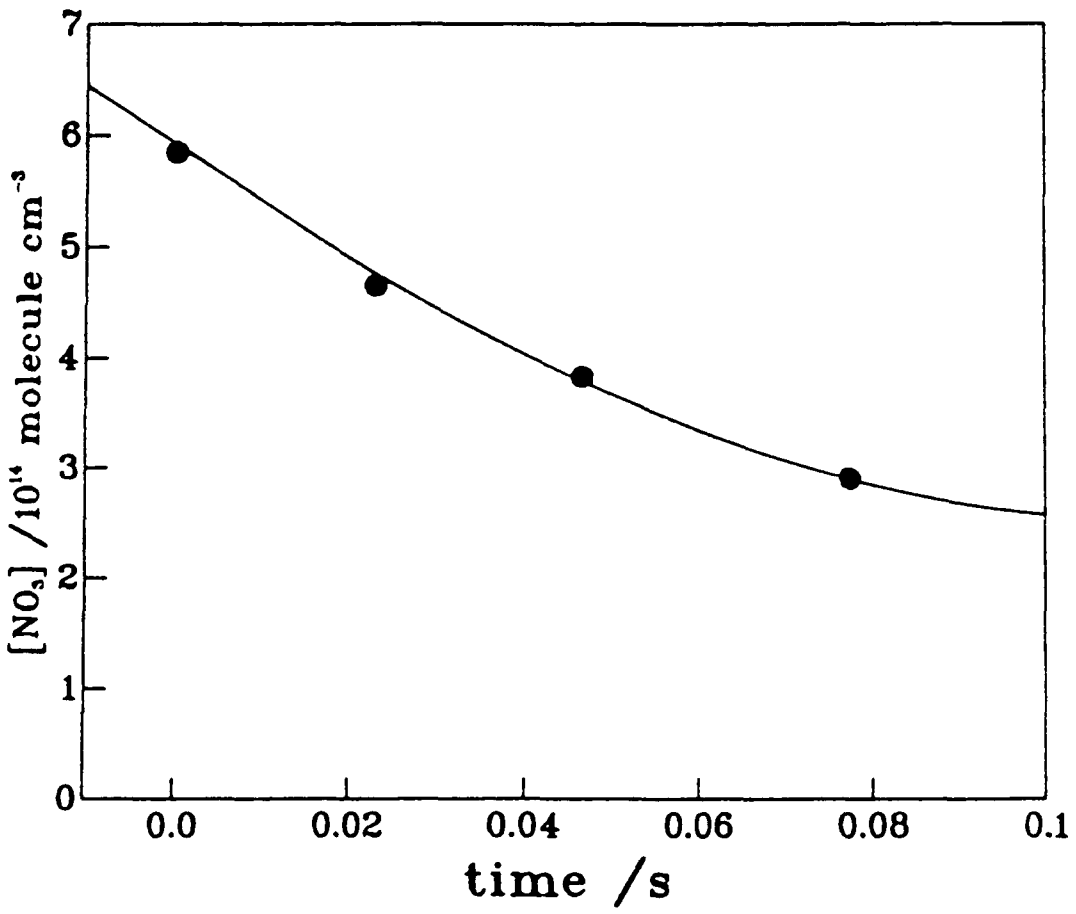

Figure 2.9 The second-order fit for the reaction of NO_3 with 1-chlorobut-2-ene: a) at T=298K; b) at T=473K.

$$k_{2.26}(t_o - t_T) = \frac{1}{[X]_T - [NO_3]_T}\left(\frac{[NO_3]_T[X]_m}{[X]_T[NO_3]_m}\right) \qquad (2.29)$$

where $[NO_3]_T$ and $[X]_T$ are obtained by applying the second-order equation in the high temperature region and are given by:

$$[NO_3]_T = \frac{[NO_3]_i([X]_i - [NO_3]_i)}{[X]_i \exp\{k_{2.26}(T)([X]_i - [NO_3]_i)(t_T - t_i)\} - [NO_3]_i} \qquad (2.30)$$

and

$$[X]_T = \frac{[X]_i([NO_3]_i - [X]_i)}{[X]_i \exp\{-k_{2.26}(T)([NO_3]_i - [X]_i)(t_T - t_i)\} - [NO_3]_i} \qquad (2.31)$$

The notation for equations (2.29), (2.30) and (2.31) are defined in Figure 2.10. A numerical technique was then used to obtain $k_{2.26}(T)$ from the measurements of $[NO_3]_m$ as a function of time.

The two methods gave rate constants which agreed to within 4%. In order to further test the procedures, the rate constant for the reaction of NO_3 with 1-butene was measured as a function of temperature under second-order conditions. The recovered rate coefficients agreed within experimental error (i.e. 2σ) with values presented in §2.4 obtained under pseudo-first-order conditions.

2.5.2 Experimental Results

The detailed results for the rates of reactions of the halo-butenes with NO_3 are summarised in Table 2.2. The data for those reactions measured above ambient temperature are listed

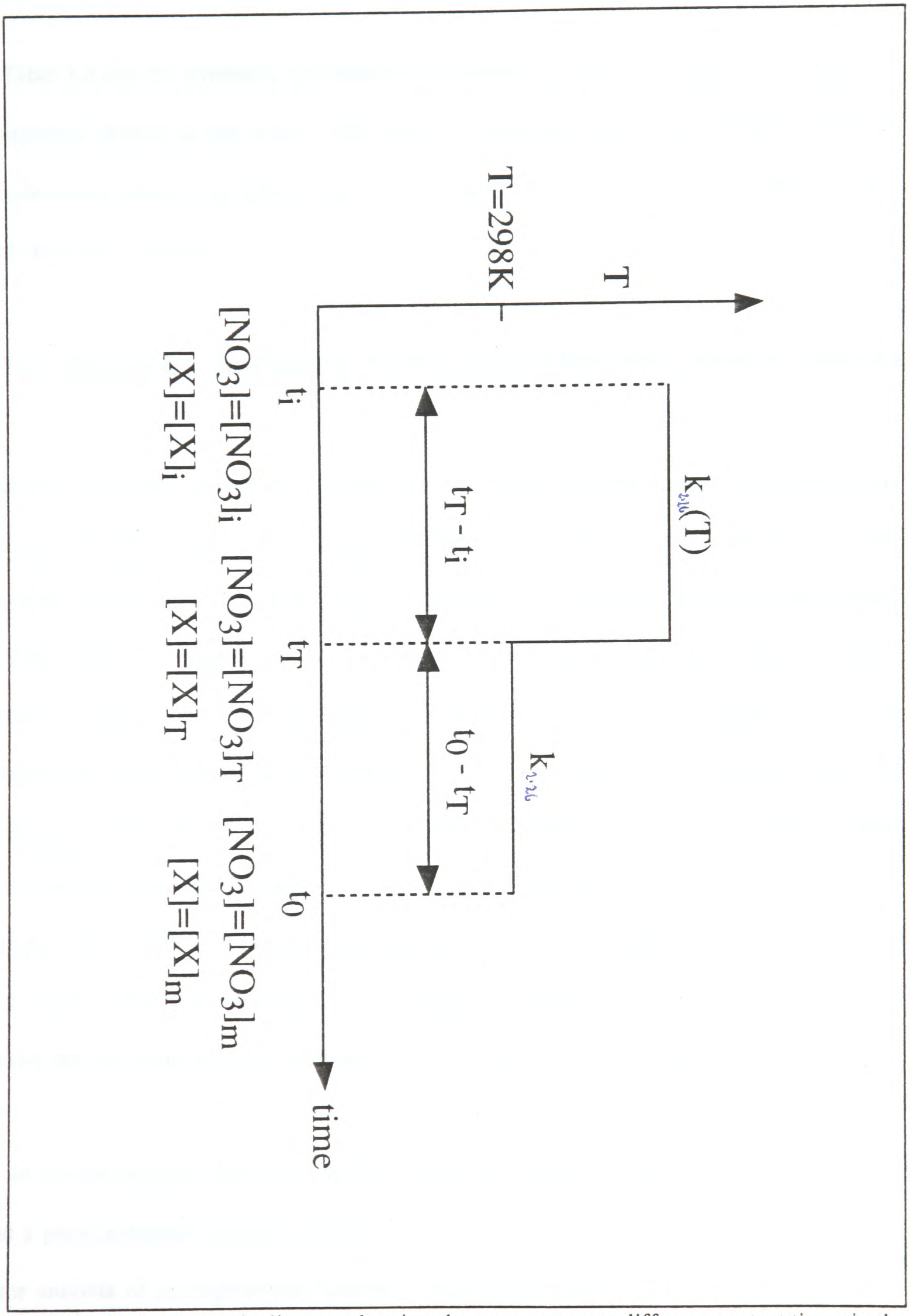

Figure 2.10 A schematic diagram showing the temperature at different contact times in the flow tube; the temperature change is assumed to be sharp.

in Table 2.2 and the Arrhenius parameters are displayed in table 2.3. Figure 2.11 shows the compounds studied in this work. The results are split into sections according to the parent unsubstituted alkene, e.g. §2.5.2.1 gives the results for the reaction of NO_3 with the halo-derivatives of 1-butene.

2.5.2.1 Results for the reaction of NO_3 with the halo-derivatives of 1-butene

The results for the reaction of 1-butene and NO_3 have been described in detail previously (§2.4). For the reactions of 1-chloro-1-butene and 2-chloro-1-butene with NO_3, *ca.* 10% mixtures of the compounds in helium were prepared. Experiments were performed solely at 298 and 299 K respectively at total carrier flow pressures between 1.2 and 1.5 Torr. Because of the magnitude of the observed NO_3 decay rates with these compounds at room temperature, with linear flow velocities of *ca.* 300 cm s^{-1}, coupled to the sensitivity for the detection of NO_3 (see §2.3.4), it was not possible to measure the rate coefficients for these compounds at increased temperatures. In the case of the reaction of NO_3 with 3-chloro-1-butene (16% in He), experiments were performed at a series of three temperatures, 298, 373 and 473 K. The data were fitted to an Arrhenius expression (equation 2.25); figure 2.12 shows the Arrhenius plot for the reaction of NO_3 with 3-chloro-1-butene.

A linear-least-squares analysis of the data yields an activation energy of (16.6±2.0) kJ mol^{-1} and a pre-exponential factor of 2.4×10^{-12} cm^3 $molecule^{-1}$ s^{-1} (see §2.4.2 for comments on the error analysis of pre-exponential factors). Both the reactions of 3-bromo-1-butene and 4-bromo-1-butene with NO_3 were studied at T = 298 K under similar experimental conditions

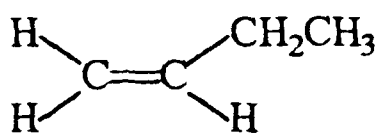

1-butene

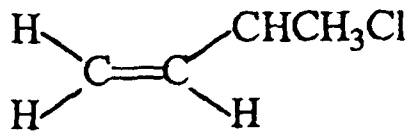

4-chloro-1-butene

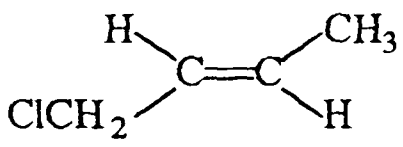

1-chloro-2-butene

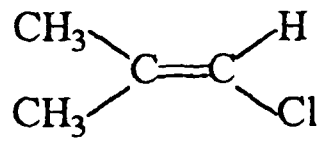

1-chloromethylpropene

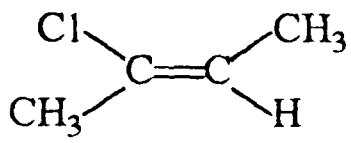

2-chloro-2-butene

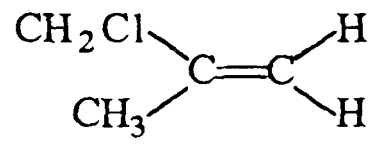

3-chloromethylpropene

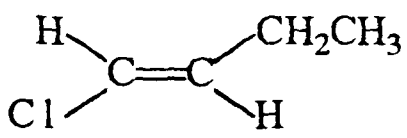

1-chloro-1-butene

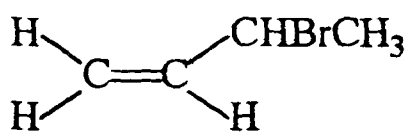

3-bromo-1-butene

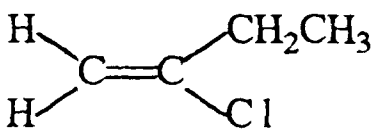

2-chloro-1-butene

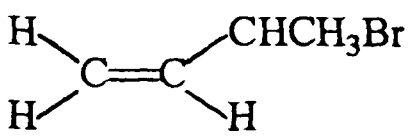

4-bromo-1-butene

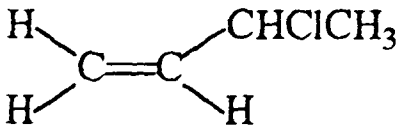

3-chloro-1-butene

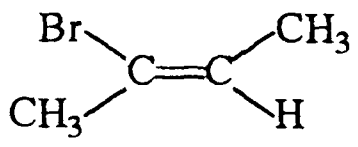

2-bromo-2-butene

Figure 2.11 The compounds studied in this work

(See table 2.2).

2.5.2.2 Results for the reaction of NO_3 with the haloderivatives of 2-butene

Experiments were conducted over the temperature range T=298 to 473K for the reaction of 1-chloro-2-butene with NO_3. The 1-chloro-2-butene was prepared as a 6.7% mixture in helium, giving concentrations of reactants under flow conditions between $1.05x10^{13}$ and $3.54x10^{14}$ molecule cm^{-3} at T=298 K. The Arrhenius plot (see §2.4.2) is shown in figure 2.13 and yields values of (8.3±2.9) kJ mol^{-1} for the activation energy and $6.0x10^{-13}$ cm^3 $molecule^{-1}$ s^{-1} for the pre-exponential factor. For similar reasons to those laid out in §2.5.2.1, it was not possible to measure the rate coefficient for the reaction of NO_3 with 2-chloro-2-butene (11.1% in He) and 2-bromo-2-butene (10.3% in He) at temperatures above ambient.

2.5.2.3 Results for the reaction of NO_3 with the chloroderivatives of methylpropene

Experiments were conducted at room temperature for the reaction of NO_3 with 1–chloromethylpropene (17.7% in He), using reactant concentrations in the range $9.3x10^{13}$ to $7.4x10^{13}$ molecule cm^{-3}. Typical [NO_3] were less than $7.4x10^{13}$ molecule cm^{-3}. In the case of 3-chloromethylpropene, the reaction with NO_3 was studied over the temperature range T=298 to 443 K. Figure 2.14 shows the Arrhenius plot for the reaction, which yields on linear-least square analysis a value of (10.5±1.7) kJ mol^{-1} for the activation energy and $1.6x10^{-12}$ cm^3 $molecule^{-1}$ s^{-1} for the pre-exponential factor.

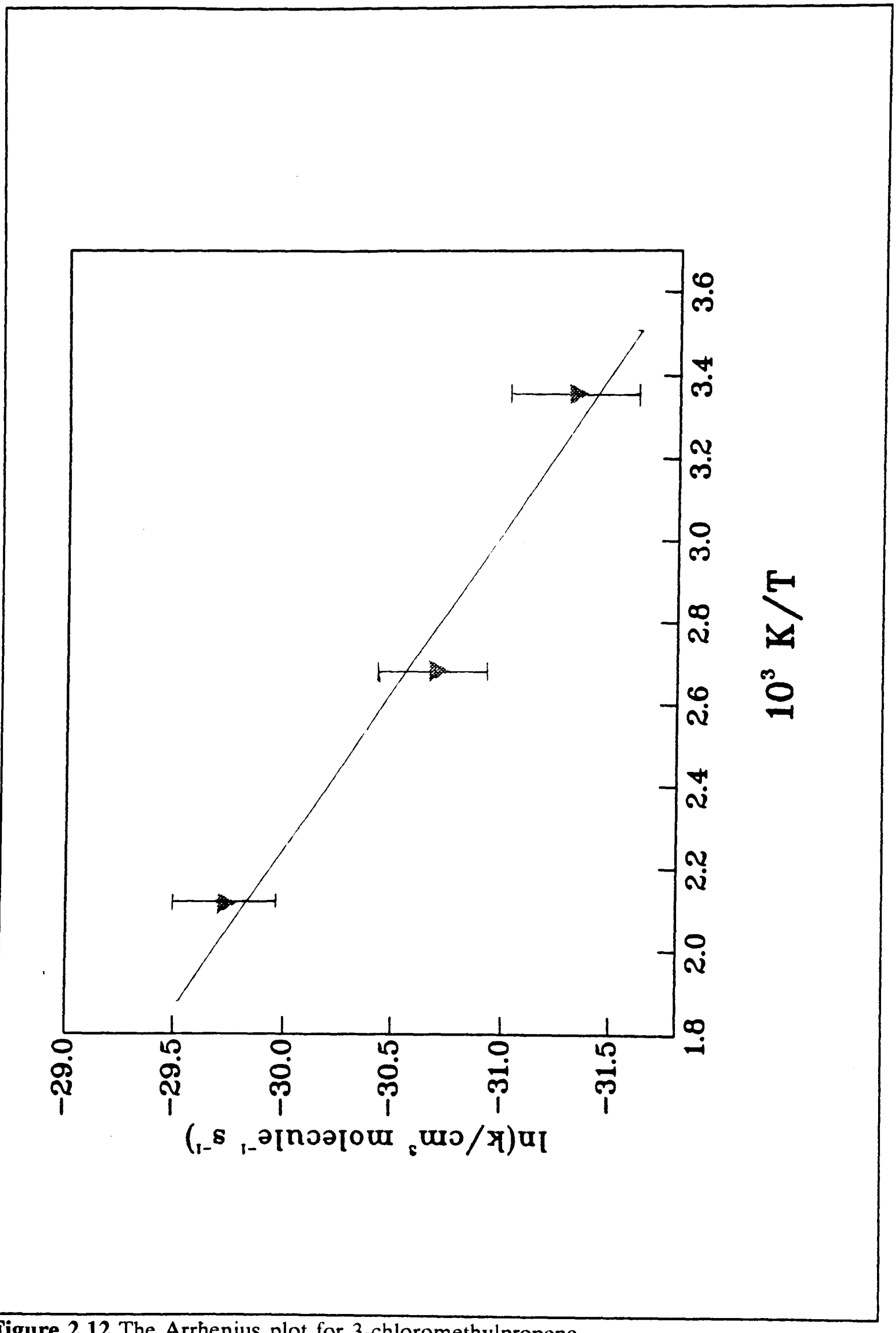

Figure 2.12 The Arrhenius plot for 3-chloromethylpropene

Table 2.2 - The kinetic measurements for the reaction of the halobutenes with the NO_3 radical.

T K	P_{Total} Torr	$10^{-14}[NO_3]$ molecule cm^{-3}	$10^{-14}[X]_o$ molecule cm^{-3}	$10^{14}k$ cm^3 molecule^{-1} s^{-1}
1-chloro-2-butene				
298	1.27-1.33	0.31	1.05-3.54	2.0±0.7
373	1.39-1.41	0.29	0.24-1.72	5.0±1.7
473	1.32-1.53	0.27-0.29	0.22-3.30	7.0±5.5
1-chloro-1-butene				
298	1.2-1.4	0.37-0.84	2.76-7.05	1.2±0.4
2-chloro-1-butene				
299	1.43-1.54	0.29	0.81-4.18	1.7±0.3
3-chloro-1-butene				
296	1.04-1.12	0.27	1.97-10.0	0.3±0.07
373	1.25-1.42	0.25	1.27-8.75	1.2±0.1
473	1.23-1.37	0.21-0.23	1.85-4.21	3.5±1.2
2-chloro-2-butene				
298	1.34-1.36	0.32-0.40	0.68-1.18	11.0±4.0
1-chloromethylpropene				
298	1.15-1.23	0.42-0.62	0.93-3.87	9.0±2.3
3-chloromethylpropene				
298	1.20-1.23	0.48-0.50	1.10-7.56	2.5±0.4
373	1.20-1.23	0.39-0.43	0.71-2.64	4.7±0.5
473	1.16-1.20	0.32-0.34	0.77-2.63	12.3±0.6
3-bromo-1-butene				
298	1.11-1.17	0.40-0.45	0.54-2.27	0.4±0.1
4-bromo-1-butene				
298	1.13-1.19	0.51-0.64	1.36-2.47	0.5±0.1
2-bromo-2-butene				
298	1.18-1.21	0.44-0.48	0.59-2.30	13.4±0.1

All errors quoted are ±2σ

Table 2.3 - The Arrhenius parameters for the reactions of some chlorobutenes with NO_3

Compound	A cm^3 $molecule^{-1}$ s^{-1}	E_a kJ mol^{-1}	Temp. Range (K)
3-chloro-1-butene	$2.4x10^{-12}$	16.6	298-473
1-chloro-2-butene	$6.0x10^{-13}$	8.2	298-473
3-chloromethylpropene	$1.6x10^{-12}$	10.5	298-473

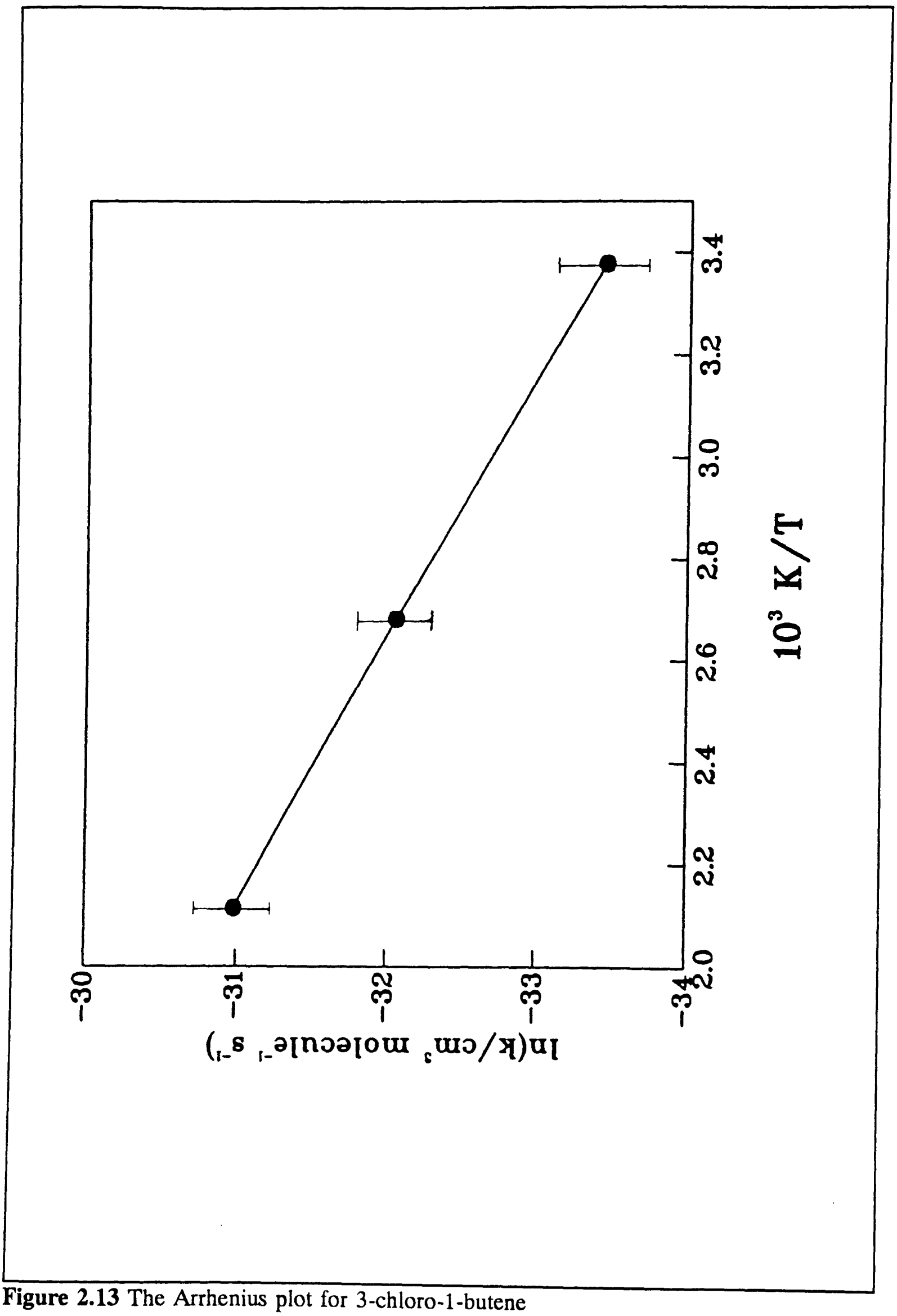

Figure 2.13 The Arrhenius plot for 3-chloro-1-butene

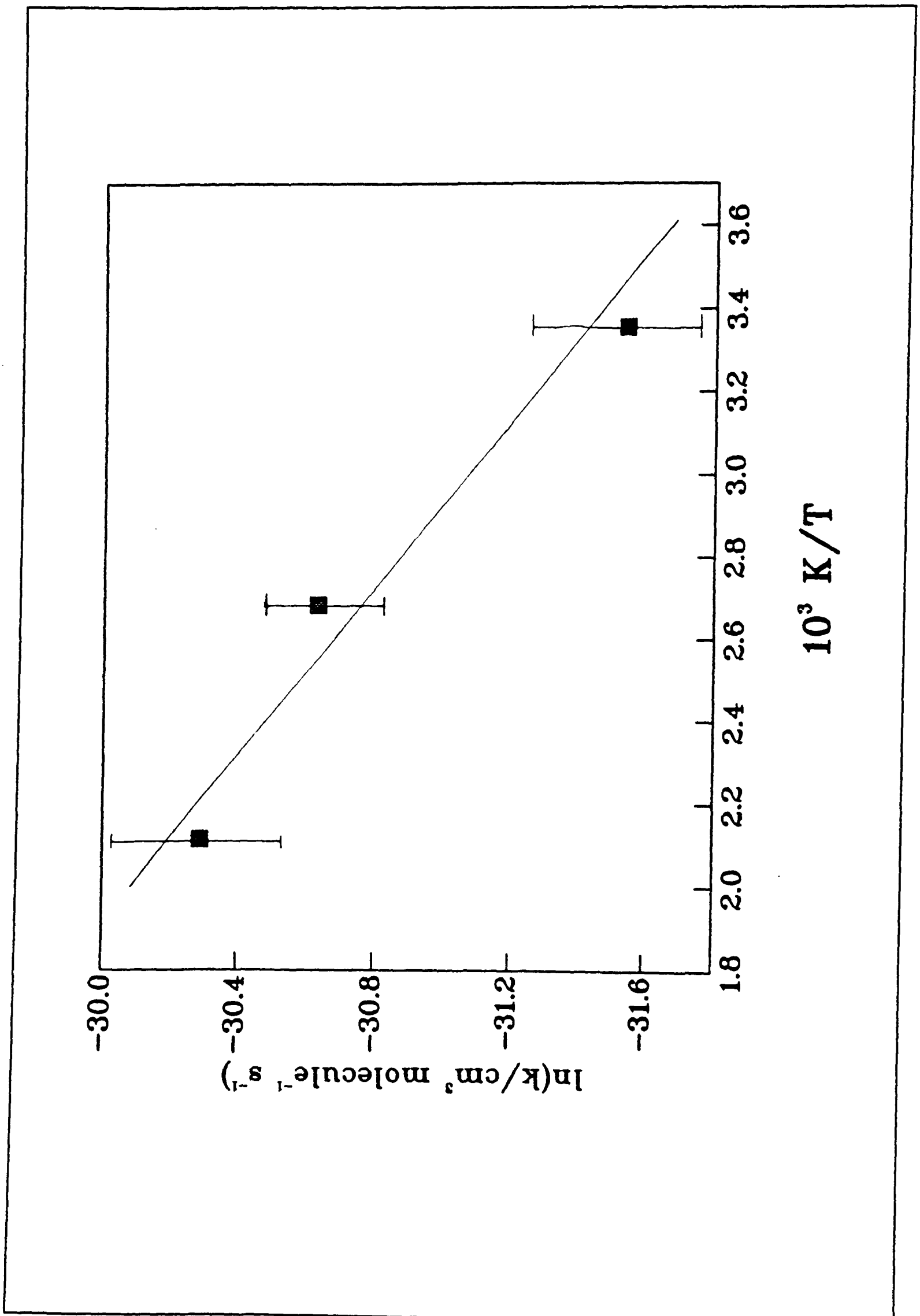

Figure 2.14 The Arrhenius plot for 1-chloro-2-butene

2.6 Discussion

The values of $k_{2.24}$ for the reaction of NO_3 with 1-butene have been measured by other groups by employing relative-rate methods (Wayne *et al.*, 1991). Atkinson *et al.* (1988) and Barnes *et al.* (1990) measured the decay of 1-butene relative to *trans*-2-butene at room temperature and at a pressure of approximately one atmosphere in air. Taking the value of the rate constant for the reaction of NO_3 with *trans*-2-butene as $(3.87\pm0.45)\times10^{-13}$ cm^3 $molecule^{-1}$ s^{-1} (Wayne *et al.*, 1991), these two groups measured a rate constant of $(1.23\pm0.16)\times10^{-14}$ and $(1.36\pm0.2)\times10^{-14}$ cm^3 $molecule^{-1}$ s^{-1} respectively, both of which are in good agreement with our value. The other technique, employed by Japar and Niki (1975) and Andersson and Ljungström (1989), is based on the increase of the decay rate of N_2O_5 in the presence of 1-butene; the derived value of $k_{2.24}$ depends upon the value of the equilibrium constant for reaction (2.17). Japar and Niki (1975) performed their experiments in a mixture of 150 Torr of O_2 and 600 Torr of Ar at T=300 K, for which temperature Atkinson (1991) suggests a value of $K_{eq} = 2.65\times10^{-11}$ cm^3 $molecule^{-1}$. The recalculated value of $k_{2.24}$ is then $(1.59\pm0.17)\times10^{-14}$ cm^3 $molecule^{-1}$ s^{-1}. The recalculated rate constant of Andersson and Ljungström (1989) for T=296 K and in one atmosphere of air ($K_{eq}=4.4\times10^{-11}$ cm^3 $molecule^{-1}$) is $(1.50\pm0.08)\times10^{-14}$ cm^3 $molecule^{-1}$ s^{-1}. Again, both these values are in reasonable agreement with our value. Possible sources of the small discrepency could lie either in the value of the equilibrium constant used or in the rate constant used for the reference reaction.

All the available data on products and kinetics (Wayne *et al.*, 1991) show that the initial reactions of the NO_3 radical with alkenes proceed predominantly *via* electrophilic addition of NO_3 to the carbon-carbon double bond to form a radical intermediate (adduct).

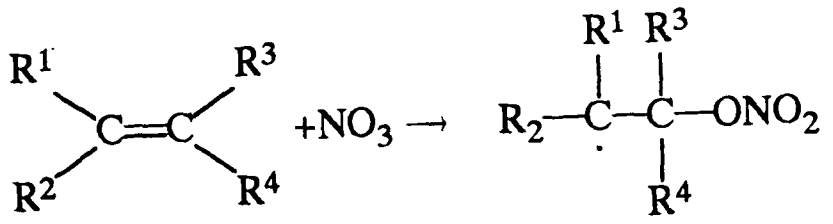

(2.32)

The primary factor that governs the rate of attack of the NO_3 radical on an unsaturated molecule is the distribution of the electron density in the π-bond. For unsymmetric alkenes, the site of attack is mainly governed by steric repulsion, which is determined not only by geometrical size but also by the partial charges on the incoming radical and the substituents present in the molecule. Thus, the NO_3 attacks the carbon atom that is least substituted (Tedder and Walton, 1980). Addition processes of this type go *via* a three-centre three-electron type of transition state (see Figure 2.15), and the transition state can be said to be "tight". In principle, it is the antibonding character of the π^*-electron that will determine the magnitude of the activation energy of such a reaction. The π-electron is shared between the three centres (Benson, 1972) of the reaction as shown in figure 2.15. The influence of an inductive effect of substituents on reactivity can be seen by looking at the homologous series ethene, propene and 1-butene (see Table 2.4). A positive inductive effect (+I) is exerted by an alkyl group, making the π-bond more susceptible to electrophilic attack. Table 2.4 shows kinetic parameters for the reaction of the homologous series C_2H_{2n} with NO_3. Ethene can be seen to be almost two orders of magnitude less reactive than propene with respect to reaction with NO_3, this marked difference in reactivity being a result primarily of the positive inductive influence of the alkyl group present in both 1-butene and propene. The effect is much stronger where more than one alkyl group is attached to the carbon atoms in the double bond: rate constants up to 4.5×10^{-11} cm^3 $molecule^{-1}$ s^{-1} have been measured for

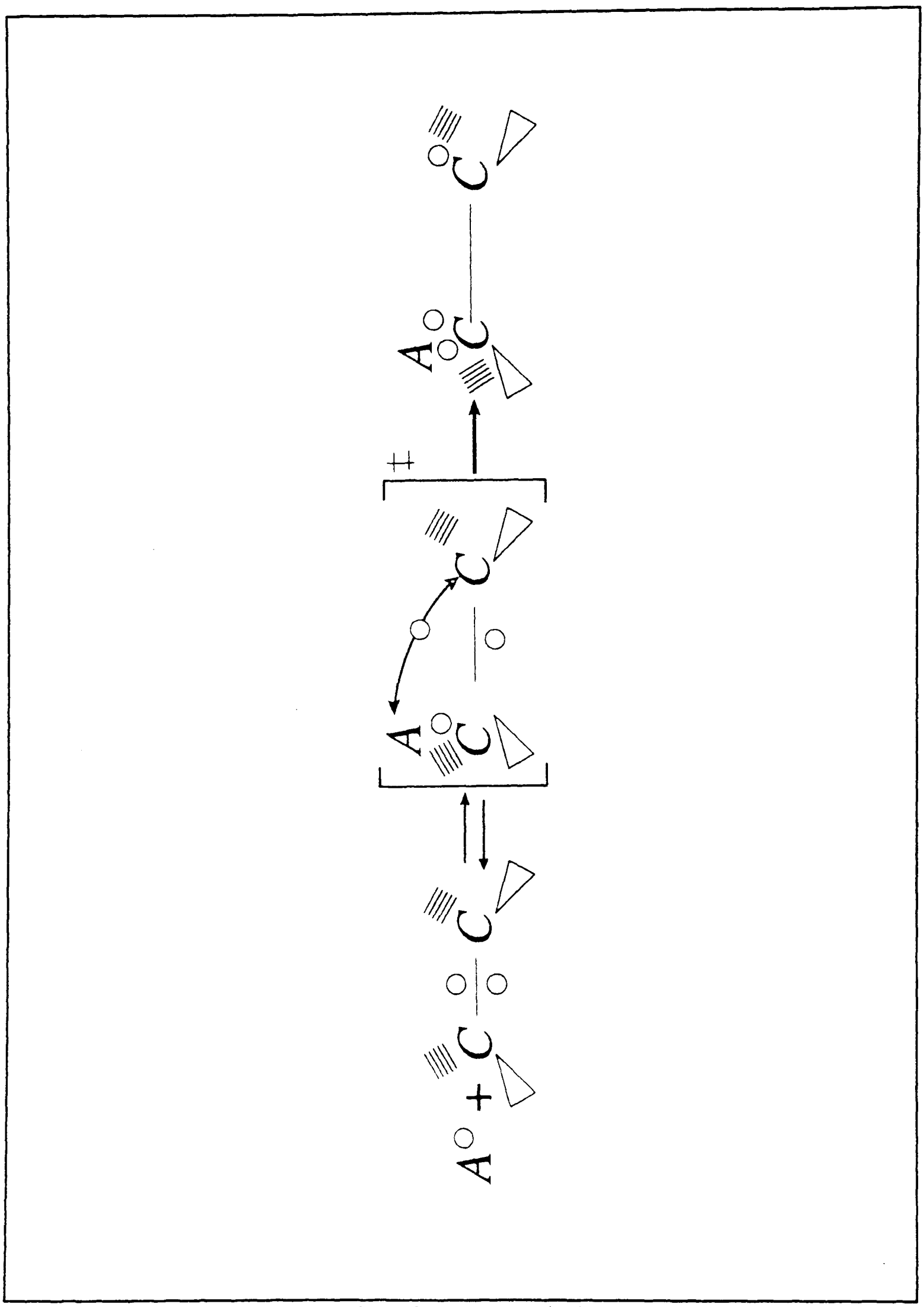

Figure 2.15 Schematic representation of atom or radical addition to a π-bond showing a three-centre, three-electron type of transition state. The antibonding electron is shared between the terminal atoms (Benson, 1972)

the reaction of NO_3 with 2,3-dimethyl-2-butene (Wayne *et al.*, 1991). The simple idea of inductive effects in the reactions of NO_3 with alkenes are discussed in more detail in Chapter 3.

Table 2.4 - Selected rate constants and activation energies for the reactions of the homologous series C_nH_{2n} with NO_3 (Wayne *et al.*, 1991)

Compound	k cm^3 $molecule^{-1}$ s^{-1}	E_a kJ mol^{-1}
ethene	$2.0x10^{-16}$	26±2
propene	$9.4x10^{-15}$	9.8±0.8[a] 7.8±0.8
1-butene	$(1.1±0.2)x10^{-14}$ [b]	7.8±0.8[b]
2-butene (cis) (trans)	$3.6x10^{-13}$ $3.8x10^{-13}$	2.7±0.8[c]
methylpropene	$3.4x10^{-13}$	-
2-methyl-2-butene	$8.9x10^{-12}$	-
2,3-dimethyl-2-butene	$4.5x10^{-11}$	-

[a] see text for discussion; [b] this work; [c] calculates from the rate constants at 298, 337 and 378K in Dlugokencky and Howard (1989)

Few data have been published on the reactions of the nitrate radical with haloalkenes (Andersson *et al.*, 1989; Atkinson *et al.*, 1987; Wangberg *et al.*, 1990), and there is only one published temperature dependence in the literature (Wayne *et al.*, 1991). Atkinson *et al.* (1987) have demonstrated that the number and position of chlorine atoms on a haloalkene systematically influence the rate of reaction with NO_3. When looking at the trends in the rates of addition reactions of a radical to a series of organic molecules, one common way of rationalising the reactivity is to use the ideas of inductive/mesomeric effects (Nonhebel, Tedder and Walton, 1979). For the rate of addition of NO_3 to the halo-substituted alkenes,

this form of argument is presented in the following pages. This form of rationalisation of reactivity is qualitative, and cannot really be used with any degree of certainty, but it serves as an interesting starting point from which to consider the observed reactivity for a series of compounds.

As stated previously, the primary factor that governs the rate of attack of the NO_3 radical on an unsaturated molecule is the distribution of the electron density in the π-bond, the polarity of which is affected by both alkyl- and halo- substitution (Tedder and Walton, 1980). With halo-substitution there will be both inductive (negative) (-I) and mesomeric (positive) (+M) effects to be taken into account. The inductive effects of halogen atoms are stronger than their mesomeric effects, so that there will be a net reduction of electron density from the bond, causing deactivation toward electrophilic attack. The "inductive deactivation" will fall off with decreasing proximity of the halogen atom and will be less marked with bromine than with chlorine since bromine has a smaller electronegativity (on the Pauling, (1932) scale Cl=3.2 and Br=3.0). The alkyl groups present in an olefin are said to exert a positive inductive effect (+I). The orientation of radical addition to unsaturated olefins, when halogen atoms are present in the molecule, is contrary to *Markownikoff's* rule (Rüchardt, 1970).

The primary influence of changes in electron density in the parent alkene on the observed reactivity does not fully explain the patterns of reactivity seen with the groups of substituted C_4 alkenes studied here. There is evidence that there is a second rate determining factor; this factor is stabilisation of the radical intermediate. The more substituted at the radical centre the radical intermediate, the more stable it will be (Rüchardt, 1970) and chlorine has a greater stabilising effect than an alkyl group (Giese, 1988). In an NO_3-alkene addition

reaction that has an appreciable activation energy (>3kJ mol^{-1}) and in which the transition-state formed is product-like, the radical intermediate formed (see e.g. equation 2.32) is a good indication of the structure of the transition-state. This premise is applied qualitatively in order to explain the increase in observed reactivity towards reaction with NO_3 of those compounds with stable radical intermediates.

The influence of an inductive effect and radical intermediate stabilisation on observed reactivity can be seen by looking again at the homologous series ethene, propene and 1-butene (see Table 2.4). The inductive effect will be the main rate-determining factor with a positive inductive effect being exerted by an alkyl group, making the π-bond more susceptible to electrophilic attack. For a methyl group, the inductive effect (σ_i) is -0.04 whereas for an ethyl group σ_i=-0.05, on the corrected Taft scale for the polar parameters of a substituent (Taft *et al.*, 1958). These parameters are given relative to hydrogen, for which σ_i=0; a negative value indicates electron donation as compared to hydrogen. Ethene reacts with NO_3 more slowly than propene by almost two orders of magnitude, this difference in reactivity being a result primarily of the positive inductive influence of the alkyl groups present in both 1-butene and propene. In ethene there is also almost no stabilisation of the radical intermediate, whereas with the alkenes of higher relative molecular mass the alkyl groups present stabilise the radical intermediate. Thus the stabilities of the intermediate in the reaction of NO_3 with simple alkenes will be in the order

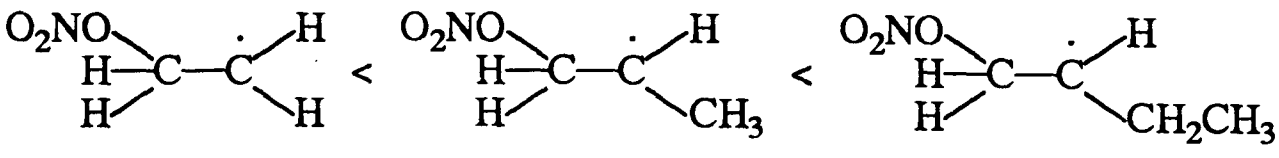

(2.33)

The effects of halo-substitution on rate are exemplified by the series of chloro-substituted 1-butene derivatives, 1-chloro-1-butene, 2-chloro-1-butene and 3-chloro-1-butene. The rate constants (see table 2.5) are in the order

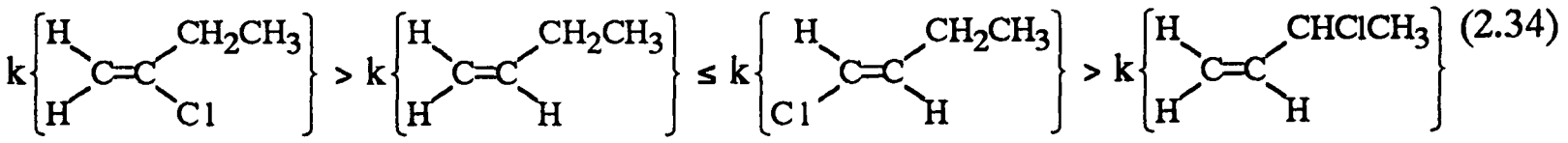

(2.34)

Table 2.5 - The room temperature rate coefficients for the reaction of NO_3 with the halo-1-butenes and 1-butene

Compound	$k_{2.26}$ cm^3 $molecule^{-1}$ s^{-1}
1-butene	$(1.1\pm0.2)\times10^{-14}$ [a]
1-chloro-1-butene	$(1.2\pm0.4)\times10^{-14}$
2-chloro-1-butene	$(1.7\pm0.3)\times10^{-14}$
3-chloro-1-butene	$(2.8\pm0.7)\times10^{-15}$
3-bromo-1-butene	$(4.0\pm1.0)\times10^{-15}$
4-bromo-1-butene	$(5.0\pm1.0)\times10^{-15}$

All errors quoted as $\pm2\sigma$; The full results are given in Table 2.2; a) See §2.4

The π-electron density of a double bond will be subject to a net decrease if a chlorine atom is present. If the electron density was the sole factor affecting rate, it would cause a decrease in the rate of reaction of the chloro-substituted derivatives as compared to the unsubstituted parent compound. The negative influence on rate is counterbalanced by the positive influence of radical-intermediate stabilisation. The radical centre can be stabilised

by both chloro and alkyl groups.

For the reaction of 2-chloro-1-butene with NO_3,

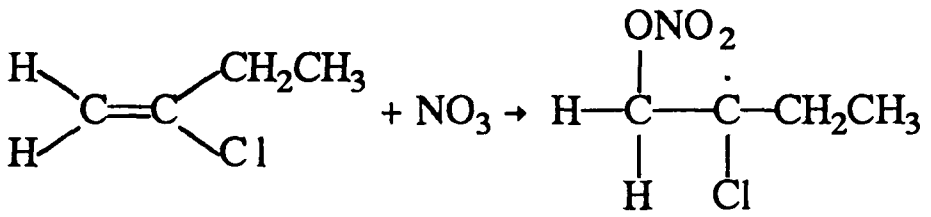

(2.35)

stabilisation of the radical-intermediate is an important factor, with both the chlorine atom and the alkyl group stabilising the radical centre. This effect outweighs the withdrawal of electron density from the π-bond by the chlorine atom. With 3-chloro-1-butene, there is little effective stabilisation of the radical centre, so that the negative inductive effect, which itself is reduced because the chlorine atom is not adjacent to the double bond, is the dominant factor affecting the rate of reaction.

In the case of 1-chloro-1-butene, the rate constant is similar to that for 1-butene. There are two radical intermediates that might possibly form

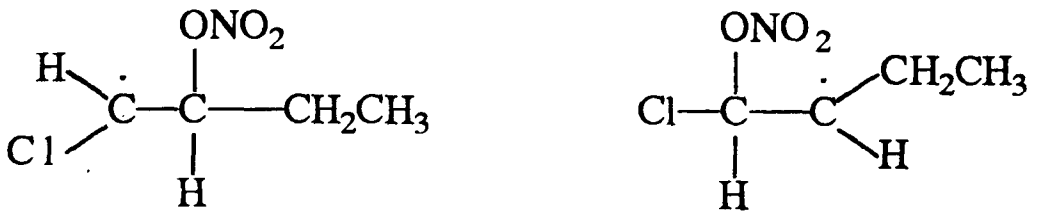

(2.36)

Steric and polar arguments suggest that (a) is the most likely, but not exclusive, intermediate to be formed. Formation of a stabilised intermediate would offset the negative influence on the observed reactivity of the chloro-inductive effect.

The 2-butene chloro-derivatives show similar trends in reactivity to those of the 1-butene derivatives, but with some important differences. The 2-butene chloro-derivatives, 1-chloro-2-butene and 2-chloro-2-butene, have rate constants (see table 2.6) in the order

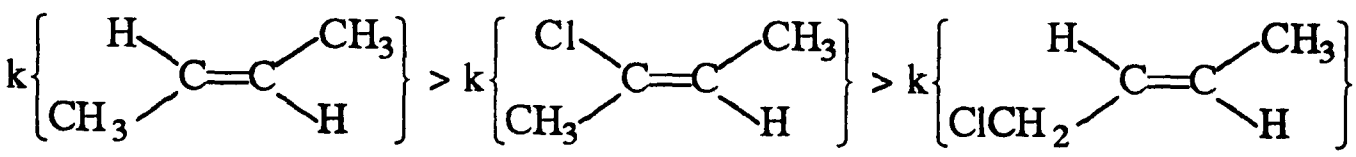

(2.37)

These reactivities contrast with those for the reaction between 1-butene chloro-derivatives and NO_3. The rate of reaction of 2-butene with NO_3 is greater than the rate of reaction of 2-chloro-2-butene with NO_3. To explain the difference, it is necessary to discuss the relative contributions of the factors discussed earlier and their influence on the rate-determining step.

Table 2.6 - The room temperature rate coefficients for the reaction of NO_3 with halo-2-butenes and t-2-butene

Compound	$k_{2.26}$ cm^3 $molecule^{-1}$ s^{-1}
t-2-butene	$(3.96\pm0.48)\times10^{-13}$ [a]
1-chloro-2-butene	$(2.0\pm0.7)\times10^{-14}$
2-chloro-2-butene	$(1.1\pm0.4)\times10^{-13}$
2-bromo-2-butene	$(1.3\pm0.1)\times10^{-13}$

All errors quoted as $\pm2\sigma$; The full results are given in table 2.2; a) taken from Wayne *et al.*, 1991.

The presence of two methyl groups activates the double bond towards electrophilic attack by NO_3 to a much greater extent than does the single ethyl group in 1-butene, leading to an increase in the initial rate of attack of the NO_3 radical. The positive inductive influence of the methyl groups on the double bond is now the main one that dominates the reaction rate

step and dictates the ordering of the reaction rates shown in sequence 2.37. This explanation is confirmed by the effect that chlorine substitution has on reactivity, a greater relative decrease in the rate of reaction (as compared to the parent alkene) being observed with halo-substitution. Stabilisation of the radical intermediate would suggest that the rate constant for the reaction of 2-chloro-2-butene with NO_3 would be greater than that measured, but the effective contribution of stabilisation to the overall rate is reduced, since the activation energy for the reaction of *trans*-2-butene is zero within experimental error, and little increase in the rate constant would be expected on additional substitution.

The order of reactivities (see table 2.7) for the other C_4 alkenes studied, the methylpropenes and their chloro-derivatives,

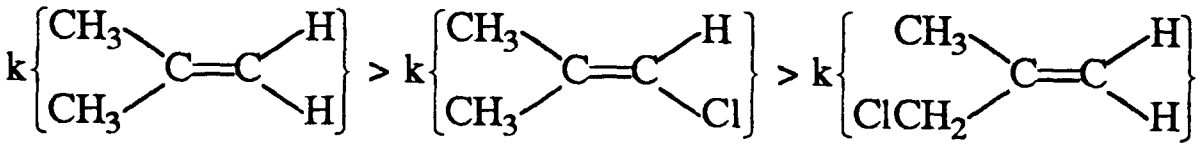

(2.38)

Table 2.7 - The room temperature rate coefficients for the reaction of NO_3 with 2-methylpropene and halo-derivatives

Compound	$k_{2.26}$ cm^3 $molecule^{-1}$ s^{-1}
2-methylpropene	$(3.38\pm0.43)\times10^{-13}$ [a]
1-chloromethylpropene	$(9.0\pm0.23)\times10^{-14}$
3-chloromethylpropene	$(2.15\pm0.4)\times10^{-14}$

All errors quoted as $\pm2\sigma$; the full results are given in table 2.2; a) taken from Wayne *et al.*, 1990.

reinforce the previous rationale presented for the reactivities of the chloro-2-butenes. Here,

the dominant factor determining the observed reactivity is the positive inductive effect of the two methyl groups, which is opposed by the negative inductive effect of the chlorine atom. In order to explain the ordering of the reactivities of these compounds, it is important to investigate the possible radical intermediates that can be formed. According to the rule previously used, these intermediates would be

(2.39)

From the postulated structure of these intermediates, it would be expected that 3-chloromethylpropene would react more slowly than 1-chloromethylpropene because the chlorine atom is further away from the double bond, and the ordering of rate constants verifies this interpretation. Even though the predicted activation energy (Wayne *et al.*, 1991) for the reaction of NO_3 with methylpropene is low (≈1 kJ mol^{-1}) the activation energies for the reaction of NO_3 with the chloro-analogues is greater than zero (≈10 kJ mol^{-1}), so that the radical intermediate plays a part in determining the rates of reaction with the substituted compounds.

The relative contribution of the inductive effect to the overall kinetics is exemplified by the reaction of NO_3 with the bromo compounds 3-bromo-1-butene and 4-bromo-1-butene. The site of substitution of a bromine atom in the α-position or the β-position is reflected in the degree of withdrawal of π-electrons and the reaction rates.

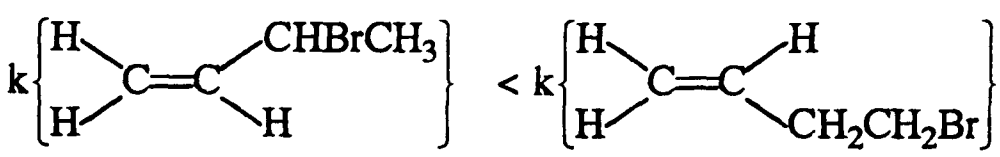

(2.40)

This result is directly analogous to the pattern of reactivity seen with the chloro-1-butenes. There is no contribution to the observed rate due to the stabilisation of the radical intermediate, as the two intermediates would be almost identical. It can also be seen that it does not matter at which C-atom of the alkyl group the substitution takes place.

A comparison of the rates of reaction of 3-chloro-1-butene and 3-bromo-1-butene shows clearly the differing relative strengths of the inductive effect. Chlorine has a relative electronegativity of 3.2 and bromine 3.0, on the Pauling scale (1932), this difference manifesting itself in a comparison in the rates of reaction of the two compounds with NO_3. The relative stabilities of the radical intermediates would again be similar.

A similar comparison of the reactivities of 2-chloro-2-butene and 2-bromo-2-butene reveals much the same trend. The reactions of the bromo-substituted butenes are, if anything, faster than those of their chlorinated counterparts. A consideration of these rates may also go some way to indicating the unimportance of steric influences in these reactions. Steric effect are not expected, since the radical approaches at an angle of 120° to the molecular plane and will interact with the π^*-orbital at the end opposite to the substituent. The magnitude of the increase in the rate of reaction from the bromo- and chloro-substituted 2-butenes also suggests that there is little enhancement of the rate due to the mesomeric effect, which is larger for bromine than for chlorine. Table 2.8 attempts to rationalise the competing substituent effects for the chloro-butenes derivatives.

Table 2.8 The possible substituent effects for the chloro–butenes

Compound	Rate a)	Inductive effect b)	Possible radical formed c)
1–butene	$1.1x10^{-14}$	+I(Et)α	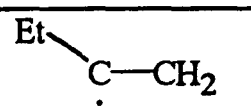 +Et
1–chloro–1–butene	$1.2x10^{-14}$	–I(Cl)β +I(Et)α	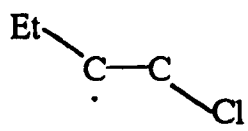 +Et/+Cl β/α
2–chloro–1–butene	$1.7x10^{-14}$	–I(Cl)α +I(Et)α	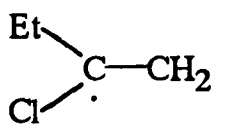 +Et/+Cl α/α
3–chloro–1–butene	$0.3x10^{-14}$	–I(Cl)β	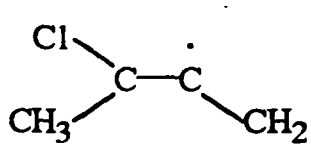 +Cl β
2–butene	$3.9x10^{-13}$	–I(Me)2xα	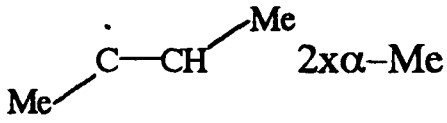 2xα–Me
1–chloro–2–butene	$2.0x10^{-14}$	–I(Cl)α +I(Me)α	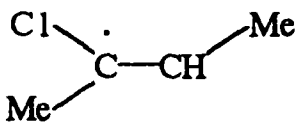 +Cl(α) +Me(α)
2–chloro–2–butene	$1.1x10^{-13}$	–I(Cl)α +I(Me)β	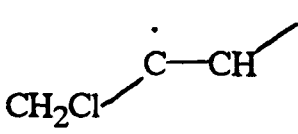 +Me(β) +Cl(β)
methylpropene	$3.6x10^{-13}$	+I(Me)2xα	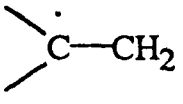 2xα–Me
1–chloromethyl–propene	$9.0x10^{-14}$	+I(Me)2xα –I(Cl)α	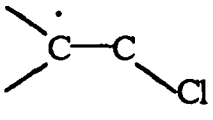 β–Cl 2xα–Me
3–chloromethyl–propene	$2.5x10^{-14}$	+I(Me)2xα –I(Cl)β	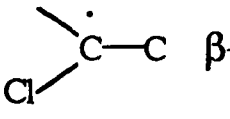 β–Cl α–Me

a) cm^3 $molecule^{-1}$ s^{-1}
b) +/– positive/negative I–Inductive Me/Et/Cl methyl/ethyl/chloro
c) structure of postulated intermediate and radical stabilizing groups present

2.7 Atmospheric Implications

In the polluted urban troposphere, as distinct from the natural troposphere, relatively high concentrations of a wide range of anthroprogenic hydrocarbons (Seinfeld, 1989) are found. In a recent survey of air quality in 35 cities of the U.S.A., 1-butene was identified as one of the 25 most abundant hydrocarbons. The median concentration for 1-butene was over 5.9 ppbc, with maximum concentrations reaching 365 ppbc (Seila and Lonneman, 1988). In the marine biosphere, 1-butene is found in oceanic surface waters. Oceanic waters are highly supersaturated with respect to the marine atmosphere by 2-3 orders of magnitude with non-methane hydrocarbons (Plass *et al.*, 1989). Average atmospheric volume mixing ratios for 1-butene in the Northern Hemisphere are 10^9. The emission rate for 1-butene in the Northern Hemisphere is 1.2×10^8 molecule^{-1} cm^2 s^{-1}.

The atmospheric half-life, $\tau_{½}$, of a compound is defined as the time taken for the concentration of a species to fall to one half of its initial value (Finlayson-Pitts and Pitts, 1986). Thus, for a simple bimolecular process

$$A + NO_3 \longrightarrow \text{Products} \qquad (2.41)$$

the lifetime of reactant A, $\tau_{½}^{A}$, is given by

$$\tau_{\frac{1}{2}}^{A} = \frac{\ln(2)}{k_{2.41}[NO_3]} \qquad (2.42)$$

According to our room temperature measurements, the atmospheric half-life of 1-butene with respect to the reaction with NO_3 during the night is 17.5 h ([NO_3] = 10^9 molecule cm^{-3} at night (Wayne *et al.*, 1991)). This lifetime can be compared to a half-life with respect to the reaction with the OH radical of 6.4h ([OH] = 10^6 molecule cm^{-3} during the day (Atkinson,

1989)). Thus the reaction of NO_3 with 1-butene makes a 27% contribution to the atmospheric scavenging of this alkene in the atmosphere, but the value must be interpreted with caution because of the regional variation and uncertainty in [OH] and [NO_3]. A further factor will be the possible removal routes for species in the troposphere, other than by homogenous gas-phase processes, e.g heterogeneous removal *via* wet and dry deposition on ocean, land and aerosol surfaces. Another interesting question is, of course, the atmospheric fate of the products of the interaction, which could be noxious or undergo further chemical transformations.

The C_4 halo-alkenes are unlikely to be of any atmospheric significance except where local pollution leads to anomalously high concentrations of these compounds. The atmospheric half-lives of these compounds with respect to reaction with NO_3 are listed in table 2.9. The rate coefficients for the reactions of OH with them have not yet been experimentally determined.

2.8 Conclusion

In this chapter the kinetic results for the reaction of NO_3 with a series of halo-butenes and 1-butene have been presented. The patterns of reactivity displayed by these compounds in terms of the rate of addition of NO_3 to the double-bond have been rationalised by invoking qualitative rather than quantitative methods i.e. substituent effects and stabilisation of the radical intermediate. In the absence of any firm quantitative basis these methods are useful to give a good first approximation. In the next Chapter, better semi-quantitative ideas based on the frontier-orbital and group additivity relationships are used to rationalise the observed

reactivity of NO_3 towards these compounds.

Table 2.9 - The atmospheric half-lives with respect to the reaction of NO_3 with some halobutenes.

Compound	$\tau_{½}$ (h) [a)]
1-chloro-1-butene	16.04
2-chloro-1-butene	11.32
3-chloro-1-butene	64.18
1-chloro-2-butene	9.62
2-chloro-2-butene	1.75
1-chloromethylpropene	2.13
3-chloromethylpropene	7.7
4-bromo-1-butene	38.5
2-bromo-2-butene	1.4

a) atmospheric $[NO_3]$ assumed to be 1.0×10^9 molecule cm^{-3}; see text.

Table 2.10 - The atmospheric half-lives with respect to the reaction of NO_3 with some halobutenes.

Compound	$\tau_{½}$ (h) [a)]
1-chloro-1-butene	80.2
2-chloro-1-butene	56.6
3-chloro-1-butene	320
1-chloro-2-butene	48.1
2-chloro-2-butene	8.7
1-chloromethylpropene	11.0
3-chloromethylpropene	38.5
4-bromo-1-butene	192
2-bromo-2-butene	7.1

a) atmospheric $[NO_3]$ assumed to be 2.0×10^8 molecule cm^{-3} i.e. 100ppt.

CHAPTER 3

Patterns of reactivity in the reactions of NO_3

3.1 Introduction

In order to assess the tropospheric lifetime of an organic compound it is necessary to have knowledge of reaction rate coefficients for its reaction with different tropospheric oxidants (Atkinson, 1987). The difficulty in measurement of rate coefficients (see Chapter 2) is exacerbated by the extremely large number of organic compounds both of anthropogenic and, to a lesser extent, biogenic origin (Seinfeld, 1989). There can also be a further problem; the very low volatility of many organic compounds, particularly of industrial origin, may make it impossible to measure the rate coefficients in the laboratory. The *a priori* prediction of tropospheric lifetimes (*via* measured rate coefficients or estimated from other molecular properties) and other environmental quantities is of importance in the development of more environmentally "friendly" organic chemicals. For example Sablić and Protić (1989) have predicted quantitatively on the basis of a structure-reactivity relationship the active toxicity of commercial chemicals on fathead minnows. The approach has also been used to look at soil sorption coefficients of organic chemicals on the basis of their molecular topology (Sablić, 1987). This approach can be extended to reaction kinetics to look at correlations between chemical reactivity (i.e. rate) and molecular properties or energies (Sablić, 1988). In this chapter we explore the patterns of reactivity in the reactions of the nitrate radical with alkenes, using the kinetic data presented in Chapter Two. First, a correlation between activation energy (E_a) and molecular polarisability (α) is demonstrated (§3.3). The observed reactivity of NO_3 to a homologous series of alkenes C_nH_{2n}, as well as the corresponding halo-substituted alkenes, is rationalised by means of a frontier-orbital approach (HOMO-LUMO) (§3.4), where data for E(HOMO) (*c.f.* ionisation potentials; see §3.6) which have not been experimentally determined are calculated using a semi-empirical method. This approach is

supplemented by looking at group-additivity factors, as suggested by Atkinson (1986,1987), in an attempt to compare the two methods for estimating rate constants. Finally, the photoelectron spectra (PES) (§3.2.2) of the halobutenes are presented in order to investigate experimentally the molecular basis for the frontier-orbital approach.

3.2 Experimental details

3.2.1 Semi-empirical methods

In this work, molecular orbital calculations were carried out using a semi-empirical method. The methods of calculating molecular orbitals (MO) can be split into two main branches. Semi-empirical methods are ones which use additional or *posterior* information (Sadlej, 1985) in comparison to the more theoretically pure non-empirical, so-called *ab-initio* methods (Richards and Cooper, 1983; Simmons, 1991). A problem with *ab-initio* methods is that they are currently very slow and routine application to any degree of accuracy is still quite difficult (Simmons, 1991). Unlike *ab-initio* methods, the accuracy of any empirical method is limited by the accuracy of the experimental data used to obtain the parameters (Dewar, 1985). The power of semi-empirical methods is that, even though they may not be theoretically rigorous, they are able to reproduce important chemical properties with little effort. In fact, for systems which have been parameterised for semi-empirical methods, the accuracy is comparable with that obtainable using *ab-initio* methods (Dewar and Storch, 1985).

A semi-empirical method is composed of a theoretical framework and a set of parameters. For calculating molecular orbitals, the starting theory is based on wave-mechanics and the Schrödinger equation. On this basis, with semi-empirical methods one makes a series of

approximations, forming the theoretical framework (Sadlej, 1985); the parameters are, in essence, an atomic basis set that describe (non-rigorously) the atomic properties. A more thorough examination of the underlying theory and the parameters has been described elsewhere (Sadlej, 1985; Dewar, 1969; Stewart, 1989a).

In this work, the MOPAC 5.0 package (Stewart, 1985) was used to implement the AM1 (Dewar *et al.*, 1985) and PM3 (Stewart, 1989a,b) parameterisations of atomic wave functions. Though MOPAC calls upon many concepts in quantum theory, thermodynamics and advanced mathematics, the user needs little knowledge of those concepts, as MOPAC is written for the non-theoretician. The features of MOPAC used in this work are described in order to highlight the applicability and usefulness of this method.

The starting point for the calculation is the input-data file or *z-matrix*. This defines the initial molecular geometry of the molecule of interest. Table 3.1 shows the *z-matrix* used to define the geometry of 1-butene and explains the nomenclature used. The *z-matrix* is then fed to the MOPAC package. In addition, the data file also contains other commands (keywords) in order to specify the type(s) of calculation to be undertaken (See Stewart, 1985). The coordinate of the first atom is defined as being at the origin of cartesian space, the second displaced by the defined bond length along the positive x-axis and the third atom is displaced by its bond length and angle into the x-y plane. The interatomic distances are checked to make sure that the smallest interatomic distance is greater than 0.8Å. The geometry is then optimised in a series of cycles to find the minimum energy geometry using the BFGS method (Broyden, 1970; Fletcher; 1970; Godfarb, 1970; Shanno, 1970).

Table 3.1 - The *z-matrix* for 1-butene

Atom	Bond length (Å)	†	Bond angle (°)	†	Dihedral angle (°)	†	N_A	N_B	N_C
C									
C	1.5	1					1		
C	1.4	1	111.0				2	1	0
C	1.3	1	124.0	1	116.0	1	3	2	1
H	1.1	1	110.0	1	170.0	1	1	2	3
H	1.1	1	110.0	1	50.0	1	1	2	3
H	1.1	1	110.0	1	299.0	1	1	2	3
H	1.1	1	109.0	1	239.0	1	2	1	3
H	1.1	1	109.0	1	122.0	1	2	1	3
H	1.1	1	114.0	1	296.0	1	3	2	1
H	1.0	1	122.8	1	350.0	1	4	3	2
H	1.0	1	122.8	1	179.0	1	4	3	2

† - mark parameter for optimisation (0,1)

N_A - Bond connectivity (i.e. is connected to atom x)
N_B - Angle connectivity (i.e. makes an angle with atom x)
N_C - Dihedral angle connectivity (i.e. makes a dihedral angle with atom x)

Therefore:

N_A - bond length
N_A:N_B - bond angle
N_A:N_B:N_C - Twist or Torsion angle

In MOPAC 5.0 (Stewart, 1985) the MO parameters for both AM1 and PM3 are optimised to reproduce the experimental heat of formation of a large set of compounds (Stewart, 1989b). For our calculations, the molecular geometries were optimised using a number of different starting geometries. A comparison of calculated values of ΔH_f for each starting geometry was used to ensure that a global energy minimum was achieved.

One of the quantities calculated using this method, in accordance with Koopman's theorem (1934),

$$I_j = -\varepsilon_j \tag{3.1}$$

is the ionisation potential (I_j) which is the negative of the energy (ε_j) of the highest occupied or highest partially occupied molecular orbital. Further information about the resultant molecular orbitals in the form of eigenvalues or energy levels is given. These eigenvalues can be broken down into the individual eigenvectors (i.e. the contribution of the individual atomic orbital to the resultant molecular orbital), which are normalised to unity, i.e. the sum of the square of the coefficients is exactly one; e.g., in molecular hydrogen

$$\sigma = c_1\phi_1 + c_2\phi_2 \tag{3.2}$$

where σ describes the electronic wavefunction i.e. the H_2 molecular orbital wavefunction, ϕ_i (where the subscript (i) refers to the number of the atom) is the atomic wavefunction of atom i and c_i, the coefficients, are a measure of the contribution which an individual atomic orbital makes to the molecular orbital. The program can also be used to calculate the molecular polarisability. A detailed discussion of this is given by Dewar and Stewart (1984) and Stewart (1985).

3.2.2 Photoelectron spectroscopy

The photoelectron spectra were recorded on a P.E.S. Laboratories Ltd. Photoelectron Spectrometer Model 0078. The spectrometer consisted of a photon source, an ionisation chamber, and an electron analyser (see figure 3.1). The photon source was a hollow cathode helium discharge lamp (Helectros Developments Ltd.). A microwave discharge on low pressures (*ca.* 0.1-1 Torr) of helium produced both He I and He II radiation ($h\nu$ = 21.21 and 40.81 eV). The samples were admitted *via* a probe which fitted onto the top of the discharge lamp. Because of the relatively high sample volatility (*ca.* 130 Torr at T=298K) the sample was held externally in a glass finger, the amount of vapour admitted into the ionisation chamber being regulated by a stainless steel needle valve (Nupro). The photoelectrons produced by the action of the ionising radiation on the sample were admitted to an electron analyser. This analyser operates by electrostatic deflection of the electrons in a 127° cylindrical sector, the potential across which is varied to scan through the range of electron kinetic energies. The electrons were detected by a Channeltron electron multiplier. Spectra were collected by repeated scans of about 60 s in order to minimise relative intensity changes due to temperature, sample pressure and changes in photon intensity. There was no apparent drift in the signal during data collection.

The spectrometer was interfaced to a Research Machines 380Z microcomputer, which allowed control of the instrument and automated collection of data (Cooper, 1984). The spectra were calibrated with reference to N_2, Xe and the helium self ionisation band shown in table 3.1 (see Lloyd, 1970). The actual position of the bands in an uncalibrated (or contact potential) spectrum is dependent on instrument and sample dependent factors (e.g. sample pressure).

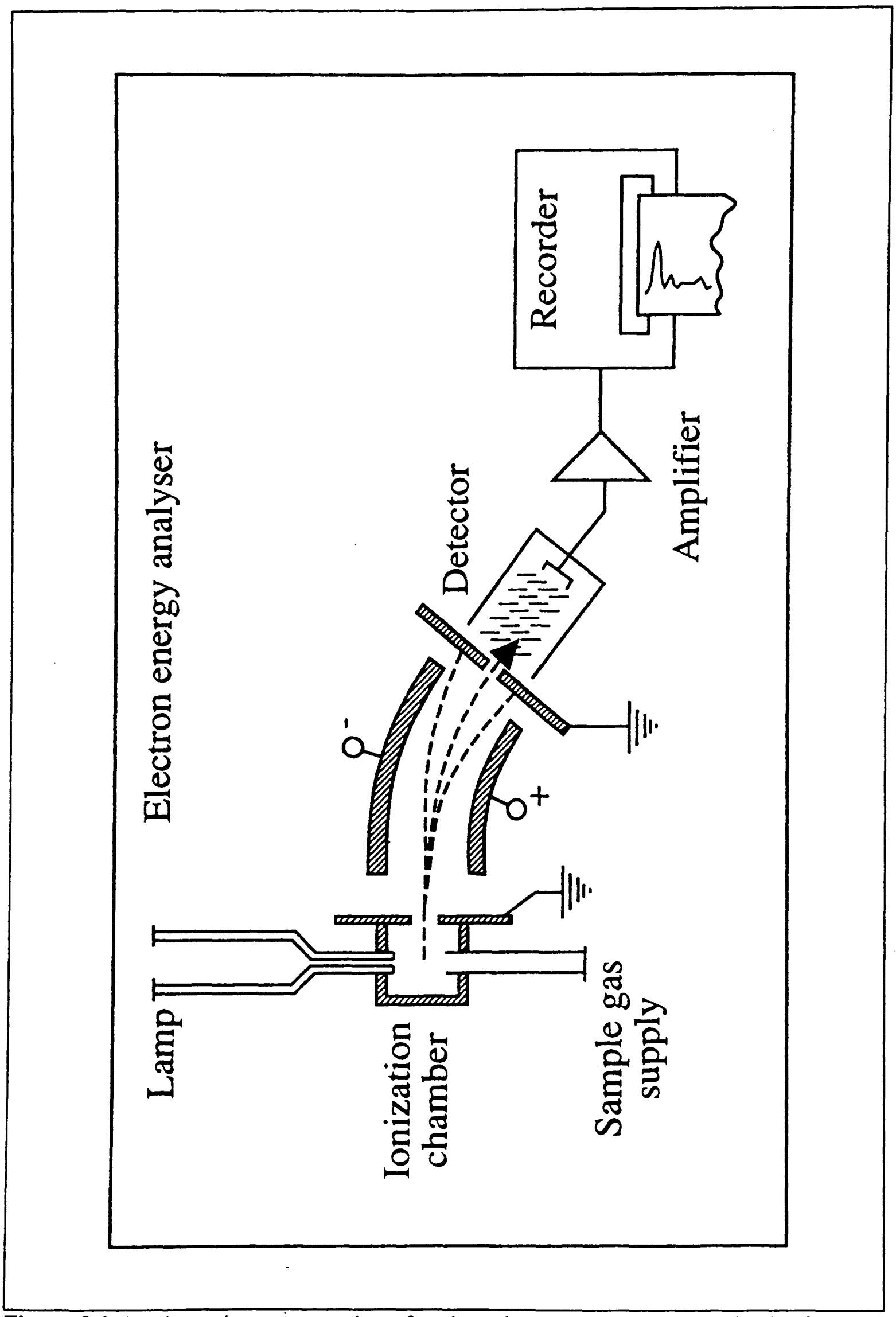

Figure 3.1 A schematic representation of a photoelectron spectrometer (Eland, 1973)

In practice, a small amount of calibrant gas mixture was admitted to the ionisation chamber and a combined sample and calibrant gas spectrum was taken. A spectral scaling factor could then be calculated using the position of the calibration lines to fix the energy scale and determine the ionisation potentials. A linear interpolation was made between the calibrant lines based on the experimentally determined potentials.

Table 3.2 - The calibration lines used for PES.

Calibrant gas	Ionic state	Ionising line	Electron energy /eV	Apparent ionisation potential† /eV
Xe	$^2P_{3/2}$	HeIα	9.088	12.130
Xe	$^2P_{1/2}$	HeIα	7.782	13.436
N_2	$^2\Sigma_0$	HeIα	2.467	18.751
He	2S	HeIIα	16.2268	4.99907
He	2S	HeIIβ	-	17.025

†As if the ionisation were by HeIα in all instances

This method allowed ionisation energies to be calculated with an accuracy of ±0.05 eV. Lloyd (1970) has shown that for electron energies below 5e V there is a deviation from linearity in the interpolation.

3.3 Variation of activation energies for the addition reactions of NO_3

A correlation can be useful for the purpose of display, comparison and evaluation of kinetic data as a function of a physical property of a substrate. There are, however, limitations arising not only from the approximate nature of the such correlations but also from the scarcity and uncertainty in the kinetic parameters. One correlation that has frequently been used in the past for a homologous series of reactions is that between the activation energy for the reaction (or the logarithm of the rate coefficient at fixed temperature, which itself is a measure of the activation energy for series of reactions for which the pre-exponential factors are expected to be the same) and the ionisation potential of the reactant (see §3.4 and §3.6). The basis for such a correlation is that the activation energy should be proportional to the difficulty of removing an electron entirely from the reactant molecule in an electrophilic process. Figure 3.2 shows the results of attempting an activation energy-ionisation potential correlation (dashed line, upper scale). There is obviously quite a good linear relation between the parameters plotted, as has been observed previously (in terms of room-temperature rate coefficients) (Wayne *et al.* 1991; Biggs *et al.*, 1990) for a similar series of reactants. However, it is also of interest to see if there is a correlation between the polarisability of the reactant molecule and the activation energy of the reaction, since the polarisability reflects the ease with which the molecule can be distorted in the initial stages of the interaction.

It has been shown by Krech and McFadden (1977a,b) that it is possible to correlate empirically the activation energy, E_a, with molecular polarisability α_{BC}, of BC for an exoergic reaction of the type

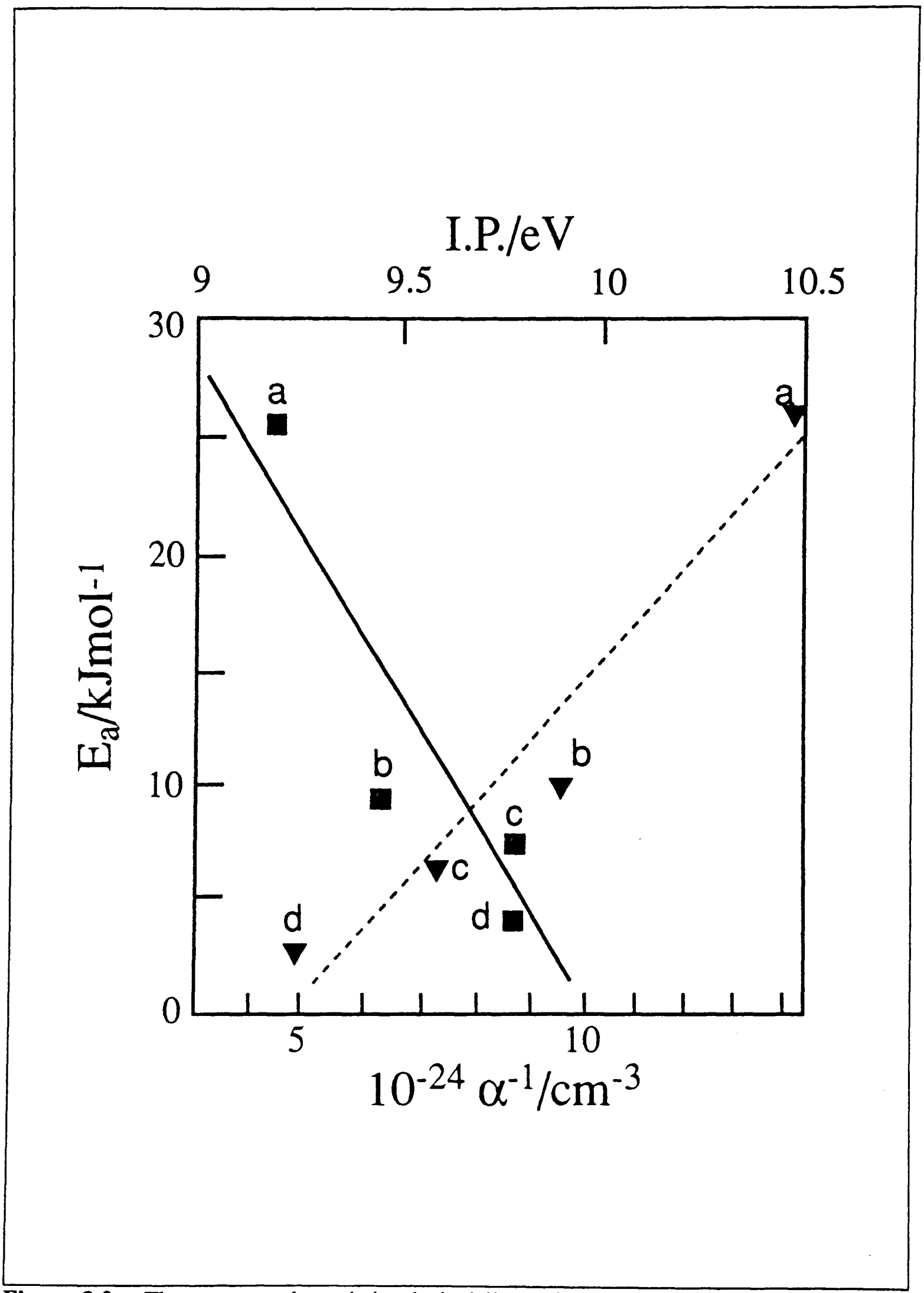

Figure 3.2 The upper scale and the dashed line refer to a correlation with ionisation potential, while the lower scale and the dashed line refer to a correlation with inverse polarisability.

$$A\bullet + BC \rightarrow AB + C\bullet \qquad (3.3)$$

by the simple equation

$$E_a = \frac{F}{\alpha_{BC}} \qquad (3.4)$$

where F is an empirical parameter. This equation has been shown to provide good quantitative representation for atom abstraction reactions (Krech and McFadden, 1977a,b).

In a recent study of the reaction of propene with NO_3, it was reported (Canosa-Mas *et al.*, 1991) that the activation energy was (9.7±0.8) kJ mol^{-1} for the temperature range 298 to 423 K. It was suggested that the abstraction of an allylic hydrogen by NO_3 can make a contribution to the measured decay of NO_3 and therefore a lower limit of (7.8±0.8)kJ mol^{-1} was proposed for the activation energy of the addition reaction. According to Dlugokencky and Howard (1989), the temperature dependence of the reaction of NO_3 with *trans*-2-butene shows non-Arrhenius behaviour between 298 K and 473 K which can be fitted using a double-exponential expression. Assuming that the data at 298, 337 and 378 K can be fitted by the conventional Arrhenius expression with a single exponential, an activation energy of (2.7±0.8) kJ mol^{-1} can be calculated for the higher temperature results of Dlugokencky and Howard. The result of plotting E_a vs. $1/\alpha$ for the homologous series of alkenes, C_nH_{2n}, is shown in figure 3.2. In all cases, the required molecular polarisabilities can be readily calculated from refractive index measurements (Landolt-Bornstein, 1951). Table 3.3 summarises the data used in this correlation. Figure 3.2 shows that the simple relationship implied by equation (3.4) does not provide a good description of the data. An expression containing two empirical parameters (I and F)

$$E_a = I + \frac{F}{\alpha_{BC}} \qquad (3.5)$$

appears to be more appropriate. The numerical values of I and F will depend on the series of reactions to which the equation is applied. For the addition reactions of NO_3, the correlation line is

$$E_{a(addition)} = -16 + \frac{18}{\alpha_{BC}} \qquad (3.6)$$

This correlation can be extended further to compounds without experimentally determined polarisabilities; table 3.3 shows the experimentally determined (α_{expt}) and calculated polarisabilities(α_{calc}). The agreement between these values is excellent, suggesting that the correlation could be extended further, to compounds without experimentally determined polarisabilities. Figure 3.3 shows a comparison of α (α_{calc} and α_{expt}) plotted against E_a. As mentioned previously, a correlation is only as reliable as the data available; in this case, the data set used was not extensive, but the correlation appears promising and may help in understanding the way NO_3 reacts with alkenes.

Table 3.3 - The data used in the E_a *vs* $1/\alpha$ correlation.

Compound	E_a /kJ mol^{-1} (a)	IP /eV (b)	IP_{calc} /eV (c)	A cm^3 molecule^{-1} s^{-1} (a)	α_{expt} /cm^3 (d)	α_{calc} /cm^3 (c)
ethene	25.8 (±1.2)	10.51	10.64 (e)	6.3×10^{-13}	4.3×10^{-24}	4.4×10^{-24}
propene	9.7 (±1.4)	9.85	10.1 (e)	4.7×10^{-13}	6.2×10^{-24}	6.8×10^{-24}
1-butene	7.8 (±1.0)	9.63	10.18 10.03 (e)	2.5×10^{-13}	8.5×10^{-24}	8.9×10^{-24}
t-2-butene	4.4 (±0.8)	9.25	-	1.8×10^{-12}	(8.5×10^{-24}) (f)	9.3×10^{-24}

a) from Wayne *et al.*, 1991; b) from Levin and Lias, 1982; c) calculated using PM3 method, see §3.2.1; d) from Landolt-Bornstein, 1951; e) from Stewart, 1989b; f) there is no differentiation in polarisability between the two geometric isomers.

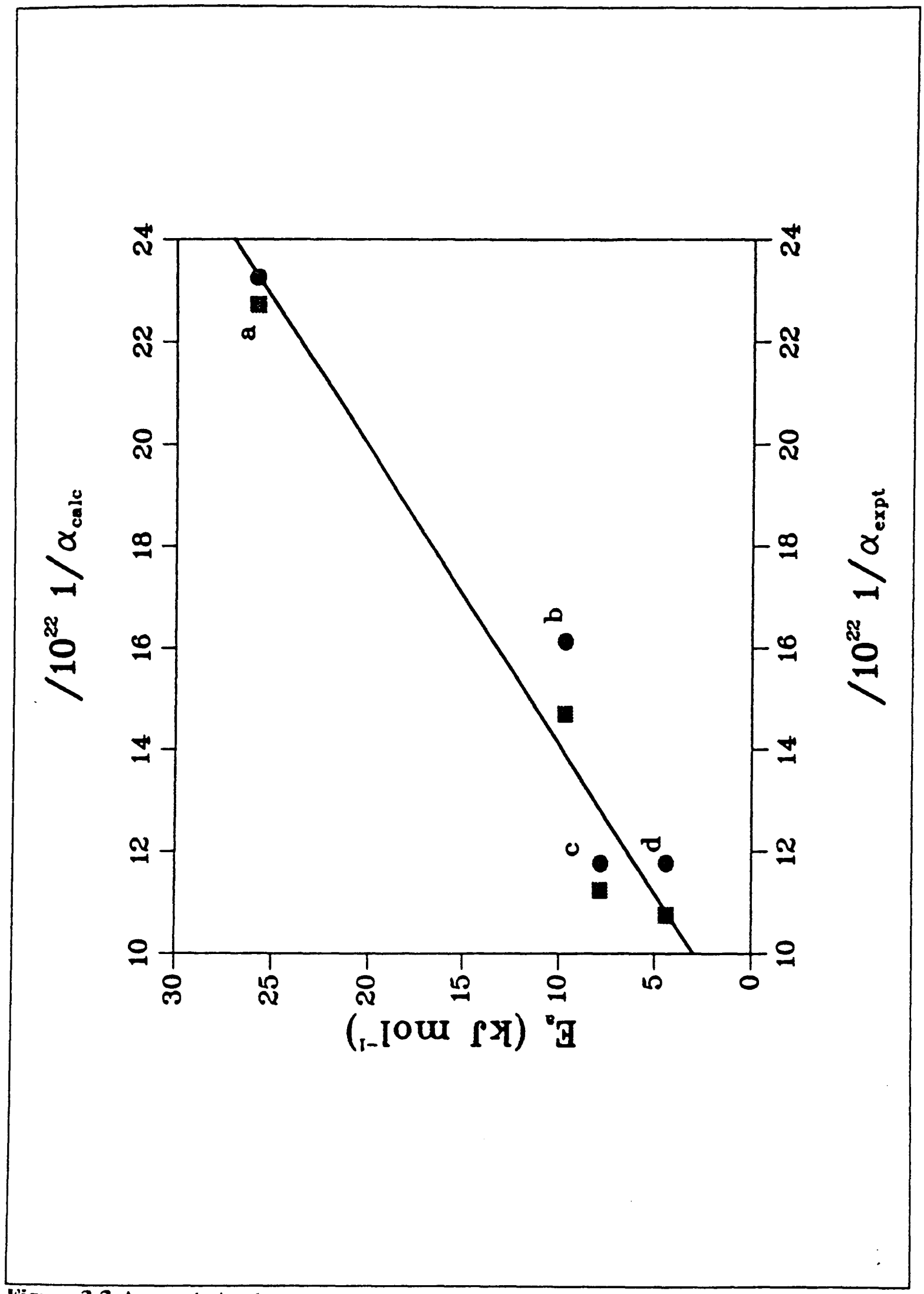

Figure 3.3 A correlation between inverse polarisability and E_a. The compounds are, a) ethene, b) propene, c) 1-butene and d) *trans*-2-butene. The ● represent the experimentally determined polarisabilities and the ■ represent the calculated values (see text).

3.4 Rationalisation of reactivity of NO_3 towards alkenes using a frontier orbital approach

In an ideal situation the rationalisation of reactivity would include the full Arrhenius parameters (i.e. A and/or E_a) but for many compounds these are either ill-determined or unknown. Thus, most quantitative rationales are based on the rate coefficient k. The frontier orbital approach described here attempts to treat on a quantitative basis the observed reactivity of NO_3 towards the series of compounds C_nH_{2n} and their halo-derivatives.

3.4.1 Frontier orbital approach

Molecular orbital theory (Dewar, 1969) is a powerful and versatile method of rationalising chemical reactivity. The basics of molecular orbital theory have now been coupled to the perturbation treatment (PMO) (Dewar and Dougherty, 1975) in order to look at how the interaction of the molecular orbitals (MO) of the starting materials influences the energy of the transition state. In order to apply this approach to a radical-molecule reaction, we shall first look at the major results of PMO. In PMO, the initial interaction of the molecular orbital of the two species is treated as a perturbation by each reactant on the other. However, this approximation breaks down as you approach the transition state, as it ceases to be a mere perturbation and the theory cannot accommodate such large energetic changes (Dewar and Dougherty, 1975).

Figure 3.4 shows the interaction, as two molecules approach each other, of a filled molecular orbital with an unfilled molecular orbital. The highest filled MO is referred to as the HOMO

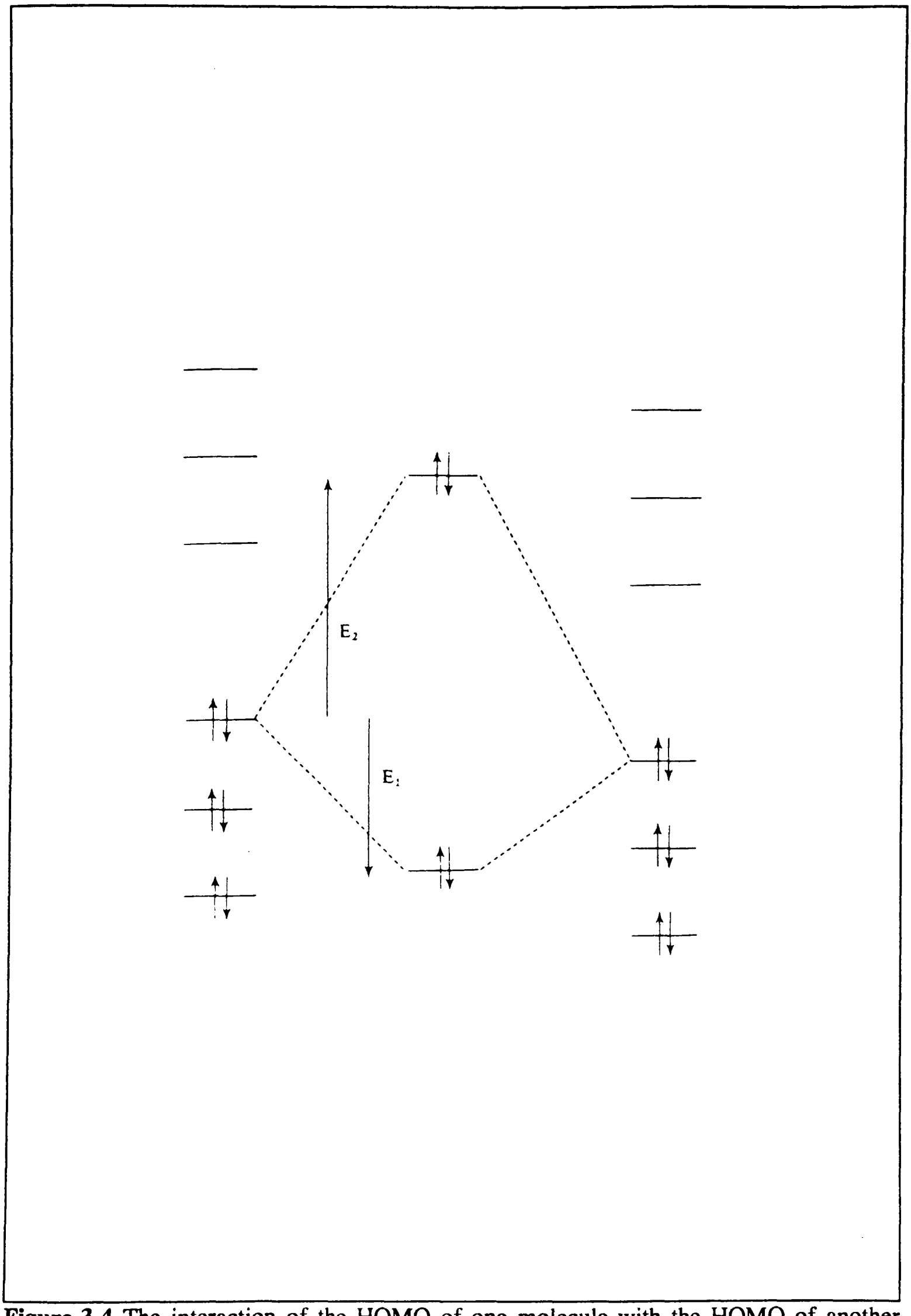

Figure 3.4 The interaction of the HOMO of one molecule with the HOMO of another (After Fleming, 1978)

(highest occupied molecular orbital) and the lowest empty MO as the LUMO (lowest unoccupied molecular orbital). The new molecular orbitals formed will be an approximation to two of the orbitals of the transition state. The formation of the bonding orbital is exothermic (E_1) and the formation of the antibonding orbital is endothermic (E_2). This will also be true for the combination of two fully occupied orbitals, whereas for the interaction of two unfilled MOs there will be no net change in the energy of the system. The HOMO-LUMO interaction causes the largest energy drop (*c.f.* HOMO-HOMO, LUMO-LUMO etc.) on the formation of the new molecular orbitals. This is the basis of the frontier orbital approach (Fukui *et al.*, 1952).

Klopman (1968) and Salem (1968a,b) used perturbation theory to derive an expression for the energy gained (or lost) on the overlap of two MOs during a reaction. The three assumptions on which their equation is based are:

1) the occupied orbitals of one molecule repel the occupied orbitals of the other;

2) any positive charge on one molecule attracts any negative charge on the other (and repels any positive);

3) the occupied orbitals (especially the HOMO's) of each interact with the unoccupied orbitals (e.g. LUMO's) of the other, causing an attraction between the molecules.

The PMO approach cannot take account of strain in the σ-framework, factors which affect entropy or steric effects.

In radical-molecule reactions, most radicals do not have charge and react with neutral

molecules. Thus, the columbic forces between the moieties are usually small while the frontier orbital interactions remain quite large. This has ramifications in how we describe reactions. The apparent electrophilic nature of these reactions is exemplified by the reactions of NO_3 with $CH_2=CH_2$ and with $(CH_3)_2C=C(CH_3)_2$. At room temperature the rate constants are $2.0x10^{-16}$ and $4.5x10^{-11}$ cm^3 $molecule^{-1}$ s^{-1} respectively, values that highlight the dramatic influence of the positive inductive effect of the methyl groups' 'building-up' the electron-density on the double-bond. That the attacking oxygen atom bears a partial negative charge relative to the nitrogen atom of NO_3 has no bearing on this argument. For radicals, the singly occupied molecular orbital (SOMO) plays the role of both HOMO and LUMO (Fleming, 1976; Abbatt and Anderson, 1991; Loewenstein and Anderson, 1987; Fenter and Anderson, 1991). An electrophilic radical is one in which the energy of its SOMO is close to, but higher than, the energy of the HOMO of the reaction partner (see figure 3.5); whereas a nucleophilic radical has a higher energy SOMO which is more likely to interact with the LUMO on the organic molecule. As the electrophilic radical approaches the organic molecule, the radical's SOMO and the organic molecule's HOMO interact, raising the SOMO energy and lowering the energy of the HOMO. Poblet *et al.* (1983) have shown, using the frontier-orbital approach, that from the two possible interactions (see figure 3.6) the SOMO-HOMO interaction is the dominant one for addition of radicals to an olefin owing to the energetic proximity of the two orbitals. Further to this, they went on to show (Shaik and Candell, 1990; Candell *et al.*, 1985) that the addition preferentially occurred at the carbon having the larger orbital coefficient in the π-orbital. The net effect of this interaction is to lower the total energy ($2E_3-E_4$) as there are two electrons in the HOMO and only one in the SOMO. The closer the HOMO and SOMO are in energy, the stronger the interaction and the greater the energy gain.

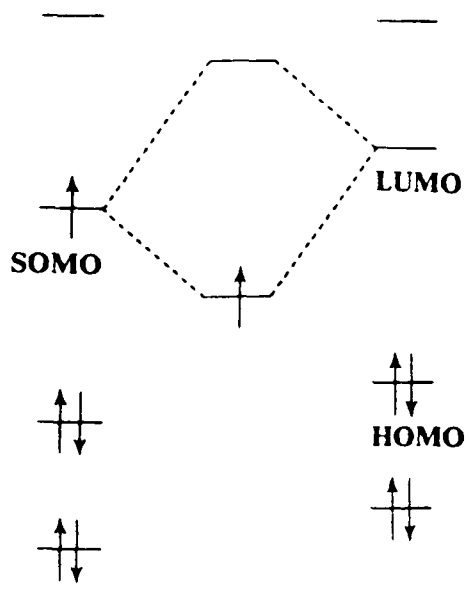

(a) *A nucleophilic radical*

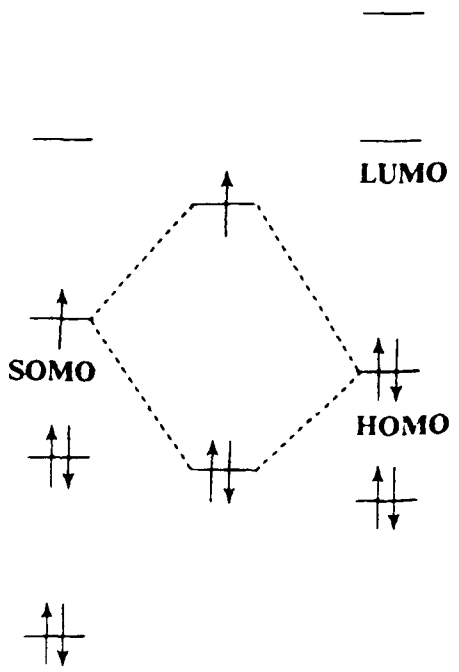

(b) *An electrophilic radical*

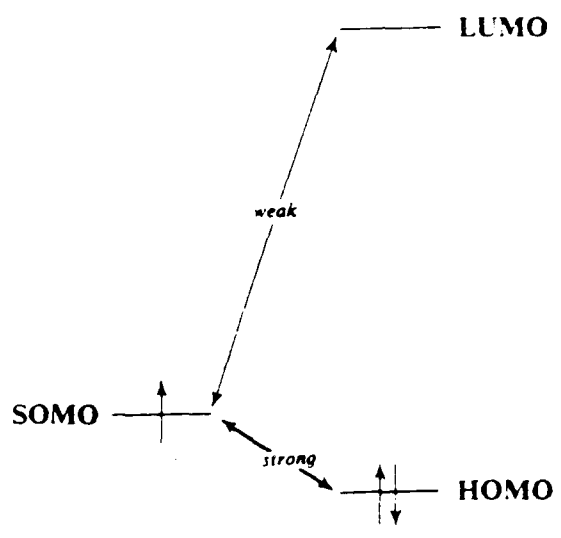

b) *An electrophilic radical*

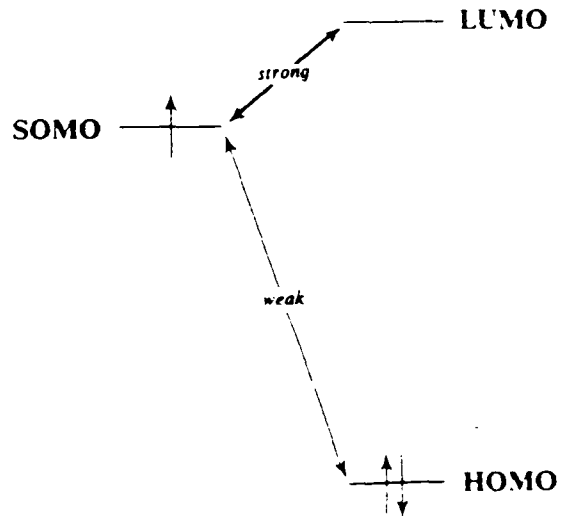

a) *A nucleophilic radical*

Figure 3.5 Important frontier orbital interactions for radicals: (a) nucleophilic radicals, and (b) electrophilic radicals.

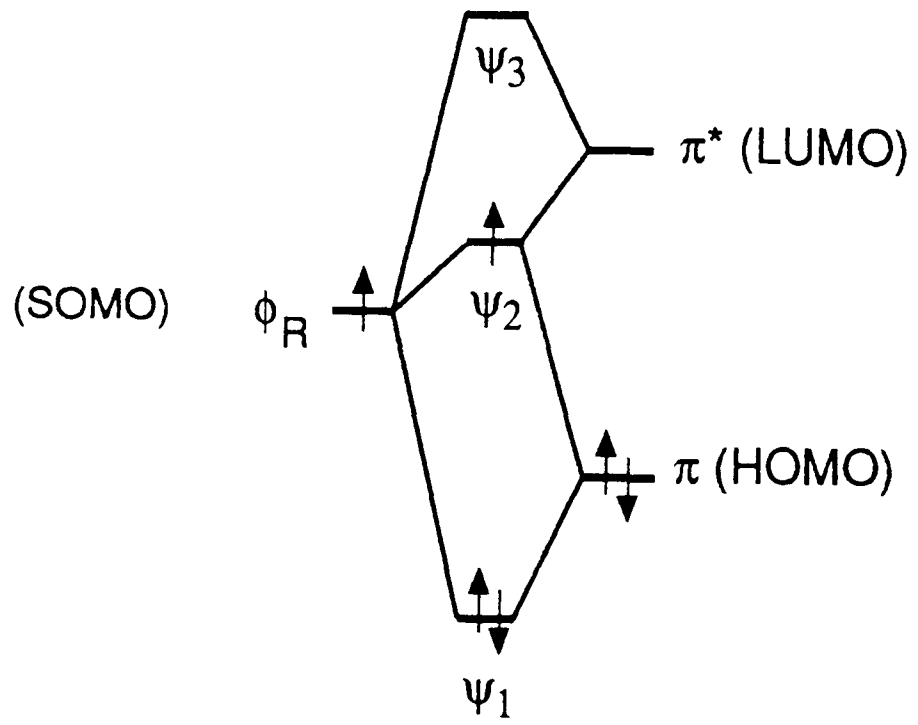

Figure 3.6 The frontier orbital interaction for a radical and an olefin (Poblet *et al.*, 1983)

Table 3.4 - **The calculated values of -E(HOMO) and E(LUMO) for a series of alkenes and the rate coefficients for their reaction with NO_3.**

Compound	-E(HOMO) eV (a)	E(LUMO) eV (a)	$k(NO_3)$ (b) 10^{-14}	E_a kJ mol^{-1}	A cm^3 $molecule^{-1}$ s^{-1}
ethene	10.62	1.31	0.02	25.8	$6.3x10^{-13}$
propene	10.1	1.17	0.95	9.7	$4.7x10^{-13}$
2-methylpropene	9.75	1.12	39	-	-
t-2-butene	9.65	1.12	36	4.4	$2.5x10^{-13}$
but-1-ene	10.18	1.17	1.1 (c)	7.8	$1.8x10^{-12}$
2-methylbut-2-ene	9.38	1.07	800	-	-
2,3-dimethyl-2-butene	9.13	1.01	4500	≤4.7	$\geq 3.0x10^{-10}$
1-chloro-1-butene	9.58	0.68	1.2 (c)	-	-
2-chloro-1-butene	9.7	0.7	1.7 (c)	-	-
3-chloro-1-butene	10.35	0.51	0.3 (c)	16.6	$2.4x10^{-12}$
1-chloro-2-butene	10.01	0.46	2.0 (c)	8.2	$6.0x10^{-13}$
2-chloro-2-butene	9.40	0.68	11.0 (c)	-	-
1-chloromethylpropene	9.32	0.66	9.0 (c)	-	-
3-chloromethylpropene	10.17	0.46	2.5 (c)	10.6	$1.6x10^{-12}$
mono-chloroethene	10.91	0.83	0.45	-	-
1,1-dichloroethene	9.74	-0.05	0.128	-	-
cis-1,2-dichloroethene	9.49	0.28	0.015	-	-
trans-1,2-dichloroethene	9.51	0.26	0.011	-	-
trichloroethene	9.37	-0.04	0.029	-	-
tetrachloroethene	9.22	-0.31	<0.0062	-	-

(a) from PM3 calculations, discussed in §3.2.1; (b) from Wayne *et al.*, 1991, the units are cm^3 $molecule^{-1}$ s^{-1}; (c) See Chapter 2.

One factor contributing towards the reactivity is therefore likely to be the lowered activation barrier when the HOMO and SOMO levels are close (however, we later show that this is not the only factor). For example, the activation energy for the reaction of NO_3 with 2,3-dimethyl-2-butene must be $\leq$4.7 kJ mol^{-1} on the basis of the room-temperature rate coefficient (Wayne *et al.*, 1991) even assuming that the A-factor is at the gas-kinetic limit. This activation energy for the reaction of NO_3 with 2,3-dimethyl-2-butene is to be compared with the much larger value (Wayne *et al.*, 1991) of 25.8 kJ mol^{-1} for the reaction with ethene. The positive inductive effect of the $-CH_3$ groups relative to H atoms pushes electrons into the $(CH_3)_2C=C(CH_3)_2$ double bond, thus increasing the energy of the π electrons relative to those in $H_2C=CH_2$: the energy separation between the organic HOMO and the radical SOMO is reduced and the activation energy is lowered. Although we are really interested in the energy difference, E(SOMO)-E(HOMO), it is necessary only to consider the energy of the HOMO when dealing with a series of reactions with the same radical, since E(SOMO) is constant. An approximation to the energy of the organic HOMO can be obtained from ionisation potential (IP) measurements (see §3.6), and correlations between reaction rates and IPs are well known (Wayne *et al.*, 1991; Atkinson, 1987; Sabljić and Güsten, 1990; Güsten *et al.*, 1984; Güsten and Klansinc, 1986). Instead of measured IPs, HOMO energies were calculated using the semi-empirical method described in the Experimental section (§3.2.1), example calculated HOMOs for 2-chloro-1-butene and 3-chloro-1-butene are shown in figure 3.7. Table 3.4 lists calculated HOMO energies for the compounds investigated in the present experiments and for a number of related molecules.

The calculation of HOMO energies puts on a more quantitative basis the usual ideas about mesomeric and inductive (see §2.6) effects commonly met in organic chemistry. Inspection

(a)

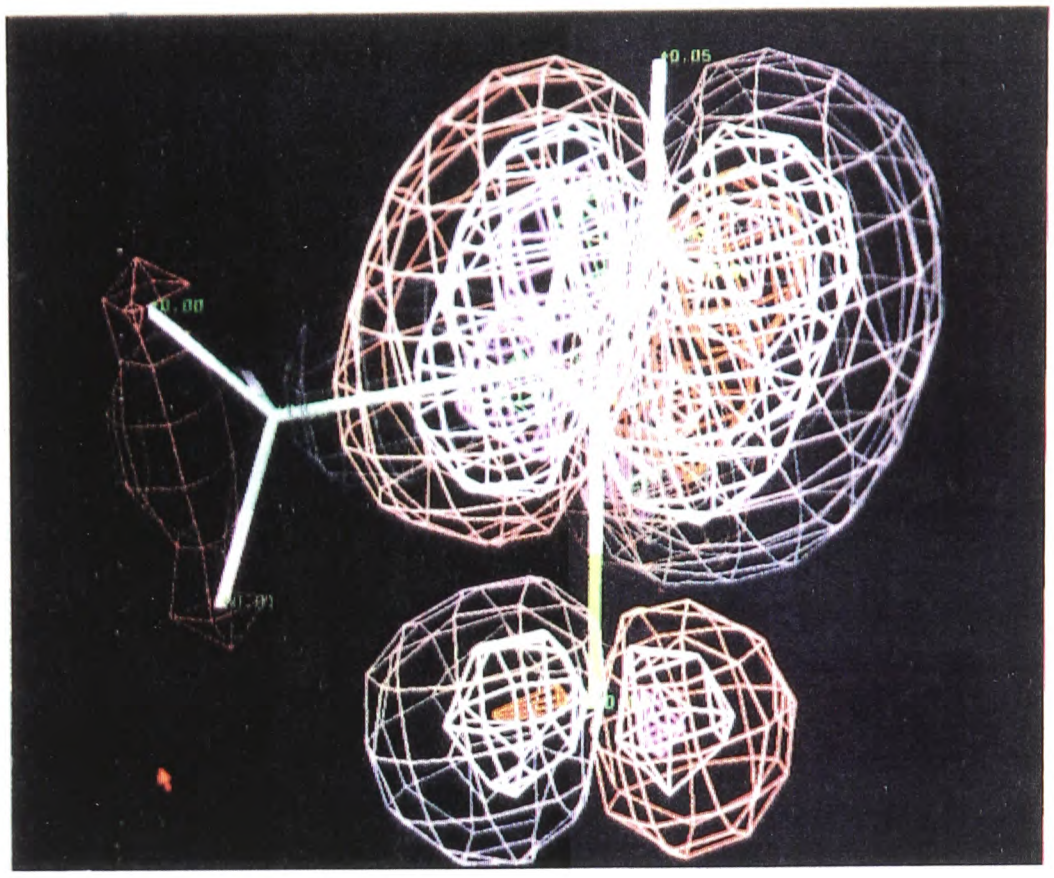

(b)

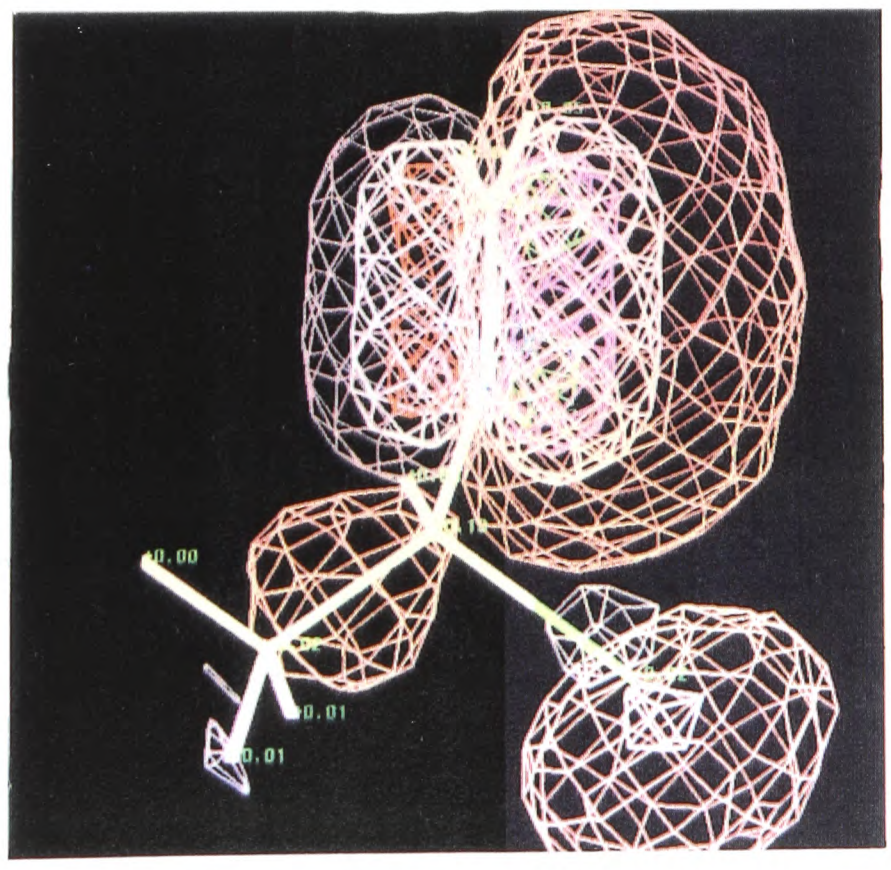

Figure 3.7 A representation of the HOMO orbital for a) 2-chloro-1-butene and b) 3-chloro-1-butene as calculated by semi-empirical methods (§3.2.1).

of table 3.4 shows that addition of alkyl groups to a double bond increases the HOMO energy (positive inductive effect), while addition of Cl atoms to the alkyl chain reduces the energy of the HOMO (negative inductive effect). When a chlorine atom is attached to a double-bonded carbon atom, the positive mesomeric effect outweighs the negative inductive effect and the energy of the orbital is increased.

It is tempting to ascribe the dependence of a rate constant on E(SOMO)-E(HOMO) solely to an influence on the activation energy for the reaction. However, it cannot be the activation energy alone that is modified by substitution; there must also be a connection between E(SOMO)-E(HOMO) and the pre-exponential factor. For example, the A-factor for the reaction of NO_3 with 2,3-dimethyl-2-butene must be two orders of magnitude bigger than that for the reaction with but-1-ene. Similar observations have been reported by other workers (Fenter and Anderson, 1991; Timonen *et al.*, 1987a,b). Even when activation energies are zero or negative, good correlations with energy-dependent parameters (e.g. E(SOMO)-E(HOMO) or ionisation potential) are often obtained. One recent example is to be found in the work of Anderson *et al.* (1991) on the addition of OH to a series of alkenes and haloalkenes. It is evident that close-lying SOMO-HOMO orbitals lead to a favourable entropy term for the transition state for at least some reactions.

The difference in reactivity between alkenes that contain a vinylic chlorine and those that do not has been noted previously (Abbatt and Anderson, 1991). The effect is related to the character of the HOMO. In alkenes with a vinylic chlorine atom, there is a strong mesomeric interaction between the orbitals of the double bond and the chlorine-atom lone pairs. Consequently, the HOMO stretches over both the double bond and the Cl atom, and

the energy of the orbital is no longer a good indicator of the reactivity of the molecule.

3.4.2 Correlations

Table 3.4 lists rate coefficients for reactions of the compounds with NO_3, and $-\log_{10}$ (k/cm^3 molecule^{-1} s^{-1}) vs. -E(HOMO) is plotted in fig. 3.8. Whatever the individual influences of E(SOMO)-E(HOMO) on the activation energy and pre-exponential factor, it is obvious that there is an excellent correlation between the calculated energy parameter and the logarithm of the rate coefficient for suitable classes of compounds. This observation suggests that the influences actually work together in such a way as to produce a dependence of the free energy of activation on the calculated energy difference in a way reminiscent of so many free-energy relationships hitherto noted in reaction kinetics (e.g. Bamford and Tipper, 1969).

Two sets of points can be identified: compounds with Cl atoms attached to the double bond are represented by open symbols, and other compounds are represented by filled symbols. The plot for the compounds not containing vinylic Cl atoms shows excellent correlation over about six orders of magnitude, and provides a basis for estimating rate constants that have not yet been measured. A linear-least squares method was used to obtain the relationship

$$\log_{10}(k/cm^3\ molecule^{-1}\ s^{-1}) = 3.45 \times E(HOMO)/eV + 21.1 \qquad (3.7)$$

between rate constant and HOMO energy for the compounds studied. For the compounds containing a chlorine atom attached to the double bond, no clear correlation can be identified. However, inspection of fig. 3.8 shows that for alkenes with Cl atoms attached to one carbon atom of the double bond, the rate constant for reaction with NO_3 is found to be about two

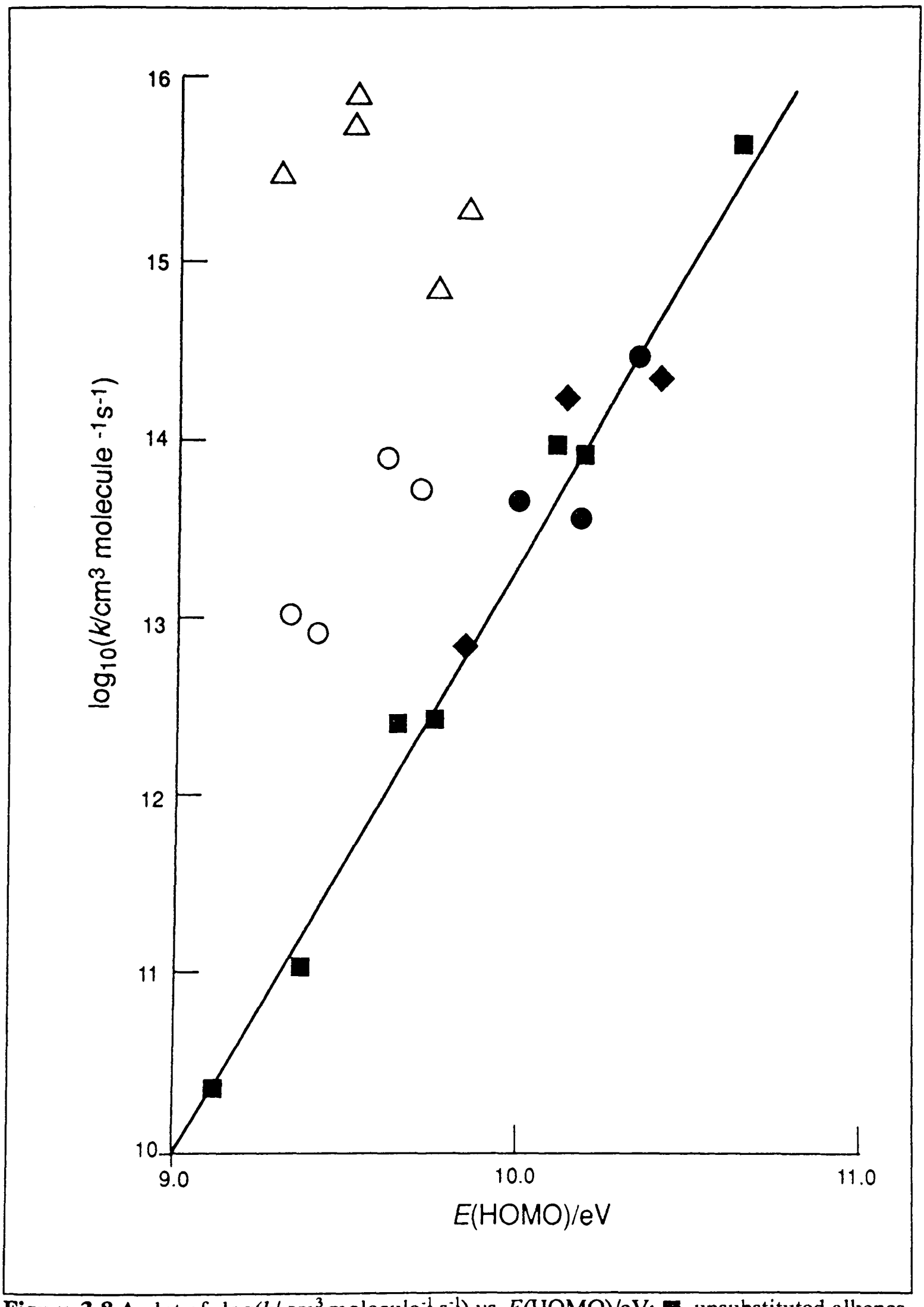

Figure 3.8 A plot of -log(k/ cm^3 molecule^{-1} s^{-1}) *vs.* E(HOMO)/eV; ■, unsubstituted alkenes, ●, chlorobutenes and ♦, bromobutenes; ○, chlorobutenes with vinylic chloro atoms and △, chloroethylenes.

orders of magnitude smaller than that indicated by equation (3.7). When Cl atoms are attached to both carbon atoms, the reactions are found to be about five orders of magnitude slower.

3.5 Group reactivity factors

From the correlation illustrated in figure 3.8, it is possible to estimate rate constants for the reactions of some types of organic compounds with NO_3. However, for compounds containing a vinylic chlorine atom the previous method breaks down. An alternative approach to the problem follows the type of structure-reactivity analysis proposed by several workers and discussed by Atkinson (1986, 1987) for the addition reactions of the OH radical. For substituted mono-alkenes, the rate coefficient can be estimated from the number, type and position of substituents at the double bond.

The rate constants for the basic structures are calculated from the rate constants for the parent alkene given in table 3.5, taking the reactivity factor for –CH3 as unity. This table also gives the set of basic structures and group factors $f(x_i)$ defined by the equation

$$k = k(basicstructure) \prod_{i=1}^{i=1-4} f(x_i) \qquad (3.8)$$

Using the experimental data obtained in this work, together with the rate constants for the reaction with NO_3 of the haloethenes, halopropene and the parent compounds (Wayne *et al.*, 1991), we have calculated the contribution of each functional group. The group factors given

Table 3.5 **Rate constants for basic structures and group factors**

Basic structure	k(basic structure) (a) /10^{-14} cm^3 $molecule^{-1}$ s^{-1}	Parent compound
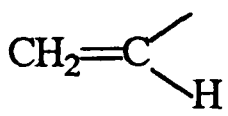	0.95	propene
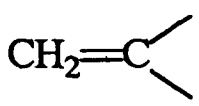	34	2–methylpropene
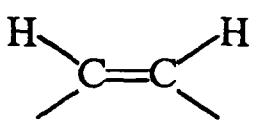	36	*cis*–2–butene
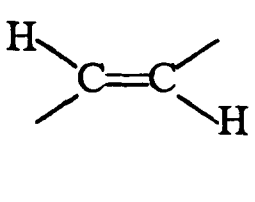	38	*trans*–2–butene
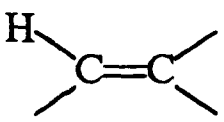	890	2–methyl–2–butene
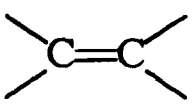	4500	2,3–dimethyl–2–butene

a) rate coefficient for the reaction of NO_3 with the parent compound taken from Wayne et al., 1991.

Group factors

$f(-CH_3) = 1$ $f(-Cl) = 0.040$ $f(-CHClCH_3) = 0.32$
$f(-CH_2CH_3) = 1.3$ $f(-CH_2Cl) = 0.062$ $f(-CH_2CH_2Cl) = 0.41$
$f(-Br)/f(-Cl) = 1.27$ (also for alkyl group containing Br and Cl)

Table 3.6 - **A comparison between predicted and experimental rate coefficients for the reaction of NO_3 with some halobutenes and estimated rate coefficients for the reaction of OH with the compounds studied in this work.**

Compound	$k(NO_3)_{expt.}$	$k(NO_3)_{calc.}$ c)	$k(OH)_{calc.}$ d)	$k(OH)_{calc.}$ e)
CH_2=CHCl	4.5×10^{-16} a)	3.8×10^{-16}	-	-
CH_2=CCl_2	1.3×10^{-15} a)	5.4×10^{-16}	-	-
cis-CHCl=CHCl	1.5×10^{-16} a)	5.8×10^{-16}	-	-
trans-CHCl=CHCl	1.1×10^{-16} a)	6.1×10^{-16}	-	-
CHCl=CCl_2	2.9×10^{-16} a)	5.7×10^{-16}	-	-
CCl_2=CCl_2	$< 6\times10^{-17}$ a)	1.2×10^{-16}	-	-
CH_2=$CHCH_2Cl$	5.6×10^{-16} a)	5.9×10^{-16}	-	-
CHCl=$CHCH_2CH_3$	1.2×10^{-14} b)	1.9×10^{-14}	1.4×10^{-11}	2.0×10^{-11}
CHClCH=$CHCH_3$	2.0×10^{-14} b)	2.3×10^{-14}	4.5×10^{-11}	2.3×10^{-11}
CH_2=$CClCH_2CH_3$	1.7×10^{-14} b)	1.8×10^{-14}	1.2×10^{-11}	2.3×10^{-11}
CH_3CCl=$CHCH_3$	1.1×10^{-13} b)	3.6×10^{-13}	1.7×10^{-11}	3.9×10^{-11}
$(CH_3)_2C$=CHCl	9.0×10^{-14} b)	3.6×10^{-13}	1.7×10^{-11}	3.7×10^{-11}
$CH_2Cl(CH_3)C$=CH_2	2.5×10^{-14} b)	2.1×10^{-14}	3.9×10^{-11}	2.5×10^{-11}
$CH_3CHClCH$=CH_2	3.0×10^{-15} f)	3.0×10^{-15} f)	-	1.3×10^{-11}
$CH_3CHBrCH$=CH_2	4.0×10^{-15} b)	3.9×10^{-15}	-	1.4×10^{-11}
CH_2BrCH_2CH=CH_2	5.0×10^{-15} b)	4.9×10^{-15}	-	1.5×10^{-11}
CH_3CBr=$CHCH_3$	1.3×10^{-13} b)	4.5×10^{-13}	2.2×10^{-11}	4.1×10^{-11}
CH_2ClCH=$CHCH_2Cl$	5.0×10^{-15} a)	1.4×10^{-15}	-	-

All units are cm^3 $molecule^{-1}$ s^{-1}

a) From Wayne *et al.*, 1991; b) see Chapter 2; c) calculated from structure-reactivity relationship - see text; d) calculated using structure-reactivity relationship from data given by Atkinson, 1986; e) calculated from regression equation - see text and Wayne *et al.*, 1991; f) see text.

in table 3.5 are the averages of these contributions selected on the basis of the reliability of the data as expressed in recent reviews (Wayne *et al.*, 1991; Atkinson, 1986). These factors may now be used in the reverse sense to estimate rate coefficients for the individual reactions, as displayed in table 3.6. For the calculation of f(-$CHClCH_3$), only one compound is available, $CH_3CHClCH{=}CH_2$, so that the estimated and experimental rate coefficients are the same.

The reasonable agreement between the calculated and experimental rate coefficients demonstrates the potential power and usefulness of the structure-reactivity method in prediction of the reactivity toward NO_3 of a wide range of alkenes. It should be emphasised, however, that this is the first attempt to apply these relationships to the reactions of the NO_3 radical, and a much larger kinetic database is required to establish a more comprehensive and reliable set of rate constants for basic structures and group factors. This limitation is particularly marked for compounds with more than one Cl atom attached to the double bond.

Rate coefficients have not yet been measured experimentally for the reactions of OH with the halobutenes discussed here. However, estimates of the rate coefficients can be obtained by two methods, and are given in table 3.6. The first method uses the structure-reactivity relationships and factors proposed by Atkinson (1986) and the second employs the relationship between the rate coefficients for the addition reactions of the NO_3 and the OH radical as expressed by the regression equation

$$\log k(NO_3) = 21.6 + 3.32 \log k(OH) \qquad (3.9)$$

proposed by Wayne *et al.* (1991). The two methods give predicted rate coefficients that are in rather good agreement.

3.6 Photoelectron spectroscopy of the halobutene compounds

3.6.1 Photoelectron spectroscopy

In view of the observed reactivity of NO_3 towards compounds containing vinylic chlorine atoms, there are two outstanding questions, arising from the frontier-orbital approach:

i) Is the reduction in E(HOMO) on substitution of a halogen atom to the double bond of the parent alkene, a real effect or an artefact of the calculation and as consequence of the former is the character a reflection of the HOMO affected under the same conditions ?

ii) Are the calculated E(HOMO) really a good approximation to the experimental IP?

These questions are approached experimentally by means of photoelectron spectroscopy. Photoelectron spectroscopy (PES) provides a direct source of experimental information about the *valence electrons* in a molecule. When intense, monochromatic, ultraviolet light interacts with a free (gaseous) molecule, it can cause an electron to be ejected, thus ionising it.

$$M + h\nu \longrightarrow M^+ + e^- \qquad (3.10)$$

The energies and abundances of these so-called photoelectrons are characteristic of the molecular orbitals from which they originate. In PES the quantity usually measured is the ionisation potential (IP). According to Koopman's theorem (1934), an individual ionisation potential for an electron in a molecular orbital (I_j) is equal to the orbital energy

$$I_j = -\varepsilon_j \tag{3.11}$$

Photoelectron spectroscopy using uv radiation as the ionising radiation was pioneered by Turner (1962, 1963) in England and simultaneously by Vilesov in Russia (1961). The radiation normally used is from a helium resonance line (He I) at λ=54 nm, which is equivalent to 21.22 eV of energy per photon. This energy is usually sufficient to ionise electrons from the *valence shell* of a molecule. An electron in any orbital j has a characteristic energy I_j, which is the minimum energy required to eject it to infinity. Thus, part of the energy of the photon ($h\nu$) must be used to overcome I_j, the rest being given in the form of kinetic energy (KE) to the ejected electrons. This kinetic energy is then given by the Einstein relationship

$$KE = h\nu - I_j \tag{3.12}$$

In a photoelectron spectrometer, the ejected photoelectrons are separated according to their kinetic energies (§3.2.2). Apart from Koopman's theorem there are two approximate rules that make the relationship between PE spectrum and molecular electronic structure simple:

1) Each band in the spectrum corresponds to ionisation from a single molecular orbital;

2) Each occupied molecular orbital of I_j less than $h\nu$ gives rise to a single band in the spectrum.

These simple empirical rules can be used to consider the energies of photoelectron bands. The intensities of bands can also give useful information. The area under a photoelectron band in a spectrum is proportional to the relative probability of ionisation to an ionic state. In closed-shell molecules the relative intensity of a band from ionisation of a given molecular orbital is proportional to the number of equivalent electrons that are available for ionisation.

and often depends also on the nature and size of the orbitals and the number of nodes. For example, going across the periodic table, the p-orbitals of sulphur have a higher ionisation cross-section than those of oxygen. The chlorine p-electrons have a higher ionisation cross-section than those of fluorine, both sulphur and chlorine p-electrons on ionisation give stronger bands than carbon p-electrons on ionisation (Price *et al.*, 1972). In this work the relative areas under bands were determined by a curve fitting program. Both symmetric and asymmetric gaussians were fitted to the spectra, the criteria of fitting being the minimum value of χ^2. Figure 3.9 shows the result of such a fit. In order to assign the bands in a photoelectron spectrum, the energies and characteristics of the molecular orbitals must be known. One common way of estimating them is to use semi-empirical calculations (Eland, 1973). The -E(HOMO) and the IP being related by Koopman's theorem. Koopman's theorem is based on certain assumptions (Eland, 1973) which under most circumstances are valid. In this work the PE spectra are used to show that the assumptions made in §3.4 are valid and that the calculated E(HOMO)s shows the same trends as the experimental IPs.

3.6.2 Results and Discussion

The He I and He II PE spectra of the halobutenes, 1-chloro-1-butene, 2-chloro-1-butene, 3-chloro-1-butene, 1-chloro-2-butene, 1-chloromethylpropene, 3-chloromethylpropene, 3-bromo-1-butene and 2-bromo-2-butene are displayed in Appendix 1. The general features of the spectra are discussed in §3.6.2.1 and the assignment of the bands are discussed in §3.6.2.2.

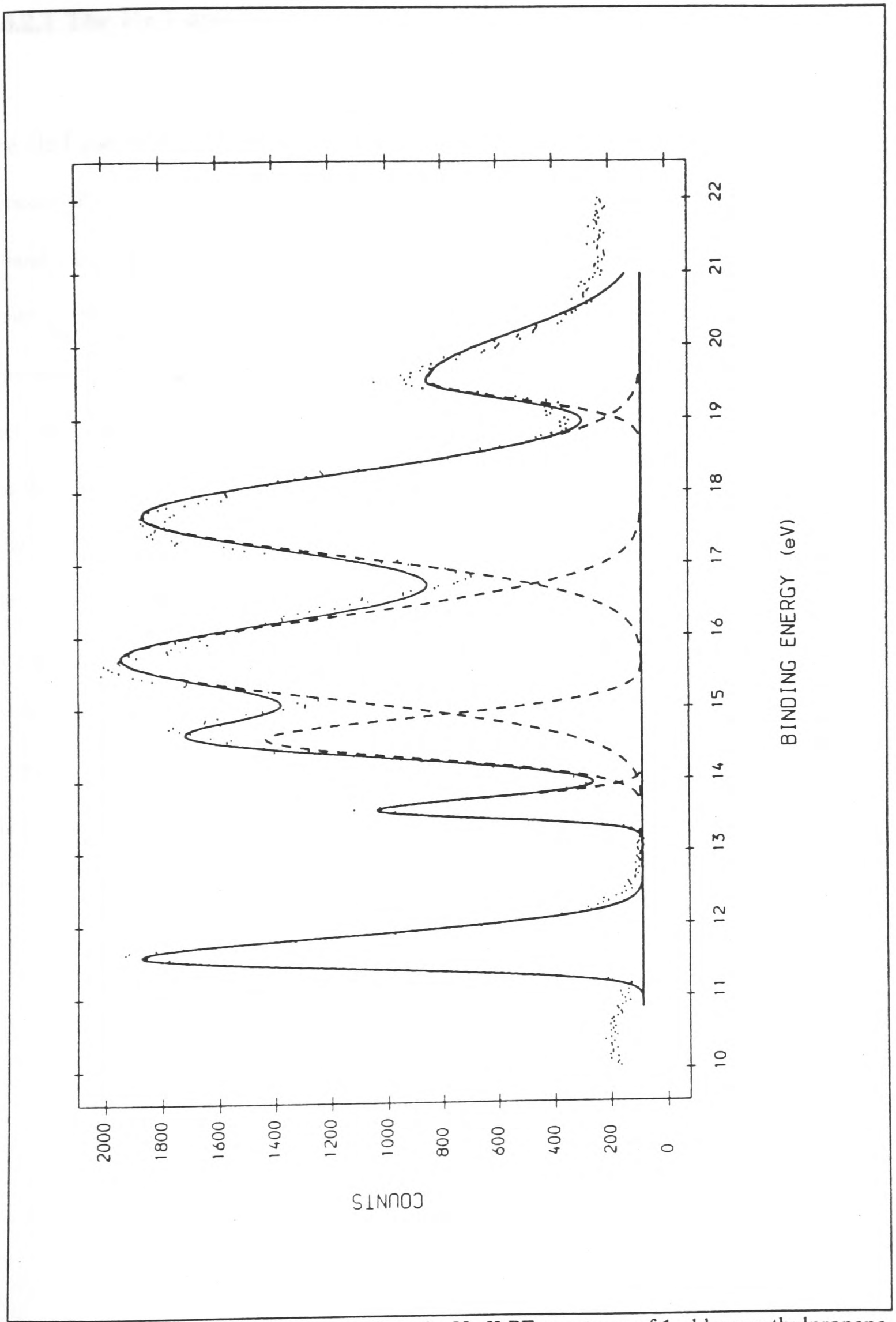

Figure 3.9 A typical gaussian curve-fit to the He II PE spectrum of 1-chloromethylpropene

3.6.2.1 The He I and He II spectra

The He I and He II PE spectra of these compounds can be split into three regions. First, between IP values of 8 and 10 eV there is the first ionisation band (IP^1). The vertical IP of a band was measured from the calculated band centre. The second region, at around 11 eV, contains the second band. The second IP (IP^2) is more intense than IP^1 and has a relatively narrower band width (See Table 3.7). At energies greater than *ca.* 12eV (the third region), there are a series of broad overlapping bands, the third IP (IP^3) being taken as the centre of the first of these. The PE spectral features are similar to those shown by simple haloalkenes (Baker and Betteridge, 1972). Values of the vertical E_i (IP) obtained from these spectra for the series of compounds 1-chloro-1-butene, 2-chloro-1-butene and 3-chloro-1-butene are given in Table 3.7. The He II spectra of these compounds (See Appendix 1) show similar features to their He I counterparts. The most noticeable difference is in the intensity of IP^2 (*ca.* 12.3eV); the relative intensity of this band is much smaller than the equivalent band in the He I spectra. The relative intensities of the equivalent bands in each spectrum, given by the area under the band, are shown in Table 3.8.

Table 3.7 - Experimental vertical ionisation potentials (E_i) and calculated eigen values (ε)

(a) 1-chloro-1-butene

E_i /eV	$-\varepsilon^{a)}$/eV	diffn.[b)]	peak asymmetry[c)]	character[d)]
9.58	9.48	-0.1	2.6	$\pi_{C=C},\pi_{Cl}$
11.35	10.46	-0.9	1.0	n_{Cl}
11.70	11.85	+0.15	0.99	$\pi_{Cl},\pi_{C=C}$
12.59	12.36 | 12.13	-0.35	-	π(CH)
13.38	13.41	+0.03	-	-
14.64	14.86 | 14.05	-0.12	-	σ_{CH} σ_{C-C}

[a)] from PM3 calculations; [b)] $E_i-\varepsilon$; [c)] Peak half width (PHW) 1 - PHW 2; [d)] from PM3 eigen vectors

b) 2-chloro-1-butene

E_i /eV	$-\varepsilon^{a)}$/eV	diffn.[b)]	peak asymmetry[c)]	character[d)]
9.47	9.70	-0.23	2.9	$\pi_{C=C},\pi_{Cl}$
11.04	(10.48)	+0.56	0.56	n_{Cl}
11.5 | 11.81	11.56	+0.09	-	π_{Cl}, $\pi_{C=C}$
12.28	12.19	-0.05	-	$\pi(CH_2)$
12.37	12.33	0.04	-	-
13.68	13.31	+0.37	-	-
14.68	14.98 | 14.15	+0.115	-	-

[a)] from PM3 calculations; [b)] $E_i-\varepsilon$; [c)] PHW 1 - PHW 2; [d)] from PM3 eigen vectors

c) 3-chloro-1-butene

E_i /eV	-ε[a]/eV	diffn.[b]	peak asymmetry[c]	character[d]
10.20	10.35	-0.15	0.25	$\pi_{C=C}$
11.04	10.45	-0.59	0.50	n_{Cl}
12.86	12.34 | 12.43	-0.48	-	$\pi_{C=C}$
13.81	13.37 | 14.43	+0.09	-	-
16.78	16.20	-0.58	-	-
17.01	16.64	-0.37	-	-

[a] from PM3 calculations; [b] E_i-ε; [c] PHW 1 - PHW 2; [d] from PM3 eigen vectors

Table 3.8 - Comparative ratios of fitted IP peak areas for He I and He II PE spectra

Compound	Incident radiation	$A(IP^1)$ (a)	$A(IP^2)$ (a)	$A(IP^1/IP^2)$	$\%A(IP^1)$ (b)	$\%A(IP^2)$
1-chloro-1-butene	He I	46398	39144	1.185	54.25	45.76
	He II	21535	8669	2.484	71.30	28.70
$A(IP^j$ He II/He I) IP^1 1.315 IP^2 0.627						
2-chloro-1-butene	He I	53422	47422	1.126	52.9	47.0
	He II	19195	7453	2.575	72.0	27.9
$A(IP^j$ He II/He I) IP^1 1.361 IP^2 0.590						
3-chloro-1-butene	He I	26686	75116	0.355	26.21	73.79
	He II	18259	16030	1.139	53.25	47.51
$A(IP^j$ He II/He I) IP^1 2.03 IP^2 0.644						
1-chloro-2-butene	He I	33748	79469	0.424	29.0	70.1
	He II	16599	11384	1.458	59.0	40.6
$A(IP^j$ He II/He I) IP^1 2.03 IP^2 0.579						
1-chloromethylpropene	He I	41430	31764	1.302	56.6	43.4
	He II	19195	7453	2.575	72.0	25.0
$A(IP^j$ He II/He I) IP^1 1.32 IP^2 0.576						
3-chloromethylpropene	He I	29420	73282	0.402	28.6	71.4
	He II	17033	10423	1.634	62.0	37.9
$A(IP^j$ He II/He I) IP^1 2.176 IP^2 0.530						
3-bromo-1-butene	He I	45477	53480	0.850	45.9	54.0
	He II	16827	24484	0.687	40.7	59.2
$A(IP^j$ He II/He I) IP^1 0.88 IP^2 1.09						
2-bromo-2-butene	He I	56375	49148	1.147	53.4	46.5
	He II	28812	13483	2.134	79.0	37.1
$A(IP^j$ He II/He I) IP^1 1.47 IP^2 0.797						

(a) A = area under peak, from fitting to an (as)symmetric gaussian in arbitrary units; (b) $\%A(IP^j) = A(IP^j)/\Sigma A(IP^j)+A(IP^{j+1})+....$ etc.

3.6.2.2 Assignment of the PE spectral bands

The series of PE spectra for the compounds 1-chloro-1-butene, 2-chloro-1-butene and 3-chloro-1-butene are used to exemplify the main features and characteristics seen throughout the spectra of these compounds. The He I spectra for these three halo-1-butenes are shown comparatively in Figure 3.10.

When attempting to assign this series of PE spectra, two assumptions are used:

1) changes in the energies of the molecular orbitals are correlated specifically with changes in the substitution pattern of the molecules;

2) the molecular orbitals are treated as being localised on an atom (e.g. a lone pair orbital) or between a relatively small number of atoms (e.g. a π-orbital).

There are two principal effects of changing the substitution patterns of a molecule that affect PE spectra. First, if the substituent changes the polarity (or partial charge distribution) within the molecule as a result of an inductive effect (§2.6) (or a change in increasing electronegativity e.g. Cl to Br) the electrons in the higher lying molecular orbitals become more tightly bound, resulting in a higher IP. Secondly, if the substituent has an orbital of such symmetry and energy that it can interact with another orbital, a so-called mesomeric interaction can take place (*cf* §2.6). For example, the influence on the inductive effect is illustrated by comparing the IPs for the homologous series C_nH_{2n} (see Table 3.9). The IP associated with the π-orbital decreases with the increasing +I effect of the alkyl groups. What can also be seen in a comparison of the IP for 1-butene and 2-butene, 9.7 and 9.37 eV respectively is that two methyl groups have a greater +I effect than one ethyl group (*c.f.* §2.6).

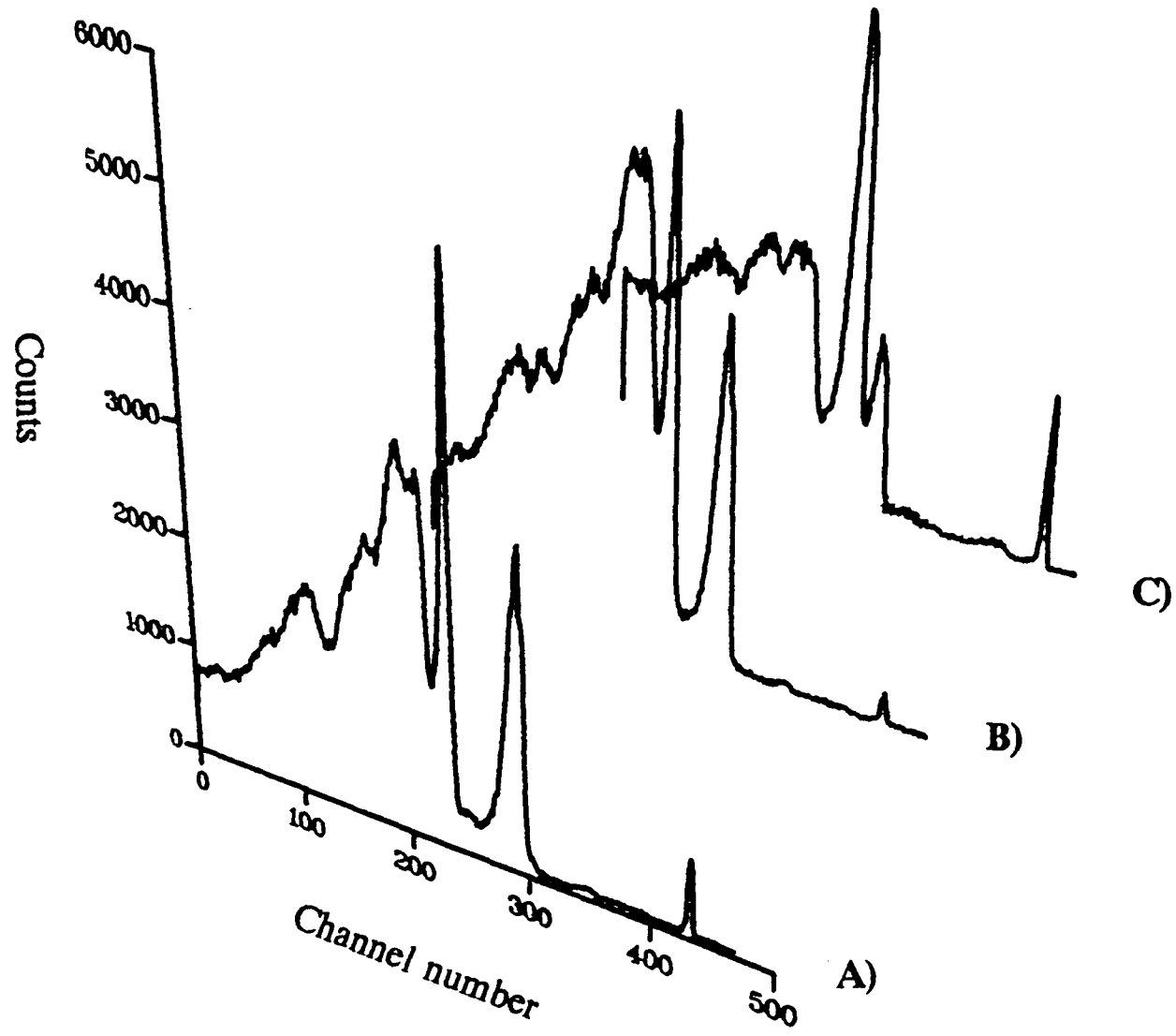

Figure 3.10 The PE spectra for the compounds a) 1-chloro-1-butene, b) 2-chloro-1-butene and c) 3-chloro-1-butene. The peak at Channel no. >400 is the helium self-ionisation peak (*ca.* 16.2 eV)

One common feature of all the PE spectra of the alkenes, is that the first ionisation band is due to ionisation from a π-orbital (Turner *et al.*, 1970).

Table 3.9 - The IP for the homologous series of alkenes C_nH_{2n}.

Compound	IP[a] (eV)
$CH_2=CH_2$	10.51
$CH_3-CH=CH_2$	9.74
$C_2H_5-CH=CH_2$	9.61
$C_3H_7-CH=CH_2$	9.51

a) From Turner, 1966.

Further evidence for this assignment can be gained by comparing the He I/He II relative band intensities (See Table 3.8). The variation in the He I/He II relative band intensities is related to the type of orbital from which the electrons are removed in photoionisation (Cannington and Ham, 1983; Schweig and Thiel, 1974).

The fact there is a reduction in intensity of *ca.* 0.5 in the first band (see Table 3.7) of each He II spectrum, relative to the corresponding He I spectrum, is an indication that the band is due to the removal of an electron from the $\pi_{C=C}$ orbital.

The second ionisation band (IP^2) in the spectra at *ca.* 11.0eV is sharp, narrow and more intense than IP^1. The narrowness and sharpness of this band is characteristic of ionisation from formal lone pairs within a molecule. This is especially marked for the outermost occupied orbitals of chlorine and bromine (Turner *et al.*, 1970). The energy of a Cl lone pair

in -CH=CH-Cl has been predicted on the basis of a non-empirical analysis of the π-conjugative effect (Bernardi *et al.*, 1978), using *ab-initio* calculations at the STO/3G level, to be 11.056 eV. The IPs for the band assigned to the Cl lone pair(s) in the series 1-chloro-1-butene, 2-chloro-1-butene, 3-chloro-1-butene are 11.357, 11.047, 11.047 eV, in excellent agreement with the predicted value. Further evidence for this assignment is in the He I/He II intensities. The ionisation cross-section of certain atomic-like orbitals falls off with decreasing wavelength of the ionising radiation (Cooper, 1976). The ionisation cross-section of Cl p-orbitals decreases more rapidly than the equivalent orbitals on carbon. In the He II spectra the second band (IP^2) has markedly decreased in intensity in comparison to IP^1.

There is an apparent anomaly in the PE spectra of 3-chloro-1-butene, the second ionisation band is much broader, and nearer to IP^1, than in the PE spectra of the other two compounds. If a non-bonding (lone-pair) p-orbital is orientated so that it has the same symmetry as the π-orbital, and the π- and p- orbitals are of comparable energy, then an interaction can take place. This interaction, illustrated in Figure 3.11, removes the degeneracy of the halogen lone-pairs and is responsible for the so-called mesomeric effect. The lone-pairs without the correct symmetry for overlap with the π-orbital remain non-bonded. In figure 3.11, the n_{Cl} lone pair is shown to be at a slightly higher energy than a truly non-bonding orbital: this is because the possibility of the interaction of the non-bonding lone-pair (n_{Cl}) with lower energy σ-orbitals of the correct symmetry, not shown in the figure 3.11, has also been considered. The character of the resulting molecular orbitals shown in figure 3.11, denoted as π_1 and π_2, depends on the relative energies of the n_{Cl} and π-orbitals. Of the resultant molecular orbitals, π_1 is likely to have more n_{Cl} character than the π_2 orbital which is likely to have more π_{Cl}-orbital character. This is confirmed by examining the third ionisation band (IP^3). In He I

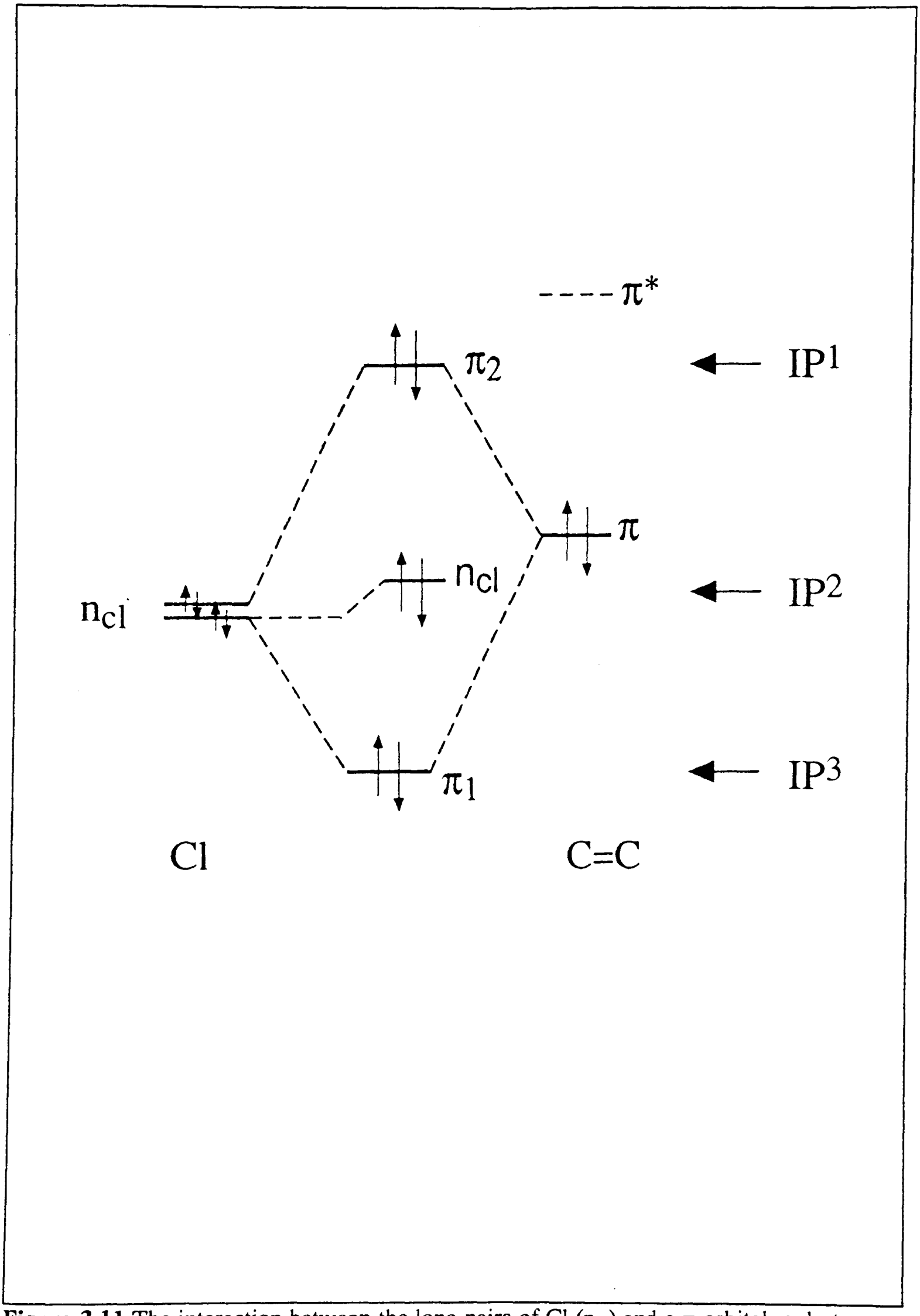

Figure 3.11 The interaction between the lone-pairs of Cl (n_{Cl}) and a π-orbital; only two n_{Cl} orbitals are shown.

PE spectra chlorine has a higher ionisation cross-section than carbon, such that molecular orbitals with more Cl character are more intense than their carbon counterparts. In both the He I PE spectra of 1-chloro-1-butene and 2-chloro-1-butene, IP^3 is more intense than IP^1. This can be ascribed to the greater π_{Cl} character of IP^3 (see figure 3.11) because of this mesomeric interaction (*cf* PE spectrum of 3-chloro-1-butene).

In the case of 3-chloro-1-butene, as there is no pπ(Cl)-interaction with the double bond, the three n_{Cl} lone-pairs are degenerate. According to the empirical rule stated in §3.6.1, the relative intensity of a PE band is proportional to the number of equivalent electrons that are available for ionisation. Thus, the relative intensity of the second ionisation band in the PE spectra of 3-chloro-1-butene can be attributed to the fact that 1.5 more equivalent electrons are available for ionisation than in either 1-chloro-1-butene or 2-chloro-1-butene.

The same arguments and observations used in interpreting the PE spectra of the halo-1-butenes can be applied to the PE spectra of 1-chloromethylpropene, 3-chloromethylpropene and 1-chloro-2-butene. In the PE spectra of the bromo compounds, 3-bromo-1-butene and 2-bromo-2-butene, there is one additional feature, spin-orbit coupling (Eland, 1973). This effect has been characterised in a number of inorganic and organic molecules (Turner, 1970).

3.6.3 Conclusions from the PE spectra of the halobutenes

The PE spectra of the halobutenes have shown two important effects of the substitution of a halogen atom to an alkene. First, in the case where the halogen substituent is adjacent to the double-bond, there is a reduction in the IP compared to that of the unsubstituted parent

Table 3.10 - Comparison of E(HOMO) and the experimentally determined IP for halobutenes and their haloderivatives

Compound	E(HOMO)[a] (eV)	IP[b] (eV)	E(HOMO)-IP
1-butene	10.03	9.7	0.33
1-chloro-1-butene	9.58	9.489	0.091
2-chloro-1-butene	9.7	9.473	0.227
3-chloro-1-butene	10.35	10.20	0.15
t-2-butene	9.65	9.25[c]	0.4
1-chloro-2-butene	10.01	9.805	0.205
2-chloro-2-butene	9.40	-	-
2-bromo-2-butene	9.84	9.16	0.68
methylpropene	9.75	9.45[c]	0.30
1-chloromethylpropene	9.32	9.014	0.306
3-chloromethylpropene	10.17	9.668	0.502

a) From PM3 calculations (§3.2.1); b) this work (§3.2.2); c) From Kimura *et al.*, 1981

alkene (see table 3.10). This difference in the energies of the mainly π-like orbitals of 1-chloro-1-butene, 2-chloro-1-butene and 1-butene could be thought of as a quantitative measure of the +M effect associated with the substituent. However, as the -I effect of the halo-substituent tends to increase the energy of the π_2-orbital IP, the result should be thought of as representing the combined +M and -I influences. Secondly, where the halogen group is not adjacent to the double-bond, there is only the -I effect as there is no interaction between pπ(Cl) and the π-orbitals of the double bond. In the next section the PES data is used in conjunction with the semi-empirical calculations in order to answer the question posed in §3.6.1

3.7 Comparisons and Conclusions

The experimentally determined IPs show the same trends in the calculated E(HOMO)s for the halobutenes (see Table 3.10). Namely, on substitution of a halogen atom to the double bond there is a decrease in the ionisation potential of the compound as compared to the IP of the parent unsubstituted alkene. From the PES work described in §3.6 this observation can be ascribed to both the positive mesomeric and negative inductive effect of the halogen atom on the π-orbital of the double-bond. This is in comparison to the compounds without a vinylic halogen group, where the resultant IPs and E(HOMO)s are greater than the parent unsubstituted alkene. Figure 3.12 shows the IP plotted against E(HOMO) for the series of compounds displayed in Table 3.10 and 3.4. From this, it can be seen that the semi-empirical calculations overestimated the IPs by, on average, 0.28 eV for the C_4H_7X (X=H,Cl,Br) compounds. In comparison the chloroethylenes lie below the 1:1 correlation line and are underestimated by the semi-empirical calculations by, on average (excluding

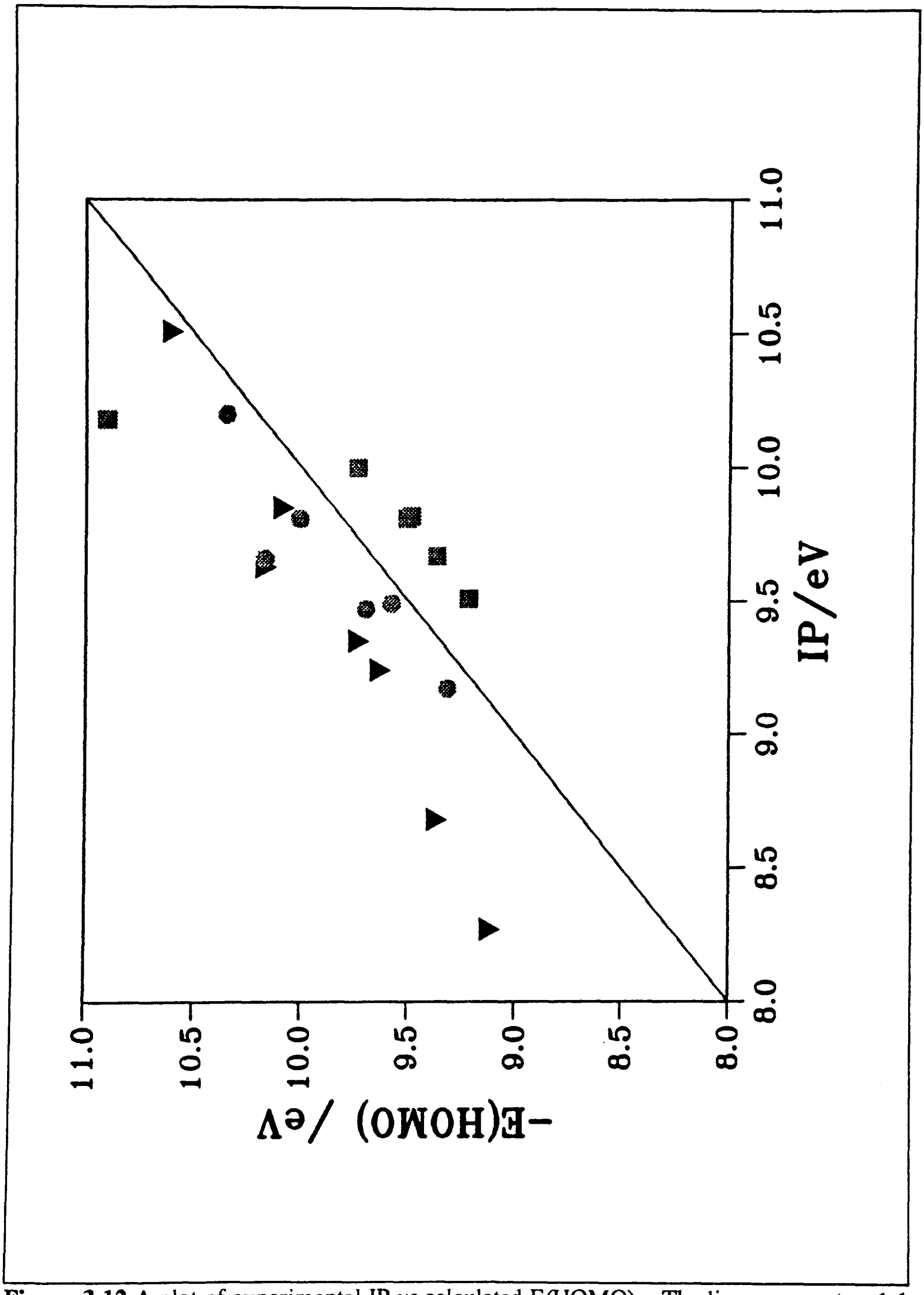

Figure 3.12 A plot of experimental IP *vs* calculated E(HOMO). The line represents a 1:1 correlation between the two quantities; The compounds are ▼, unsubstituted alkenes, ●, halobutenes and ■ , chloroethenes.

monochloroethylene), 0.3 eV (see Table 3.10).

The $\log_{10}k(NO_3)$ *vs* IP correlation (see figure 3.13) shows the same trends as seen in the corresponding plot using -E(HOMO) (see figure 3.8), with the compounds containing vinylic chlorine groups not lying on the regression line. The linear regression is characterised by the equation

$$\log_{10}k(NO_3) = (10.0_0 \pm 1.0) - (2.44_1 \pm 0.1_6) \times \text{IP} \qquad (3.13)$$

with r=-0.988, a strong correlation. Wayne *et al.* (1991), using 43 NO_3-alkene addition reactions, obtained an expression of

$$\log_{10}k(NO_3) = (7.6_9 \pm 0.7) - (2.22_2 \pm 0.1_6) \times \text{IP} \qquad (3.14)$$

with r=-0.972. Both these results are consistent with those obtained by Sablić and Güsten (1990) for 62 data pairs of

$$\log_{10}k(NO_3) = (6.6 \pm 0.7) - (2.1 \pm 0.1) \times \text{IP} \qquad (3.15)$$

Both groups of workers noted that halogenated compounds do not fit on their regression lines but mistakenly assign this to the fact that the IPs represent ionisation at the 'lone-pair' orbitals of the halogen atom, a position in the molecule which is not close to the centre of attack. This may be true for NO_3 abstraction reactions but is definitely not correct for NO_3 addition reactions, particularly in the case of the reaction of NO_3 with halo-alkenes.

The reactivity of NO_3 towards compounds with vinylic chloro-atoms can be rationalised by examining the orbital coefficients (§3.2.1). Poblet *et al.* (1983), noted that the addition of a radical to an olefin preferentially occurs at the carbon having the larger coefficient in the π-orbital. Recent *ab-initio* calculations by Arnaud (1991) confirm this result. Table

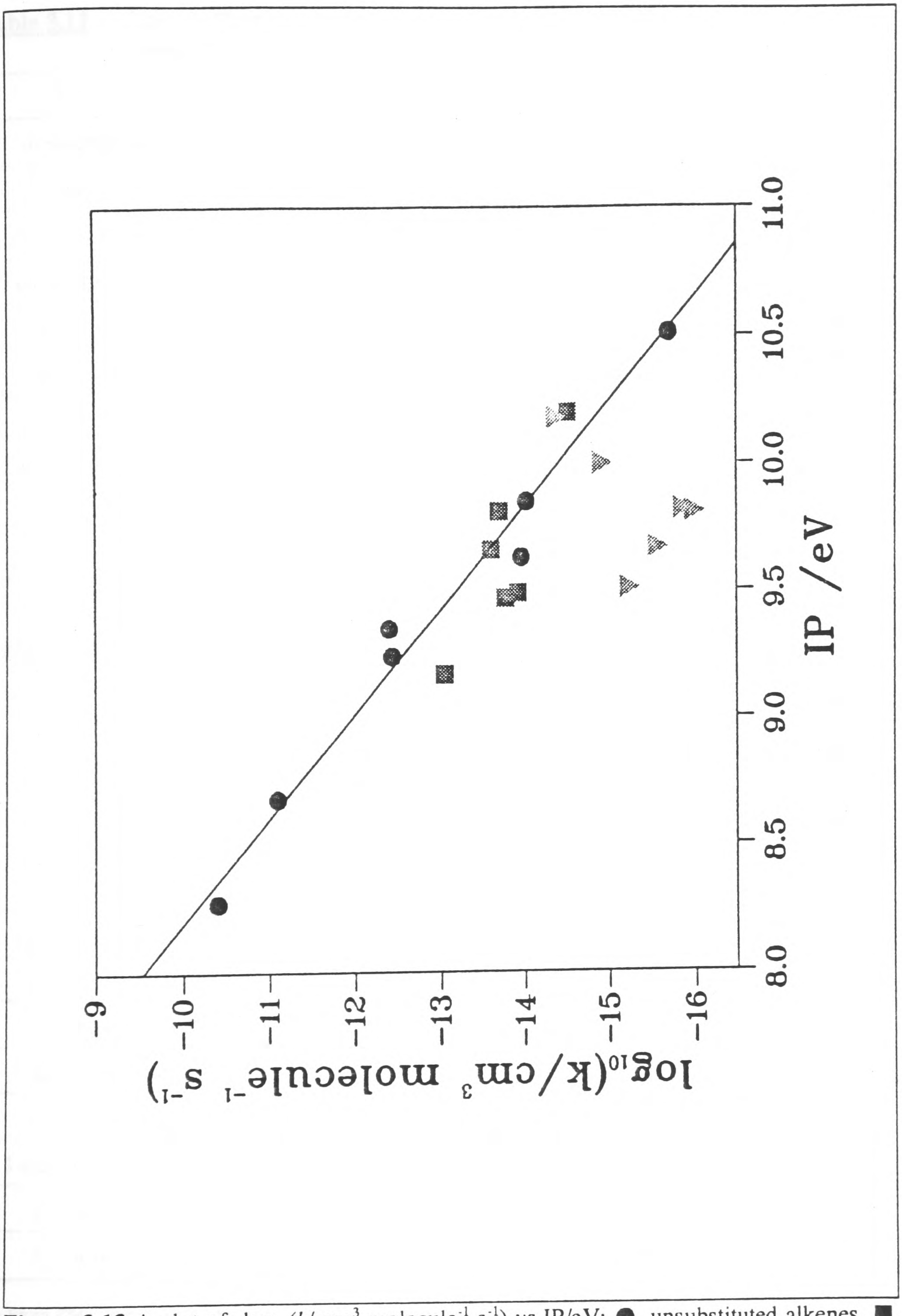

Figure 3.13 A plot of $-\log_{10}(k/\ cm^3\ molecule^{-1}\ s^{-1})$ *vs* IP/eV; ●, unsubstituted alkenes, ■, halobutenes and ▾, chloroethylenes.

Table 3.11 - **The coefficients (eigen-vectors) for the Carbon and Chlorine atoms for compounds with halo-groups adjacent to the double-bond**

Compound	C_1	C_2	Cl_1	Cl_2	Cl_3	Cl_4	ΣC_C^2
monochloroethene	-0.393	0.54	0.745	-	-	-	0.45
1,1-dichloroethene	-0.38	-0.58	0.51	0.51	-	-	0.48
c-1,2-dichloroethene	-0.434	-0.44	0.55	0.55	-	-	0.39
t-1,2-dichloroethene	0.44	0.44	-0.56	-0.56	-	-	0.39
trichloroethene	0.41	0.46	-0.52	-0.41	-0.42	-	0.38
tetrachloroethene	-0.43	-0.43	0.40	0.40	0.40	0.40	0.37
2-chloro-2-butene	0.473	0.564	-0.60	-	-	-	0.54
1-chloromethylpropene	0.49	0.53	-0.62	-	-	-	0.52
1-chloro-1-butene	0.44	0.54	-0.69	-	-	-	0.49
2-chloro-1-butene	0.57	0.41	0.70	-	-	-	0.49

Table 3.12 - **The predicted and experimental rate coefficients for compounds with vinylic halogen groups**

Compound	E(HOMO) (eV) a)	$-\log_{10}(k_{exp.}$ /cm^3 molecule^{-1} s^{-1}) b)	$-\log_{10}(k_{pred.}$ /cm^3 molecule^{-1} s^{-1}) c)	$\log_{10}k_{exp.} - \log_{10}k_{pred.}$	ΣC^2 d)
monochloroethene	9.80	15.35	12.71	2.64	0.45
1,1-dichloroethene	9.74	14.89	12.50	2.39	0.48
c-1,2-dichloroethene	9.49	15.82	11.64	4.18	0.39
t-1,2-dichloroethene	9.51	15.95	11.71	4.24	0.39
trichloroethene	9.37	15.53	11.22	4.30	0.38
tetrachloroethene	9.22	>16.21	10.71	>5.50	0.37
2-chloro-2-butene	9.40	12.96	11.33	1.63	0.54
1-chloromethylpropene	9.32	13.05	11.05	2.0	0.52
1-chloro-1-butene	9.58	13.92	11.95	1.97	0.49
2-chloro-1-butene	9.70	13.77	12.37	1.40	0.49

a) From PM3 calculations (see §3.2.1); b) predicted from regression equation (3.7) given in §3.4.2; c) from Wayne *et al.*, 1991; d) taken from Table 3.11

3.11 shows the coefficients for the carbon atoms (C_C) on either end of the double bond. A plot of ΣC_C^2 *vs* $\log_{10}(k_{pred.}-k_{exp.})$, where $k_{pred.}$ is the rate constant predicted from the E(HOMO) correlation presented in §3.4.2 and ΣC_C^2 is the sum of the squares of the coefficients of the carbon atoms at each end of the double bond (See table 3.12), can be fitted to the expression

$$\log_{10}k_{pred.} - \log_{10}k_{exp} = 6.0 \times \exp(-6.84 \times (\Sigma C_C^2 - 0.342)) \qquad (3.16)$$

as shown in figure 3.14. This expression can be used as a correction factor, based on the coefficients, which can take account of the contribution of vinylic chlorine atoms to E(HOMO) giving the equation

$$\log_{10}k_{exp} = (3.45\times -E(HOMO)+21.1)-(6.0\times\exp(-6.84\times(\Sigma C_C^2-0.342))) \qquad (3.17)$$

where ΣC_C^2 is unity when there are no vinylic chlorine atoms present in the compound. Figure 3.15 shows the full E(HOMO) *vs* $\log_{10}k_{exp}$ correlation for all the compounds shown in table 3.4 and 3.12 using equation 3.17. Again, there is a strong correlation between $\log_{10}k_{corr}$ and E(HOMO) but all the compounds containing vinylic chlorine atoms also lie on the line (*cf* figure 3.8).

In conclusion, using the rate constants for the reaction of NO_3 with a number of halobutenes, the trends in the reactivity of these and other substituted alkenes have been investigated. A strong correlation between the energy of the HOMO and the rate constant for reaction exists for alkenes not containing vinylic Cl atoms. Using this correlation, we are able to make estimates of rate constants for the reactions of NO_3 with substituted alkenes; the group-reactivity method provides another means of making these estimates. Table 3.13 shows rate coefficients predicted both by the group reactivity method and by regression equation (3.7) which represents the HOMO energy-rate-coefficient correlation. The rate coefficients

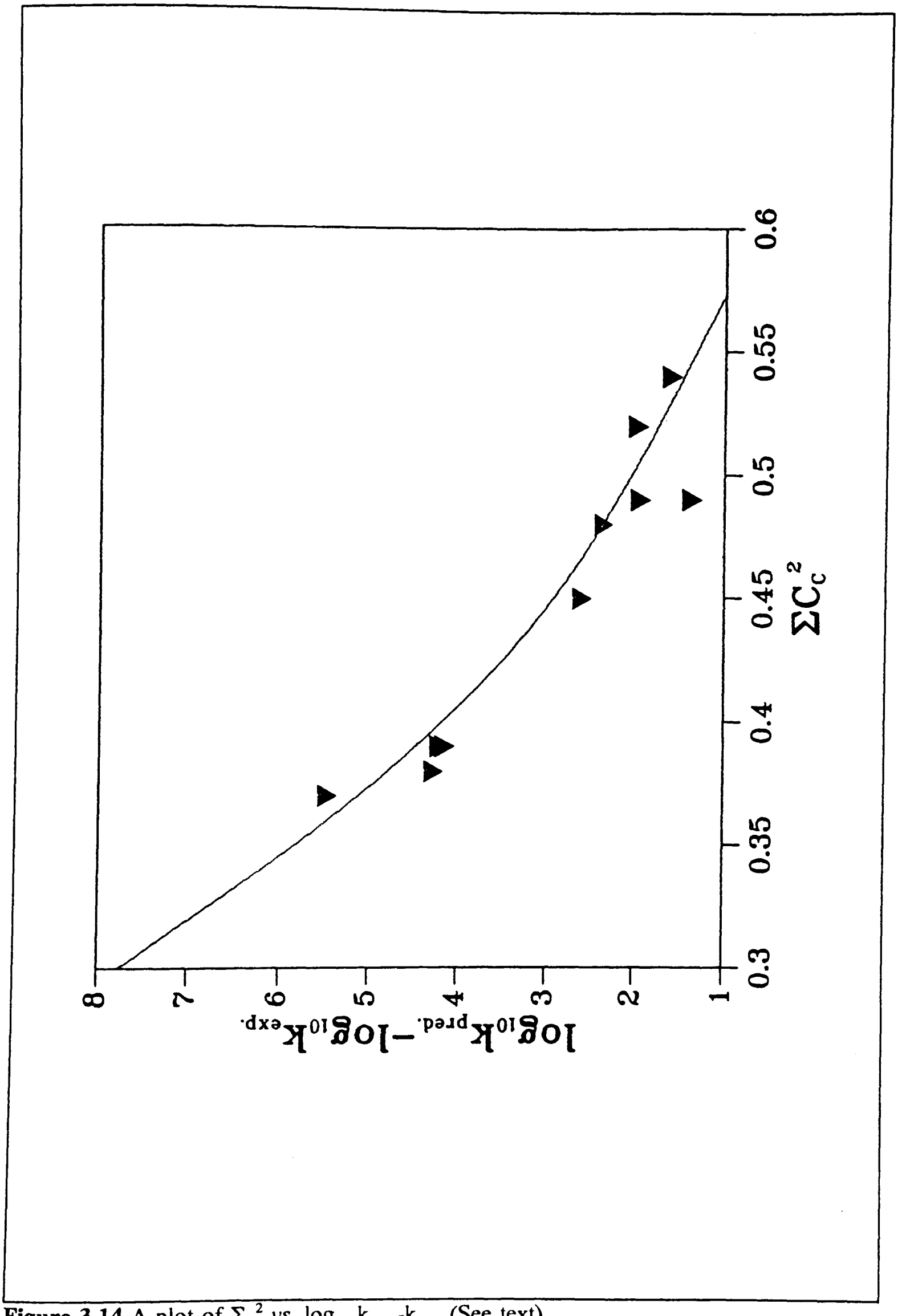

Figure 3.14 A plot of $\Sigma_C{}^2$ *vs.* $\log_{10} k_{pred.}$-$k_{exp.}$ (See text)

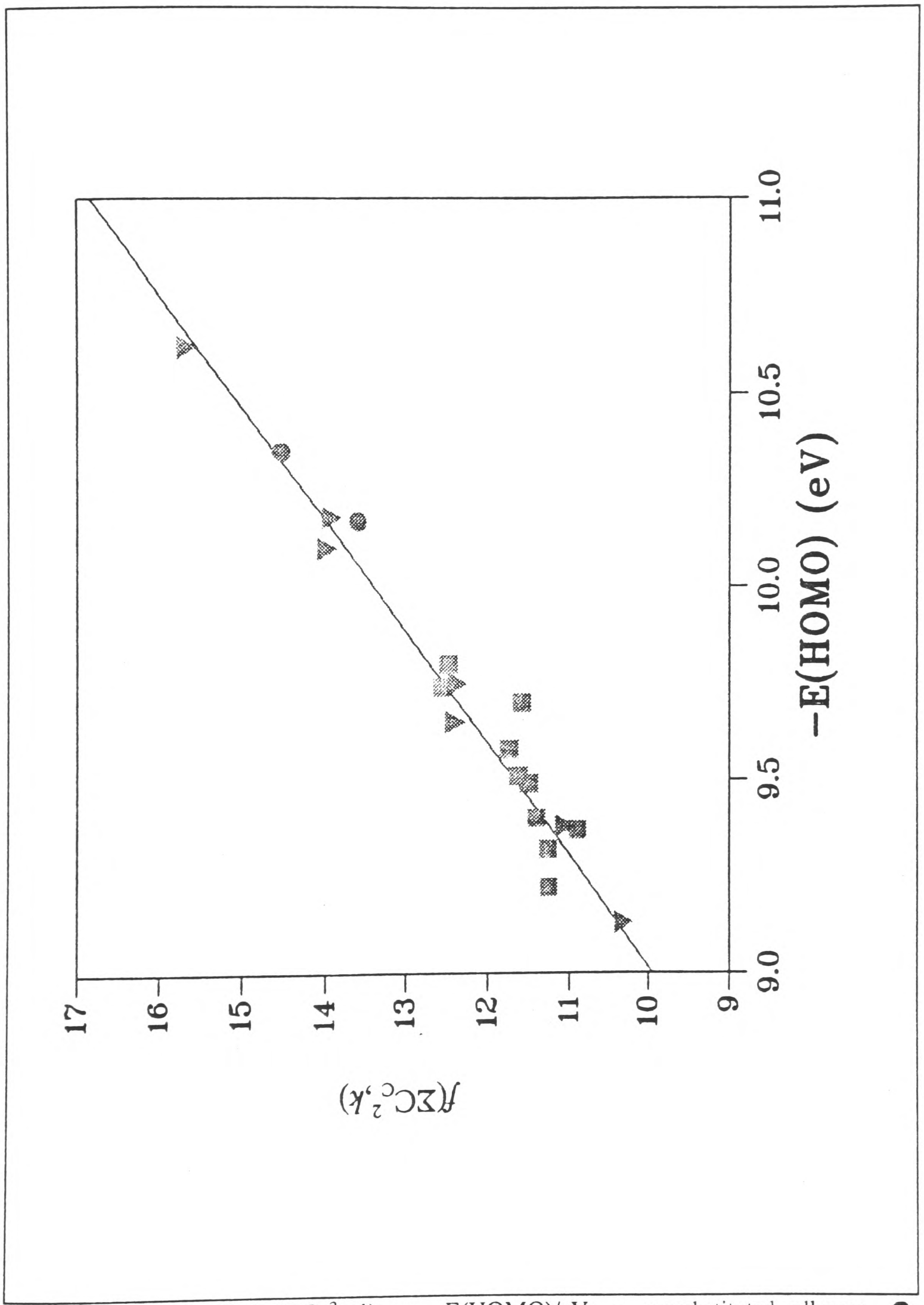

Figure 3.15 A plot of $f(\Sigma C_C^2, k)$ *vs.* -E(HOMO)/eV; ▾, unsubstituted alkenes, ●, halobutenes without vinylic halogen groups; ■, haloalkenes (see Table 3.11) with vinylic halogen groups.

predicted have not yet been measured experimentally. It can be seen that both sets of predicted rate coefficients are in reasonable agreement. This approach has been further explored by experimentally determining the ionisation potential of the frontier orbitals by PES and calculating a correction factor for compounds with vinylic halogen groups based on the orbital coefficients.

Table 3.13 **Predicted rate coefficients for the reaction of NO_3 with a series of chloro substituted and unsubstituted alkenes.**

Compound	-E(HOMO) eV a)	k_{calc} b) cm^3 $molecule^{-1}$ s^{-1}	k_{calc} c) cm^3 $molecule^{-1}$ s^{-1}
pent-1-ene	10.03	$3.9x10^{-14}$	$1.6x10^{-14}$
pent-2-ene	9.6	$1.2x10^{-12}$	$4.8x10^{-12}$
4-chloropent-1-ene	-	-	$5.1x10^{-15}$
3-chloropent-1-ene	-	-	$4.0x10^{-15}$
2-methylbut-1-ene	9.7	$5.4x10^{-13}$	$4.4x10^{-13}$
hex-1-ene	10.03	$3.9x10^{-14}$	$2.1x10^{-14}$
1-chloropropene	-	-	$1.5x10^{-14}$
2-chloropropene	-	-	$1.4x10^{-14}$
3,4-dichlorobut-2-ene	-	-	$7.2x10^{-14}$
1,4-dichlorobut-2-ene	10.3	$4.6x10^{-15}$	$1.5x10^{-15}$
chloromethyl-1-chloropropene	10.27	$5.9x10^{-15}$	$1.3x10^{-15}$
1,1-dichloromethylpropene	-	-	$7.2x10^{-14}$
4-chlorobut-1-ene	10.3	$4.6x10^{-15}$	$3.9x10^{-15}$

a) From PM3 calculations, discussed in §3.2.1; b) calculated from regression equation (3.10), see text; c) calculated using group additivity factors, see §3.6.

CHAPTER 4

The self-reaction of NO_3

4.1 Introduction

The kinetics of the reactions of the nitrate radical with atoms or other simple free radicals have been investigated in recent years in order to elucidate the mechanisms which occur in chemical systems used in the laboratory for studies of the atmospheric reactions of NO_3. Studies of this type also aim to lend support to ideas on the relationship between the structure of a species and the patterns of reactivity exhibited towards reaction with the nitrate radical.

A major part of research on radical–radical reactions has been directed towards an understanding the of kinetics, dynamics and theory of radical association reactions (Smith, 1991)

$$R_1\cdot + R_2\cdot \longrightarrow R_3 \text{ or } (R_1R_2) \qquad (4.1)$$

A special case in radical association reactions is the self-reactions (where $R_1\cdot \equiv R_2\cdot$). The kinetics of such reactions are second-order in the radical concentration. To a certain degree, these systems are easier to study because there is not the problem of producing and detecting the required concentrations of two 'unstable' radicals in a controlled manner. It is necessary though, to be able to measure absolute concentrations of the radical in order to extract rate constants from the observed mainly second-order decays of the radical concentration (Slagle *et al.*, 1988).

The work presented here is the first direct determination of the kinetics of the NO_3 self-reaction. The reaction is studied by a non-conventional variant of the flash photolysis kinetic technique. The rate of the self-reaction was measured over a pressure range of 3-100 Torr in He. A detailed consideration is given to the mechanism of the reaction and the validity

of the fitting procedures used.

4.2 Flash photolysis

The kinetic technique of *flash photolysis* was developed by Norrish and Porter in the 1950's (Norrish and Thrush, 1956). The technique was developed in an attempt to identify reactive intermediates present in photochemical systems. Previous to this time there was no way of detecting by absorption spectroscopy intermediates such as radicals, atoms and excited species present in low concentrations in a photochemical system. Flash photolysis is a good example of a 'pump'-'probe' type of experiment. There are many variations of these flash-initiated types of kinetic experiments (Wayne, 1988). The general principle of flash photolysis is that an extremely high-intensity light source, either a halogen-arc flash-lamp (e.g. Bamford and Tipper, 1969) or a laser, initiates a reaction by photodissociation of one or more precursors producing transient concentrations of intermediates, such as radicals, which are sufficiently large for spectroscopic observation. This is the 'pump' phase of the experiment. Ideally, the pulse of light is of short duration compared to the kinetic timescale of interest and possesses a very narrow wavelength band-width. A second, either pulsed or continuous-wave light source is employed to 'probe' spectroscopically for a species of interest. This cycle of 'pump' and 'probe' can be repeated any number of times in order to average relatively weak signals. Some experiments follow the decay of a radical generated directly by photolysis of the precursors (e.g. Anastasi *et al.*, 1986) or by following the rise and decay of the concentration of a radical produced by the subsequent chemistry (e.g. Smith and Zellner, 1973). Flash-photolysis has now been extended to the sub-picosecond time-scale (Fleming, 1986).

4.3 A comparison of flow tube and flash-photolysis kinetic techniques
(Howard, 1979; Kaufman, 1984; Wayne, 1991)

The discharge-flow and flash-photolysis kinetic techniques are the mainstay in the production of thermal kinetic data. It is therefore instructive to make a comparison of these two techniques. The use of the discharge-flow technique was described in Chapter 2 (§2.2) to measure the kinetics of the reaction of various butenes with NO_3 and the flash photolysis method is used in this Chapter to look at the self-reaction of the same radical. The criteria for the comparison are summarised in Table 4.1. Where possible the reactions of NO_3 are used for comparison.

Table 4.1 - Comparison of flow tube and flash-photolysis kinetic techniques (After Howard, 1979)

Criteria	Discharge flow	Flash photolysis
Temperature range	200-600K	100-600K
Pressure range	1-10 Torr	1 Torr - several atmospheres
Rate constant range	$(10^{-10} - 10^{-16})$ cm^3 $molecule^{-1}$ s^{-1}	$(10^{-10} - 10^{-18})$ cm^3 $molecule^{-1}$ s^{-1}
Detection versatility	excellent	requires fast detector
Reactant Versatility	excellent	limited
Heterogenous reactions	can be serious	none
Expense	low	moderate

The temperature range for which both techniques can measure valid data are similar. In kinetic studies the upper temperature limit is normally determined by the thermal instability of the reactants, whereas the lower limit is governed more by heterogenous destruction of the radical species. For the reactions of NO_3, the study of the reaction with *trans*-2-butene by

Hammer and Dlugokencky (1989) in a flow tube was measured down to 204 K. The highest temperature used for the study of NO_3 kinetics was for the reaction with ethane in a discharge flow system which has been measured at temperatures up to 558 K by Canosa-Mas *et al.* (1988). A special flow reactor has been used by Fontijn *et al.* (1979) to measure kinetics at temperatures up to 2000 K, but the criteria of reactant thermal stability has made this only useful for reactions of metals with metal oxides.

The flow tube, in comparison to flash photolysis, is basically a low pressure technique. Above about 10 Torr the assumption of plug-flow (See Chapter 2) becomes invalid, leading to a need for more complex analysis. This is coupled to the problems of production and detection of radicals at higher pressures. Flash photolysis can be used to measure rates of reaction at pressures of up to a few atmospheres, the main limitation being the ability to detect radicals under these conditions. This flexibility in the pressure regime makes the measurement of termolecular reactions more attractive by flash photolysis. For example the reaction of NO_3 + NO_2 has been studied in the region from 20 Torr to 200 atm by flash photolysis (20-70 Torr, Kircher *et al.*, 1984; 2-200 atm, Croce de Cobos *et al.*, 1984) Recently, there have been advances in high-pressure discharge-flow experiment by Abbatt and Anderson (1990, 1991) who have measured the reaction of OH with various chloroethenes at pressures of up to 100 Torr.

Both the discharge-flow and flash-photolysis techniques can be used to measure fast reactions with rates up to gas kinetic collision rates. Because of the greater pressure range available in flash photolysis experiments, larger reactant concentrations can be used, hence smaller rate constants can be measured. Recently, Biggs *et al.* (1991) have described a novel discharge

stopped-flow technique for the measurement of overall rate constants in the range 10^{-15} - 10^{-19} cm^3 $molecule^{-1}$ s^{-1}. The stopped-flow technique has been applied specifically to the measurement of reactions of the nitrate radical with organic molecules.

One of the major advantages discharge flow has over flash photolysis, is the plethora of methods available for the detection of reactants. This advantage is derived from the steady-state nature of discharge flow. In discharge flow the concentration of the reactants is constant at any given point (i.e. reaction time), leading to less of a constraint on the response time of the detector. On the other hand, flash photolysis is a real-time experiment, such that the detector should respond at least in 1/10th the period of the experiment. In the case of NO_3, the relatively low reactivity of the radical means that long timescales are generally used, such that the response speed of the detector is not a limiting factor.

Probably the greatest disadvantage of flash photolysis is in the limited number of suitable reactants. This problem is twofold first; the photochemical sources of the radical plus co-reactants should not produce unwanted reactive species on reaction with the fragments of the photochemically generated radical. This problem does not manifest itself to the same extent in discharge-flow kinetics. For example in the case of production of NO_3 by photolysis of $Cl_2/ClONO_2$ mixtures (e.g. Kircher *et al.*, 1984); the Cl atoms were produced by photolysis of the Cl_2

$$Cl + ClONO_2 \longrightarrow Cl_2 + NO_3 \qquad (4.2)$$

$k_{4.2} = 1.2x10^{-11}$ cm^3 $molecule^{-1}$ s^{-1} (DeMore *et al.*, 1990)

and/or

$$ClONO_2 + h\nu \longrightarrow Cl + NO_3 \qquad (4.3)$$

This chemical system exemplifies the second problem. In the presence of organic co-reactants (Wallington *et al.*, 1986) competition for the Cl radicals severely reduces initial concentrations of NO_3 and leads to the presence of unwanted organic radicals. This problem can be relieved in certain chemical systems if a common precursor is used for both reactants e.g. OH and NO_3 from photolysis of HNO_3 (Ewig *et al.*, 1988).

An important advantage of the flash photolysis technique is that, if conducted at the centre of a large reactor, the possibility become less. This advantage must be offset against the effect of diffusion of photochemically produced reactants out of a photolysis volume. In discharge-flow, the problem of heterogenous reactions can be critical to the determination of absolute rate coefficients, as well as the reactor surface being an impediment to the study of vibrationally or electronically excited molecules. The role of heterogenous reactions in the observed kinetics is not a particular problem in the study of NO_3 kinetics, as the wall losses even on uncoated surfaces are quite small.

4.4 Apparatus

The apparatus is represented schematically in Figure 4.1. It consists of a reaction cell, a photolysis light source, gas-handling manifolds and a multi-pass White's optics absorption system for detection of radical species.

4.4.1 The reaction cell and gas-handling manifolds

The reaction cell was made from quartz tubing and had an internal diameter of 35 mm and

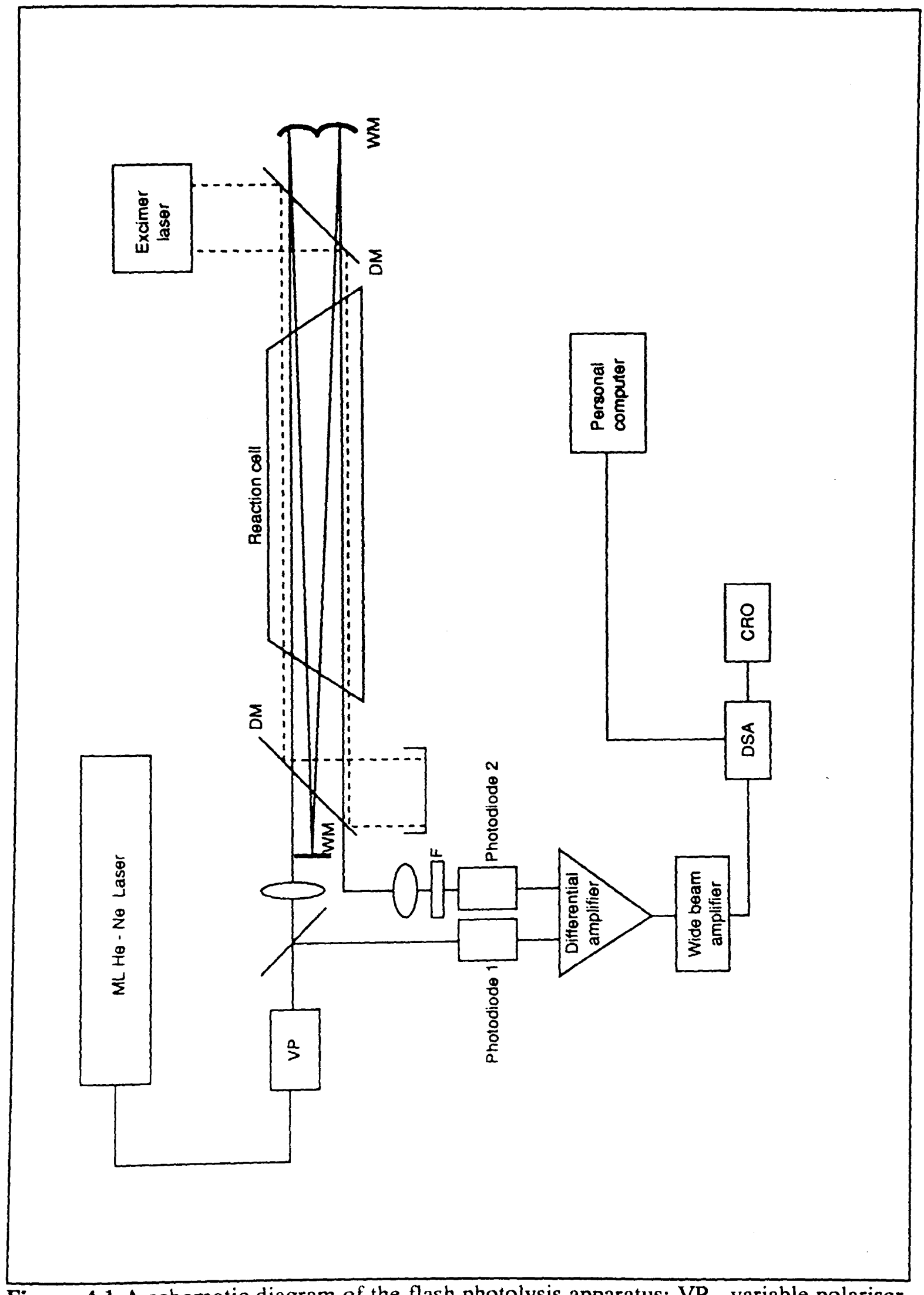

Figure 4.1 A schematic diagram of the flash photolysis apparatus; VP - variable polariser, WM - White mirror, DM - Dichroic mirror, DSA - digital storage adaptor, CRO - cathode ray oscilloscope.

a base length of 20 cm. The windows were Quartz and transmitted light above λ=200 nm they were mounted using halocarbon wax (series 1500, KMZ chemicals) at the Brewster angle (Δ~55°32' at a refractive index of 1.456), this minimised the amount of light scattered from the windows. The cell had two arms, the first was connected *via* steel bellows (Cajon) or glass tubing to a vacuum system consisting of a 2 inch diameter diffusion pump (Edwards) backed by a rotary pump. Alternatively this system could be pumped *via* a glass trap held at liquid nitrogen temperature (77 K) to a rotary pump (Edwards). The pressure in this system was measured by a capacitance manometer (MKS Baratron 170M 1000 Torr range). The second arm of the cell was similarly connected but to a 4-way stainless steel (Swagelock) inlet system which was in turn coupled to the gas-handling manifolds.

The gas handling manifolds were constructed from Pyrex with PTFE taps (Youngs Scientific Ltd.). There were two manifolds, the first consisted of the storage bulbs (5 dm^3) required for the fluorine mixtures and was directly connected to the inlet system; the second was connected to an oil-diffusion pump (Edwards). Pressures within the manifolds were measured with a variety of communal gauges depending upon the pressure. A capacitance manometer (MKS Baratron 170M 1000 Torr range), a Pirani gauge (Edwards, < 1 Torr range), a Penning gauge (Edwards, $<10^{-2}$ Torr range) and a Torriccelli mercury manometer (Perry, 1941).

4.4.2 Production of NO_3

The nitrate radical was produced by photolysis of fluorine and nitric acid mixtures.

$$F_2 + h\nu \longrightarrow F + F \qquad (4.4)$$

$$F + HNO_3 \longrightarrow NO_3 + HF \qquad (4.5)$$

Sufficient time (up to 15 minutes at pressures of 100 Torr) was allowed on introduction of gas mixtures into the cell to allow for complete mixing. Diluted fluorine (B.O.C. 5% in helium) was used as supplied and the HNO_3 was taken as a vapour (*ca.* 10 Torr at 298 K) from a 1:2 mixture with sulphuric acid. The photolysis light source was provided by an excimer laser (Questek 2000), operating on the XeCl line at λ=308nm. A typical laser pulse energy was 100 mJ at repetition rates variable between 10 and 80 Hz. The laser was triggered internally. The photolysis light produced by the laser was directed along the length of the cell by a pair of dichroic mirrors. The mirrors were coated to enable only the U.V. light to be reflected whilst still allowing efficient transmission of visible radiation. The λ=308 nm radiation is not just absorbed by F_2, but also by the HNO_3 (absorption cross-sections of 1.68×10^{-20} molecule^{-1} cm^2 and 1.0×10^{-21} molecule^{-1} cm^2 (Okabe, 1978) respectively) are such that at equal concentrations, *ca.* 10% of the photolysis will be of HNO_3, consequently it was necessary to ensure that the $[F_2]$ was always significantly greater than that of $[HNO_3]$. The primary process for the photolysis of HNO_3 (Johnston *et al.*, 1974) is

$$HNO_3 + h\nu \longrightarrow OH + NO_2 \qquad (4.6)$$

The production of NO_2 from the photolysis of HNO_3 is discussed later. On photolysis of mixtures of up 100 Torr of F_2/HNO_3/He, NO_3 concentrations of up to 9.0×10^{14} molecule cm^{-3} were produced. The photolysis/decay cycles were not as in conventional flash-photolysis experiments (Wayne, 1988) but the mixtures were photolysed at such a repetition rate that a maximum equilibrium concentration was built up, then on cessation of photolysis the decay was followed for a period of up to 50 s.

4.4.3 Detection of NO_3

The source of the probe beam for the detection of NO_3, was a multi-line He-Ne laser (Spindler and Hoyer, ML500). Wavelength selection was achieved using an intra-cavity Quartz-birefringent filter (Siegman, 1986). The lines available for detection of NO_3 by laser absorption are shown in table 4.2. The probe beam was multi-passed up to 28 times through the reaction cell using White's optical arrangement (White, 1942), with absorption path lengths up to 5.6 m. The geometry was arranged such that the multi-pass plane was enclosed by the much larger rectangular cross-section of the photolysis volume. In order to minimise the effects of noise caused by intensity fluctuations of the probe beam, a reference beam was first split from the probe beam prior to it entering the reaction cell and directed to a detector.

Table 4.2 - The output wavelengths of the ML500 He-Ne laser and their coincidence with the NO_3 absorption spectrum.

Wavelength (nm)	Output power /mW (with λ selector)[a)]	Output power /mW (without λ selector)[a)]	$\sigma(NO_3)$ /10^{-19} cm^2 $molecule^{-1}$ [b)]
611.8	0.3	1.0	19.1
629.4	0.6	-	69.8
632.4	3.0	5.0	32.7
635.9	0.2	-	14.4
640.1	1.0	1.5	12.3
730.5	-	0.3	-

a) intra-cavity birefringent filter (see text); b) from Wayne *et al.*, 1991

The probe and reference beams were both incident on identical photodiodes (2.4 mm x 2.8 mm, BPW21, rise time 3.5 μs), the outputs of which were balanced by either a variable

polariser used to alter the fraction of the light reflected by the beam splitter or by attenuating the amount of light incident on the reference photodiode with neutral filters of varying optical densities. The sample photodiode was protected from stray excimer light by a band-pass filter and a long hood.

4.4.4 Signal processing and recording of data

The resultant signals from the photodiodes were fed to a differential amplifier (PCL construction) which subtracted the signal produced due to incident light on the reference photodiode from that on the sample diode. The resultant difference signal was buffered and amplified by a fast operational amplifier (LH002CN) and passed to a wide-band video amplifier (Phillips E592) were it was amplified another 10 times. This signal was fed to a digitiser (Thurlby, DSA 524) were it could be stored and passed to a personal computer. Typical absorbances were less than 55% following photolysis of *ca.* 40 Torr of F_2/HNO_3 mixture.

The decay trace was stored on the computer in 8 bit (Binary) form and was converted into ASCII format by a C-program (Biggs, 1990), which took account of the time base and voltage per division during the conversion. The resultant ASCII data consisted of 4028 time-voltage points. The data file was subsequently transferred to a VAX computer where it was converted into a time-concentration profile. The program which facilitated this conversion is shown in Appendix II. The operation of the program is explained to show the basis for the validity of the fitting procedures explained later. The data is read from the uncalibrated (raw) ASCII file and a base-line is removed. The uncalibrated trace is shown in Figure 4.2.

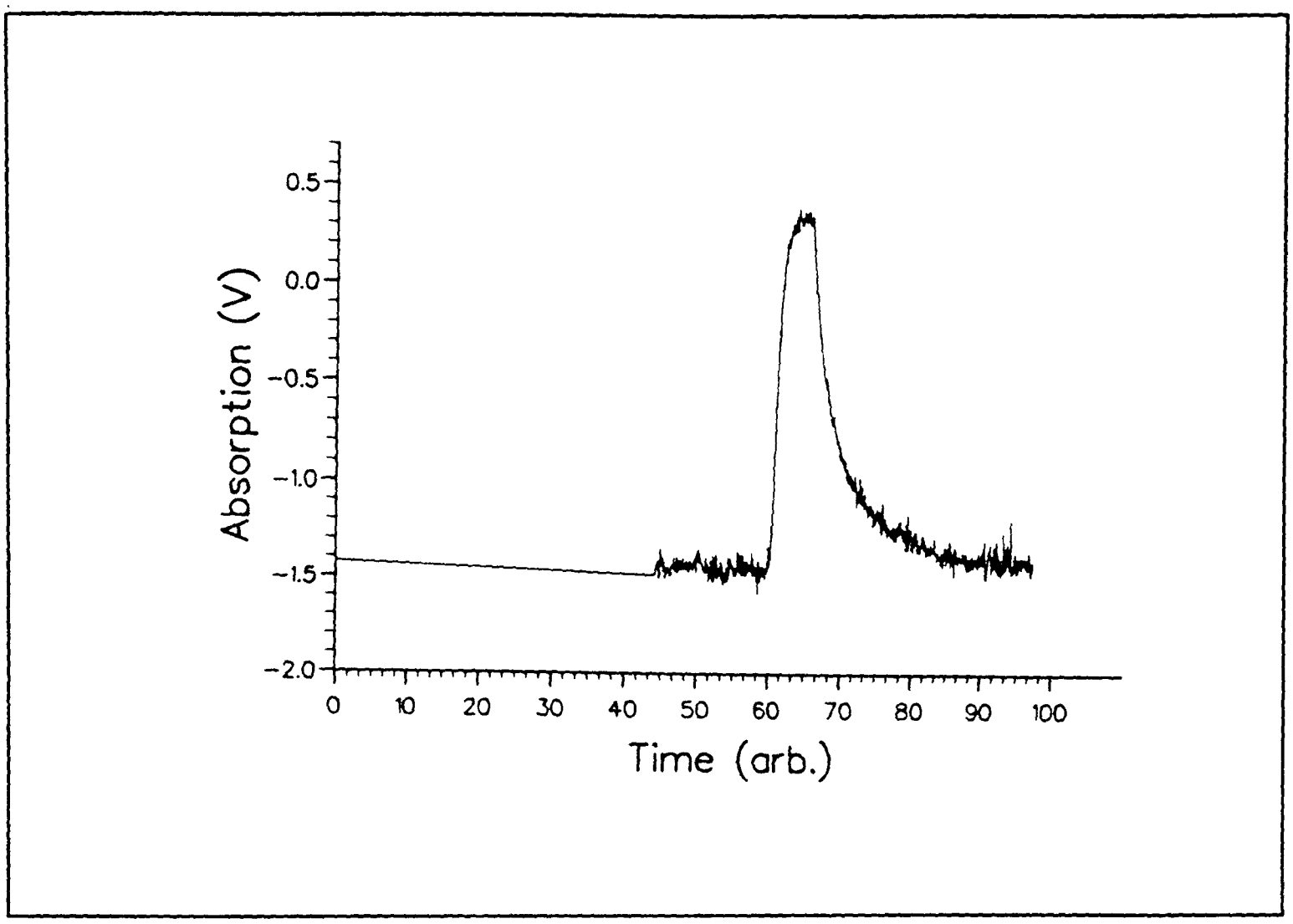

Figure 4.2 The uncalibrated data as read in to the program.

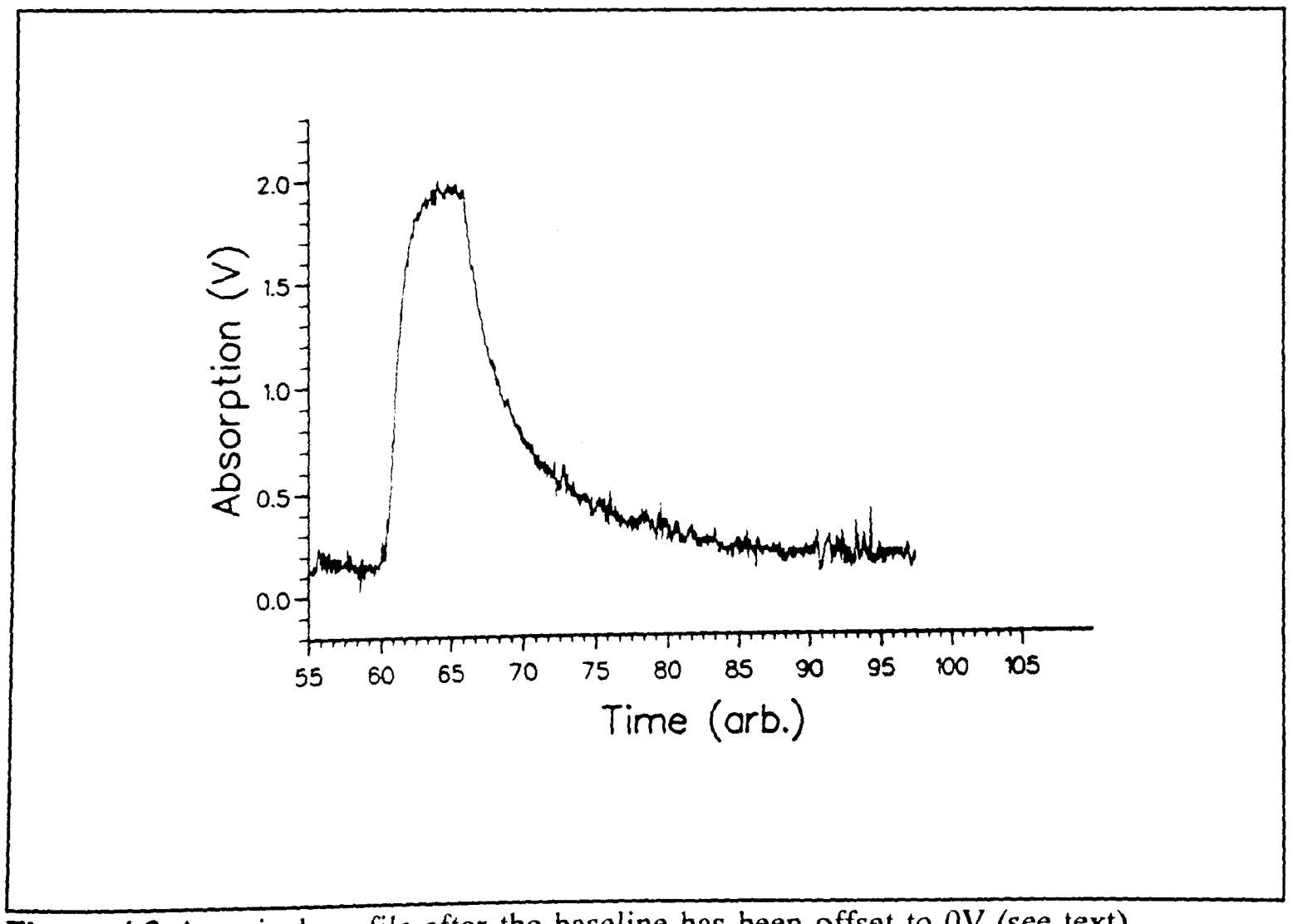

Figure 4.3 A typical profile after the baseline has been offset to 0V (see text).

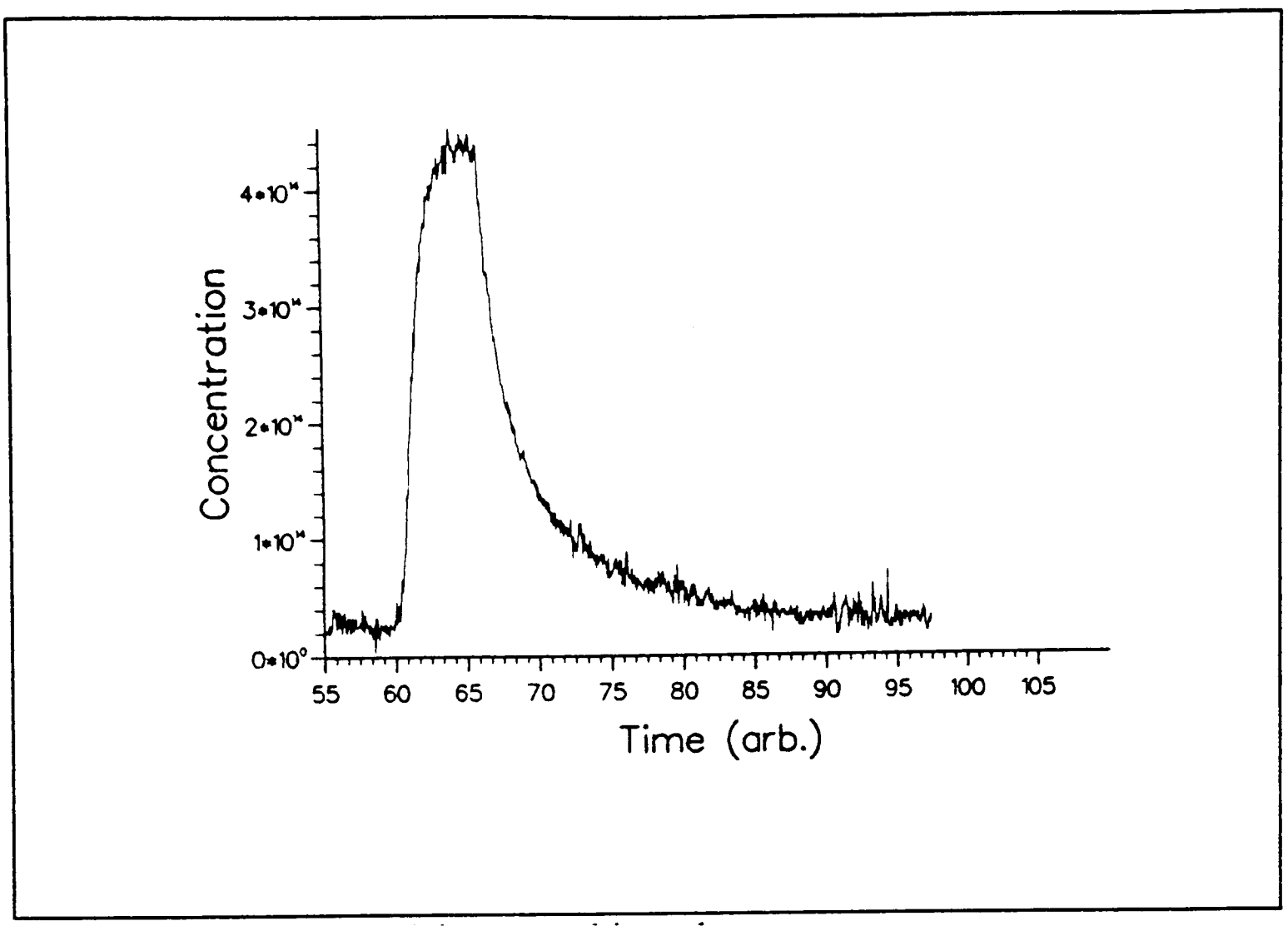

Figure 4.4 A typical time *vs.* [NO_3] profile generated using the program in AppendixII (see text).

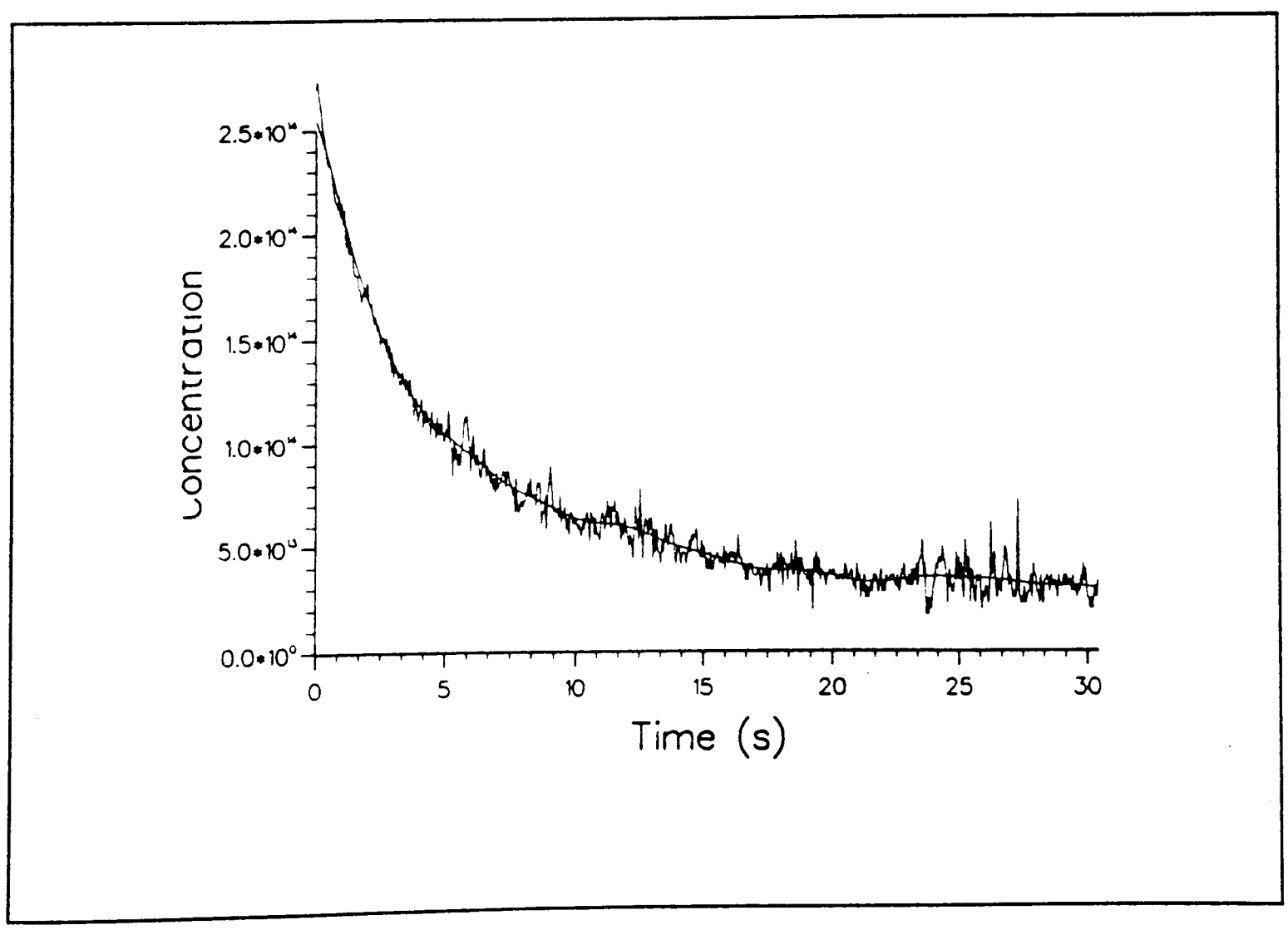

Figure 4.5 A typical time *vs.* [NO_3] decay curve generated using the program in Appendix II(see text). The line through the experimental data is a smoothed curve (see text).

This trace is displayed on the screen and a baseline which represents 0V is selected using a cursor. The profile is then offset to 0V as shown in Figure 4.3. The voltage at the peak of the build-up portion of the curve, I_{max}, is checked against an original oscilloscope trace. If these two do not match within ± 0.1V, the previous steps are repeated until there is a match. The profile is then converted into $[NO_3]$ by use of the Beer-Lambert law

$$[NO_3]_t = \frac{1}{\sigma l} \ln\left(\frac{I_o}{I_o - I_{abs}}\right) \qquad (4.7)$$

were σ is the absorption cross-section at a given λ, l is the geometric path length, I_o is the absorption when no NO_3 is present, and I_{abs} is the absorption in the presence of NO_3 at a time t. The resultant concentration profile is shown in Figure 4.4. A portion of the curve is then selected according to the analysis to be undertaken (see §4.5). The first point of the curve selection is set to t=0, the time difference between individual points having been scaled from the original conversion (See Figure 4.5). In this final output, two different types of data were output to separate files. The first, was the calibrated data from the selected region. The second, was data representing a smooth curve drawn through the original data. The smoothing was achieved using a '*semi-parametric*' Fast Fourier transform (FFT) smoothing routine (Press *et al.*, 1978). The FFT was used as a low-pass filter the data, the smoothing factor being set to a 15 point average. The smoothed curve is shown later to have the same kinetic characteristics as the original curve, but is of more use in minimising the errors on fitting the data.

4.5 Results I

On filling the cell with a mixture of He, F_2 and HNO_3 and photolysing at a repetitively a modulated steady-state concentration of NO_3 was built up. Average peak concentrations of

NO_3 after photolysis were in the region $1.0x10^{14}$-$9.0x10^{14}$ molecule cm^{-3}. On cessation of the photolysis, the NO_3 concentration was seen to decay over a period up to 50 s. Figure 4.6 shows a typical NO_3 signal build-up and decay from photolysis of *ca.* 40 Torr of F_2/HNO_3 mixture.

4.5.1 Simple considerations

The experimental conditions for production of NO_3 were chosen so that the self-reaction was the dominant second-order process. As a first approximation the only reactions taking place after the photolysis phase were said to be

$$NO_3 \longrightarrow \text{Wall} \qquad (4.8)$$

$$NO_3 + NO_3 \longrightarrow \text{Products} \qquad (4.9)$$

An assumption implicit in this simple mechanism is that any products of the reactions (4.8 and 4.9) (See §4.6.6) have no influence on the observed concentration of NO_3. Further, any impurities, such as NO_2, which can react with NO_3 are assumed to be consumed during the build-up of the large concentration of NO_3 during the photolysis phase. Thus, the rate equation for the loss of NO_3 is

$$\frac{d[NO_3]}{dt} = -k_{4.8}[NO_3] - k_{4.9}[NO_3]^2 \qquad (4.10)$$

This can be integrated and solved explicitly to give the expression

$$[NO_3]_t = \frac{k_{4.8}[NO_3]_o}{(e^{-tk_{4.8}}(k_{4.8}+k_{4.9}[NO_3]_o)-k_{4.9}[NO_3]_o)} \qquad (4.11)$$

Equation 4.11 was used in a two-parameter non-linear-least square fit using $k_{4.8}$ and $k_{4.9}$ as the

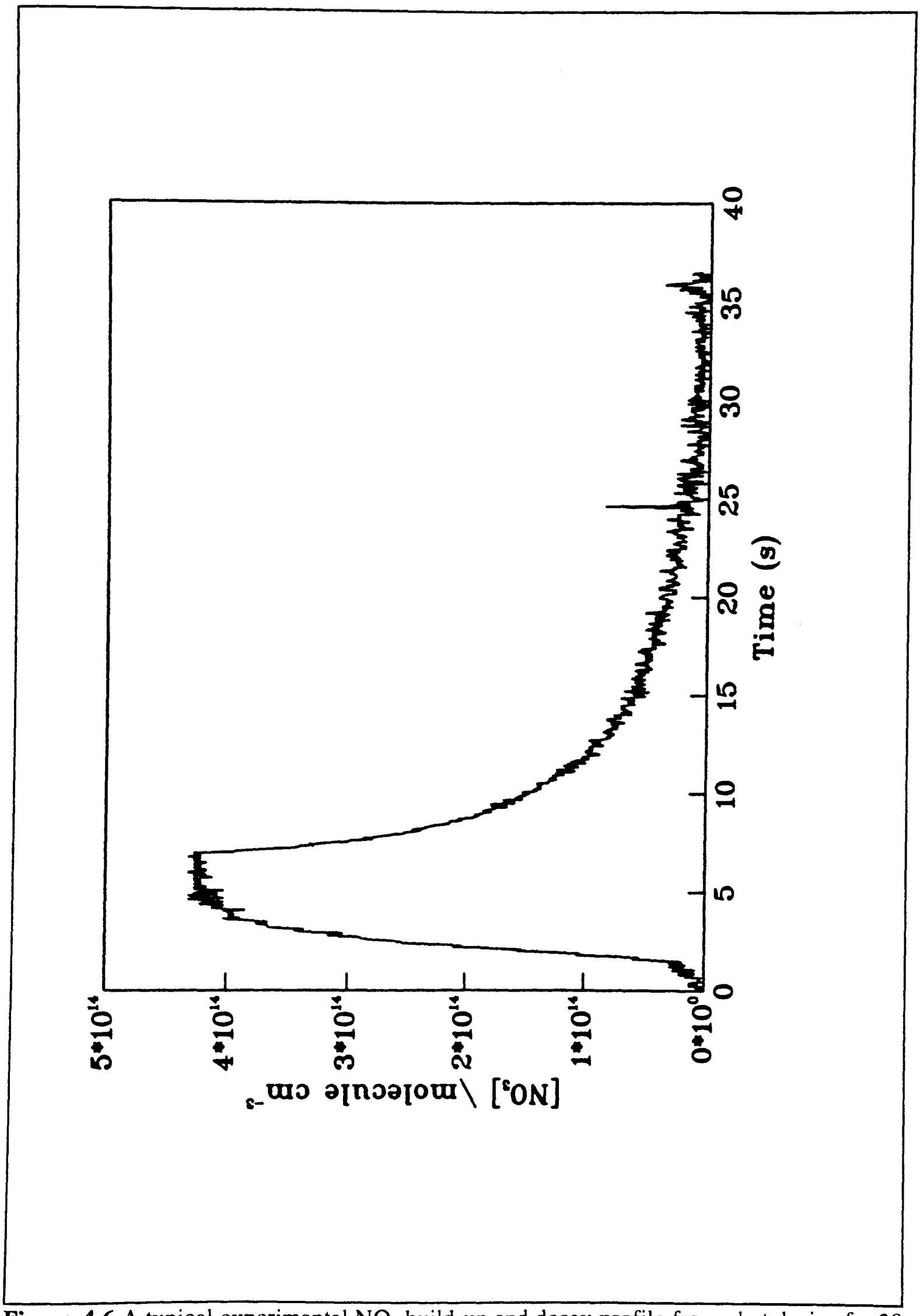

Figure 4.6 A typical experimental NO_3 build-up and decay profile from photolysis of a 30 Torr mixture of F_2, HNO_3 and helium.

floating parameters. The routine used for this fit was a version of the Levenberg-Marquadt (L-M) method (Press *et al.*, 1986), which involved an iterative process in which the parameters were varied to minimise χ^2, the sum of the square of the residuals, where the residual R for a time point j is defined as R_j = *constant* × *(observed data point j - calculated point j)/ scale factor.* An example fit, to an observed $[NO_3]$ decay profile, obtained by this method is shown in Figure 4.7. Example results obtained from fitting of the data to a number of experimentally obtained profiles, as described above, are shown in table 4.3. The errors on these fits are $\sigma(k_{4.8})=\pm 0.1$ and $\sigma(k_{4.9})=\pm 0.2$ from an error analysis of the L-M method.

Table 4.3 - Example results from fitting of data to equation 4.11 using L-M method

Run	P_T /Torr	$[NO_3]_o$ /molecule cm^{-3}	$k_{4.8}$ /s^{-1}	$k_{4.9}$ /cm^3 molecule^{-1} s^{-1}	No. of points used in fit
2208G	37.8	4.9×10^{14}	0.07	7.5×10^{-16}	64
2208E	40.3	9.1×10^{14}	0.08	9.1×10^{-16}	63
2208H	39.8	3.5×10^{14}	0.06	8.3×10^{-16}	56
2208C	8.0	1.6×10^{14}	0.24	5.7×10^{-16}	64
2208D	38.0	3.6×10^{14}	0.09	8.2×10^{-16}	58
2208A	29.0	2.6×10^{14}	0.16	2.7×10^{-16}	62
2208B	30.0	3.0×10^{14}	0.11	6.5×10^{-16}	61
2208I	39.0	2.8×10^{14}	0.07	8.2×10^{-16}	59
2208K	41.2	4.0×10^{14}	0.08	7.9×10^{-16}	63
			0.09[a)]	7.3×10^{-16}[a)]	

a) The average was calculated excluding run 2208C because of the difference in pressure as compared to the other runs

The results shown in table 4.3 were obtained from fitting of equation 4.11 to the data taken from the whole of a decay curve (t=0 to <50 s). From a consideration of equation 4.10, the

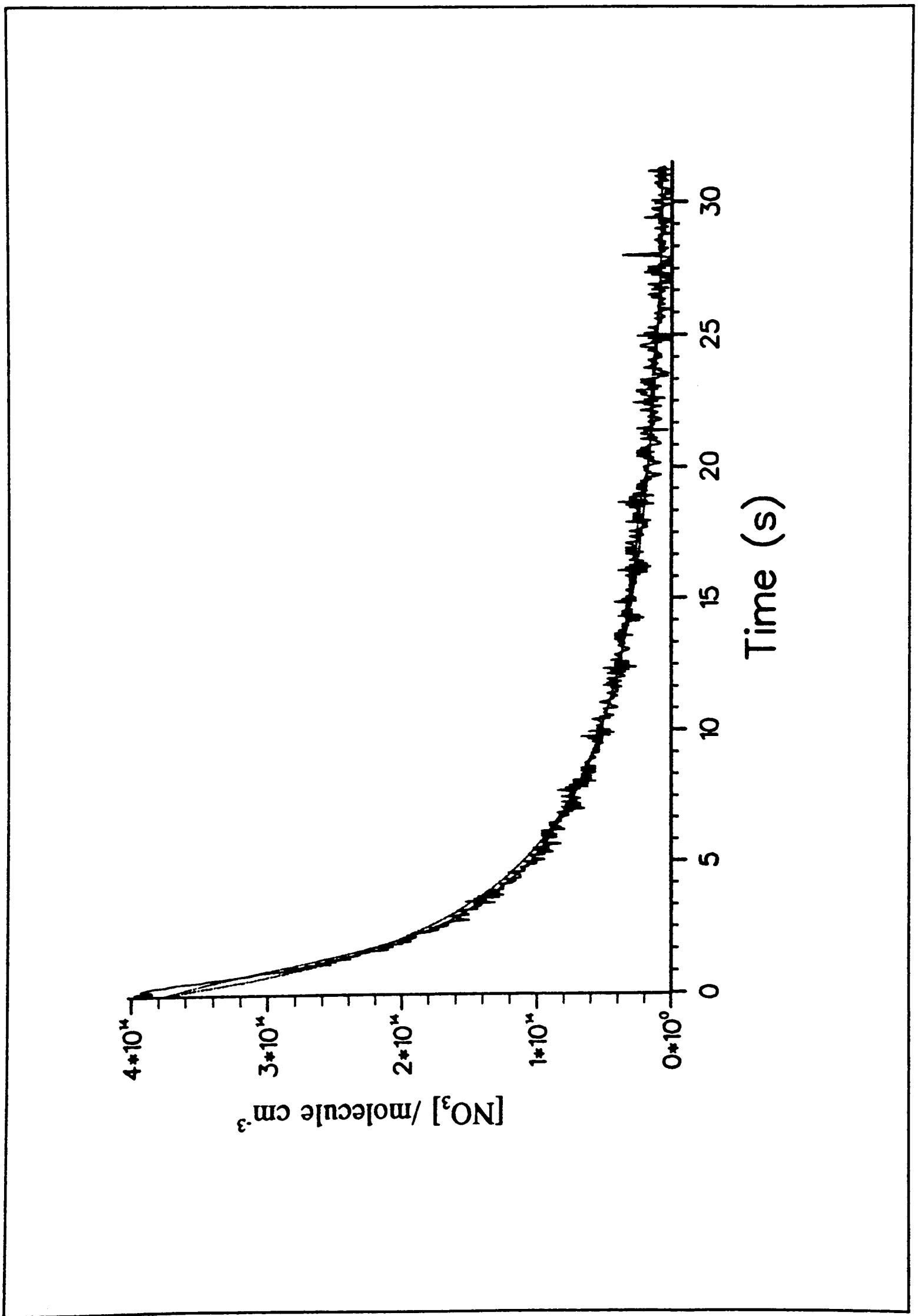

Figure 4.7 An typical fit to an experimental time *vs.* $[NO_3]$ decay curve using the L-M method of fitting to equation 4.11.

second order component of a decay is more dominant when $[NO_3]$ is large. In order to extract the second-order component of a decay, different portions of the decay curve where used, as shown in Table 4.4. From the results presented so far in both Tables 4.3 and 4.4, it can be seen the L-M fitting to the explicit solution of the rate equation (4.11) does not fit the data with any consistency. An explanation of this phenomenon is that the assumptions inherent in equations 4.8 and 4.9 are not valid. The next step is to look in detail at the possible reactions and their product channels in the NO_3 build up and decay phases by means of a model-simulation.

Table 4.4 - Fit to different decay times of a typical run

Portion of curve used	Data type[a)]	$[NO_3]_o$ /molecule cm^{-3}	$k_{4.8}$ $/s^{-1}$	$k_{4.9}$ $/cm^3$ molecule^{-1} s^{-1}	No. of points used in fit
Full curve	SM	$4.12x10^{14}$	0.08	$9.8x10^{-16}$	59
d=0-10s	SM	$4.12x10^{14}$	0.08	$1.0x10^{-15}$	66
d=0-5s	SM	$4.12x10^{14}$	0.07	$1.0x10^{-15}$	40
d=0-2s	SM	$4.12x10^{14}$	0.32	$2.6x10^{-16}$	40
Full Curve	RW	$4.26x10^{14}$	0.07	$1.0x10^{-15}$	59
d=0-10s	RW	$4.26x10^{14}$	0.06	$1.1x10^{-15}$	66
d=0-5s	RW	$4.26x10^{14}$	0.03	$1.2x10^{-15}$	40
d=0-2s	RW	$4.26x10^{14}$	0.15	$8.7x10^{-16}$	40

[a)] SM - smoothed line through data points; RW - raw calibrated data (see §4.4.4)

4.6. Simulation and fitting of a photolysis build-up and decay; Mechanistic considerations

In this section, the chemistry occurring in the NO_3 build-up (§4.6.1-5) during photolysis and the decay period (§4.6.6) is considered in the light of a model-simulation of the chemistry. During the build-up phase the contribution of excited species to the observed chemistry is ignored, because of the likelihood of the rapid quenching of such species under typical experimental conditions (Pressure(Total) (P_T) ≈ 40 Torr $He/HNO_3/F_2$).

4.6.1 Kinetic modelling of the build-up/photolysis phase of the reaction

As stated previously in §4.4.2, the nitrate radical was produced by the reaction

$$F + HNO_3 \longrightarrow NO_3 + HF \qquad (4.5)$$

$k_{4.5} = (2.7\pm0.5)\times10^{-11}$ cm^3 $molecule^{-1}$ s^{-1} (Mellouki *et al.*, 1987)

In order to simulate the build-up in concentration of NO_3, the [F] and [HNO_3] must be determined. Typical initial concentrations before photolysis were 20 Torr of 5% F_2 in He, and 10 Torr of HNO_3, i.e. 3.2×10^{16} and 3.2×10^{17} molecule cm^{-3} respectively.

The frequency of the excimer laser operating at λ=308nm, given by $c = \nu\lambda$, is 9.73×10^{14} s^{-1}. As $E=h\nu$ the energy of one photon at this wavelength is 6.45×10^{-19} J, with an average laser pulse energy of 100mJ this leads to *ca.* 1.55×10^{17} photons per pulse. For photolysis at λ=308nm the absorption cross-section for fluorine ($\sigma(F_2)$) is 1.68×10^{-20} $molecule^{-1}$ cm^2. The base pathlength (l) for the cell was 1.82m. Thus, by application of the Beer-Lambert law using I_o as the number of photons per pulse makes $I = 1.53\times10^{17}$. Therefore the number of

$$\frac{I_0}{I} = \exp(\sigma(F_2)\ [F_2]\ l) \qquad (4.12)$$

photons absorbed (i.e. I_o - I) is $1.51x10^{15}$. Thus as photolysis of F_2 produces two F atoms the theoretical maximum concentration is $3.0x10^{15}$ molecule. The number of photons absorbed by F_2 per cm^3 is $3.0x10^{15}$/photolysis volume ($\approx$150cm^3). The [F] per pulse is therefore $1.1x10^{13}$ molecule cm^{-3}. This simple calculation, assumes homogeneous photolysis and that light is not being lost by reflection either on the cell windows or upon the dichroic mirrors. This result can then be used in a model to simulate the build-up of NO_3 as shown in Figure 4.8. The model simulation comprised of the reaction scheme shown in Table 4.5 and a variable for [F] per pulse according to the repetition rate of the laser. The simulation was produced using a numerical integration package [FACSIMILE (Curtis, 1979; Pilling and Smith, 1987)]. Any complex chemical reaction scheme consists of a number of elementary steps and the time dependencies of the component chemical species are described by ordinary differential equations of the type

$$\frac{dy_i}{dt} = f_i(y_1,y_2,.....,y_n) \qquad (4.13)$$

where y_i is the concentration of the ith species and the function f_i contains rate parameters which may not necessarily be linear in y_i. In FACSIMILE the coupled differential equations are numerically integrated by means of a Gear (1971) algorithm which is a hybrid explicit-implicit, so called predictor-corrector, method.

For simulation of the build-up phase of the photolysis cycle, all reactions among the set of species {F, FO, FO_2, NO, NO_2, NO_3, N_2O_5, O_2} were initially included in the model. Some reactions, especially amongst the F and FO_x family of reactions, were discarded on the basis

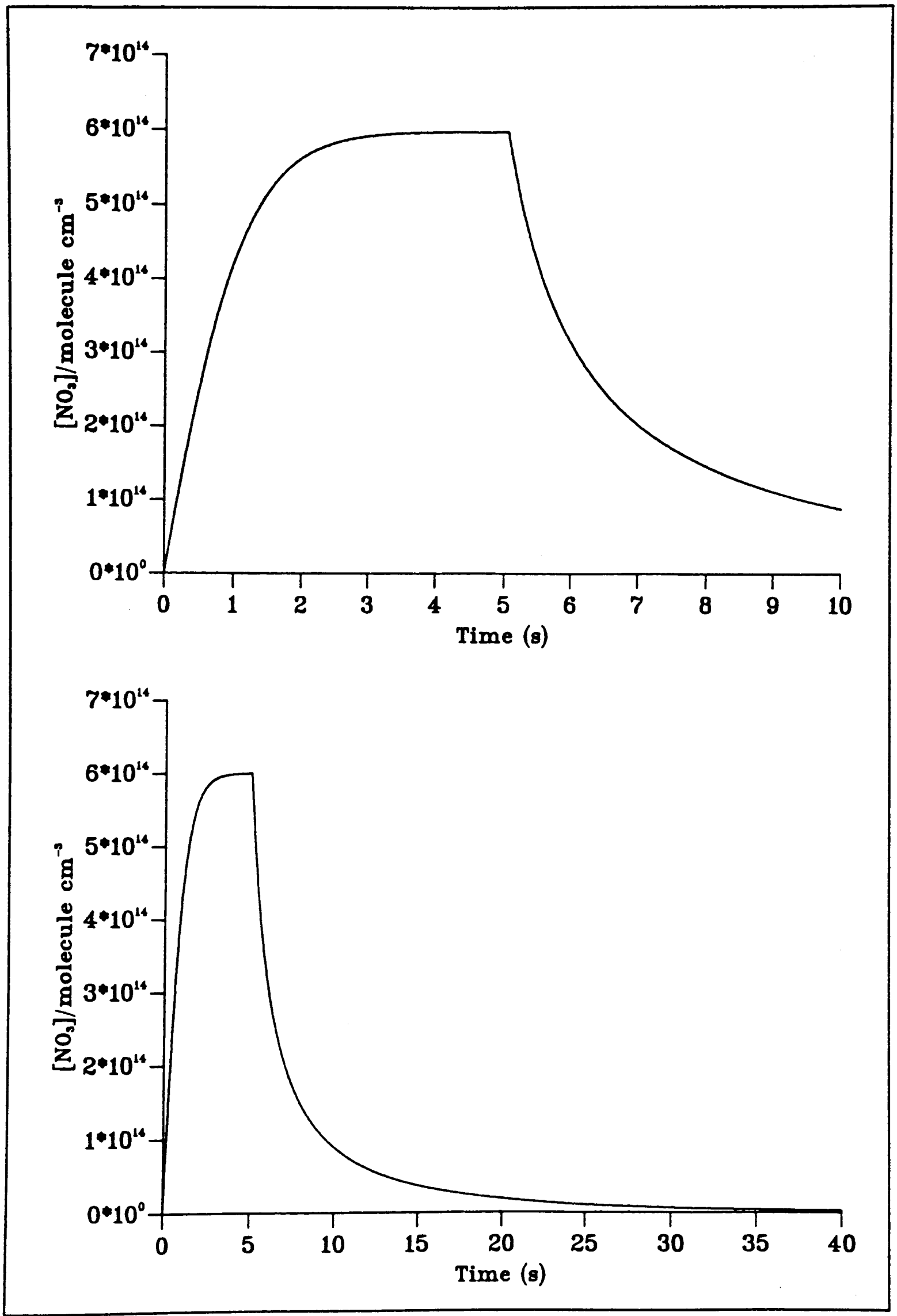

Figure 4.8 A simulated temporal profile of NO_3 concentration.

of being too slow to be important during this phase, or because they had no net effect on the production of NO_3; e.g. it was not necessary to include slow reactions of low concentration products of secondary reactions. A crude sensitivity analysis (Pilling and Smith, 1987) was also used to evaluate the contribution of individual reactions on the production of NO_3. This form of analysis involved varying either an input parameter (e.g. initial concentration of a reactant (or secondary product)) or a rate constant/product channel for an ill-characterised reaction, and following the effect to $[NO_3]$. The mechanism presented in Table 4.5 was also used to create time-concentration curves for species other than NO_3. The outcome of this approach is outlined in §4.6.2-4. The initial results from simulation of the profile for the NO_3 build-up phase bear a good resemblance to an experimentally obtained profile (*cf* Figure 4.6).

4.6.2 Possible production of NO_3 from photolysis of HNO_3

The primary process (Johnston *et al.*, 1974) for photolysis of HNO_3 in the wavelength region λ=200 to 300nm is

$$HNO_3 + h\nu \longrightarrow OH + NO_2 \qquad (4.6)$$

The quantum yield for production of NO_2 and OH being nearly unity . Hussain and Norrish (1963) showed that NO_3 was produced by the subsequent reaction of OH with HNO_3

$$OH + HNO_3 \longrightarrow H_2O + NO_3 \qquad (4.14)$$

The formation of NO_3 from this reaction was found (Poulet *et al.*, 1981) to be both fast and efficient, the hydrogen abstraction process being exothermic by 81kJ mol^{-1}. The OH produced in reaction 4.6 can also react with NO_3

$$OH + NO_3 \longrightarrow NO_2 + HO_2 \qquad (4.15)$$

$k_{4.15} = (2.0\pm0.6)\times10^{-11}$ cm^3 $molecule^{-1}$ s^{-1} (Boodaghians *et al.*, 1988)

Table 4.5 - **The reactions used to simulate the flash photolysis build-up and decay profile of NO_3**

Reaction	k /cm^3 $molecule^{-1}$ s^{-1}	Reaction No.	Ref. (see below)
$F + HNO_3 \rightarrow HF + NO_3$	$2.7x10^{-11}$	4.5	1
$NO_3 + F \rightarrow NO_2 + FO_2$	$3.0x10^{-11}$	4.16	2
$FO + NO_3 \rightarrow NO_2 + FO_2$	$1.0x10^{-12}$	4.17	2
$NO_3 + NO_2 + M \rightleftharpoons N_2O_5 + M$	$5.9x10^{-13}$ a)	4.19a	3
$N_2O_5 + M \rightleftharpoons NO_3 + NO_2 + M$	$8.3x10^{-3}$ b)	-4.19a	4
$F + NO_2 + M \rightarrow FONO + M$	$1.1x10^{-12}$ c)	-	5
$FO + FO \rightarrow F + F + O_2$	$1.5x10^{-11}$	-	6
$FO + NO_2 + M \rightarrow FONO_2 + M$	$2.8x10^{-13}$ c)	-	6
$NO_3 + NO_3 \rightarrow NO_2 + NO_2 + O_2$	$2.3x10^{-16}$	-	7
$NO_3 \rightarrow$ (Wall)	0.08 d)	4.8	7
$NO_3 + NO_2 \rightarrow NO + NO_2 + O_2$	$9.1x10^{-16}$	4.19b	6
$NO_3 + NO \rightarrow NO_2 + NO_2$	$3.0x10^{-11}$	4.26	4
$NO + FO \rightarrow F + NO_2$	$2.6x10^{-11}$	-	8
$F + O_2 \rightarrow FO_2$	$1.6x10^{-16}$	-	6

a) Calculated at P = 40 Torr using the Troe expression and the parameters as quoted in Wayne *et al.* (1991); b) units are s^{-1}; c) Calculated at P = 40 Torr using the Troe expression and parameters as quoted in DeMore *et al.* (1990); d) units are s^{-1}

1. Mellouki *et al.*, 1989; 2. Rahman *et al.*, 1988; 3. Smith *et al.*, 1985; 4. Wayne *et al.*, 1991; 5. Fasano *et al.*, 1983; 6. DeMore *et al.*, 1990; 7. This work; 8. Ray *et al.*, 1981

The HO_2 produced as a secondary product can go on to react with NO_3. The NO_2 produced both in reactions (4.16) and (4.15) will also deplete NO_3 *via* reaction (4.19a). Figure 4.9 shows an experimentally obtained trace following the $[NO_3]$ from photolysis of 13.8 Torr ($4.5x10^{17}$ molecule cm^{-3}) of HNO_3. This trace appears to be quite noisy, with spikes of NO_3 at regular intervals, the peak concentration of NO_3 was *ca.* $1.0x10^{14}$ molecule cm^{-3}. In order to verify that this behaviour was real and not an artefact, a similar simulation to that laid out in §4.6.1 was carried out, following both [OH] and $[NO_3]$. In this calculation, the new assessment of the absolute absorption cross-section of HNO_3 (Ratigan, 1991) in the long wavelength tail ($\lambda > 300$ nm) was used at λ=308 nm. This value is higher at $1.0x10^{-19}$ molecule^{-1} cm^2 than the previously recommended one of $1.0x10^{-21}$ molecule^{-1} cm^2(Okabe, 1987). The result of this calculation is shown in Figure 4.10. A further modification to this mechanism in order to simulate the 'slow' ($t \approx 10s$) build-up in $[NO_3]$ is to consider the possible contribution of the photolysis of NO_2 in this wavelength region.

$$NO_2 + h\nu \longrightarrow NO + O \qquad (4.15a)$$

The NO_2 absorption cross-section at λ=308nm is $18.67x10^{-20}$ molecule^{-1} cm^2, the quantum yield for the product channel ($\Phi_{4.15a}$) being 0.996 (DeMore *et al.*, 1990). The simulation using a fractional channel for NO_2 photolysis leads to an experimental-like build-up. Though the simulated data do not exactly correspond to the experimental data, the simulation showed that within the time-response of our detection system, the spikes in $[NO_3]$ are not an artefact. Since at λ=308 nm, HNO_3 has a photolysis cross-section of $1.0x10^{-19}$ molecule^{-1} cm^2, it could be a possible additional source of NO_3 in our experiments contributing < 5% of the $[NO_3]$ detected in the build-up phase.

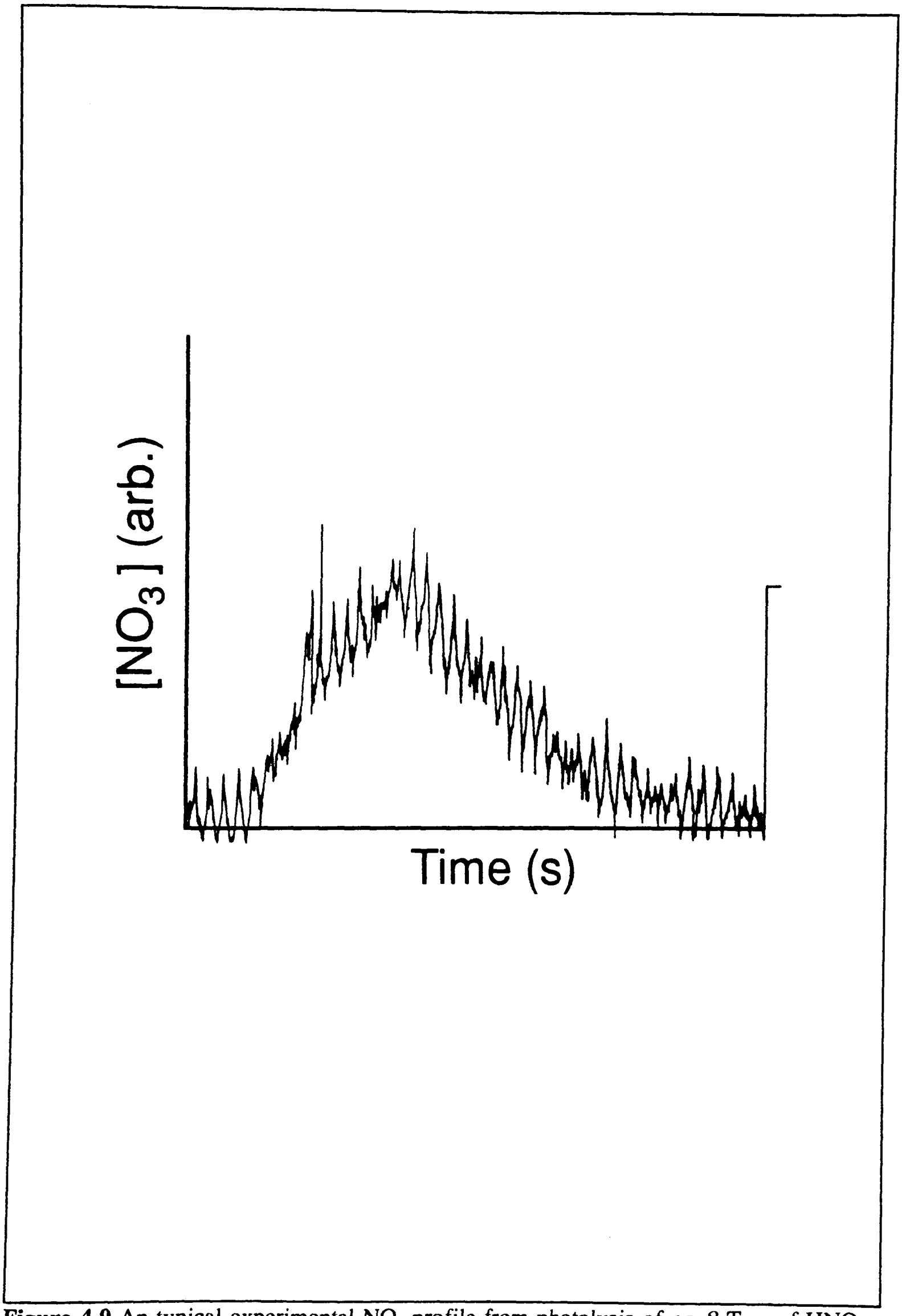

Figure 4.9 An typical experimental NO_3 profile from photolysis of *ca.* 8 Torr of HNO_3.

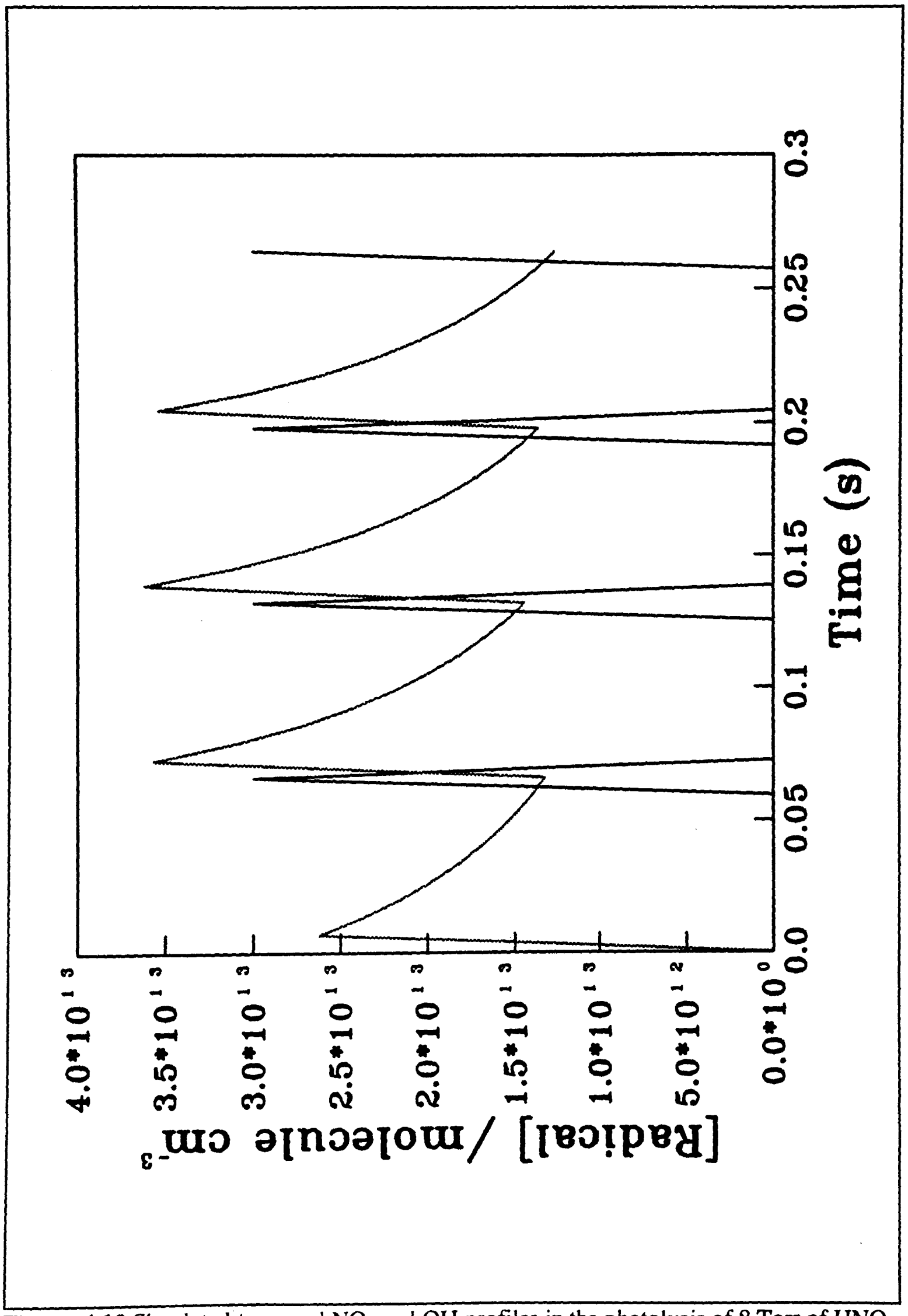

Figure 4.10 Simulated temporal NO_3 and OH profiles in the photolysis of 8 Torr of HNO_3. The OH is represented as — and the NO_3 as ▨.

4.6.3 Products of the reaction NO_3 + F; FO_x chemistry

When considering the production of NO_3 by the reaction of F atoms with nitric acid, careful consideration was given to the role of FO_x chemistry. It is clear that F atoms can also react with the NO_3

$$F + NO_3 \longrightarrow FO + NO_2 \qquad (4.16)$$

$k_{4.16} = 3.0\times10^{-11}$ cm^3 molecule^{-1} s^{-1} (Rahman *et al.*, 1988)

and that secondary reactions involving FO and NO_3 such as

$$FO + NO_3 \longrightarrow FO_2 + NO_2 \qquad (4.17)$$

$k_{4.17} = 1.0\times10^{-12}$ cm^3 molecule^{-1} s^{-1} (Rahman *et al.*, 1988)

$$FO + FO \longrightarrow F + F + O_2 \qquad (4.18)$$

$k_{4.18} = 1.5\times10^{-11}$ cm^3 molecule^{-1} s^{-1} (De More *et al.*, 1991)

can occur, leading to a complex interplay between reactants produced by secondary chemistry and NO_3. The NO_2 produced in reactions (4.16) and (4.17) can go on to react with the NO_3 in the reaction

$$NO_2 + NO_3 + M \rightleftharpoons N_2O_5 + M \qquad (4.19a)$$

This reaction is pressure dependent and the rate constant was evaluated using the Troe expression and the parameters quoted in Wayne *et al.* (1991) at a total pressure of 40 Torr. Because [HNO_3] were typically large (*ca.* 1×10^{17} molecule cm^{-3}), and HNO_3 is a very efficient 3rd body, reaction (4.19a) is likely to be at the high pressure limit of 1.5×10^{-12} cm^3 molecule^{-1} s^{-1}.

The FO produced as a result of reaction (4.16) is partitioned between two reactions (4.17 and 4.18). The products of the FO self-reaction have been determined by Wagner *et al.* (1972)

to be F atoms and oxygen. Thus, FO formed *via* reaction (4.16) re-cycles back to F atoms and catalytically destroys NO_3, while FO_2 produced in reaction (4.17) acts as an effective reservoir species, taking no further part in the reaction scheme (see Table 4.5). Rahman *et al.* (1988) followed the production of FO in this type of chemical system in a discharge-flow system coupled to mass spectrometric detection at m/e=35 and ascribed its presence to being the product of reaction 4.16. It was also found experimentally that the reactions

$$F_2 + NO_3 \longrightarrow \text{Products} \qquad (4.20)$$

$$F_2 + FO \longrightarrow \text{Products} \qquad (4.21)$$

as well as the analogous one for HNO_3 could be ignored as possible loss processes for these reactants. However, there was still a need for a further, still undefined loss mechanism with a rate constant of $k \sim 1 \times 10^{-12}$ cm^3 molecule^{-1} s^{-1} in order to describe the observed [FO]. This reaction was postulated to be the heterogenous reaction

$$FO + \text{Wall} \longrightarrow \text{Products} \qquad (4.22)$$

Under the conditions of flash photolysis (See §4.3) heterogenous reactions are not usually of any importance. Rahman *et al.* (1988) also noted that for initial conditions where [HNO_3] >> [F], such that reaction 4.6 would be expected to predominate, FO was still detectable. Another possible source of FO, the O-abstraction from HNO_3 by F-atoms, is thought to be unlikely on thermodynamic grounds.

Initially, for the simulations, the products of reaction (4.16) were set to FO + NO_2, but the extra F atoms produced by the cycling of FO through its self-reaction produced the simulated NO_3 build-up curves shown in figures 4.11 and 4.12. This simulated build-up is 'slow' in comparison with the experimentally obtained profiles and, given the calculated concentration of F-atoms per flash, which at best due to the inherent assumptions could be presumed to be

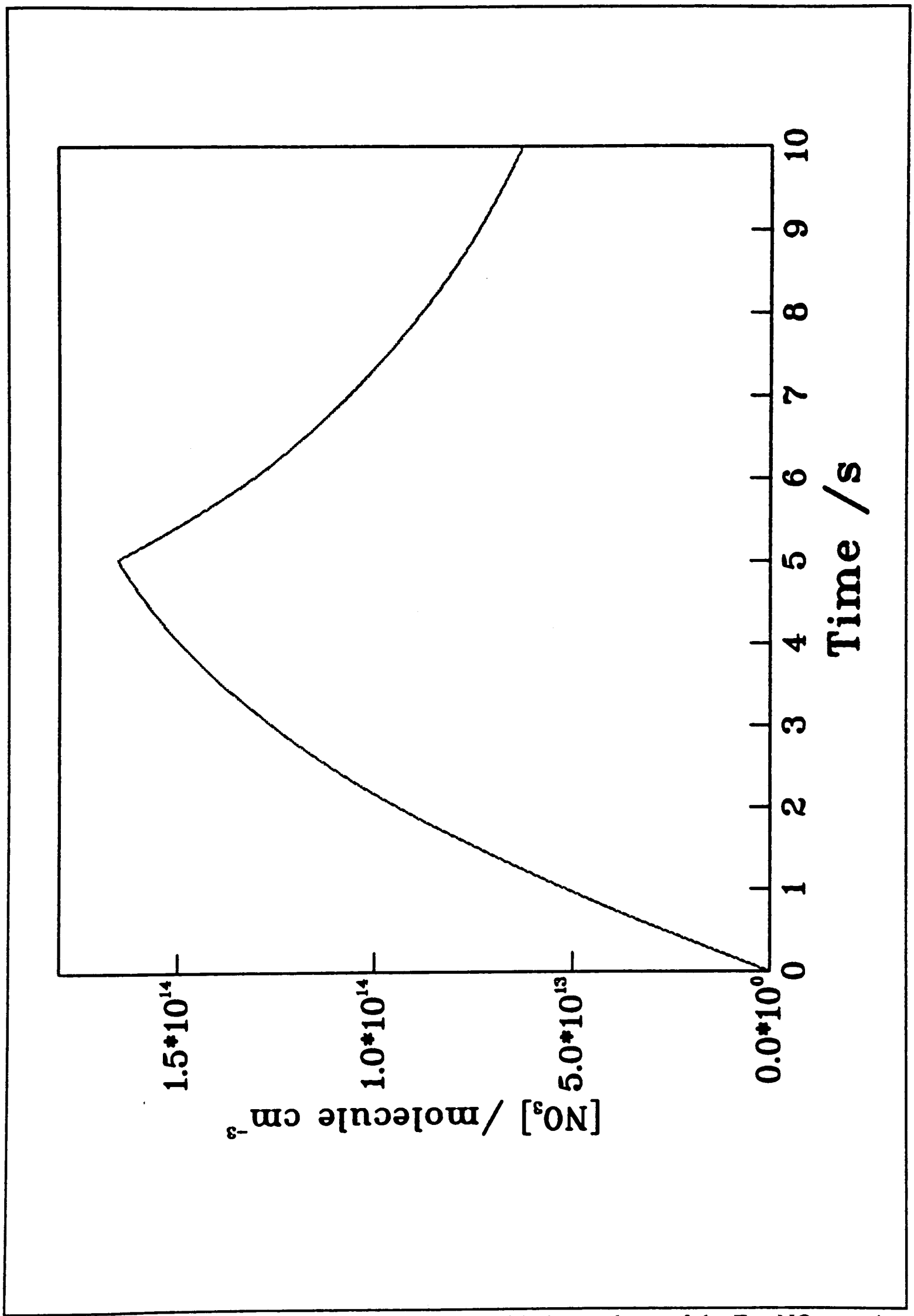

Figure 4.11 Simulated temporal profile of NO_3 with the products of the F + NO_3 reaction set to FO and NO_2 (see text).

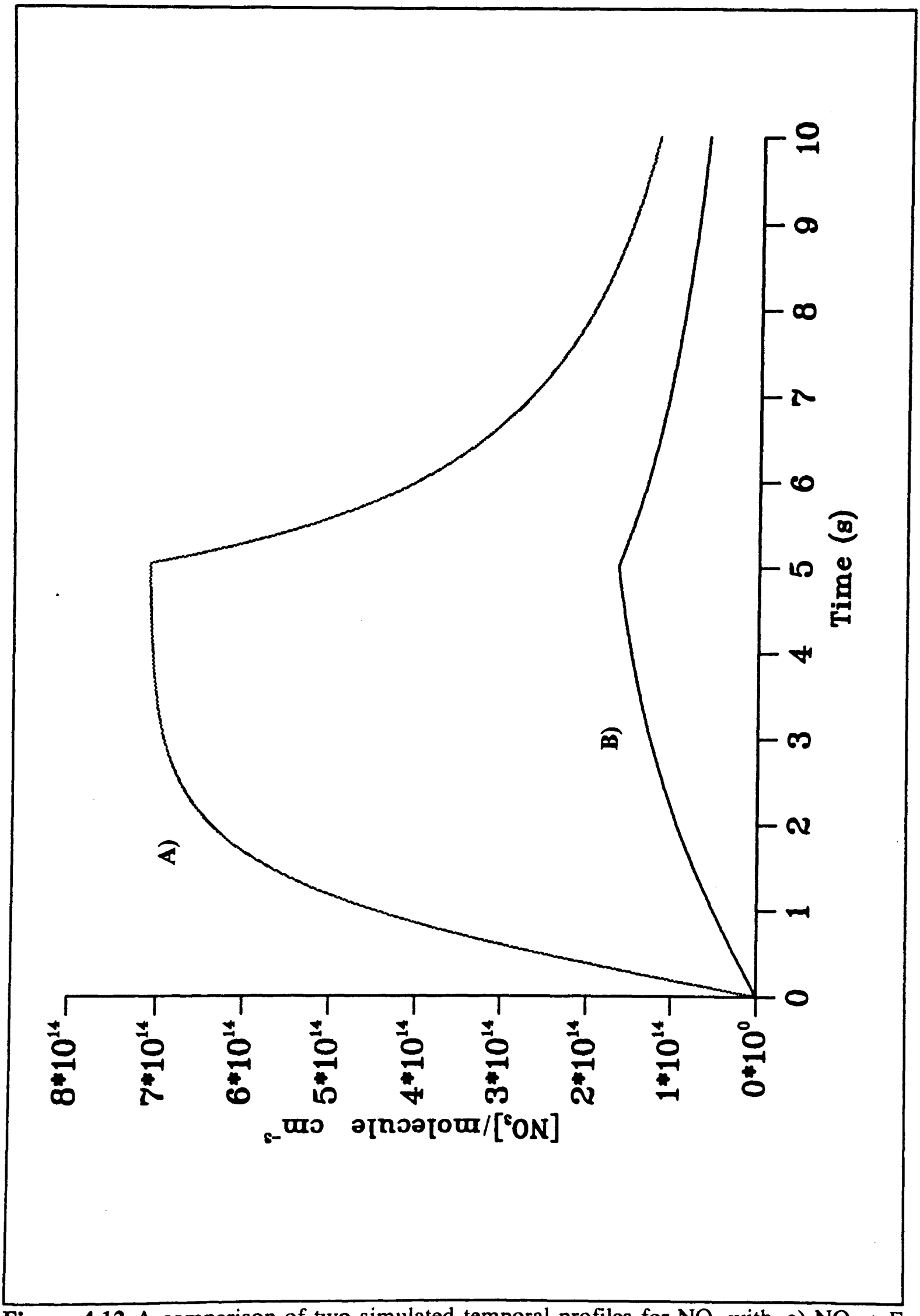

Figure 4.12 A comparison of two simulated temporal profiles for NO_3 with, a) $NO_3 + F \rightarrow FO + NO_2$ and b) $NO_3 + F \rightarrow NO_2 + Products$.

the expected maximum, gives a modulated steady-state concentration of NO_3 of the order of $1.5x10^{14}$ molecule cm^{-3}. When the product channel was altered to

$$NO_3 + F \longrightarrow \text{Products} \qquad (4.23)$$

the absence of NO_2 as a product had little effect on the NO_3 build-up characteristic too. If the products were changed to

$$2\ NO_3 + F \longrightarrow 2\ NO_2 + FO_2 \qquad (4.24)$$

such that FO_2, the effective reservoir species, was a product, an experimental-like profile (See Figures 4.6 and 4.8) was produced from the simulation. If large $[F_2]$ in He were used in a mixture, the build-up in signal on photolysis was followed by a rapid decay, as shown in Figure 4.13. This enhanced rate of loss of NO_3 can be explained by the pre-dominance of the secondary reaction between NO_3 and F.

The sensitivity of the shape of the simulated NO_3 build-profile to FO_x chemistry merits further direct experimentation. In order to simulate a NO_3 build-up similar to an experimentally obtained profile the products of the NO_3 + F reaction had to be set to NO_2 + FO_2, such that all FO secondary chemistry was excluded from the model. Typically simulated concentration of FO_2 in the modulated steady-state was $1.3x10^{12}$ molecule cm^{-3}

4.6.4 The effect of $[NO_2]_o$ on the NO_3 build-up profile

The chemistry of the NO_3 radical is very closely linked with that of the rest of the nitrogen oxides, in particular NO_2 and N_2O_5. Dinitrogen pentoxide is formed when NO_3 is created in the presence of NO_2, and thermally decomposes back to the starting molecules, so that the equilibrium

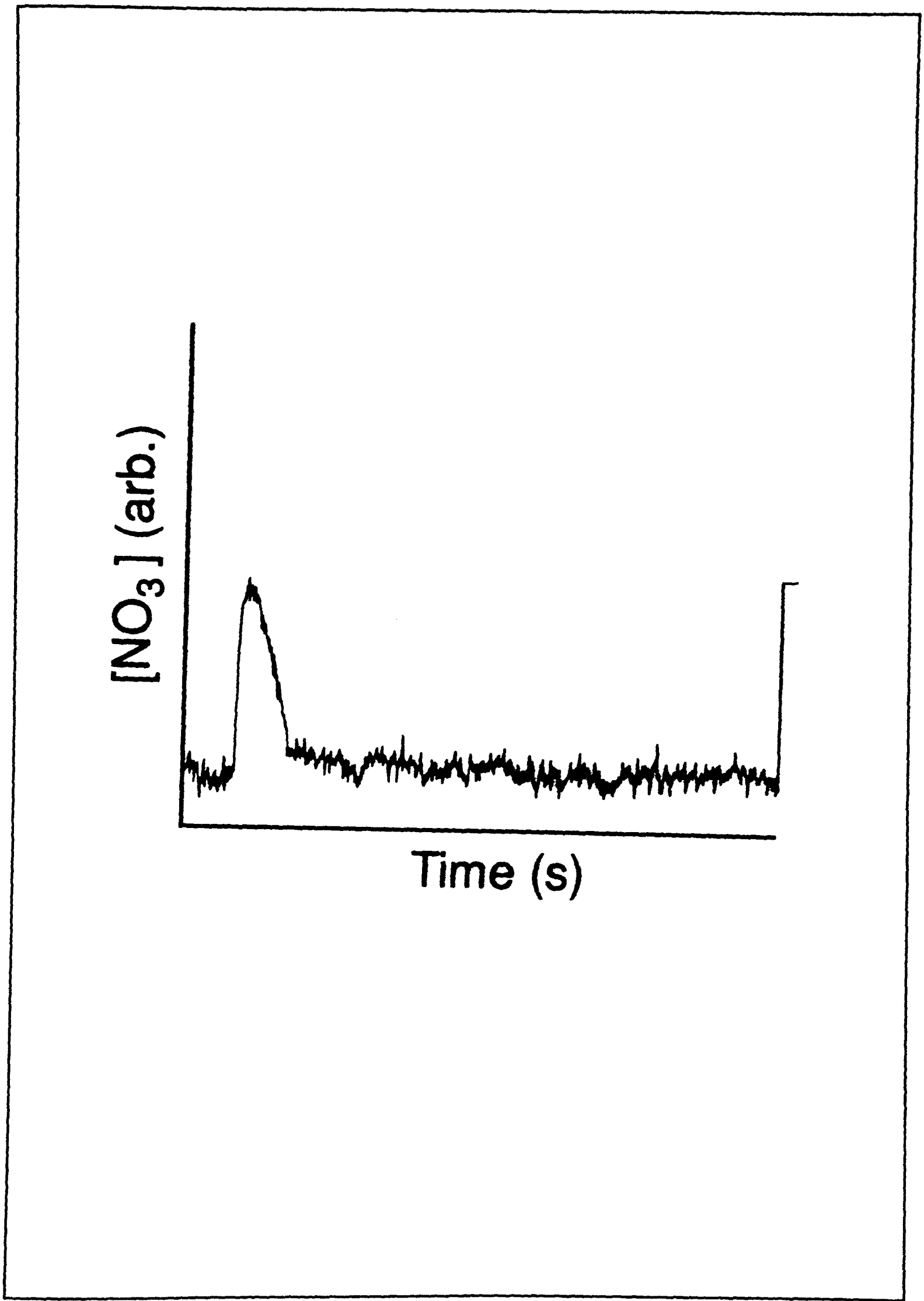

Figure 4.13 A typical experimental temporal profile for NO_3 in presence of *ca.* 70 Torr of F_2.

$$NO_3 + NO_2 + M \rightleftharpoons N_2O_5 + M \qquad (4.19a)$$

is established. One of the problems associated with the use of HNO_3 as a precursor for NO_3 production has been the presence of NO_2 as an impurity (see §5.4). There is a second slower channel for reaction 4.19 which is discussed in §4.6.6. A noticeable feature of an experimental NO_3 build-up profile is the presence of an apparently short ($t < 0.3$ s) induction period at the start of photolysis before the rapid ($t \approx 3$ s) build-up to the plateau region of the modulated steady-state. Figure 4.14 shows the difference in the shape of the simulated NO_3 build-up profiles with and without an initial starting concentration of NO_2 ($[NO_2]_o = 1.0 \times 10^{14}$ molecule cm^{-3}). This represents about a 100mTorr impurity of NO_2 present before photolysis. The influence of $[NO_2]_o$ was used as a variable dependent which was dependent on the magnitude of this induction period. Resultant concentrations from the simulation of NO_2 in the modulated steady-state were typically about 3.5×10^{11} molecule cm^{-3}. This inference about the presence and effect of NO_2 in the reaction system has implications for the kinetic analysis of the post photolysis period as will be discussed in §4.6.6.

4.6.5 The modulated steady-state

The final stage of the build-up phase is the plateau region where $[NO_3]$ is nearly constant. In this Chapter, this plateau region in $[NO_3]$ has been described as a modulated steady-state. The photochemistry in this plateau region being modulated by the incident laser light (see §4.4.2). A plot of laser repetition rate *vs.* $[NO_3]$ in the modulated steady state for mixtures consisting of 8.8 Torr HNO_3 and 31.0 Torr of 5% F_2 in He is shown in Figure 4.15. The maximum $[NO_3]$ was produced at a repetition rate of 50 Hz and took a value of 5.0×10^{14} molecule cm^{-3}. There is a linear relationship between $[NO_3]$ and laser repetition rate of

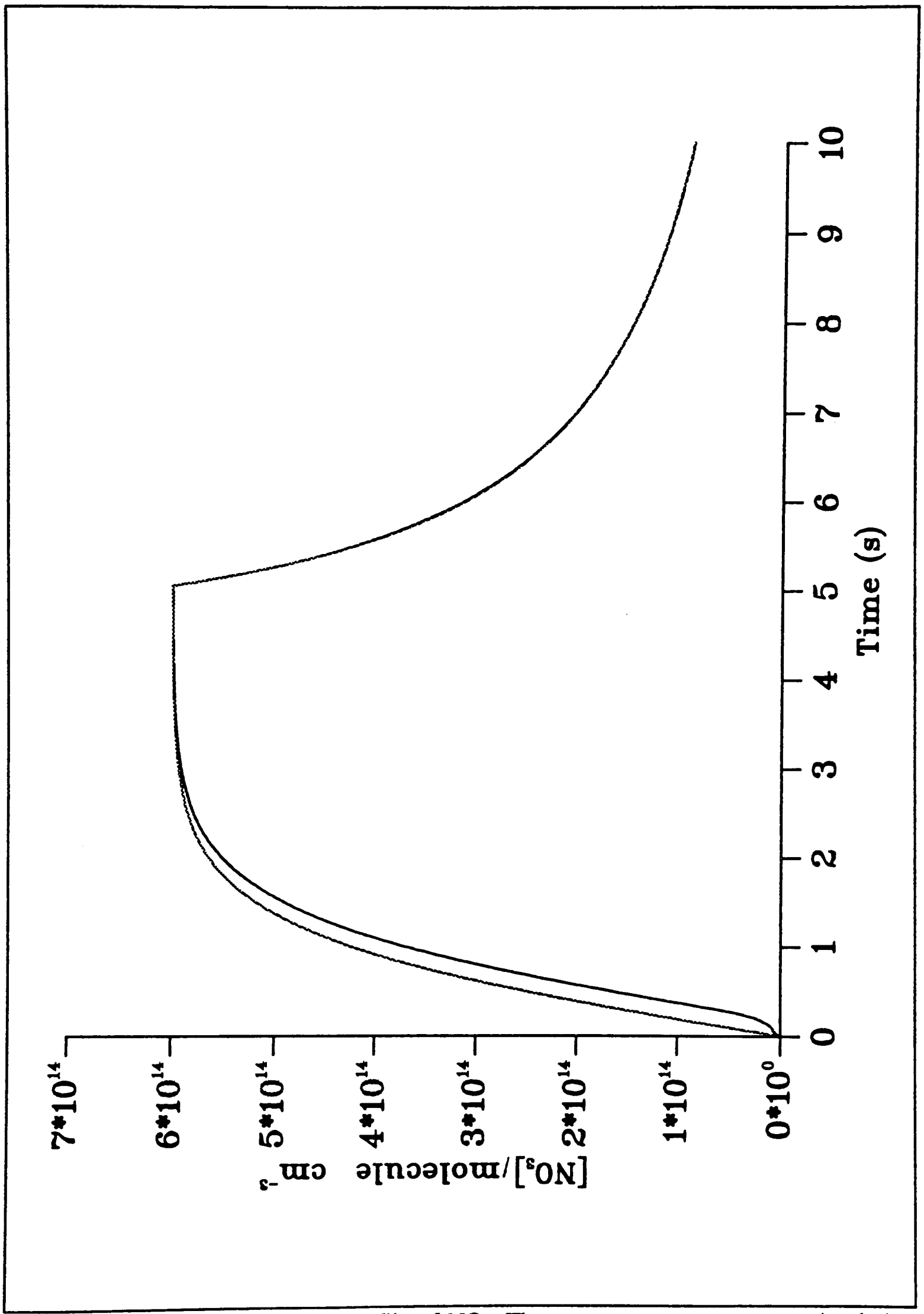

Figure 4.14 Simulated temporal profile of NO_3; The upper curve represents a simulation with the $[NO_2]_0$=1.0x10^{14} molecule cm^{-3} and the lower curve with $[NO_2]_0$=0 molecule cm^{-3}.

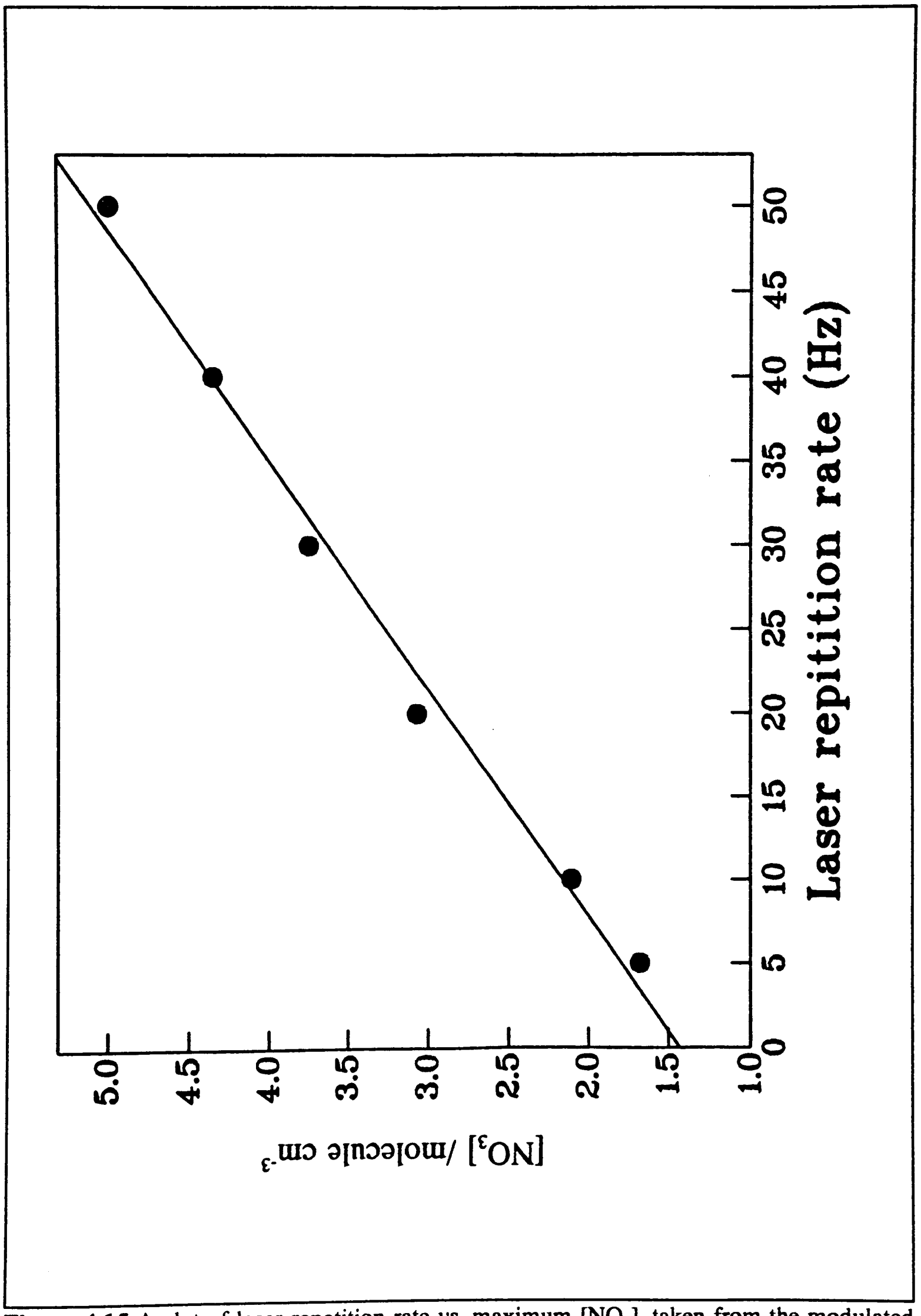

Figure 4.15 A plot of laser repetition rate *vs.* maximum $[NO_3]$, taken from the modulated steady-state.

$$[NO_3]\ /molecule\ cm^{-3} = 7.3\times10^{12} * Laser\ rep.\ rate\ /Hz + 1.4\times10^{14} \quad (4.25)$$

The parameters of this equation are dependent on $[F_2]/[HNO_3]$ and the values given here are only valid for a ratio of (0.17±0.1). Experiments were conducted in which the photolysis was continued for a period of up to 20 s after reaching the plateau region in $[NO_3]$ (See Figure 4.16a). The observed dependence of the NO_3 modulated steady state to varying ratios of $[F_2]/[HNO_3]$ could be reproduced using the model (as shown in Table 4.5), the average $[NO_3]$ in this region being dependent on the [F] per flash (see Figure 4.16a,b). The simulation was conducted with a laser repetition rate of 50 Hz for an extended photolysis period (τ_p) of up to 6 s. The model simulates quite well the characteristics of the modulated steady state under the conditions of extended photolysis.

4.6.6 Products of the NO_3 + NO_3 reaction

Under the conditions of the simulation, [F] fell to zero within 1 ms at the end of the photolysis period, allowing the active F-based chemistry to be ignored. The chemistry occurring in this decay period can be said to be only the active nitrogen chemistry, namely

$$NO_3 + NO_3 \longrightarrow \text{Products} \quad (4.9)$$

$$NO_3 \longrightarrow \text{Wall} \quad (4.8)$$

$$NO_3 + NO_2 + M \rightleftharpoons N_2O_5 + M \quad (4.19a)$$

$$NO_3 + NO_2 \longrightarrow NO + NO_2 + O_2 \quad (4.19b)$$

$k_{4.19b} = 9.1\times10^{-16}$ cm^3 molecule^{-1} s^{-1} (DeMore *et al.*, 1990)

$$NO + NO_3 \longrightarrow NO_2 + NO_2 \quad (4.26)$$

$k_{4.26} = 3.0\times10^{-11}$ cm^3 molecules^{-1} s^{-1} (Wayne *et al.*, 1991)

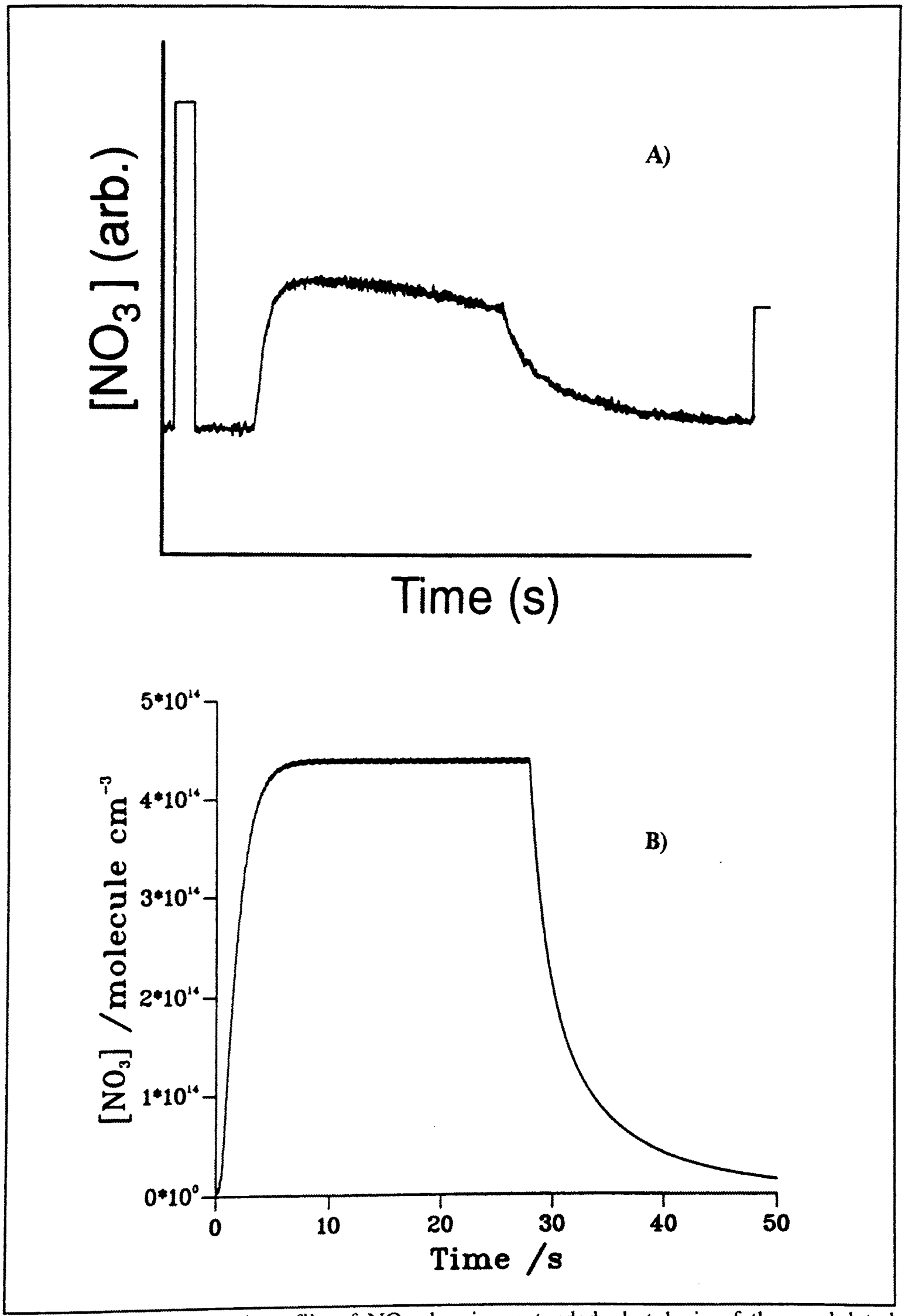

Figure 4.16 A temporal profile of NO_3 showing extended photolysis of the modulated steady-state; a) - experimental and b) - simulated profiles.

There is no direct experimental evidence for the products of the NO_3 self-reaction (4.9) (Wayne *et al.*, 1991). Table 4.6 shows the heats of reaction ($\Delta H_{r,298}$) for several possible product channels. The heats of formation for all the species except NO_3 were taken from Atkinson *et al.* (1989). The heat of formation of NO_3, $\Delta H_{f,298}(NO_3)$ = (64.4±3.1) kJ mol^{-1} was taken as the suggested value from Wayne *et al.* (1991). The heat of formation for N_2O_6 is unknown to date. As routes 4.27b and 4.27d are endothermic they are unlikely to occur at room temperature. The most exothermic route (4.27f) is unlikely to occur because of the number of bonds that have to be formed and broken. If N_2O_4 was produced *via* route 4.27e it would be in a dynamic equilibrium with NO_2 (4.28, -4.28)

$$NO_2 + NO_2 + M \rightleftharpoons N_2O_4 + M \qquad (4.28,\text{-}4.28)$$

This reaction has been extensively studied since 1922 (Bodenstein, 1922). Recent work on the pressure and temperature dependence of this reaction with various bath gases (Brunning *et al.*, 1988; Borrell *et al.*, 1988) indicates that at pressures of less than 760 Torr of

Table 4.6 - Thermochemistry of the possible product channels

Reaction	Products	Reaction No. (4.27)	ΔH_r (kJ mol^{-1})
$NO_3 + NO_3$	$\longrightarrow NO_2 + NO_2 + O_2$	a	-62.8
	$\longrightarrow NO + NO + 2O_2$	b	51.6
	$\longrightarrow N_2O_6$	c	?
	$\longrightarrow N_2O_5 + O$	d	131.7
	$\longrightarrow N_2O_4 + O_2$	e	-119.6
	$\longrightarrow N_2 + 3O_2$	f	-128.8

bath gas (M) reaction (4.28) is at the low pressure limit (k^o) given by

$$k^o_{-4.28} = 1.29\times10^{-5}\left(\frac{T}{300K}\right)^{-3.8} \exp\left(\frac{-6460K}{T}\right) [M]\ s^{-1} \qquad (4.29)$$

(Borrell *et al.*, 1988)

Using this expression and correcting for M=He gives a value for $k^o_{-4.28}$ of *ca.* 5700 s^{-1} at T=300K and [He]=1.0×10^{18} molecule cm^{-3}. While for the corresponding association reaction, using the expression

$$k^o_{4.28} = 1.40\times10^{-33}\left(\frac{T}{300K}\right)^{-3.8} [M]\ cm^3\ molecule^{-1}\ s^{-1} \qquad (4.30)$$

(Borrell *et al.*, 1988)

gives a value for $k^o_{4.28}$ of 1.4×10^{-15} cm^3 $molecule^{-1}$ s^{-1} at T=300 K and [He]=1.0×10^{18} molecule cm^{-3}. Both the expressions (4.29 and 4.30) for the low pressure limit of reaction 4.28 were evaluated using Troe-like analysis (Borrell *et al.*, 1988). These results infer that if N_2O_4 is produced *via* pathway (4.27e), it would rapidly dissociate to NO_2. Thus, if the reaction goes *via* either pathway (4.27a) or (4.27e), the product will be NO_2.

In section §4.6.4, we discussed the influence of NO_2 on the NO_3 build-up profile. It was noted, that small $[NO_2]_0$ were needed to model the small induction period at the start of the NO_3 build-up profile. The inference that NO_2 is still present at the beginning of the decay period is now looked at in terms of how it will affect $[NO_3]$ in the post photolysis period.

The simulation of $[NO_2]$ *vs.* time, assuming that the sole source of NO_2 in the system is a product from the self-reaction of NO_3 (i.e. $[NO_2]_{t=0} = 0$) is shown in Figure 4.17. The consequence of this assumption on the NO_3 decay profile is illustrated in Figure 4.18. These

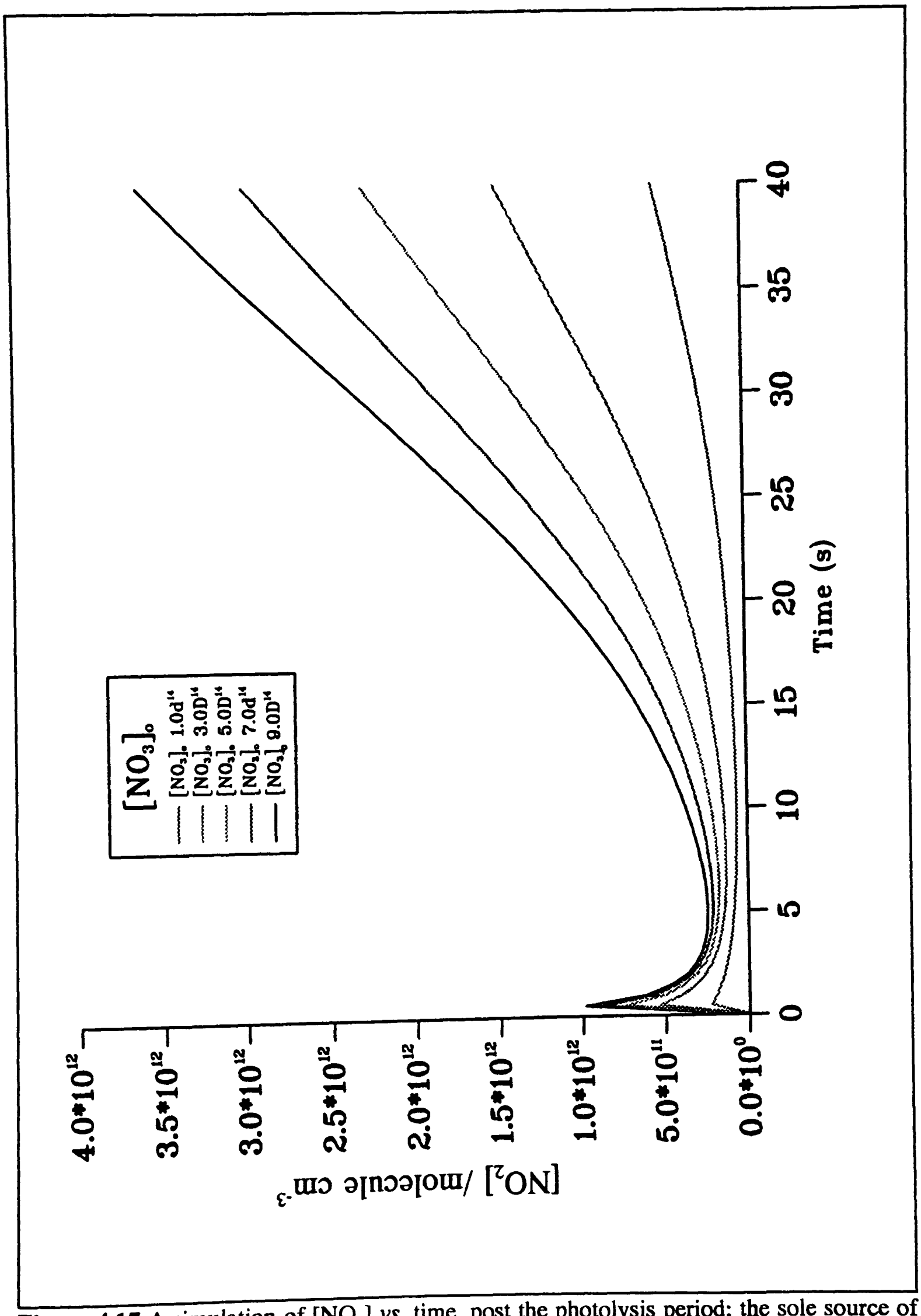

Figure 4.17 A simulation of $[NO_2]$ *vs.* time, post the photolysis period; the sole source of NO_2 in the simulation is as a product of the NO_3 + NO_3 self-reaction (see text).

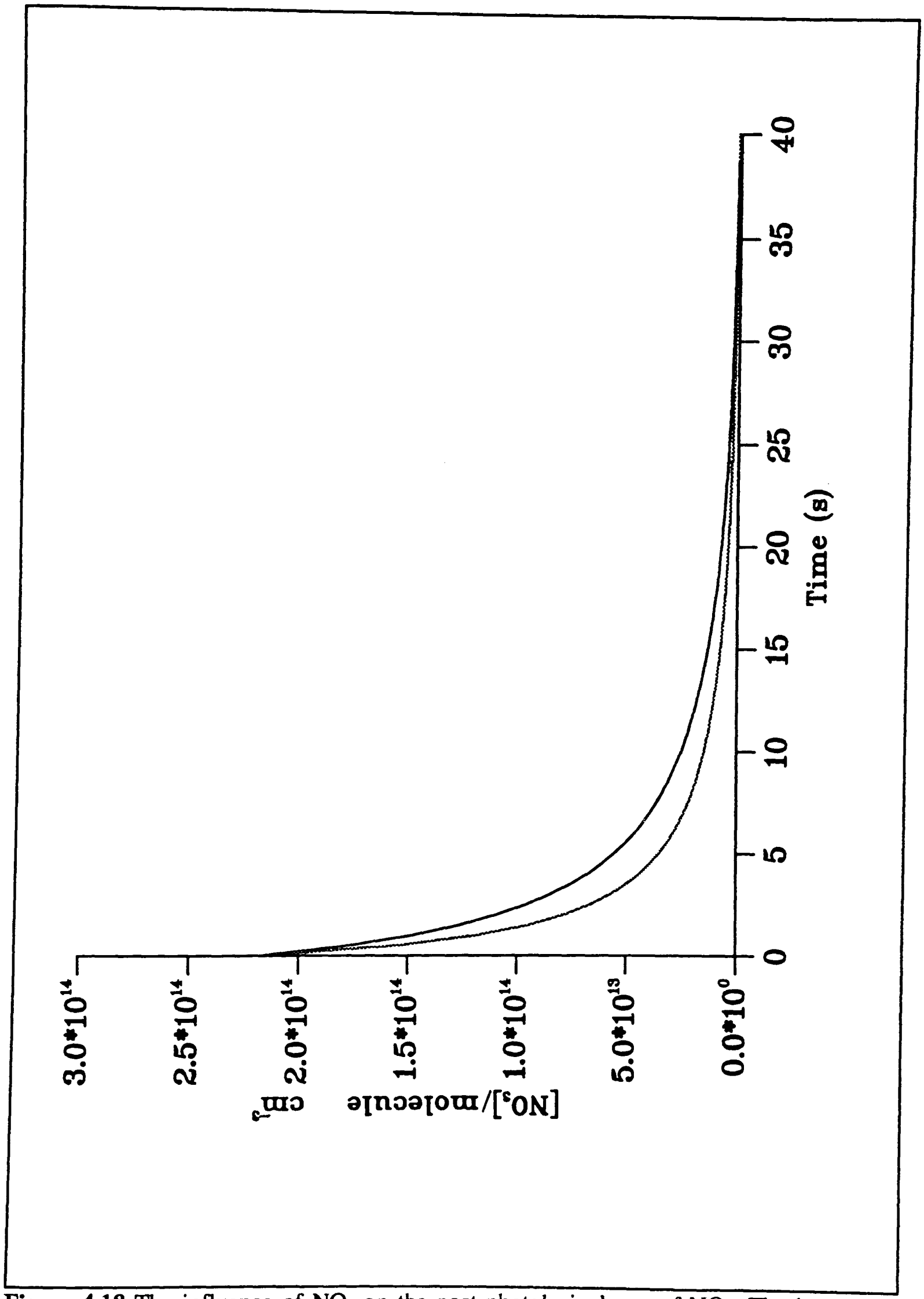

Figure 4.18 The influence of NO_2 on the post-photolysis decay of NO_3. The lower line represents a simulation with $[NO_2]_0=1.0\times10^{14}$, the upper $[NO_2]_0=0$ molecule cm^{-3}.

simulations were repeated for various $[NO_3]_0$, and the effect on both $[NO_2]$ and $[NO_3]$ was followed. Figure 4.17 has three marked regions of behaviour in $[NO_2]$. The first (t < 1 s) is a rapid build-up, the maximum concentration of NO_2 being dependent on $[NO_3]_0$. The second is a slow decay in $[NO_2]$ over the time period t = *ca.* 1-15 s, where $[NO_3]$ is still high such that the bimolecular reaction 4.19a is the dominant process. After this period the reverse reaction (-4.19a) the unimolecular decomposition of N_2O_5, becomes the dominant process. Recent results on this chemical system (Boyd, 1991) suggest that the heavily temperature dependent nature of the equilibrium constant,

$$K_{eq}^{4.19}(T) = 6.84\times10^{-27}\exp(\frac{10815}{T})\ cm^3\ molecule^{-1} \qquad (4.31)$$

(Cantrell *et al.*, 1988)

must be taken into account in the modelling of such systems. The second channel for the $NO_2 + NO_3$ reaction, 4.19b, also produces NO_2 on this timescale, but again will have a dependence on $[NO_3]$.

Thus, for simulation of the decay period $[NO_2]_o$ was used as a variable, the NO_2 being partitioned into reactions 4.19a,b. It was found that, for an accurate simulation of the decay period, there was no need for the addition of extra $[NO_2]$ at the end of the photolysis period.

4.6.7 The outcome

The result of fitting a model-simulation to an experimentally obtained profile is shown in Figure 4.19. The parameters, [F] per pulse and $[NO_2]_o$ were set to $6.0\text{x}10^{12}$ and $1.0\text{x}10^{14}$ molecule cm^{-3} respectively. Rate constants for reaction (4.8) of 0.08 s^{-1} and reaction (4.9),

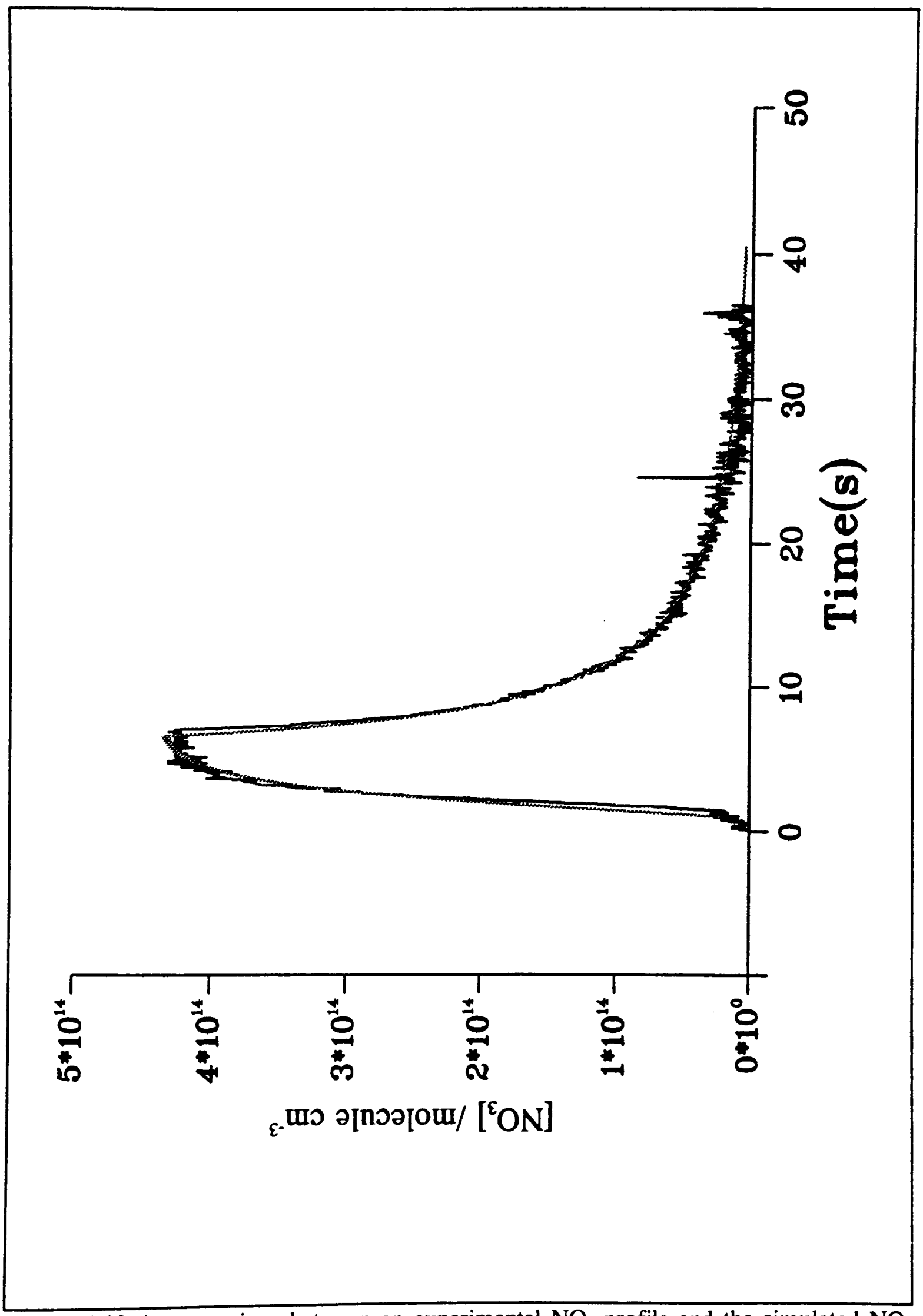

Figure 4.19 A comparison between an experimental NO_3 profile and the simulated NO_3 profile (see text).

the self-reaction, of $2.3x10^{-16}$ cm^3 $molecule^{-1}$ s^{-1} were used. The overall fit obtained is remarkably good given the complexity of the system and the number of parameters used to fit it. The information gained by the procedure outlined §4.6.1-4.6.6 can now be used to develop a kinetic model for quantitative fitting of a $[NO_3]$ decay curve.

4.7 Development of a kinetic model, for quantitative fitting of the NO_3 decays

A series of models were developed for the kinetic fitting of the post-photolysis $[NO_3]$, the so-called NO_3 decays. The methodology used in this development stage in order to verify the fitting procedures was to first produce a test data set with pre-determined rate parameters for a reaction scheme. This was done by numerical integration of the differential equations which represented the reaction scheme, the resultant test data set consisted of time *vs.* $[NO_3]$. The next step was to use these test data as an input to the fitting procedure (§4.7.1) and attempt to recover the pre-determined rate parameters. Some test data sets had artificial noise added to them in order to simulate the characteristics of experimental-like data. Figure 4.20 shows the time *vs.* $[NO_3]$ profile for a set of test data produced with only the reactions $k_{4.8}(NO_3 \rightarrow) = 0.1\ s^{-1}$ and $k_{4.9}(NO_3 + NO_3 \rightarrow) = 2.3x10^{-16}\ cm^3\ molecule^{-1}\ s^{-1}$. This figure also illustrates the relative contributions to the overall decay of the first-order component (reaction 4.8) and the second-order component (reaction 4.9).

4.7.1 Fitting procedures

A fitting procedure, more correctly a parameter (P) fitting procedure, compares experimental

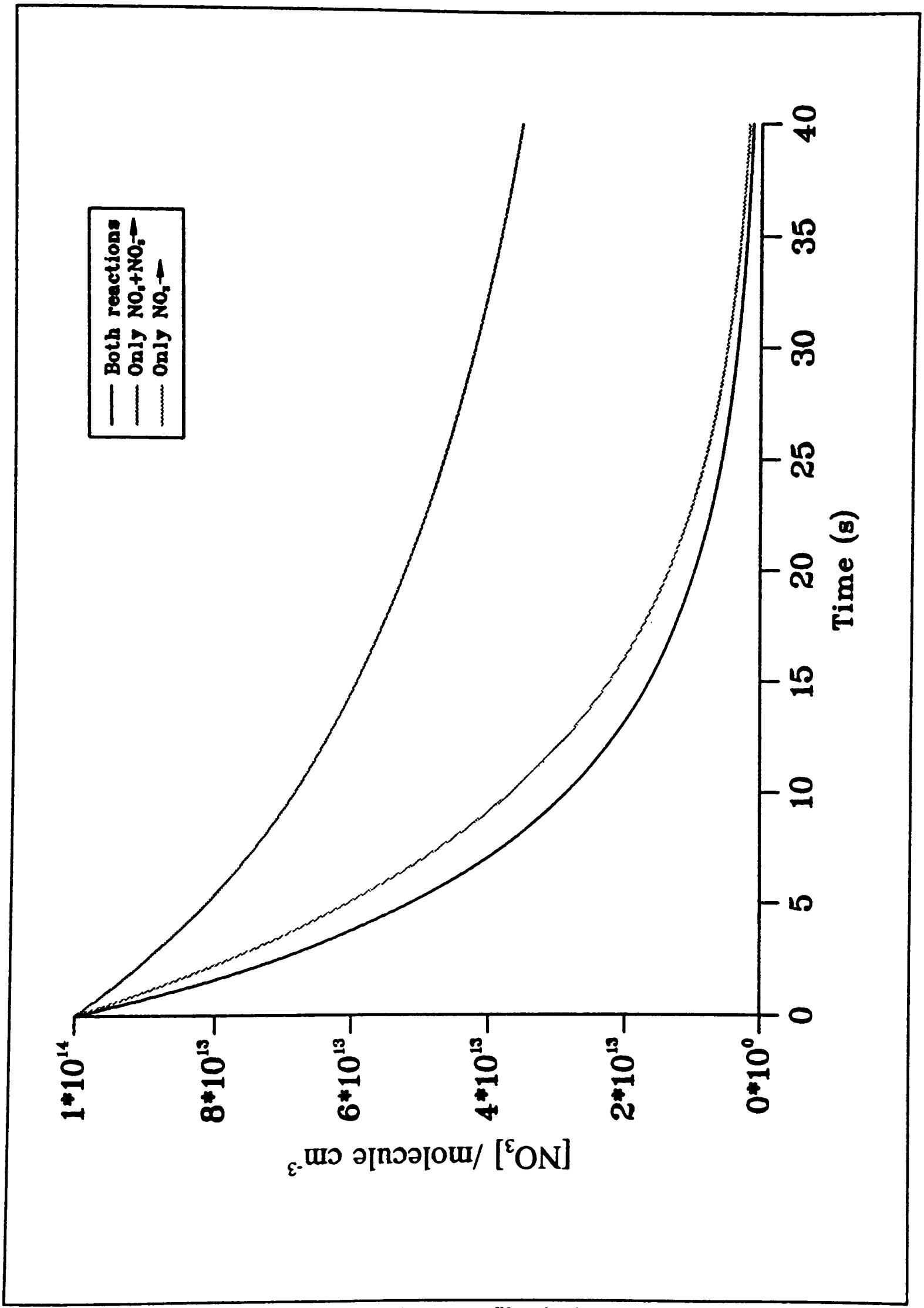

Figure 4.20 A simulated NO_3 *vs.* time decay profile; the legend on the figure describes the types of decay profile.

data with simulated data. In gas-phase reaction kinetics, the simulated data are produced by numerical integration (see §4.5.1) of a series of ordinary differential equations which represent the time dependent change in the concentration of a species. The simulated and experimental data are compared, and the parameter(s) varied until the sum of the squares (χ^2) of the residuals (see §4.5.1) is minimised. The programs work better if the numbers of variables are kept to a minimum. There are various methods for looking at the goodness-of-fit (Bevington, 1969), the most commonly used is inspection of the residuals i.e. $y_i - \hat{y}_i$, where y_i is the i^{th} (experimental) point and $\hat{y}_i$ is the corresponding simulated data point. In FACSIMILE (see §4.6.1) the residuals are calculated as

$$R_i = (y_i - \hat{y}_i / s_i)\sigma_i \qquad (4.32)$$

where s_i is a scaling factor and σ_i is the standard error on the data point *i*. FACSIMILE also calculates a sensitivity matrix of the dependence of R_i on each parameter, this can be used to estimate the variances and covariances of the fitted parameter. In this work the minimum χ^2 was used as the fitting criterion. Estimated uncertainties in fitted values were given as the sensitivity of χ^2 to small changes in parameter values. Different starting values of the variable parameters were used in order to ensure that a fit represented the true minimum on the χ^2 hypersurface.

4.7.2 A re-appraisal of the L-M method *versus* FACSIMILE for non-linear fitting of the experimental data

The simple reaction scheme

$$NO_3 \longrightarrow \text{Product} \qquad (4.8)$$

$$NO_3 + NO_3 \longrightarrow \text{Product} \qquad (4.9)$$

presented in §4.5.1 was used in a two parameter fit ($k_{4.8}$, $k_{4.9}$), using FACSIMILE, to the same set of experimental data as used in §4.5.1. Table 4.7 and Figure 4.21 show a comparison in the fitted values of $k_{4.8}$ and $k_{4.9}$ for both methods using the two different forms of the data as well as varying portions of the decay. The figure shows that the L-M method consistently over-estimates the value of $k_{4.9}$. The probable causes of this are that the L-M method is prone to finding false minima in the χ^2 surface and/or that the procedure for selection of points is random such that they are not representative of the decay as a whole. These problems are coupled to the ones with the method as a whole (Press *et al.*, 1986) the L-M routine varies the parameters during the fit, such that it over-estimates the contribution of the 1st order parameter because of the "stiffness" of the system. In addition, to the probable mathematical difficulties with the L-M method, there is the fact that the explicit formulation (4.11) takes no account of products of reaction (4.8) and (4.9), especially the small but significant contribution of NO_2 (*via.* reaction 4.19a) to the observed NO_3 decay.

Figure 4.22 shows the residuals from the fitting of the simple mechanism to some test data produced using $k_{4.8}$ = 0.1 s^{-1} and $k_{4.9}$ = 2.3x10^{-16} cm^3 $molecule^{-1}$ s^{-1}. The recovered values from a FACSIMILE fit for these rate coefficients are $k_{4.8}$ = 0.1 s^{-1} and $k_{4.9}$ 2.28x10^{-16} cm^3 $molecule^{-1}$ s^{-1}. The ability to recover test parameters from a fit shows that if the simple mechanism is applicable under our experimental conditions it would be possible to accurately fit a NO_3 decay. Still the problem pertains in the validity of fitting using only the limited chemistry (reactions 4.8, 4.9), in the light of the results in §4.6.

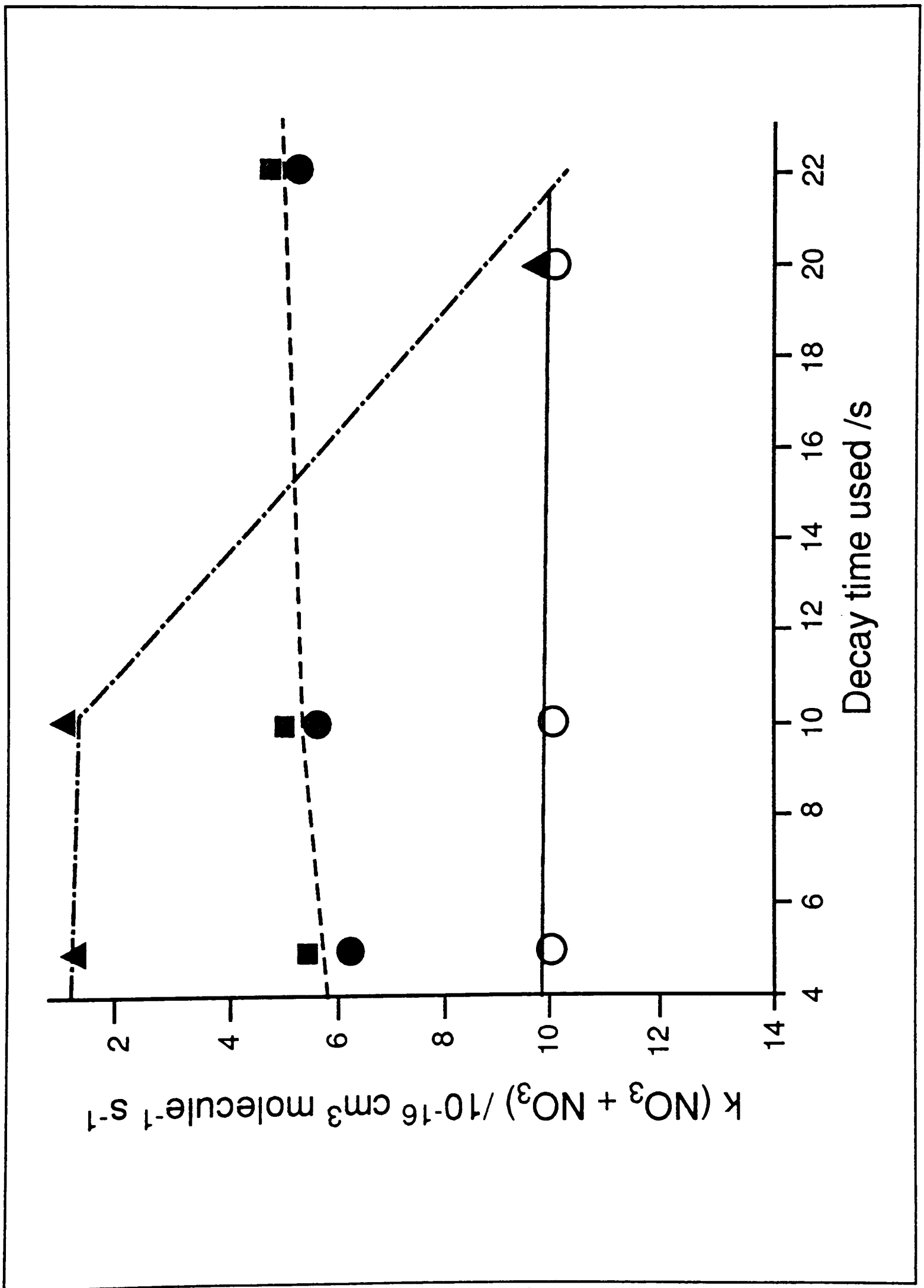

Figure 4.21 A comparison of the value of the derived rate constant for the NO_3 + NO_3 reaction and the fitting method used; ▲, L-M to SM data, O, L-M to RW data, ■, FACSIMILE to SM data and ●, FACSIMILE to RW data.

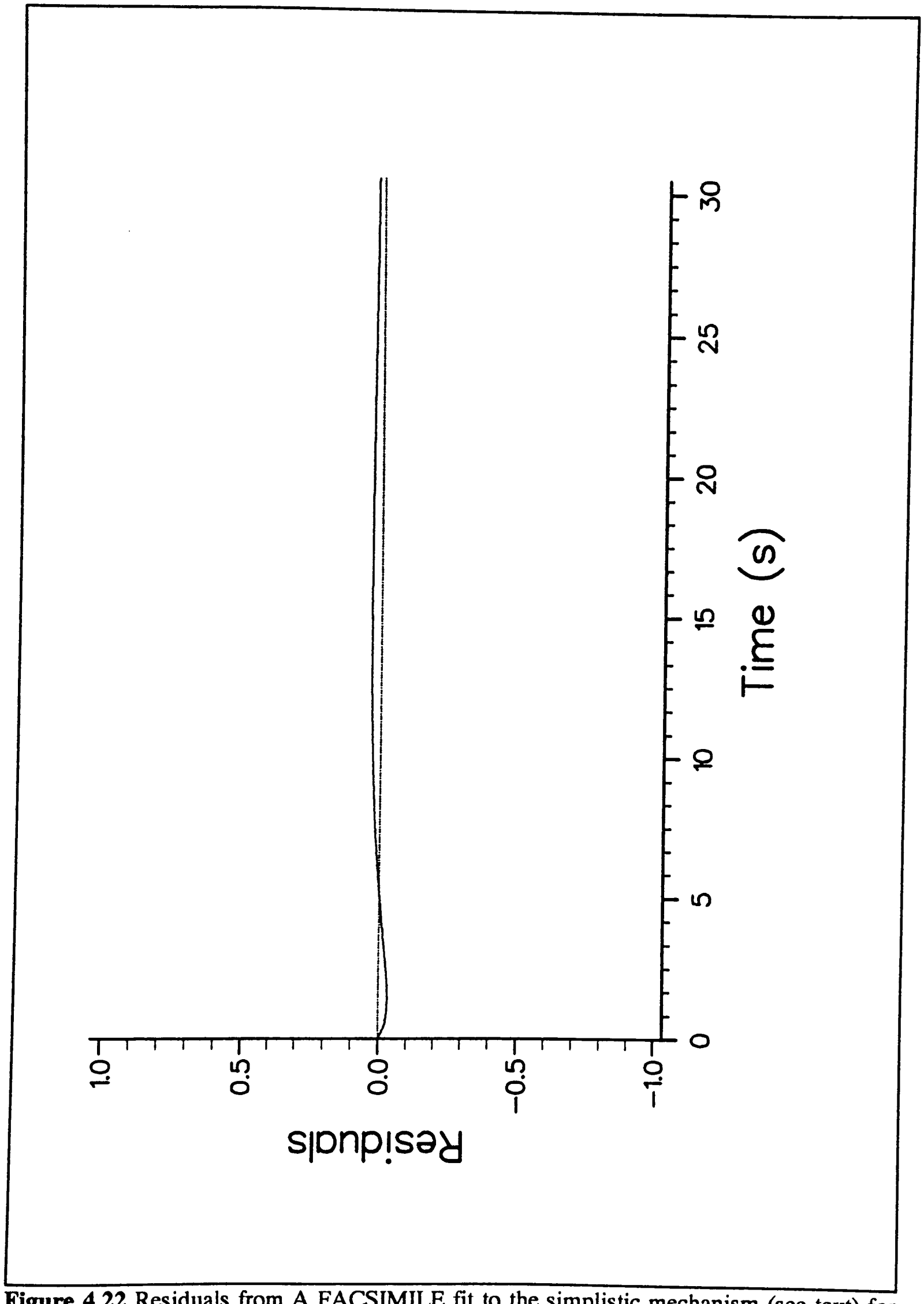

Figure 4.22 Residuals from A FACSIMILE fit to the simplistic mechanism (see text) for a set of test data.

Table 4.7 - A comparison of the L-M method *versus* FACSIMILE fitting for the same decay

Method a)	Data type b)	$[NO_3]_0$ /10^{14} molecule cm^{-3} c)	$k_{4.8}$ /s^{-1} d)	$k_{4.9}$ /cm^3 molecule^{-1} s^{-1} d)	No. of points in fit
L-M	SM/t=0-20s	4.12	0.08	$9.8x10^{-16}$	59
	RW/t=0-20s	4.26	0.07	$1.0x10^{-15}$	59
FAC	RW/t=0-20s	4.26	0.07	$5.3x10^{-16}$	580
	SM/t=0-20s	4.12	0.08	$4.9x10^{-16}$	596
L-M	SM/t=0-10s	4.12	0.08	$1.0x10^{-15}$	40
	RW/t=0-10s	4.26	0.06	$1.1x10^{-16}$	46
FAC	SM/t=0-10s	4.12	0.08	$5.0x10^{-16}$	200
	RW/t=0-10s	4.26	0.04	$6.3x10^{-16}$	200
L-M	SM/t=0-5s	4.12	0.07	$1.0x10^{-15}$	40
	RW/t=0-5s	4.26	0.03	$1.2x10^{-15}$	40
FAC	SM/t=0-5s	4.12	0.06	$5.3x10^{-16}$	120
	RW/t=0-5s	4.26	0.03	$6.2x10^{-16}$	120
L-M	SM/t=0-2s	4.12	0.31	$2.6x10^{-16}$	40
	RW/t=0-2s	4.26	0.15	$8.7x10^{-16}$	40
FAC	SM/t=0-2s	4.12	0.32	$1.1x10^{-16}$	41
	RW/t=0-2s	4.26	0.1	$4.7x10^{-16}$	41

a) L-M method see §4.5.1, FAC - FACSIMILE fit to reactions 4.8, 4.9; b) SM/RW data types see §4.4.4, t = time portion of the decay used; c) initial concentration of $[NO_3]$ at t=0; d) fitted value, no errors quoted (see text).

4.7.3 Kinetic fitting to a more complex scheme

In §4.6.6 for the purposes of non-quantitative fitting (simulating) of the NO_3 decay period, we assumed that the only chemistry affecting $[NO_3]$ was the active NO_x chemistry as shown in Table 4.8. Sets of test data were produced using the reactions shown in Table 4.8 with the parameters $k_{4.8}$= 0.1s^{-1}, $k_{4.9}$= 2.31x10^{-16} cm^3 $molecule^{-1}$ s^{-1}, $[NO_3]_o$ = 5.0x10^{14} and $[NO_2]_o$ = 1.0x10^{14} molecule cm^{-3}. For the fit, $[NO_2]_o$ was set to 1.0x10^{14} molecule cm^{-3} and $[NO_3]_o$ was varied, the residuals from the fit are shown in Figure 4.22. The recovered parameters were $[NO_3]_o$ = 5.0x10^{14} molecule cm^{-3}, $k_{4.8}$ = 0.103 s^{-1} and $k_{4.9}$ = 2.29x10^{-16} cm^3 $molecule^{-1}$ s^{-1}.

From the shape of the residuals at t < 5s an estimate of the experimental accuracy of $[NO_3]_o$ could be gained. The next step was to vary $[NO_2]_0$ as a parameter in the fitting procedure. Using a three parameter ($k_{4.8}$, $k_{4.9}$, $[NO_2]_0$) fit to the test data, the recovered values for $k_{4.8}$ = 9.84x10^{-2} s^{-1}, $k_{4.9}$ = 2.31x10^{-16} cm^3 $molecule^{-1}$ s^{-1} and $[NO_2]_o$ = 1.0x10^{14} molecule cm^{-3}. The minimum total error of this fitting process is

$$k_{4.8} \pm 0.1x10^{-2}\ s^{-1}$$
$$k_{4.9} \pm 0.1x10^{-16}\ cm^3\ molecule^{-1}\ s^{-1}$$
$$[NO_2]_o \pm 0.0x10^{14}\ molecule\ cm^{-3}$$

The residuals for the optimum fit are shown in Figure 4.23. The decay time used for this optimum fit in order to recover the test parameters, was t = 0-10s, as shown in Figure 4.24. When this three parameter fitting procedure is applied to experimental data, a global minimum is searched for in $[NO_2]_o$, $k_{4.8}$, $k_{4.9}$. An example fit to experimental data is shown in figure 4.25. Both data types (see §4.4.4) gave the same values within error for $k_{4.8}$, $k_{4.9}$ from fitting to this scheme. The analysis was also shown to be invariant to the selected value of $k_{4.19a}$ in the pressure region 1-100 Torr of He.

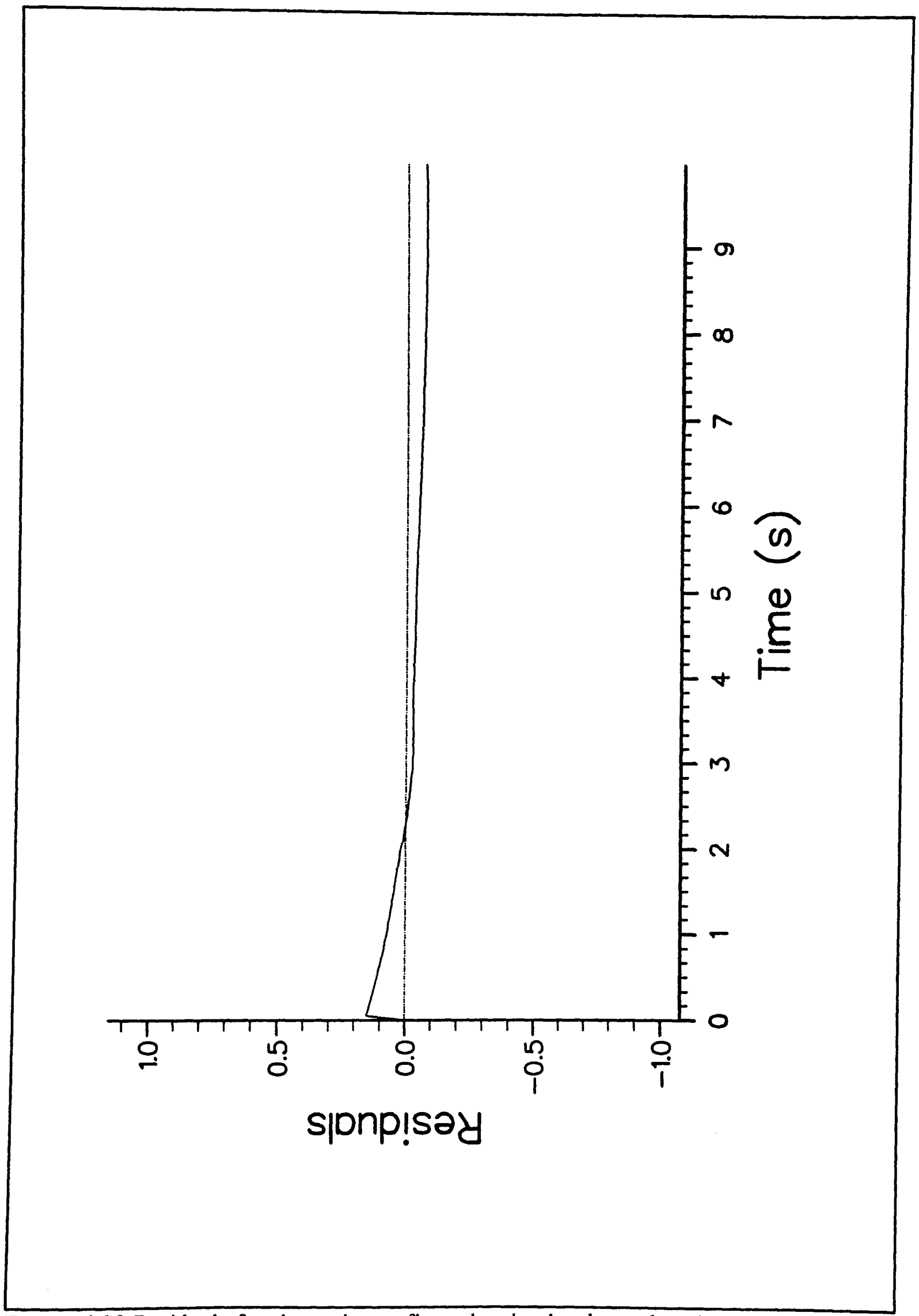

Figure 4.23 Residuals for the optimum fit to the simulated test data (see text).

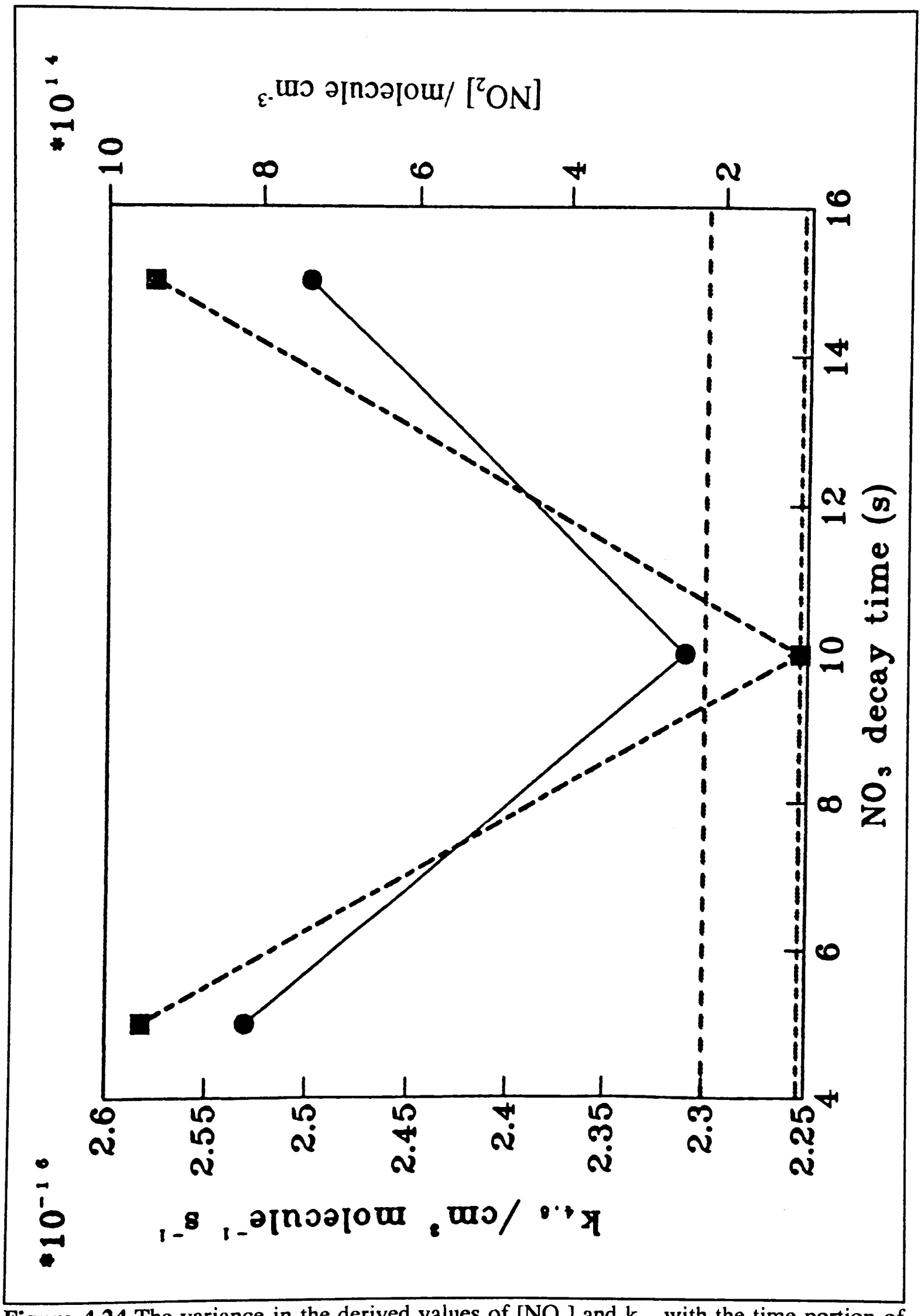

Figure 4.24 The variance in the derived values of $[NO_2]$ and $k_{4.9}$ with the time-portion of the decay used to fit to; the ● represent values of $k_{4.9}$ and the ■ NO_2.

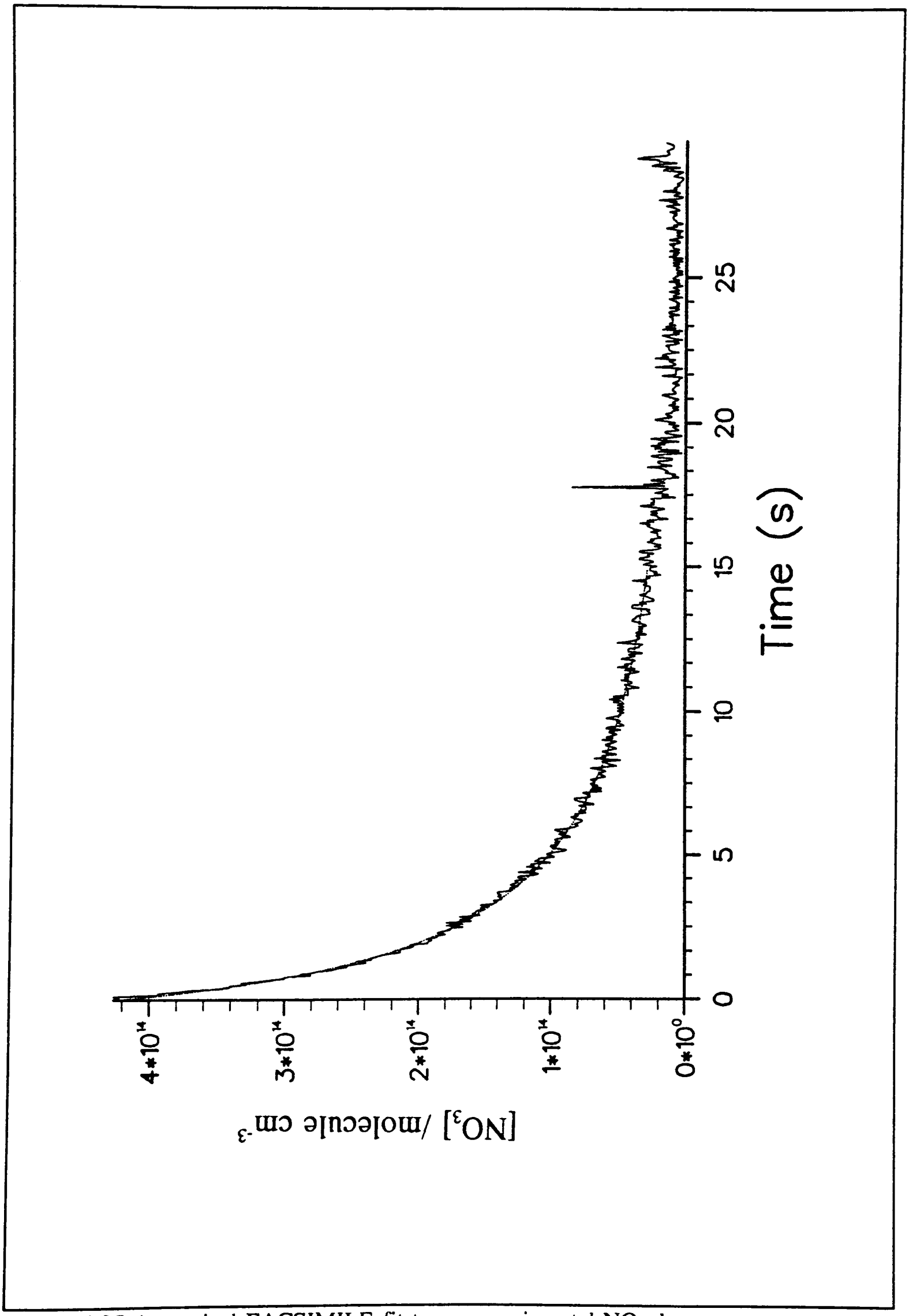

Figure 4.25 An typical FACSIMILE fit to an experimental NO_3 decay-curve.

Table 4.8 - **The reactions used in the kinetic fitting of the decay period**

Reaction	Reaction No.	k /cm^3 molecule^{-1} s^{-1}
$NO_3 + NO_3 \longrightarrow NO_2 + NO_2 + O_2$	4.9	Parameter
$NO_3 \longrightarrow$ Wall	4.8	Parameter
$NO_3 + NO_2 \rightleftharpoons N_2O_5$	4.19a,-4.19a	5.9×10^{-13};8.3×10^{-3}
$NO_3 + NO_2 \longrightarrow NO + NO_2 + O_2$	4.19b	9.1×10^{-16}
$NO + NO_3 \longrightarrow NO_2 + NO_2$	4.26	3.0×10^{-11}

4.8 Results II

The results documented in this section, consist of measurements of the kinetics of the NO_3 + NO_3 reaction. The validity of the fitting procedure used for the extraction of the rate coefficients from NO_3 decay curves has been described in detail previously (§4.7). The reaction was studied at room temperature (T=298±2 K), typical $[NO_3]_o$ being *ca.* 3.0×10^{14} molecule cm^{-3}. Table 4.9 shows sample results taken from over 40 analyses. The reaction was studied over pressure (P_T) range 8-100 Torr. The low pressure range (P_T < 15 Torr) measurements were particularly difficult to analyse as $[NO_3]_o$ was low, such that the residuals on extraction of the second-order component of the decay were outside the error limits. The errors quoted in Table 4.9 come from the calculated 95% confidence limits from the FACSIMILE fitting of the data with an added factor for the minimum error for an optimum fit (see §4.7.3). The confidence limits are calculated as the true value of ln(P) lies within a factor $\exp(\pm\alpha\sigma)$, where α depends on the level of confidence required. For 95% confidence limits the value of α=1.645, this implies that the calculated parameter has a 95%

Table 4.9 - Typical results

$[NO_3]_0/10^{14}$ molecule cm^{-3}	P_T Torr	$k_{4.9}/10^{-16}$ cm^3 $molecule^{-1}$ s^{-1} (a)	$k_{4.9}/10^{-16}$ cm^3 $molecule^{-1}$ s^{-1} (b)
4.4	38	(2.3±0.4)	(2.1±0.2)
1.6	8	(2.6±0.6)	-
4.2	41	(2.9±1.0)	(2.16±0.8)
3.0	39	(2.8±0.9)	(2.25±0.6)
3.9	40	(3.2±1.4)	(2.3±0.9)
3.8	30	(3.2±0.7)	(2.4±0.8)
3.0	29	(1.9±0.2)	(2.0±0.2)
4.6	38	(3.1±0.6)	(2.4±0.4)
4.1	40	(2.7±0.7)	-
2.1	20	(4.0±1.2)	(2.9±1.0)

(a) RW - raw data (see §4.4.4), errors are quoted as 95% confidence limits (see text); (b) SM - smoothed data (see §4.4.4), errors as (a).

probability that it lies below the upper limit and a 5% probability that the true value lies below the lower limit. Other experimental errors can be quoted as ±20% because of the uncertainty in the absorption cross-section and the effective geometric path length in the absorption set-up for detection of NO_3. There is the possibility of further systematic errors in for example pressure measurement, which are more difficult to estimate.

The average value for $k_{4.9}$ ($NO_3 + NO_3 \rightarrow$) at a total pressure of 40 Torr $He/HNO_3/F_2$ from the analysis of seven runs of varying $[F_2]_o/[HNO_3]_o$ is $(2.2\pm1.0)\times10^{-16}$ cm^3 $molecule^{-1}$ s^{-1}. The possibility of the self-reaction being pressure-dependent is discussed in §4.9.

4.9 Discussion

4.9.1 Comparison and trends

The kinetics of the self-reaction of NO_3 have only been studied previously by one group of workers (Graham and Johnston, 1978), as part of a study on the N_2O_5-O_3 system. The purpose of their work was to obtain quantum yields for the photolysis of NO_3 produced by the reaction

$$NO_2 + O_3 \longrightarrow NO_3 + O_2 \qquad (4.33)$$

In order to determine this quantity it was necessary to measure several kinetic parameters including the equilibrium constant for the reaction

$$NO_2 + NO_3 + M \rightleftharpoons N_2O_5 + M \qquad (4.19a)$$

The complex treatment of the equations governing the time dependence of the concentration of the species involved a 15-step photochemical mechanism. Analysis of the data yielded a rate expression of $(8.5\pm2.8)\times10^{-13}$ exp[-(2450±100)/T] cm^3 $molecule^{-1}$ s^{-1}, giving a rate coefficient of 2.3×10^{-16} cm^3 $molecule^{-1}$ s^{-1} at T=298 K. From the evaluation of their photochemical system Graham and Johnston (1978) inferred the products of the NO_3 + NO_3 reaction were indeed NO_2 and O_2.

Table 4.10 - A comparison of kinetic measurements of the reaction NO_3 + NO_3

k (cm^3 $molecule^{-1}$ s^{-1})	Temp. (K)	Technique (a)	Reference
2.3×10^{-16}	298	MP	1
2.2×10^{-16}	298	FP	2

(a) MP, modulated photolysis; FP, flash photolysis
References - 1. Graham and Johnston (1978); 2. This Work

The calculated values for $k_{4.9}$ ($NO_3 + NO_3 \rightarrow$) were dependent on the absorption cross-sections for both NO_3 and O_3 and errors in these cross-sections could introduce systematic errors in the expression for the rate coefficients. As can be seen from table 4.10, there is excellent agreement between this work and that of Graham and Johnston (1978) as to the value of $k_{4.9}(NO_3+NO_3\rightarrow)$. From table 4.11 it can be seen that for the series of reactions of the nitrogen oxides with NO_3, there is a trend in reactivity such that the rate of reaction increases with increasing exothermicity.

Table 4.11 - Comparison of the rates of reaction of the nitrogen oxides with NO_3

Reaction	$\Delta H_{r\,(a)}$ kJ mol^{-1}	k_{298} cm^3 molecule^{-1} s^{-1}	Ref.
$NO + NO_3 \longrightarrow NO_2 + NO_2$	-88.6	2.9×10^{-11}	1
$NO_2 + NO_3 \rightleftharpoons N_2O_5$	-86.1	1.2×10^{-12}	2
$NO_3 + NO_3 \longrightarrow NO_2 + NO_2 + O_2$	-62.8	2.2×10^{-16}	3

(a) Values taken from Atkinson *et. al*, 1986, ΔH_r is the enthalpy of reaction
References - 1. DeMore *et al.*, 1990; 2. Wayne *et al.*, 1991, calculated as k^∞; 3. This work.

The activation energy (E_a) of a reaction is empirically related to the enthalpy of reaction by the Evans and Polanyi relationship (1938). The relationship may be expressed simply as

$$E_a = \alpha \Delta H_r + c \qquad (4.34)$$

where α is a constant taking values between zero and unity. The full theoretical background and further modifications to this relationship are described in full elsewhere (Laidler. 1987). As the data on these reactions are scarce it suffices to say that these reactions follow the trend suggested in equation 4.34. Wayne *et al.* (1991) suggest a further trend in reactivity in the

reactions of NO_3 with atoms and radicals. If the reactants in such a reaction pass over to products on a single potential energy surface, then the probability of reaction appears to be inversely proportional to the degeneracy of the system. This is shown to be applicable to the series H (^2S), Cl (^2P, J=3/2), O (^3P, J=2,1,0) where the general trend in reactivity is that the rate decreases as the degeneracy increases. Wayne *et al.* (1991) go on to suggest that in reactions where no direct oxygen transfer can take place and which may involve as part of a more complex scheme, a multi-centre transition state, then the reactivity is greatly reduced. Perhaps the decreasing reactivity in the series of reactions shown in Table 4.11 could be ascribed to the increasing complexity in the transition state. This premise is difficult to apply quantitatively in any rigorous theoretical manner to this system.

4.9.2 Pressure dependence of the NO_3 + NO_3 reaction?

The NO_3 self-reaction was measured for various $[F]_0/[HNO_3]_0$ over a pressure range of 4 to 90 Torr in helium. Figure 4.26 shows a plot of total pressure *vs.* $k(NO_3 + NO_3)$ for over 40 separate experimental determinations. Also, shown on this figure plotted on a third axis is the initial concentration of NO_3. Figure 4.26 is plotted in this way to illustrate the independence of the derived rate coefficient from $[NO_3]_o$. This plot would seem to suggest, within the limits of experimental accuracy, that the self-reaction is pressure independent or, at best, not very strongly pressure dependent within this regime.

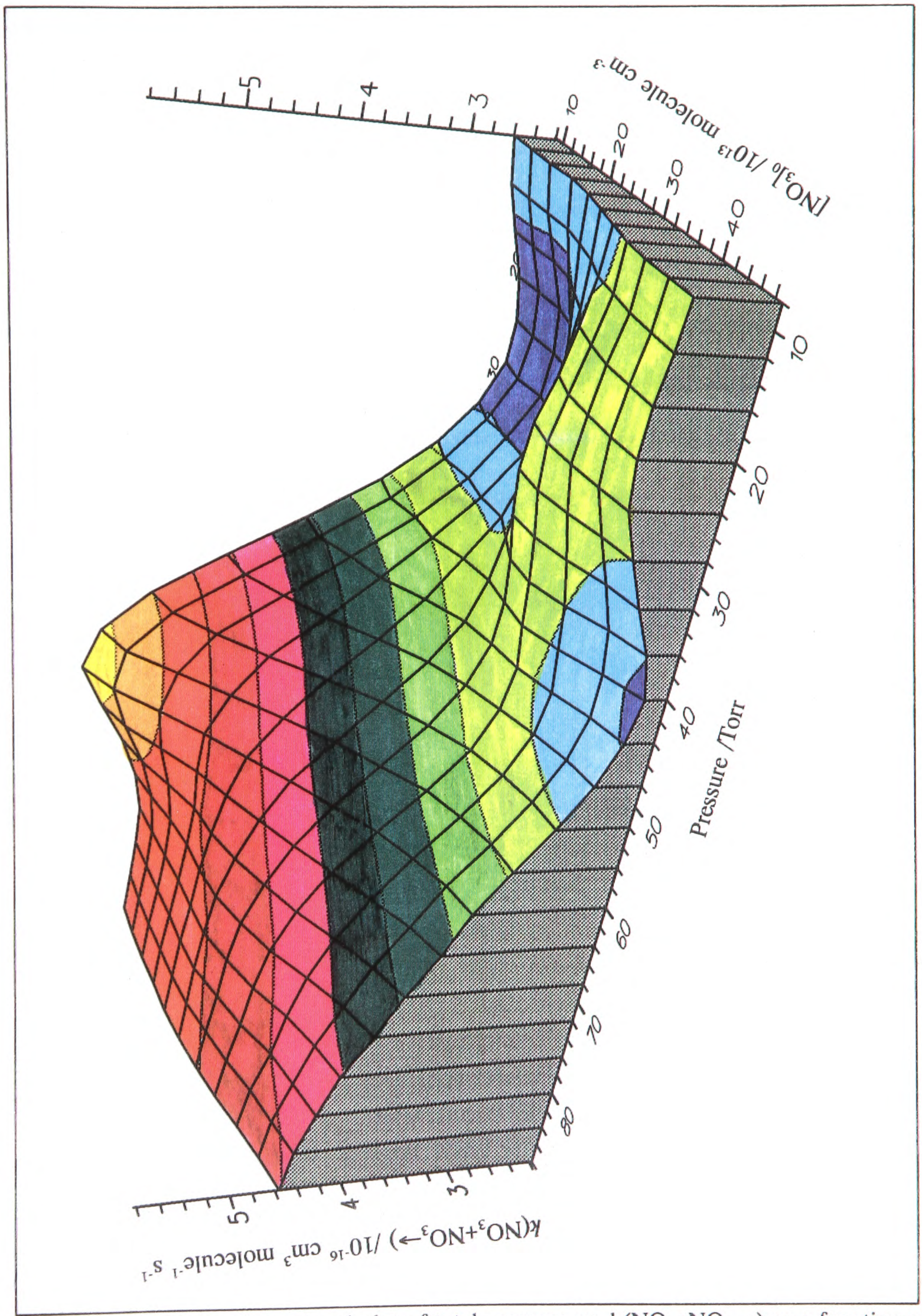

Figure 4.26 A three-dimensional plot of total pressure *vs.* $k(NO_3+NO_3\rightarrow)$ as a function of initial concentration of NO_3.

4.10 Conclusions

A variant of the conventional flash-photolysis system has been used to determine the rate coefficient for the self-reaction of the nitrate radical. The derived rate coefficient is 2.3×10^{-16} cm^3 $molecule^{-1}$ s^{-1} at T=298 K, and is in agreement with the only other, indirect, study of this reaction. Seemingly, within experimental accuracy the derived rate of the self-reaction is pressure independent. New computer programs have been developed and tested for the acquisition and analysis of the data. Kinetic models have also been developed, not only for quantitative fitting of the decay period, but also for modelling of the initial build-up and subsequent decay of NO_3.

CHAPTER 5

The Laser-induced fluorescence of NO_3

5.1 Introduction

To investigate the reaction kinetics of a bimolecular reaction, it is necessary to follow as a function of time the concentrations of one or more reactants (See Chapter 2). Under the conditions most commonly used, one of the reactants is in such excess over the other that the decay of the minor constituent exhibits first order kinetic behaviour, the concentration of the majority species being effectively constant. The contribution of secondary chemistry to the observed rate of decay of the minor constituent must also be taken into consideration. Secondary chemistry involves reactions which follow the primary kinetic step that may directly or indirectly affect the concentration of the minor constituent. Unless recognised and accounted for secondary processes can invalidate the results of an experiment. Secondary chemistry can be a particular problem with regard to the study of NO_3 kinetics; often the rate constant for the primary step is relatively slow in comparison to those of the ensuing secondary chemistry (e.g. Boyd *et al.*, 1991). One way of alleviating the effect of secondary chemistry on the observed kinetics is to start with a low concentration of the minority constituent. This can be exemplified by considering the simple reaction system

$$A + B \longrightarrow X \tag{5.1}$$

$$X + B \longrightarrow Y \tag{5.2}$$

where B is the minority constituent. The rate equation describing the loss of B is

$$-\frac{d[B]}{dt} = k_{5.1}[A][B] + k_{5.2}[X][B] \tag{5.3}$$

In principle the maximum concentration of X will be $\Delta[B]$ (i.e $[B]_0$-$[B]_t$). Thus, as the ratio of $\Delta[B]/[A]$ decreases, the contribution to the observed rate of reaction 5.2 will also decrease.

Of the plethora of methods available for the detection of atoms and radicals in kinetic experiments, in particular NO_3, fluorescence experiments are an extremely attractive method of detecting low concentrations. This is because, if spurious scattering is minimised, there is no signal in the absence of the excited species. In kinetic experiments there are two commonly used forms of fluorescence/emission spectroscopy, namely resonance-fluorescence (R-F) (Davis and Braun, 1968) and laser-induced fluorescence (LIF).

In this chapter a series of preliminary experiments on the LIF of NO_3 are presented. These experiments were conducted as a fore-runner to the application of this method as a means of detection of the radical in a discharge-flow experiment.

5.2 Laser-induced fluorescence

There are three major techniques using lasers for the detection of gas-phase species, namely laser-induced fluorescence, multiple-photon ionisation and laser absorption (see Chapter 4). All three techniques rely on the provision of light with a frequency that is matched to a spectral feature of the species of interest. The advantage that lasers have over the conventional light source, the lamp (for a comparison see Schäfer, 1988), is that the light produced is more intense, is monochromatic, can be of shorter duration, coherent and polarised (Demtröder, 1988). These properties are exploited in the study of gas-phase species (Hancock, 1988; Wolfrum, 1988).

In principle, laser-induced fluorescence, a form of optical emission spectroscopy, presents an advantage over absorption techniques. In absorption experiments good sensitivity is gained

by accurate measurement of I/I_o (See Chapter 2) but I/I_o are very similar quantities when absorption is low; *noise* and fluctuation in intensity of the absorption probe beam causes problems. In emission, there is no radiation produced unless the excited species is present, and the signal, in principle, is measured against a zero background.

Laser induced fluorescence operates on the following principles: when a laser of wavelength λ_L is tuned to an absorbing molecular transition $E_u \leftarrow E_l$, where E_u and E_l are energies of upper and lower energy levels, the number of photons absorbed per second $n_{abs.}$ over a pathlength l is

$$n_{abs.} = N_l \, \sigma_{ul} \, n_L \, l \tag{5.4}$$

where n_L is the laser flux in photons per second, σ_{ul} the molecular absorption cross section and N_l the density of molecules in the absorbing state. The number of photons of fluorescence emitted per second $n_{fluor.}$ from the excited level E_u is given by

$$n_{fluor.} = N_u \, A_u = n_u \eta_u \tag{5.5}$$

where A_u is a transition probability to all the lower states. The quantum efficiency η_u, contains a term to express the deactivation rate of E_u *via* radiationless transitions (R_u) (e.g. collision-induced transitions) and is expressed as

$$\eta_u = \frac{A_u}{A_u + R_u} \tag{5.6}$$

The amount of fluorescence detected is really only limited by the efficiency of the

photomultiplier and the collection optics. With modern photomultipliers using photon counting techniques it is possible to detect molecular concentrations down to 10^2 molecule cm^{-3} (Fairbanks *et al.*, 1975).

When λ_L (the wavelength of the probe laser) is scanned across the spectral range of absorption lines, the emission intensity $I_{fluor.}$ is given by

$$I_{fluor.}(\lambda_L) \propto n_L \sigma_{ul} N_l \qquad (5.7)$$

and the resultant spectrum is called the *excitation spectrum*. This excitation spectrum directly reflects the absorption spectrum in regard to the position of the lines but the relative intensities of the different lines $I(\lambda)$ are not identical to those in the absorption spectrum unless the following conditions are fulfilled:

a) The quantum efficiency (η_u as in equation 5.6) is the same for all the excited states (E_u);

b) The photomultiplier that detects the emission has linear response to the wavelength of the incident emission over a spectral range;

c) The detection system collects the total emission from the excited states. This requirement encompasses problems such as diffusion out of the observation region of species with long lived emissions.

d) The power of the exciting radiation is constant over the range of λ

Quantitative LIF concentration measurement is more complex as it requires knowledge of the fluorescence quantum yield, which depends on both the radiative and collisional processes that occur following electronic excitation (Crosley, 1986).

5.2.1 Laser-induced fluorescence of NO_3

In order to ascertain whether an excited species fluoresces in a given wavelength region, the photodissociation must be characterised. The quantum yields (Φ) for the photolysis of NO_3,

$$NO_3 + h\nu \longrightarrow NO + O_2 \qquad \Phi_1 \qquad (5.8)$$

$$\longrightarrow NO_2 + O \qquad \Phi_2 \qquad (5.9)$$

have been measured by quantitatively following the production of NO and $O(^3P)$ (Magnotta and Johnston, 1980). Φ_2 was found to be fairly constant from λ=470nm to 580nm dropping to zero at λ=635nm, whereas Φ_1 rises to a peak at λ~586nm before falling back to zero at λ=640nm (Magnotta and Johnson, 1980). Between the λ=640nm threshold to λ=680nm there is no photochemical activity. These quantum yields can be used to estimate the atmospheric photodissociation rates of NO_3 (Magnotta and Johnson, 1980).

The possible channels for photodissociation of NO_3 are

$$NO_3 + h\nu \rightarrow NO(X^2\Pi) + O_2(X^3\Sigma_g^-) \quad \lambda<8000nm \qquad (5.10)$$

$$\rightarrow NO(X^2\Pi) + O_2(a^1\Delta_g) \quad \lambda<1100nm \qquad (5.11)$$

$$\rightarrow NO(X^2\Pi) + O_2(b^1\Sigma_g^+) \quad \lambda<700nm \qquad (5.12)$$

$$\rightarrow NO_2(X^2A_1) + O(^3P) \quad \lambda<580nm \qquad (5.13)$$

All three product channels which lead to NO are accessible at wavelengths less than λ=700nm but there is no evidence for the dissociation of NO_3 when excited at λ=662nm (Graham and Johnston, 1978; Magnotta and Johnston, 1980).

In 1979, Magnotta (1979) reported that there was no visible fluorescence from the laser

excitation of NO_3. This conflicted with the predictions of Mitchell *et al.* (1980) who, on the basis of direct detection of the photolysis products, predicted that the fluorescence quantum yield for excitation of NO_3 would be non-zero. Subsequently, in 1983, the first LIF emission and excitation spectra were recorded for NO_3 (Nelson *et al.*, 1983a,b; Ishiwata *et al.*, 1983). Figures 5.1 and 5.2 show the excitation and emission LIF spectra of NO_3. All the studies show six broad bands in excitation, and the profile of the spectrum is fairly consistent with the visible absorption spectrum.

The first reported application of LIF to the kinetic studies of NO_3 was in a discharge-flow system to study the reaction of *trans*-but-2-ene (Ravishankara and Mauldin, 1985). In this study a Nd:YAG pulsed laser was used to pump a dye-laser which emitted light at λ=662nm. Continuous wave (CW) excitation of NO_3 was used in discharge-flow studies by Hammer *et al.* (1986) and Dlugocencky and Howard (1988,1989). The detection limit for a 15 s integration time was *ca.* 10^8 molecule cm^{-3}, which is vastly superior to the sensitivity which can be achieved with optical absorption. In order for LIF to be of use as a measure of the concentration of NO_3 under flow tube conditions, the fluorescence (emission processes) should be largely unaffected by the experimental conditions, such as pressure, composition (i.e. quenching) and laser saturation of the transition.

Hammer *et al.* (1986) showed, by continuous wave excitation of NO_3 at λ=662nm, that the Stern-Volmer plot of $1/I_{fluor.}$ *vs.* total pressure of helium was linear over a pressure region of 1.1-10 Torr. The same was true of saturation effects, $I_{fluor.}$ *vs.* the laser power being also linear over a 400mW range.

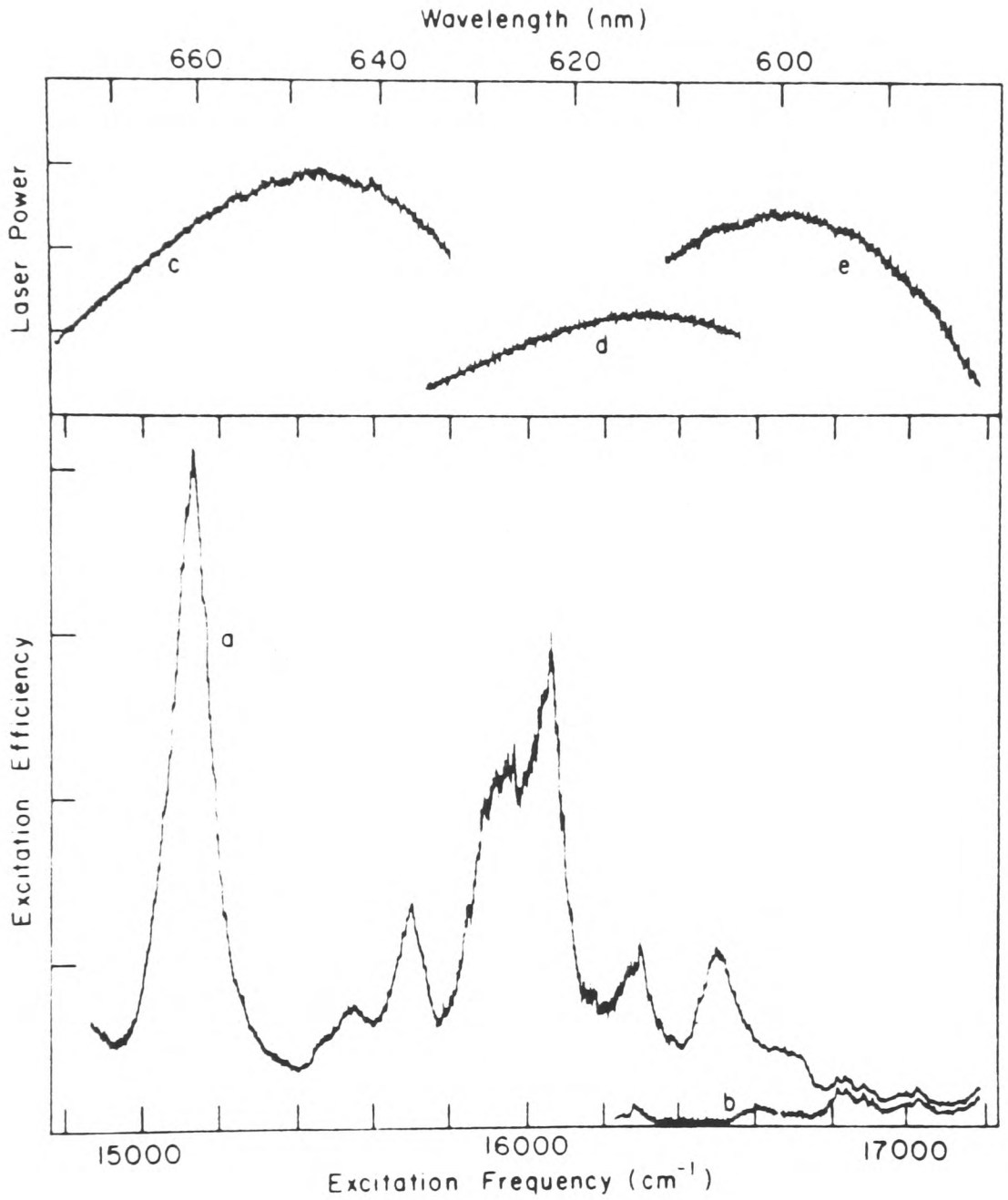

Figure 5.1 Fluorescence excitation spectrum of the NO_3 radical: a spectrum normalised by using the dye-laser power curves (c=Rhodamine 640 in methanol-water, d=Rhodamine 590 soap-water, e=Rhodamine 590 in methanol-water): b= spectrum of NO_2 (Nelson *et al.*, 1983a).

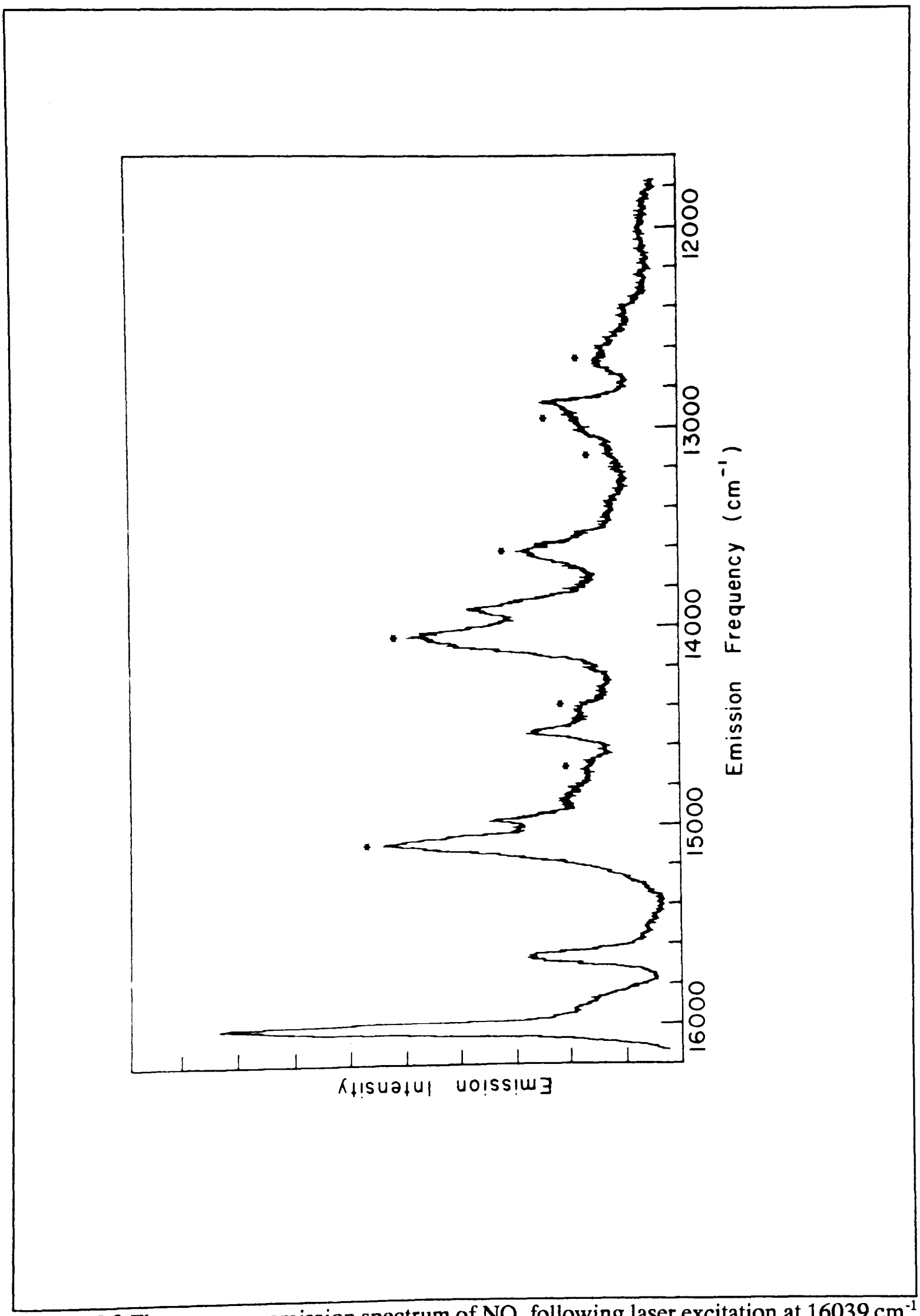

Figure 5.2 Fluorescence emission spectrum of NO_3 following laser excitation at 16039 cm^{-1} (λ=623nm) (Nelson *et al.*, 1983b).

5.3. Experimental

The apparatus used is schematically represented in Figure 5.3. It consists of a laser system for producing light of a known wavelength, a reaction cell for production of the radical species and their subsequent excitation, an optical detection system and the requisite electronics for data collection and analysis.

5.3.1 Laser system

The probe beam was provided by an excimer-laser pumped dye-laser system. The excimer laser (Lambda Physik EMG 101 MSC) operating on the XeCl line at λ=308nm pumped a dye laser (Lambda Physik FL2002) operating with a solution of Rhodamine-101 dye (Spectra-Physics LC6400, 0.75gl^{-1}). The peak output of *ca.* 10mJ for this dye is at λ=623nm. The dye laser output could be tuned between λ= 614 and 670nm by means of a grating in the dye laser. For excitation of NO_3 at λ=662nm a solution containing the dye DCM (Spectra-Physics LC6500, 0.71gl^{-1}) (Marason, 1981) was used, the laser output of which was tunable over the range λ=632 to 690nm. Typical laser pulse energies were 80mJ and 10mJ per pulse at a repetition rate of 10Hz for the excimer and dye laser respectively.

The laser was triggered by a pulse-delay generator (PCL construction) which was capable of producing three separate pulses at any desired delay after an initial pulse. The initial pulse rate could be varied between 1 and 50 Hz. The output laser beam from the dye laser contained both laser light and fluorescence; the non-laser light was removed by a series of irises mounted on an optical bench. The probe laser beam was directed into the cell by means of a prism and a set of lenses.

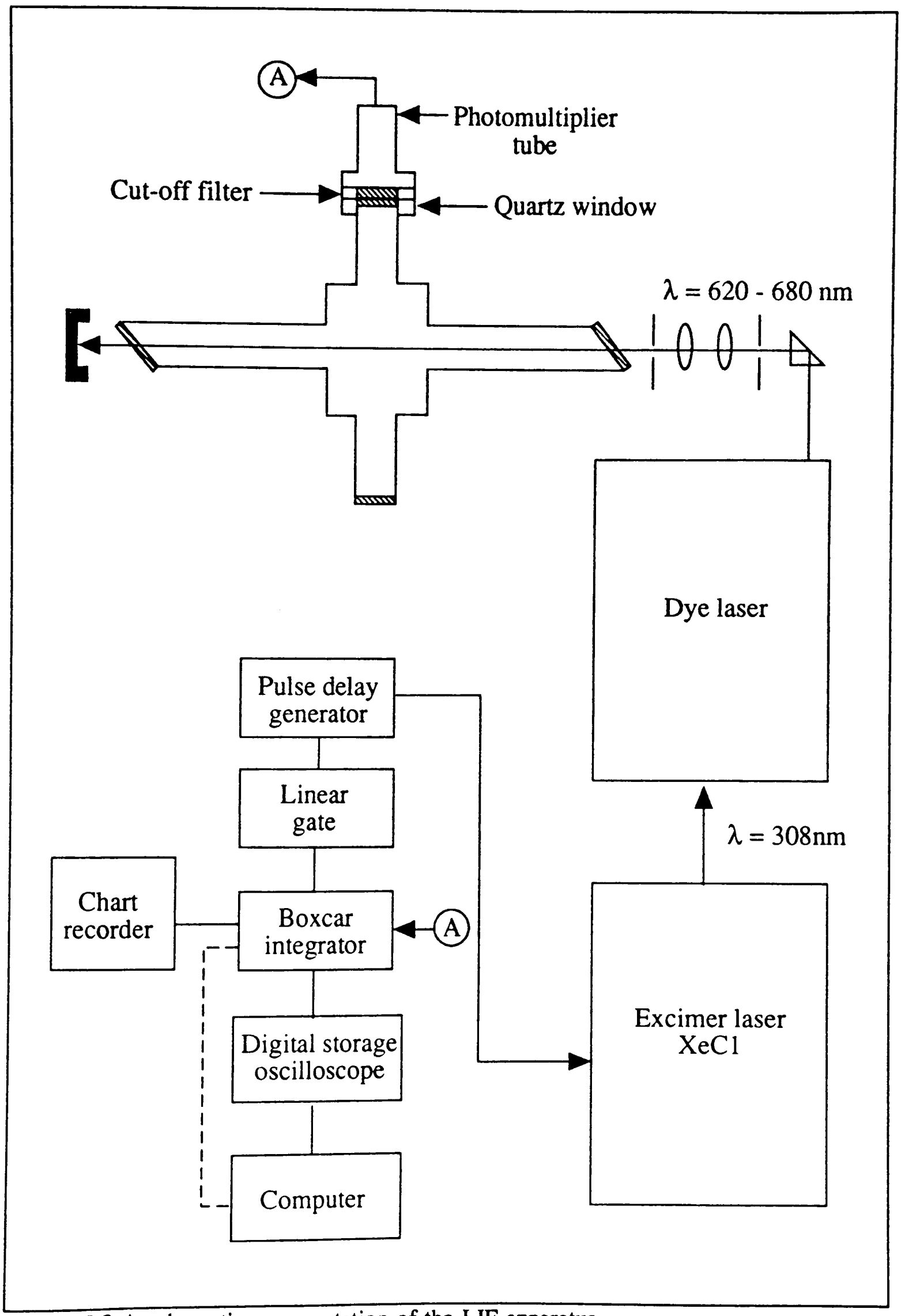

Figure 5.3 A schematic representation of the LIF apparatus

5.3.2 The reaction cell

The NO_3 radical was formed in a glass Y-piece equipped with Wood's horns (Moore *et al.*, 1989) to ensure stray light from the microwave discharge did not enter the detection region. The end of the Y-piece was positioned *ca.* 0.5mm above the height of the laser beam. The cell itself consisted of a central cube with six arms, one from each face of the cube (See Figure 5.3). The probe beam was directed orthogonally into the cell through Quartz Brewster angle windows at the end of one of the arms of the cell which was in the horizontal plane of the laboratory. The arms through which the laser probe beam passed were 80cm long and contained baffle rings of decreasing aperture which reduced the amount of scattered laser light able to pass into the cell (Pruett and Zare, 1976). The PMT (photomultiplier tube) was mounted orthogonally to the arm that propagated the probe-laser beam (see §5.3.3). The cell was pumped by a rotary pump (Edwards ES2000) which provided "slow" flow conditions. The cell could also alternatively be pumped by an Edwards diffusion pump which was used to remove both NO_2 and HNO_3 from the cell walls between experiments. The system was light-tight; no effect of room light could be observed by the detection system. The NO_3 radical was produced by the reactions

$$F_2 + \mu\text{-wave} \longrightarrow F + F \qquad (5.14)$$

$$F + HNO_3 \longrightarrow NO_3 + HF \qquad (5.15)$$

which have been previously described in detail in Chapter 2.

5.3.3 LIF collection optics

The photomultiplier tube (PMT) (EMI type 9558B) was positioned *ca.* 40cm from the centre of the cell. The PMT housing assembly was mounted on a series of flanges. The first flange contained a quartz window and isolated the PMT set-up from the cell, the second

flange provided a mounting for cut-off filters, which were placed in front of the PMT tube in order to keep out stray probe-beam laser light but allow the emission at λ>700nm through. For excitation of NO_3 at λ=623nm a Schott cut-off filter (RG665) which has 50% transmission at λ=665nm was used. For excitation at λ=662nm a RG695 was used which has a 50% transmission at λ=695nm. The PMT was run typically at a voltage of 1.1kV provided by a high voltage power supply unit (Brandenburg).

5.3.4 Signal processing and recording

The PMT passed a D.C. current *via* a 50Ω resistance load to a digital storage adaptor (DSA) (Thurlby DSA 525), the display device for which was a standard oscilloscope (Tektronic 2225 20MHz). The 50Ω natural load of the system meant that signals were measured without any resistance-load broadening. The DSA had a 20MHz data-bus speed and was capable of averaging up to 255 signals on a shot to shot basis on a 5μs time base. The PMT signal was also passed to a boxcar integrator (Brookdale linear gate 9415) which had variable integration times between 1ms and 10s. The gating offset and width was provided by a scan delay generator (Brookdale scan delay generator 9425), which allowed gate widths of between 10ns and 100μs to be selected. The scan delay generator and the DSA were triggered by the same delay generator as described in §5.3.1. The boxcar output was fed to either a chart recorder (Goertz Servoscribe) or a microcomputer (BBC master computer). The DSA was connected *via* a serial IEEE interface to a computer (IBM compatible, Zenith datasystems, 286), which allowed computer control of the D.S.A. and storage of oscilloscope traces. The recorded signal intensity was optimised by changing the gate offset and width. A gate of width 50ns, positioned 2μs after the trigger pulse, was found to be the optimum for detection of the signal from the emission of excited NO_3. The variation of signal intensity with different pressures

of the precursors was also measured at a series of wavelengths. The results, as shown in Fig. 5.4, were used to find the optimum conditions for NO_3 emission.

For radiative lifetime measurements, two different data collection methods were used. The first was to automatically scan the boxcar detection gate over the total decay emission between 1 and 100μs in the time following an excitation pulse. The second was to digitise a 100 shot average of the signal using the DSA. A computer subtraction was performed, removing the laser-only background signal from the emission decay. A portion of the resultant decay could then be selected for further analysis.

5.4 Results

On discharging a mixture of *ca.* 0.6 Torr of F_2/He and adding this to a flow of *ca.* 0.4 Torr of HNO_3/He a signal was recorded. The bottom line (d) in Figure 5.4 shows the excitation spectrum acquired on scanning the wavelength of the probe beam between λ=614nm and 630nm. The intensity of the signal acquired on excitation was linearly dependent on the intensity on the incident probe beam. Figure 5.5 also shows the spectra recorded on successive addition of the various precursors. The lack of signal without the microwave on was taken as an indication of non-excitation of the precursors. The resultant excitation spectrum bears a resemblance to the excitation spectrum of NO_3 as described by Nelson *et al.* (1983b) (See Figure 5.1). The intensity of the emission signal after excitation at λ=623nm was optimised by changing the reactant conditions and linear-gate offset and widths. The resultant emission spectrum for the optimal signal intensity is shown in Figure 5.6. There is an obvious anomaly in this spectrum, since the lower line represents the signal when F atoms are not present, but this should be the baseline which represents solely the change

in output intensity of the laser dye to which the spectrum is normalised. The spurious signal was detectable for up to *ca.* 25 minutes with a small (< 1 Torr) quantity of the F_2/He/HNO_3 mixture isolated in the cell, the signal was identified as the LIF spectrum of NO_2, the excitation spectrum of *ca.* 0.2 Torr of NO_2 (Zhao *et al.*, 1988) being identical to that observed.

The limit of sensitivity of detection for [NO_2] was *ca.* $1x10^8$ molecule cm^{-3}, which is similar to the sensitivity achieved by Dlugocenkcy and Howard (1983) using the light from an Ar^+ laser as the exciting radiation. Our limiting sensitivity was measured by isolation of known concentrations of NO_2 in the cell. The probable source of NO_2 in this simple system is

$$F + HNO_3 \longrightarrow HF + NO_3 \qquad (5.16)$$

$$F + NO_3 \longrightarrow NO_2 + FO \qquad (5.17)$$

$k_{5.17} = 3.0x10^{-11}$ cm^3 $molecule^{-1}$ s^{-1} (Rahman *et al.*, 1988)

The NO_2 produced in reactions (5.16) and (5.17) was adsorbed on the uncoated stainless steel walls of the LIF cell and took as long as 40 minutes to desorb. A perceived problem with the production of HNO_3 vapour for subsequent reaction with F atoms in order to produce NO_3 has been the presence of NO_2 impurities. There are two methods commonly used to produce HNO_3 vapour. The first is the action of conc.H_2SO_4 on either $NaNO_3$ or KNO_3 under vacuum, to produce $HNO_3(\ell)$ which is then purified by trap to trap distillation (e.g. Crowley *et al.*, 1990). The purified $HNO_3(\ell)$ is vaporised by passing a stream of carrier gas through the liquid held at a suitable temperature. Sander (1986) has shown by direct U.V. absorption measurements that [HNO_3] is consistent with complete saturation of the carrier gas. This procedure suffers from being tedious and slow.

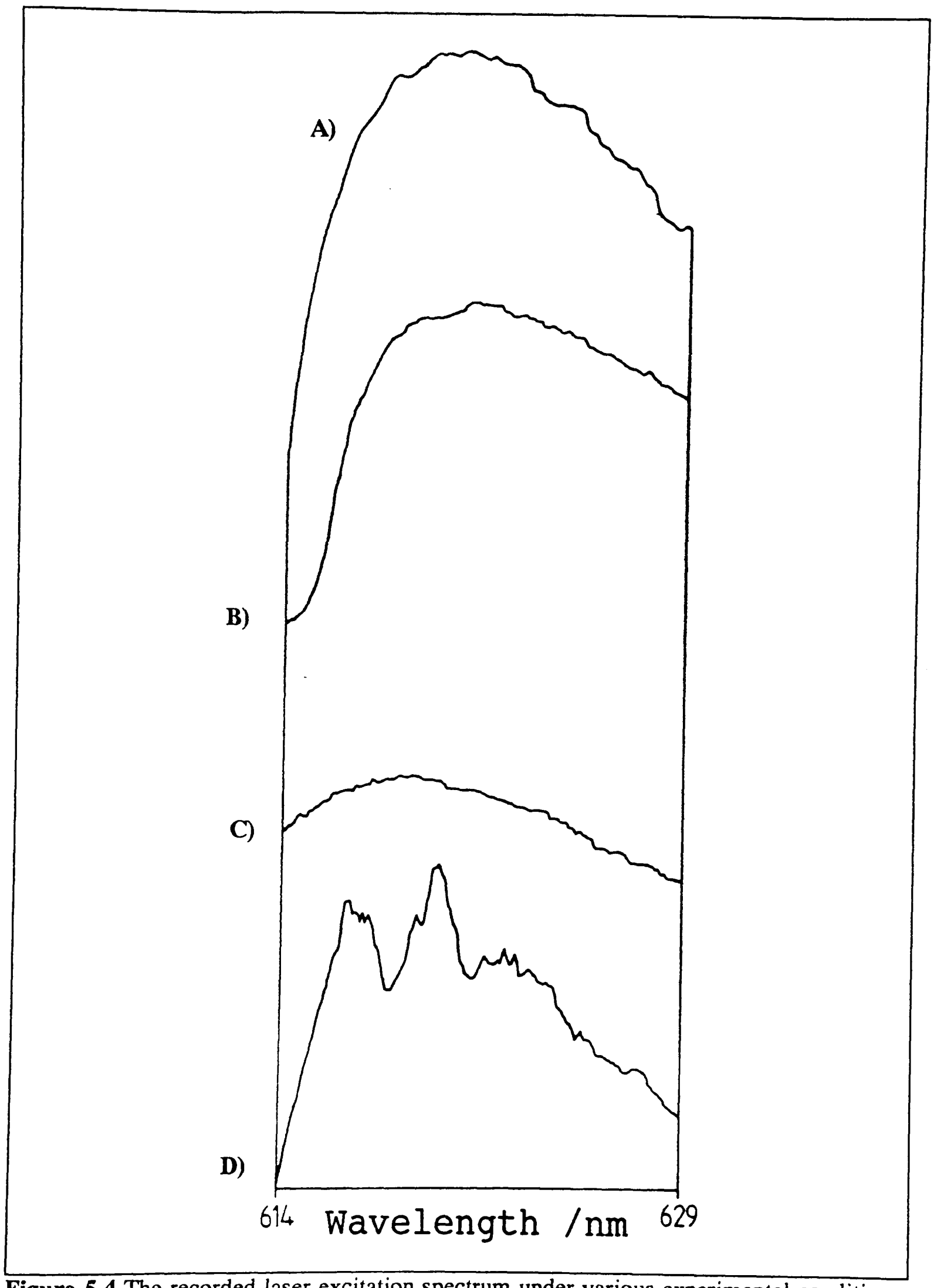

Figure 5.4 The recorded laser excitation spectrum under various experimental conditions; a) laser only; b) ca. 0.4 Torr HNO_3/He; c) HNO_3/He/F_2 = 1.1 Torr; d) with F atom production.

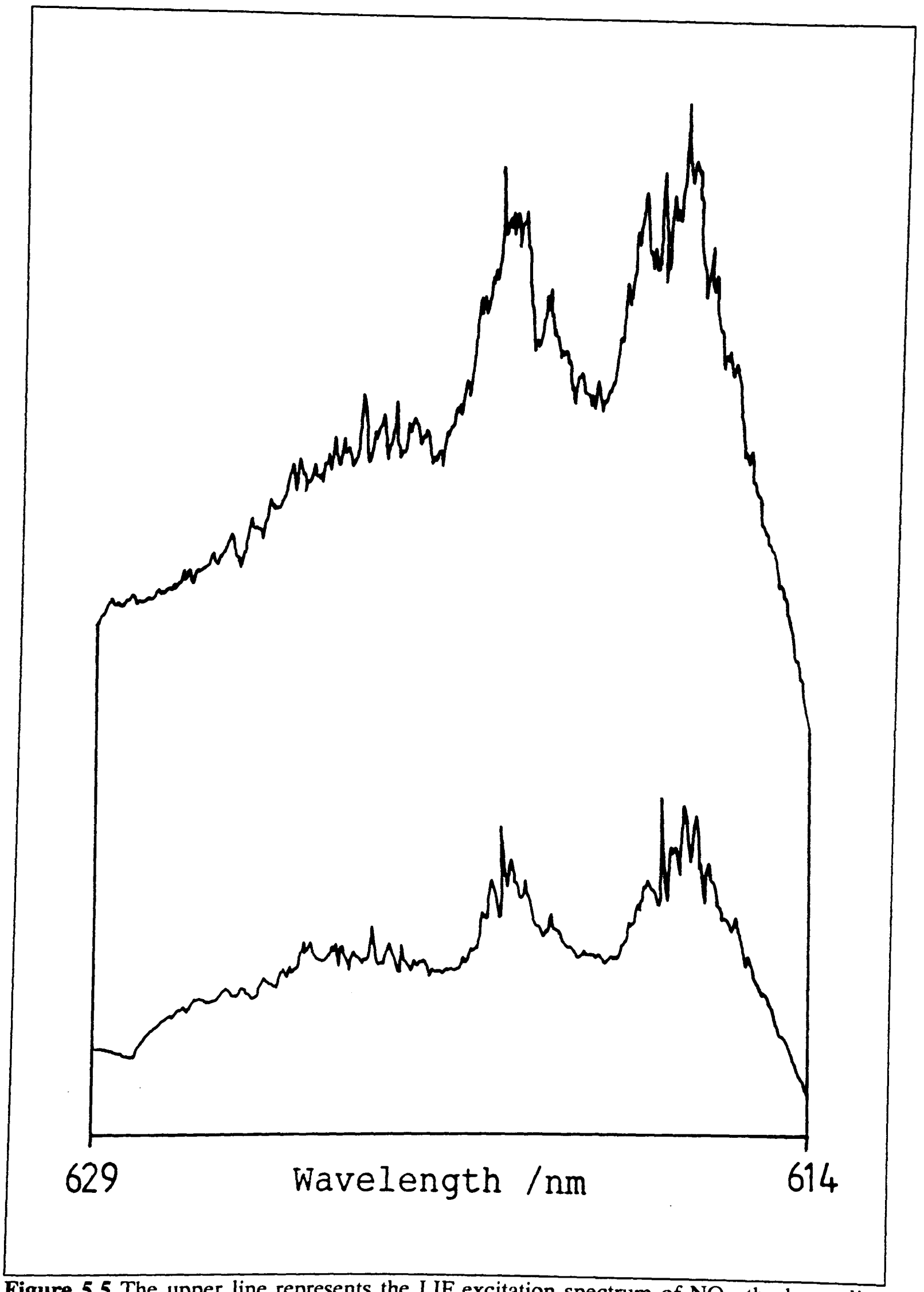

Figure 5.5 The upper line represents the LIF excitation spectrum of NO_2; the lower line represents the laser only background signal (See text).

The second, more recent, method (as used in Chapter 2) is to pass a stream of carrier gas through a 2:1 mixture of conc.H_2SO_4/conc.HNO_3. There has long been the feeling that this method was unreliable because of the unknown amount of a trace impurity of NO_2. Therefore, it was recommended that the mixture was bubbled for a prolonged period before use and kept at temperatures of -10°C. In these experiments, where the second method was used for production of HNO_3 vapour, we were able, over a period of up to 20 minutes, while bubbling freshly prepared mixtures of HNO_3/H_2SO_4 held at -12°C, to follow the NO_2 emission signal following excitation at λ=620nm before [NO_2] dropped below the detection limit.

5.4.1 Detection of NO_3

On reduction of [F] (pressure of F_2/He *ca.* 0.1 Torr), the wavelength dependence of the fluorescence signal changed. Figures 5.6 and 5.7 show the excitation spectra for NO_3 over the wavelength region λ=619nm to 679nm (R101). All the spectra presented here are normalised to the dye laser power curves with wavelength calibration from the grating in the dye-laser. The position of the bands present in the excitation spectrum exciting at around λ=623nm are in good agreement with those presented by both Nelson *et al.* (1983b) and Ishiwata *et al.* (1983). At λ>642nm, there is a rapid fall-off in the lasing efficiency of the R101 dye, but the spectral features from excitation at λ=671.2 and λ=676.9nm are accentuated by an increase in the incident dye-laser power in this region. These features are relatively weak in the absorption spectrum. For comparison, the spectrum by excitation in the region of λ=662nm (See figure 5.8) using the laser output from the DCM dye (c.f. Hammer *et al.*, 1986) does not highlight these weaker bands. DCM has a constant dye laser power curve in this region. The positions of the bands are listed in Table 5.1.

Table 5.1 The position of bands in the NO_3 excitation spectrum

λ[a] nm	Laser Dye	λ[b] nm	λ[c] nm	Assignment[b] (See Text)
676.9	R101	-	-	-
671.2	R101	-	-	-
661.8	R101/DCM	661.6	661.8	0-0[d]
651.0	R101	-	-	-
637.0	R101	637.9	636.8	ν_1-352
629.4	R101[e]	627.8	627.7	ν_2
626.9	R101[e]			
623.5	R101	623.5	623.5	ν_1

[a] uncalibrated, see text; [b] From Nelson *et al.*, 1983b; assignments assume C_{2v} ground state symmetry; [c] From Ishiwata *et al.*, 1983; [d] Assignment from Ramsay, 1963; [e] The band is very diffuse; no obvious band centre.

In absorption, the nitrate radical exhibits a structured electronic spectrum (Ramsay, 1963) consisting of *ca.* 20 diffuse bands in the visible region in the range λ=400 to 665nm. These are similar to those shown in the excitation spectra (See figures 5.6-5.8). All of the bands even under high resolution were found to be diffuse (Auty, 1990). This observation may suggest that the molecule predissociates in the excited state. However, that suggestion is not consistent with LIF lifetime data (See §5.4.2 and Nelson *et al.*, 1983a). The apparent diffuseness in both absorption and emission is more likely to be attributable to the rotational level density in the ground and excited state, which may be extremely high, leading to sequence congestion. Assignment of the spectral bands is difficult because of the uncertainty about the nature of the electronic states involved in the spectra (Wayne *et al.*, 1991).

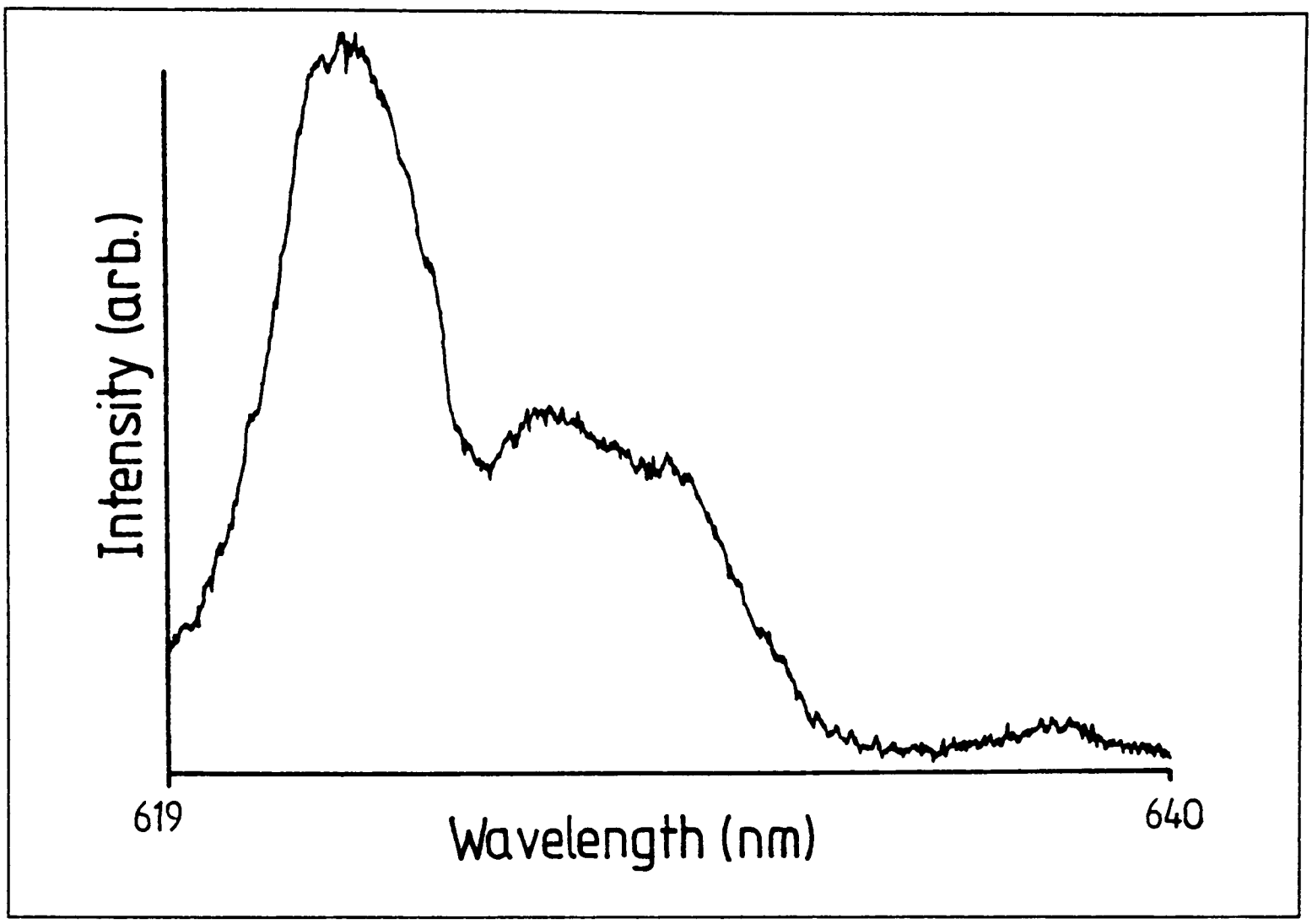

Figure 5.6 The fluorescence excitation spectrum of NO_3 centred at λ=623nm (R101).

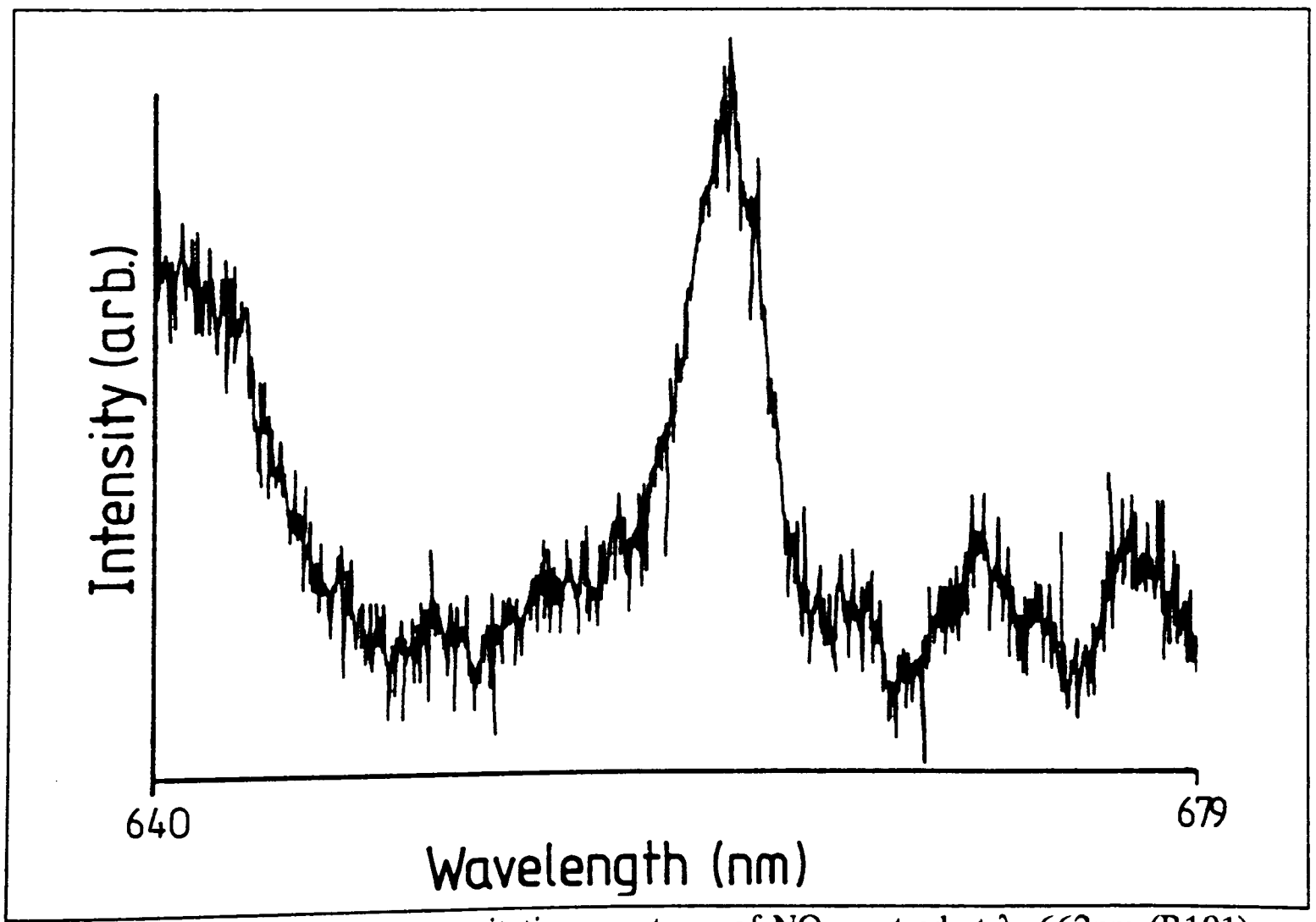

Figure 5.7 The fluorescence excitation spectrum of NO_3 centred at λ=662nm (R101).

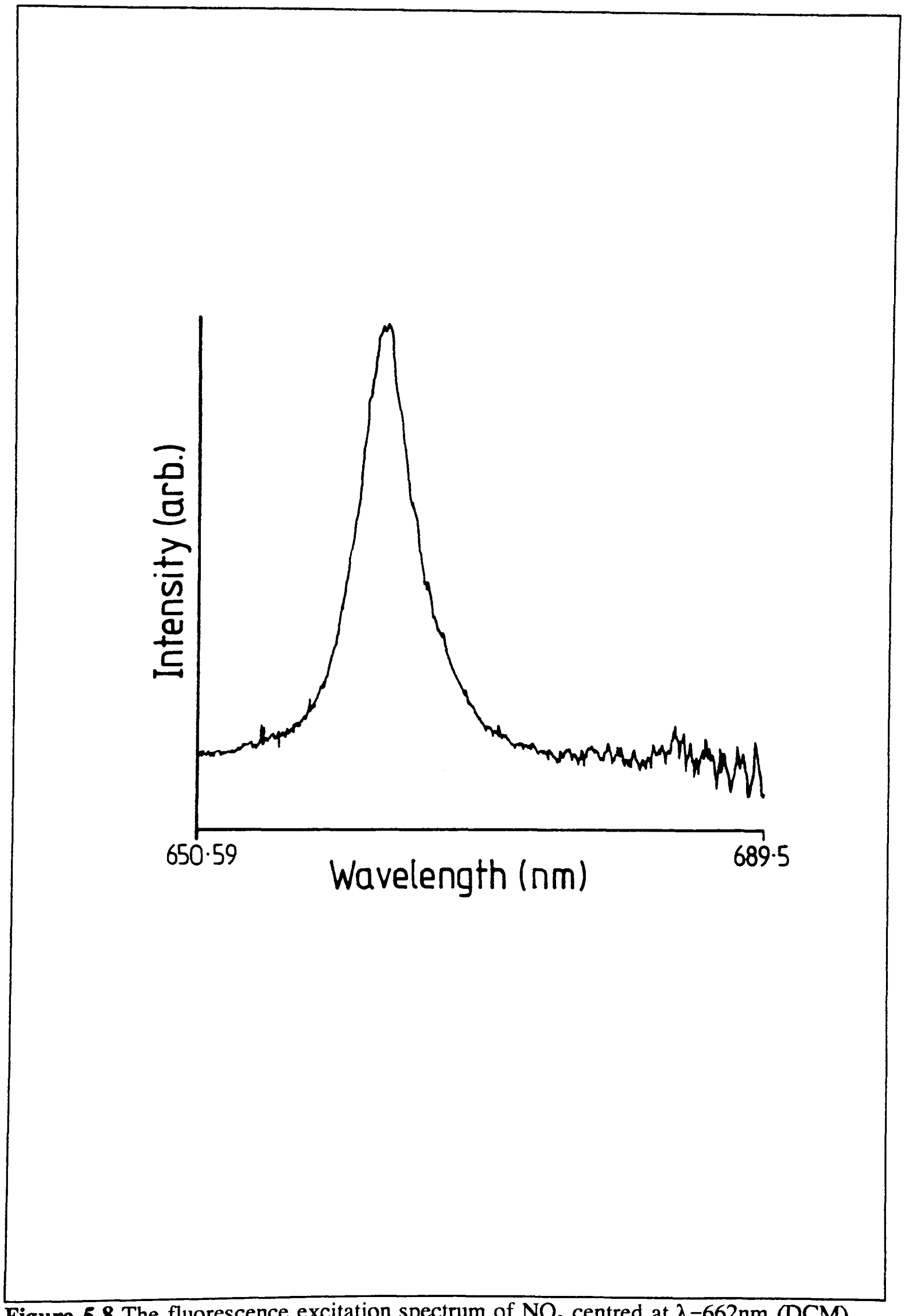

Figure 5.8 The fluorescence excitation spectrum of NO_3 centred at λ=662nm (DCM).

5.4.2 Lifetime of emission decays for excited NO_3

The lifetimes of the NO_3 fluorescence were measured as described in §5.3.4. After computer subtraction of the laser-only background signal from the fluorescence signal, a portion of the fluorescence decay was selected for analysis. Under our experimental conditions this decay was found to be exponential with the longest measured decay times being *ca.* 5μs. The full results are shown in Table 5.2, and an example decay and signal to background ratio are shown in Fig. 5.9 and Fig. 5.10. The signal to noise ratio for the emission after excitation at λ=623nm was *ca.* 450:1, which fell off to 23:1 at λ=672nm using R101. Our experimental conditions P_T = 1.8 Torr are similar to those used in the kinetic experiments described in Chapter 2, average $[NO_3]$ under these conditions where *ca.* $5x10^{12}$ molecule cm^{-3}. Given the S/N ratios of both experiments, the theoretical lower limit for measurement of NO_3 by LIF would be *ca.* $1x10^{10}$ molecule cm^{-3}. The wavelength dependency of the decay time was measured over λ=621 to 633nm and found to be linear i.e. the decay times showed little variance with wavelength, as shown in Fig. 5.11.

In order to understand the dependency of the signal on the concentration of the various gas-phase constituents we must consider the effect of quenching on the NO_3 fluorescence. In previous studies of the fluorescence lifetimes of excited NO_3 ($^2E'$) (Nelson *et al.*, 1983a), at lower pressures (P_T < 175mTorr), the decays were found to be bi-exponential. The long-lived exponential part of the decay (τ_{long}, up to 340μs) was taken in order to determine collision-free lifetimes. A plot of the inverse of the lifetime (τ) as a function of the concentration of a quencher gives an intercept which in the absence of any other quenchers is the collision-free lifetime. The plot is commonly known as a Stern-Volmer plot (e.g. Wayne, 1988).

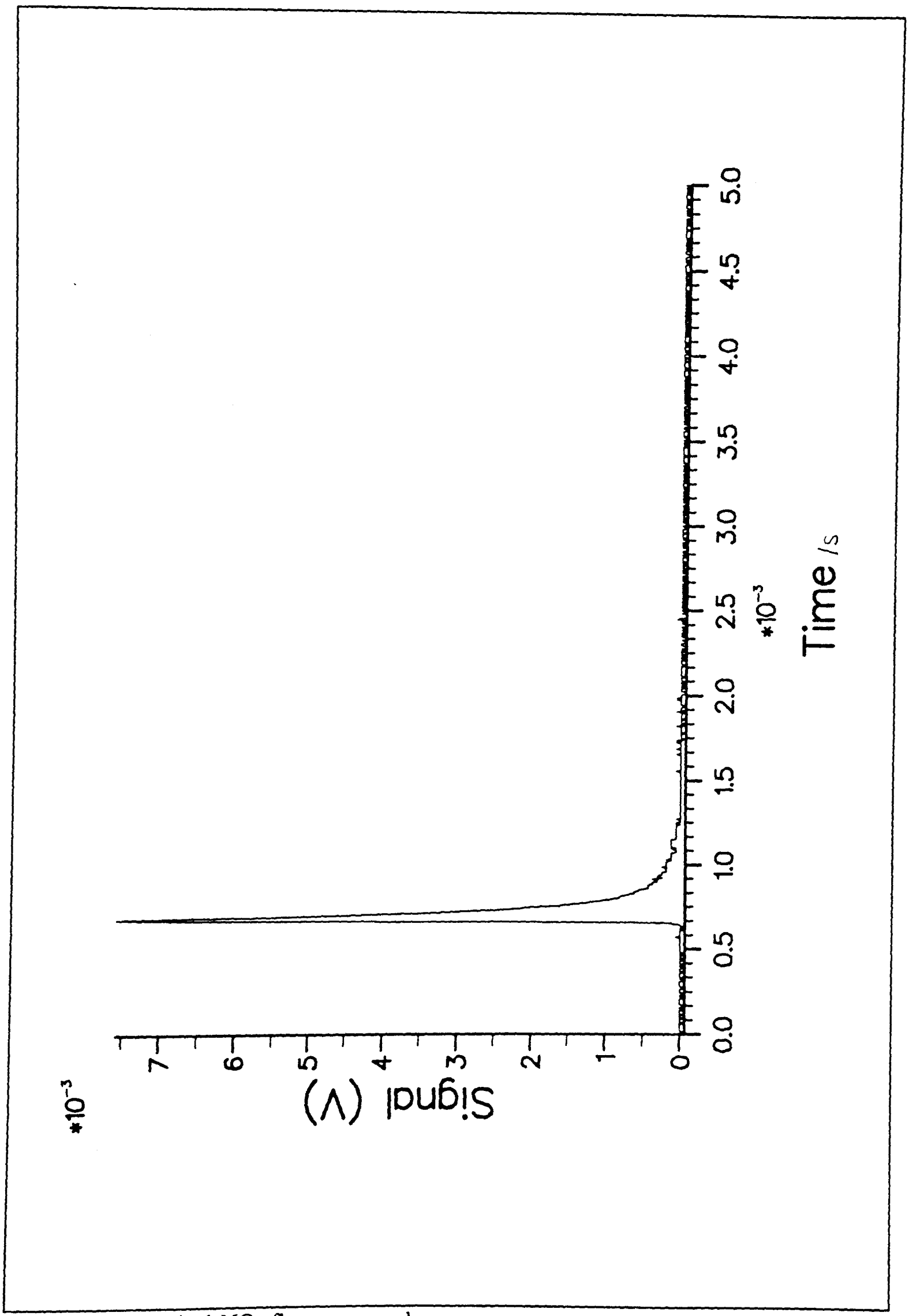

Figure 5.9 A typical NO_3 fluorescence decay.

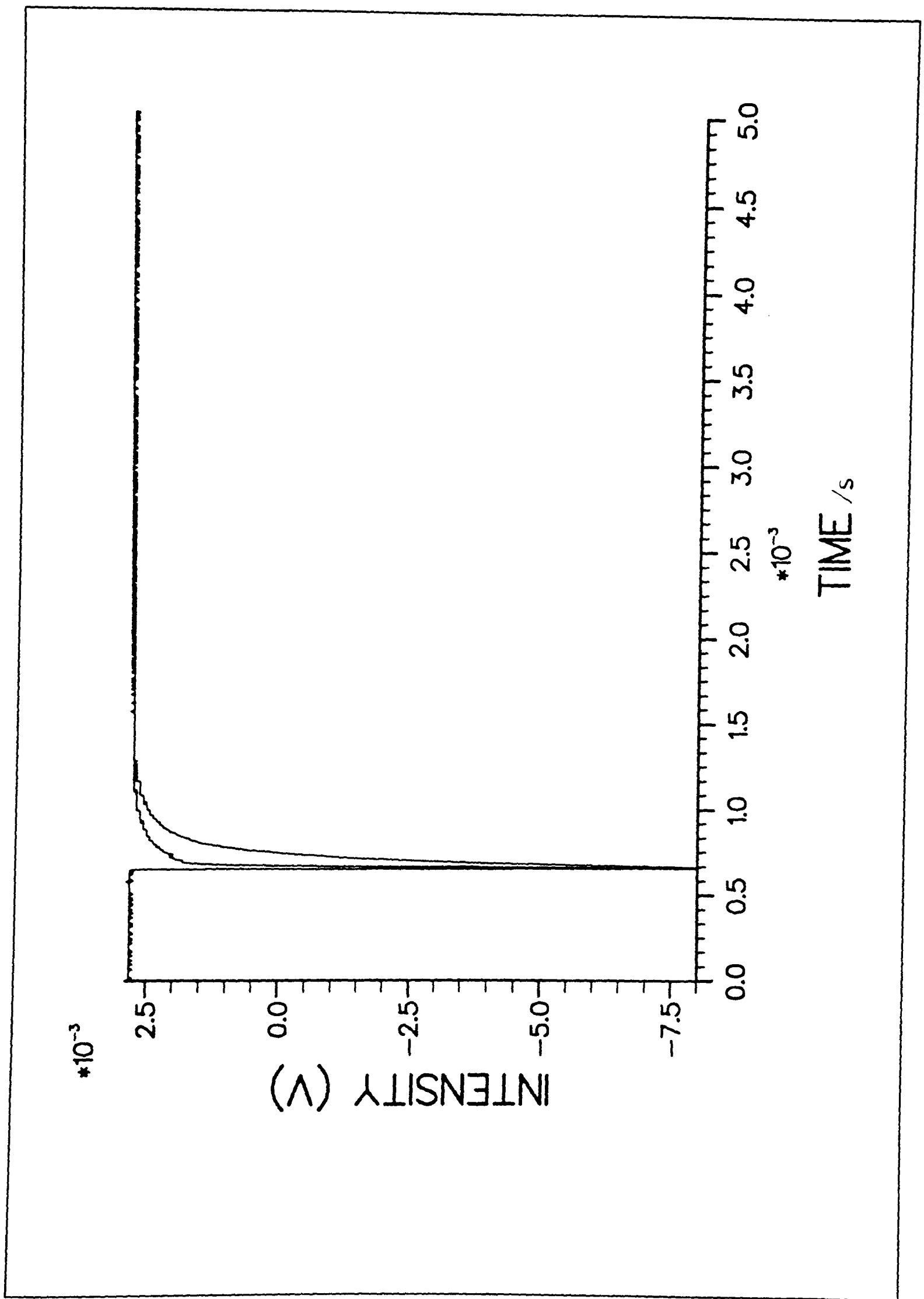

Figure 5.10 A typical NO_3 emission signal-to-background following excitation at λ=623 nm.

Table 5.2 - The experimentally measured fluorescence lifetimes, from excitation at λ=623nm.

Run	P(HNO_3/He) Torr	P(Total) Torr	τ μs	1/τ s^{-1}
19AULT1	1.89	2.06	0.12	$8.6x10^6$
19AULT3	1.08	1.19	0.16	$6.3x10^6$
19AULT5	4.00	4.41	0.07	$14.0x10^6$
19AULT6	0.213	0.247	0.55	$1.8x10^6$
19AULT7	3.07	3.37	0.07	$14.0x10^6$
19AULT8	0.64	0.74	0.17	$6.0x10^6$
19AULT9	2.58	2.84	0.08	$11.9x10^6$
19AULT10	1.61	1.77	0.12	$8.3x10^6$
19AULT11	1.87	2.27	0.07	$14.0x10^6$
19AULT13	1.89	2.29	0.12	$8.9x10^6$
19AULT14	1.89	2.08	0.09	$10.26x10^6$
19AULT15	4.49	4.69	0.08	$13.27x10^6$
19AULT16	1.19	1.39	0.14	$6.9x10^6$
19AULT17	1.95	3.15	0.07	$13.53x10^6$

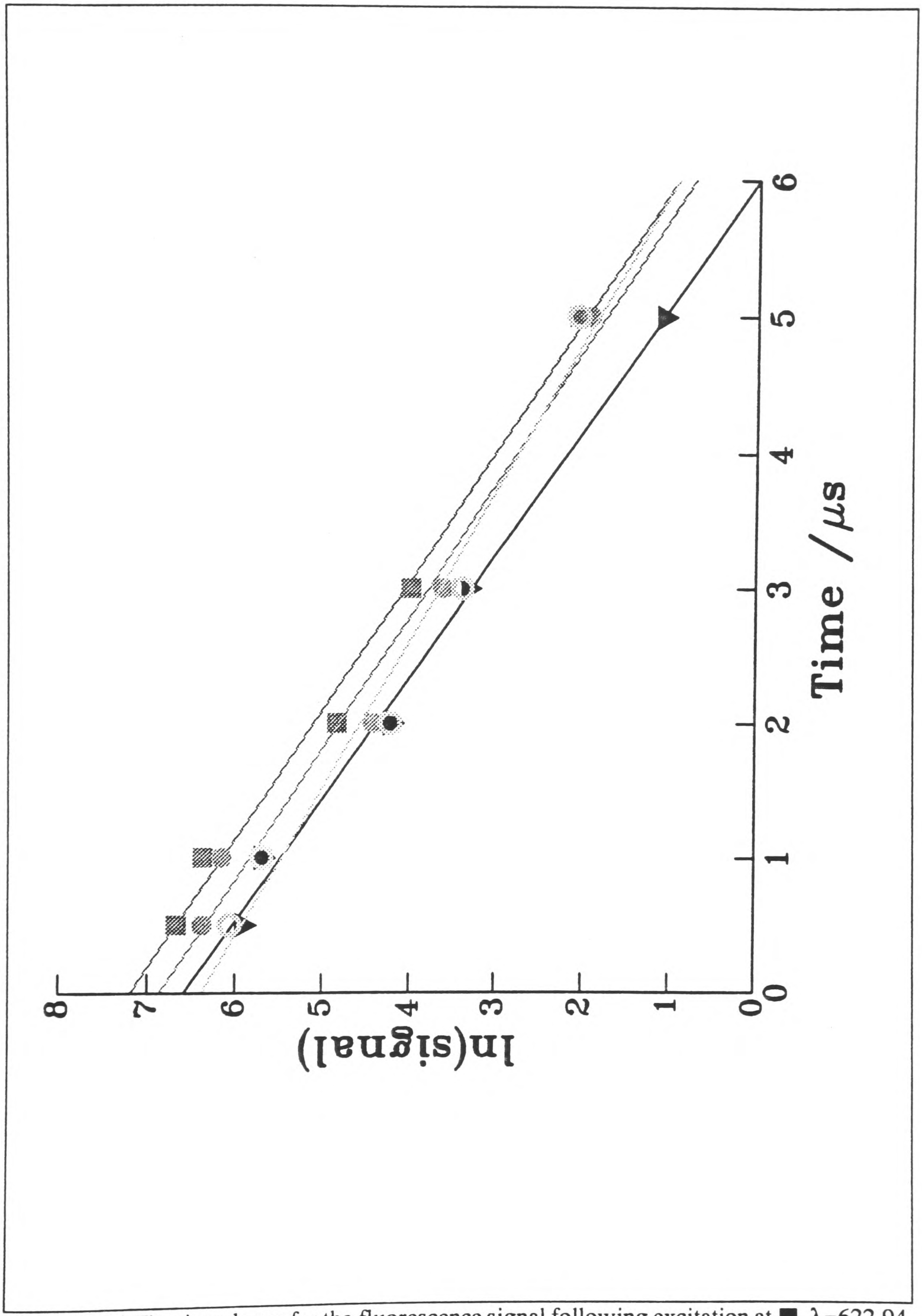

Figure 5.11 The time decay for the fluorescence signal following excitation at ■, λ=622.94, ○, λ=623.11, ●, λ=624.24 and ▾, λ=626.99 (all nm).

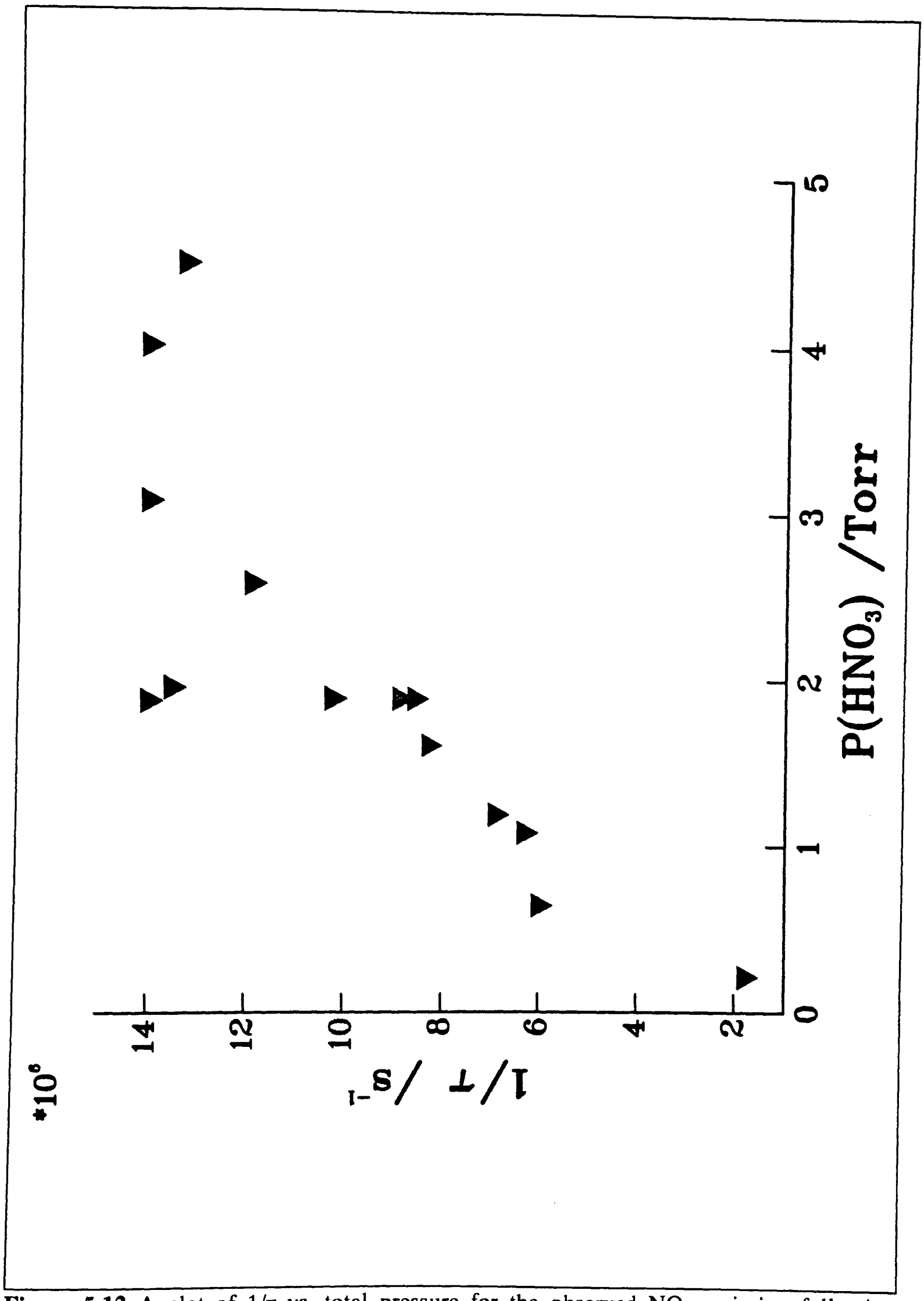

Figure 5.12 A plot of $1/\tau$ *vs.* total pressure for the observed NO_3 emission following excitation at λ=623nm.

The bimolecular fluorescence quenching rate constants for NO_3 which have been previously estimated using this method are shown in Table 5.3 It can be seen from Table 5.3 that both HNO_3 and C_3H_8 quench excited $NO_3(^2E')$ at a rate very near the hard-sphere collision rate, whereas N_2 and O_2 are a factor of 10-20 less efficient. This means that under our experimental conditions of pressure and concentration the fluorescence quenching (k_Q) is controlled solely by HNO_3 electronic quenching as $k_Q[HNO_3] >> k_{rad.}$.

Table 5.3 - The rates of fluorescence quenching for NO_3 (from Nelson *et al.*, 1983a)

Quencher	k_Q [a] (10^{-10} cm^3 molecule^{-1} s^{-1})
He	0.12±0.01
N_2	0.17±0.02
O_2	0.21±0.02
O_3	0.39±0.03 [b]
Propane	1.09±0.16
HNO_3	3.07±0.24

a) errors are quoted as ±2σ b) From Ishiwata *et al.*, 1983

Figure 5.12 shows the result of plotting $P(HNO_3/He)$ versus $1/\tau$ for NO_3 emission, in essence a Stern-Volmer plot. Unfortunately, there is insufficient data in the low pressure region to make the extrapolation to zero-pressure with any degree of certainty. In previous studies, collision-free lifetimes for excited $NO_3(^2E')$ have been determined to be $(2.8\pm0.3)\times10^{-6}$ s and $(3.4\pm0.2)\times10^{-4}$ s by Ishiwata *et al.* (1983) and Nelson *et al.* (1983a). The lifetimes measured by Nelson *et al.* (1983a) are anomalously long and they suggest there is mixing between the vibrational levels of the excited state and the higher lying levels of the ground state (Hirota *et al.*, 1991). The possible interference of NO_2 emission was considered in the lifetime

studies. NO_2 like NO_3 has an apparently anomalously long collision free lifetime ($\tau > 23\mu s$) (Zhao *et al.*, 1989), attributable to vibronic mixing of the ground state and the excited state (Persch *et al.*, 1988, Lehmann *et al.*, 1988). The lifetime is *ca.* 15 times shorter than the radiative lifetime of NO_3 (Nelson *et al.*, 1983a). This and the previously noted sensitivity for detection of NO_2 by LIF, if combined with comparable quenching rates for excited NO_2, would suggest there should be little interference from small concentrations of NO_2 in the determination of the lifetime of NO_3.

The wavelength dependencies of both the effective decay and the signal intensity *versus* pressure over the range λ=623nm to λ=672nm show the same characteristics. The lifetime decays measured at different wavelengths (Figure 5.13) have comparable τ of $\sim$0.1μs. These data may be interpreted in light of the previously described photodissociation results (§5.2.1). That is, all the measurements on the first several bands near the electronic origin (0-0 at λ=662nm) of the NO_3 spectrum (λ=620 to 670nm) are consistent with a zero quantum yield for unimolecular photolysis. Our data on various spectral properties of the NO_3 fluorescence are also consonant with this result.

5.5 Comparison of methods used for detection of NO_3 in kinetic studies

We began this study with the aforementioned aim of looking at the viability of LIF detection of NO_3 for discharge-flow type kinetic studies. It is worth considering in the light of our results the advantages and disadvantages of the commonly used methods of detection for NO_3 in such experiments. Table 5.4 compares the various techniques used for detection of the nitrate radical in laboratory based studies.

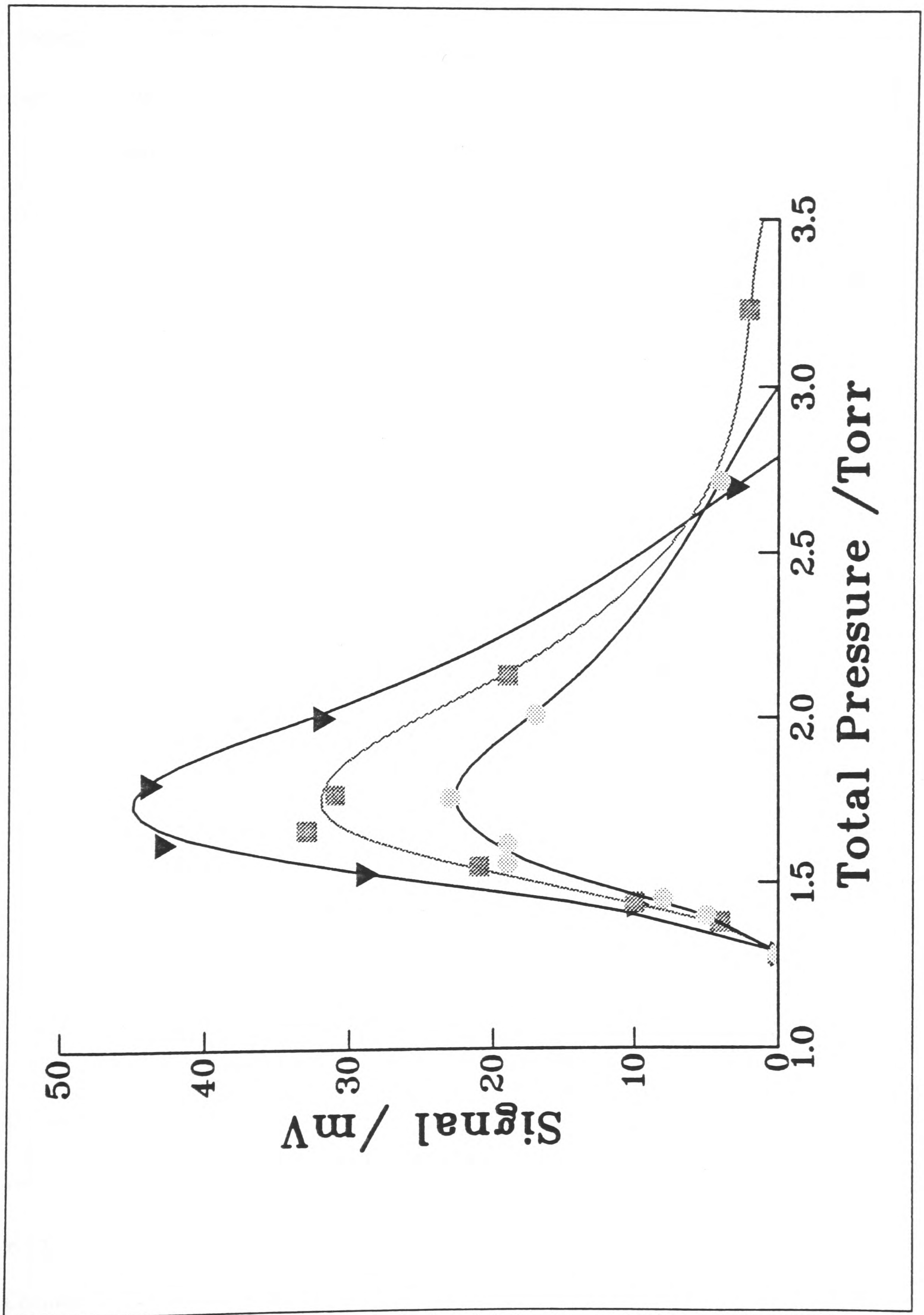

Figure 5.13 A plot of total pressure *vs.* signal following excitation at ▾, λ=623 (reduced by a factor 10), ■, λ=662, ●, λ=672 (all nm).

Of these, the most commonly used technique for detection of NO_3 is that of optical absorption. The nitrate radical was probably one of the first transient species to be detected by optical absorption, over 100 years ago, by Hautefeuille and Chapuis (1881, 1882a,b). One of the first applications of their discovery to kinetics was to follow $[NO_3]$ in shock-tube studies (Schott and Davidson, 1958).

Table 5.4 - A comparison of the limiting sensitivity for the various methods used for the detection of NO_3 in kinetic studies.

Technique	Principle used	Limiting detectabilty molecule cm^{-3}	Notes
Optical Absorption	Absorption	$5x10^{10}$	At λ=661.9nm given a 10m pathlength and σ= $2x10^{17}$ $cm^3molecule^{-1}$
Laser-induced fluorescence	Emission	$1x10^{8}$	(Dlugokencky and Howard, 1988)
Infrared absorption	Absorption	$1x10^{12}$	With a pathlength of 10m and a fractional absorbance of 10^{-3} (Friedel and Sander, 1987)
Mass spectrometry	Ionisation	$4x10^{11}$	(Schönle *et al.*, 1987)

Absolute sensitivities in absorption experiments depend crucially upon the sources of noise in the experiment and the time resolution required. Some of the problems in absorption detection are overcome by using multi-pass optics to increase pathlength, for which low-divergence laser sources are particularly useful, e.g. Ravishankara *et al.* (1982) used an argon-ion pumped dye-laser system to achieve up to 170 passes. The ultimate sensitivity in absorption experiments is limited by the accuracy with which can be measured I/I_o (See Chapter 2); quantities of which are very similar when the absorption is low. There is also the auxiliary problem in absorption spectroscopy of species having overlapping spectra; in

the case of NO_3 in the visible region there is the possibility of interference from NO_2 absorptions. As shown in Table 5.4, optical absorption is reasonably sensitive with a detection limit of *ca.* $5x10^{10}$ molecule cm^{-3}.

The second absorption technique for detection of NO_3 is that using infrared (IR) radiation. IR absorption measurements possess the great virtue of specificity for small species but there is the possibility of interference from other N-containing molecules (Friedl and Sander, 1987). The problem with this method of detection is not only the cost, but the difficulty in achieving the requisite S/N ratios for the small fractional absorbances (*ca.* 10^{-3}) obtainable in the IR region.

Mass spectrometry (MS) has been used for detection of the parent ion at m/e=62 from low energy ionisation of NO_3 (e.g. Schönle *et al.*, 1987). Sampling is by normal molecular beam methods, with tuning-fork modulation of the sample beam. Electron impact energies of *ca.* 25eV are normally employed in such studies. The quoted sensitivity for $[NO_3]$ is about $4x10^{11}$ molecule cm^{-3}. The sensitivity seems to be limited by contributions to the m/e=63 peak from heterogenous reactions between F_2 and HNO_3 used for the NO_3 source. A general advantage MS has over the other techniques is versatility, as it can also be used to monitor products from reactions (e.g. Wille *et al.*, 1990).

In principle, of the four methods used for the detection of NO_3, LIF is the most attractive. It has comparably better sensitivity and lacks the problems of selectivity. It has been further demonstrated in this chapter that the emission from excitation both at λ=623nm and λ=662nm is relatively easily detectable over a wide range of discharge-flow type conditions. The main

disadvantage of LIF detection in the case of NO_3 would be the difficulty of extracting absolute concentrations. This is offset by the greater ability to obtain pseudo-first order conditions with a wide range of co-reactants. Another possible disadvantage of LIF generated emission detection may be the effect of reactant fluorescence quenching. As shown in §5.4.2, HNO_3 quenches the fluorescence at nearly the gas-kinetic rate, but even at fairly large [HNO_3] the fluorescence quantum yield is large enough for there to be some detectable emission. A further modification to the LIF detection of NO_3 could be envisaged. As the emission spectrum of NO_3 extends to longer wavelengths than the excitation wavelength; any of these bands could be measured without interference from the exciting radiation.

5.6 Conclusions

The purpose of these experiments was to demonstrate the applicability of LIF as a method of detection of NO_3 in a flow tube. Hence, the experiments were carried out under experimental conditions of pressure and concentration of precursors similar to those used in the discharge-flow experiments described in Chapter 2. The results of our LIF experiments seem concordant with the premise that LIF is a 'well-behaved' (Wayne *et al.*, 1991) experimental method for detection of NO_3 in flow-type experiments. Because of the aforementioned application of this work, the data presented were not taken under ideal conditions for LIF lifetime studies but are still valuable in understanding the limitations in the application of this method to flow studies. The spectroscopic data presented are in agreement with the excitation spectra in the literature. In conclusion, it can be seen that of all the available techniques for detection of NO_3 under flow conditions, LIF excitation at either λ=623nm or λ=662nm seems to offer a viable alternative to optical absorption.

Appendix I

The Photoelectron spectra of the halobutenes

I.I Glossary of terms

1C1B	1-chloro-1-butene
2C1B	2-chloro-1-butene
3C1B	3-chloro-1-butene
1C2B	1-chloro-2-butene
1CMP	1-chloromethylpropene
3CMP	3-chloromethylpropene
2B2B	2-bromo-2-butene
3B1B	3-bromo-1-butene
He I	Ionising radiation He Iα (λ=58.4nm)
He II	Ionising radiation He IIα (λ=30.3nm)
K.E.	Kinetic energy
I.E.	Ionisation energy (potential)
eV	electron volts

I.II The spectra

Both the He I and He II PE spectra of the compounds, listed in §I.I, are presented here. The individual spectra are discussed in §3.6.

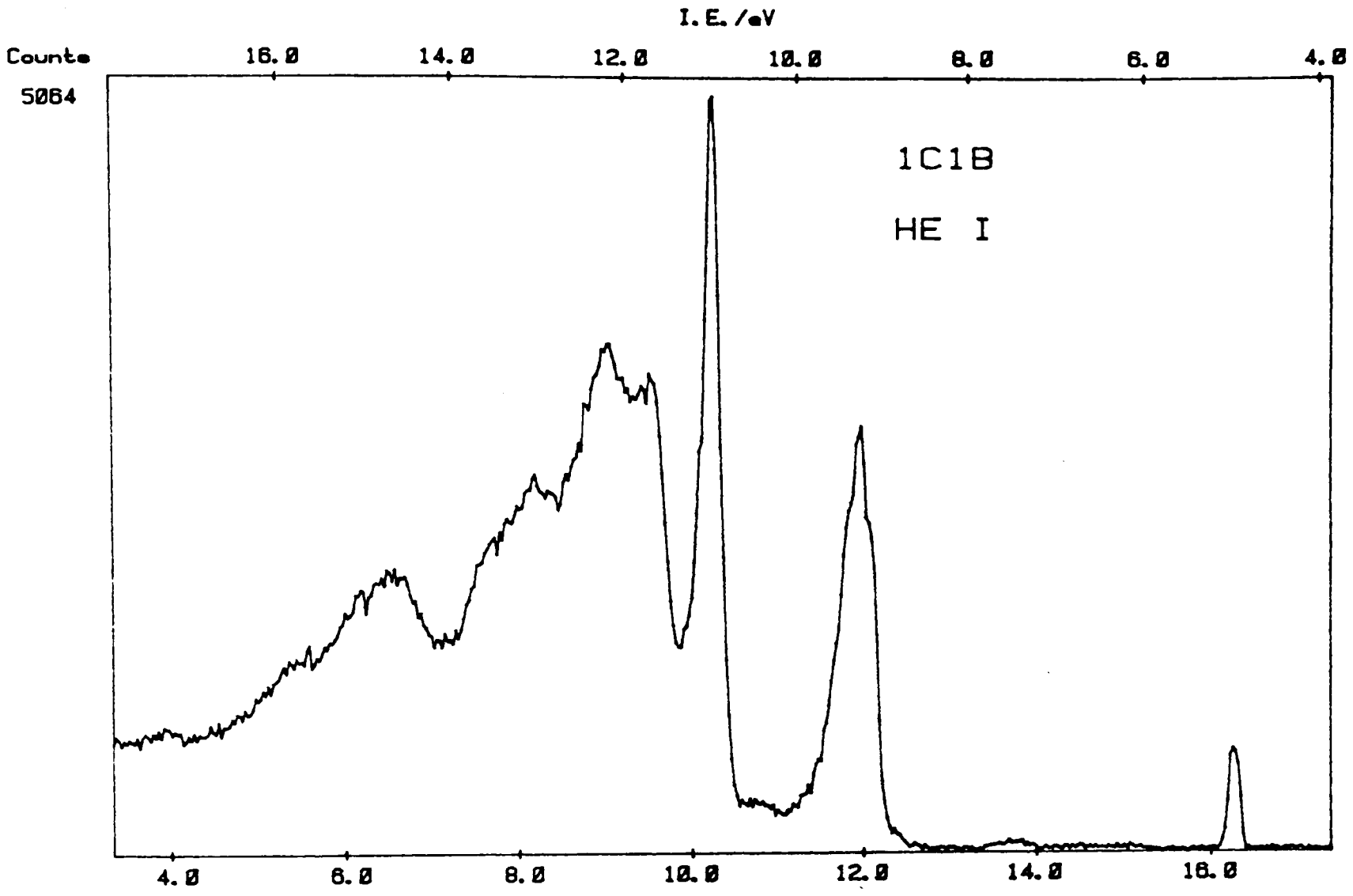
I.E. /eV
Counts
5064
16.0
14.0
12.0
10.0
8.0
6.0
4.0
1C1B
HE I
4.0
6.0
8.0
10.0
12.0
14.0
16.0
K.E. /eV
I.E. /eV
Counts
1412
19.0
17.0
15.0
13.0
11.0
9.0
1C1B
HE II
20.0
22.0
24.0
26.0
28.0
30.0
32.0
K.E. /eV

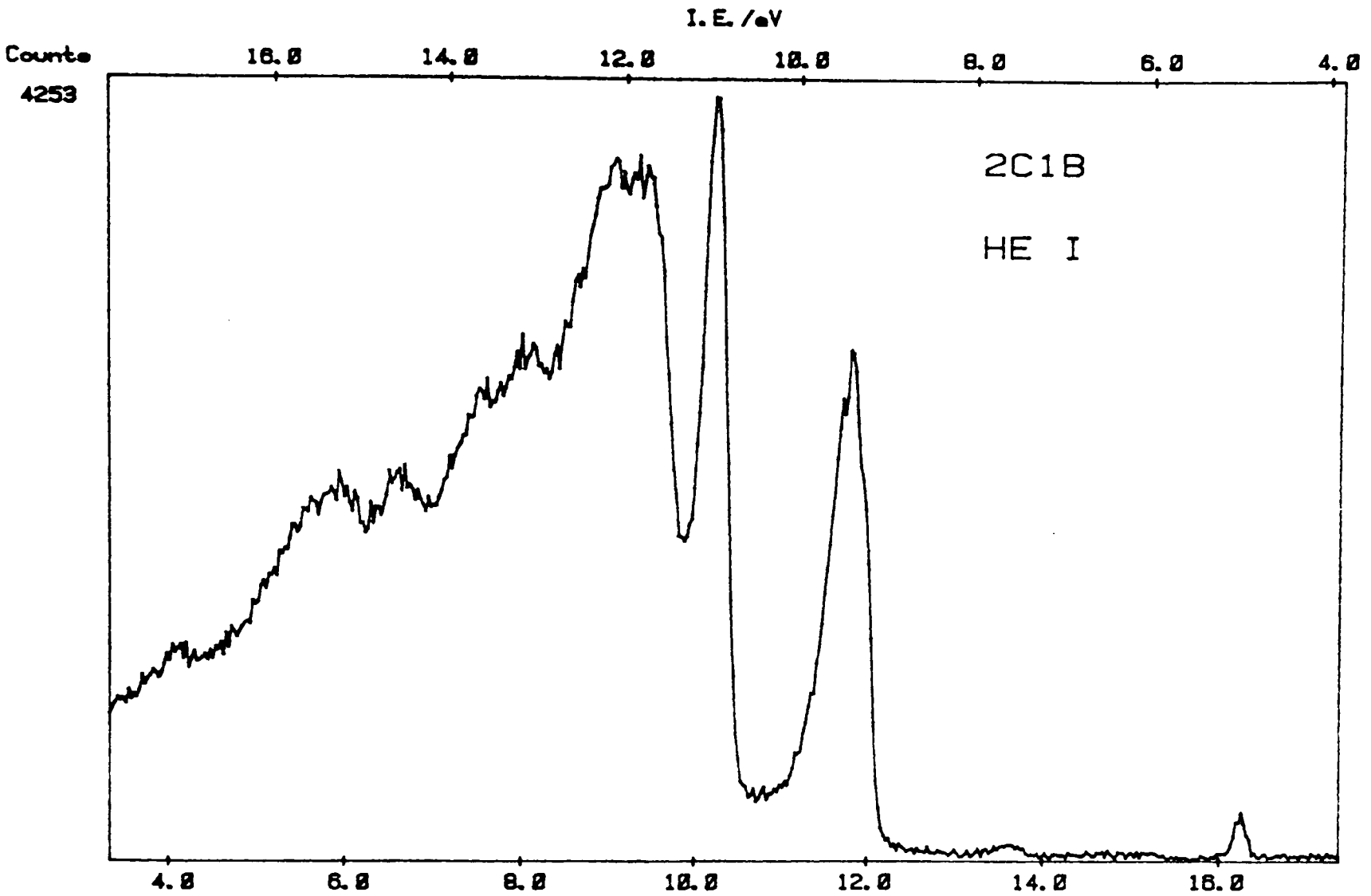
I.E./eV
Counts
4253
16.0
14.0
12.0
10.0
8.0
6.0
4.0
2C1B
HE I
4.0
6.0
8.0
10.0
12.0
14.0
16.0

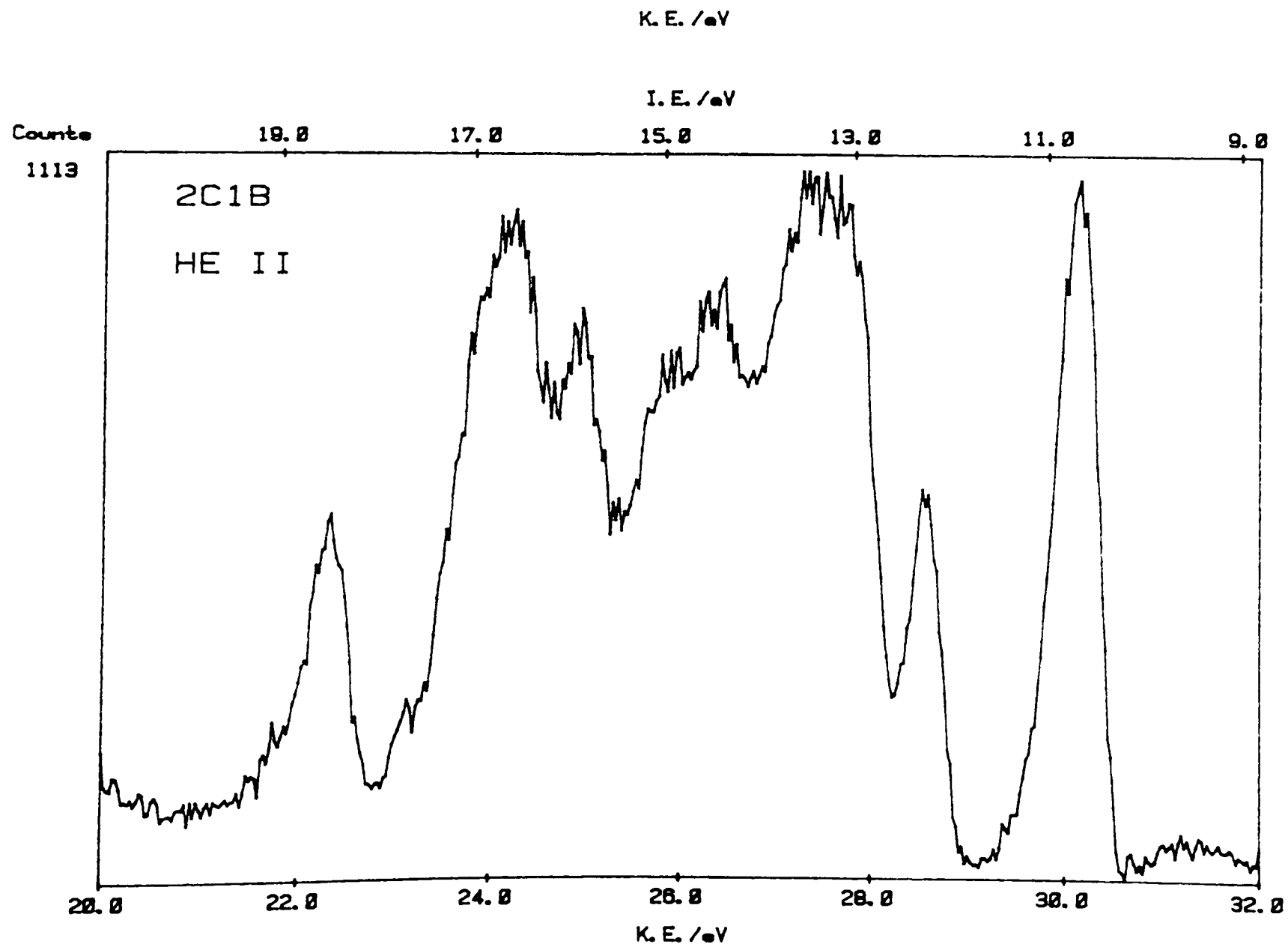
K.E./eV
I.E./eV
Counts
1113
19.0
17.0
15.0
13.0
11.0
9.0
2C1B
HE II
20.0
22.0
24.0
26.0
28.0
30.0
32.0
K.E./eV

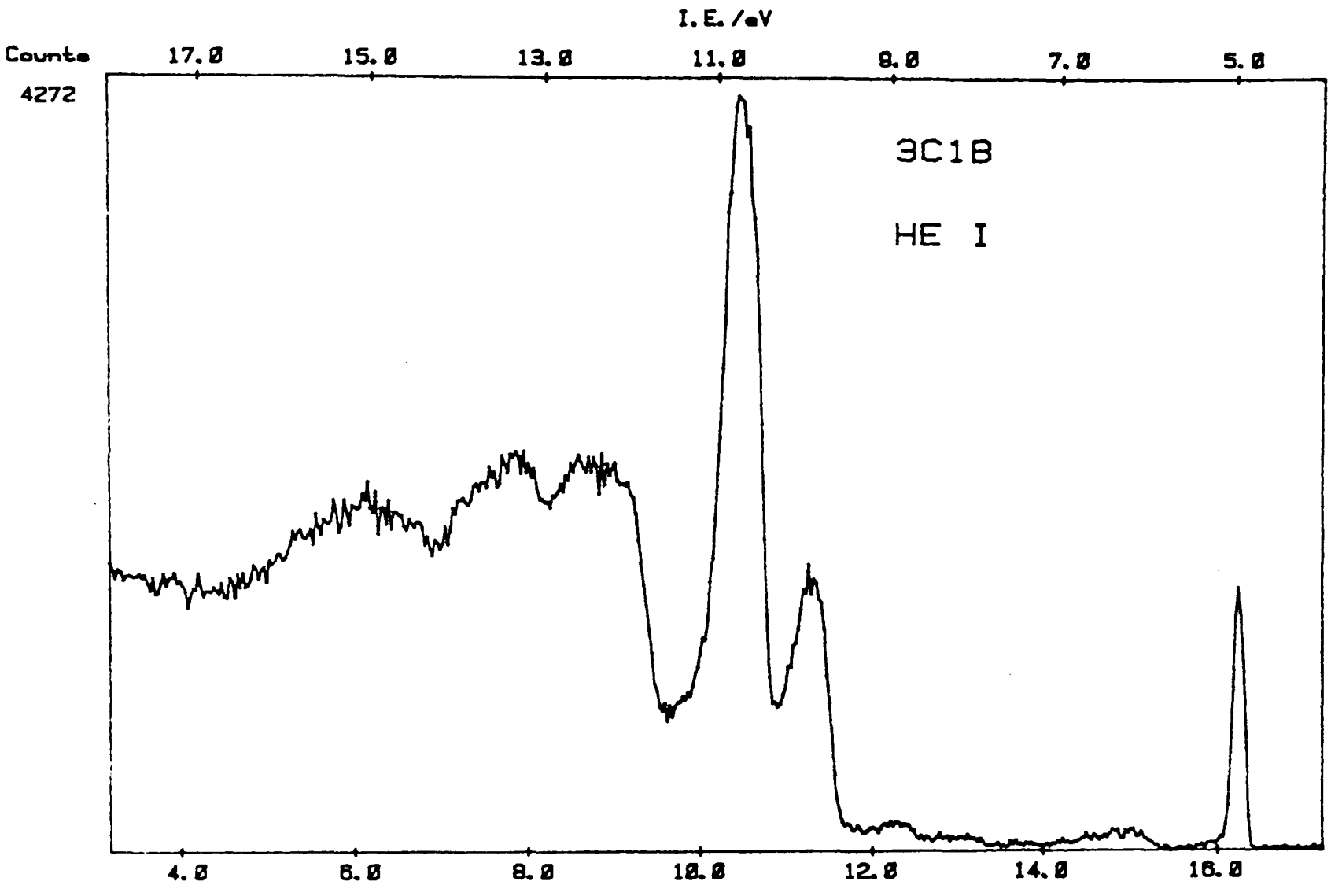
I.E. /eV
Counts
4272
17.0
15.0
13.0
11.0
9.0
7.0
5.0
3C1B
HE I
4.0
6.0
8.0
10.0
12.0
14.0
16.0
K.E. /eV

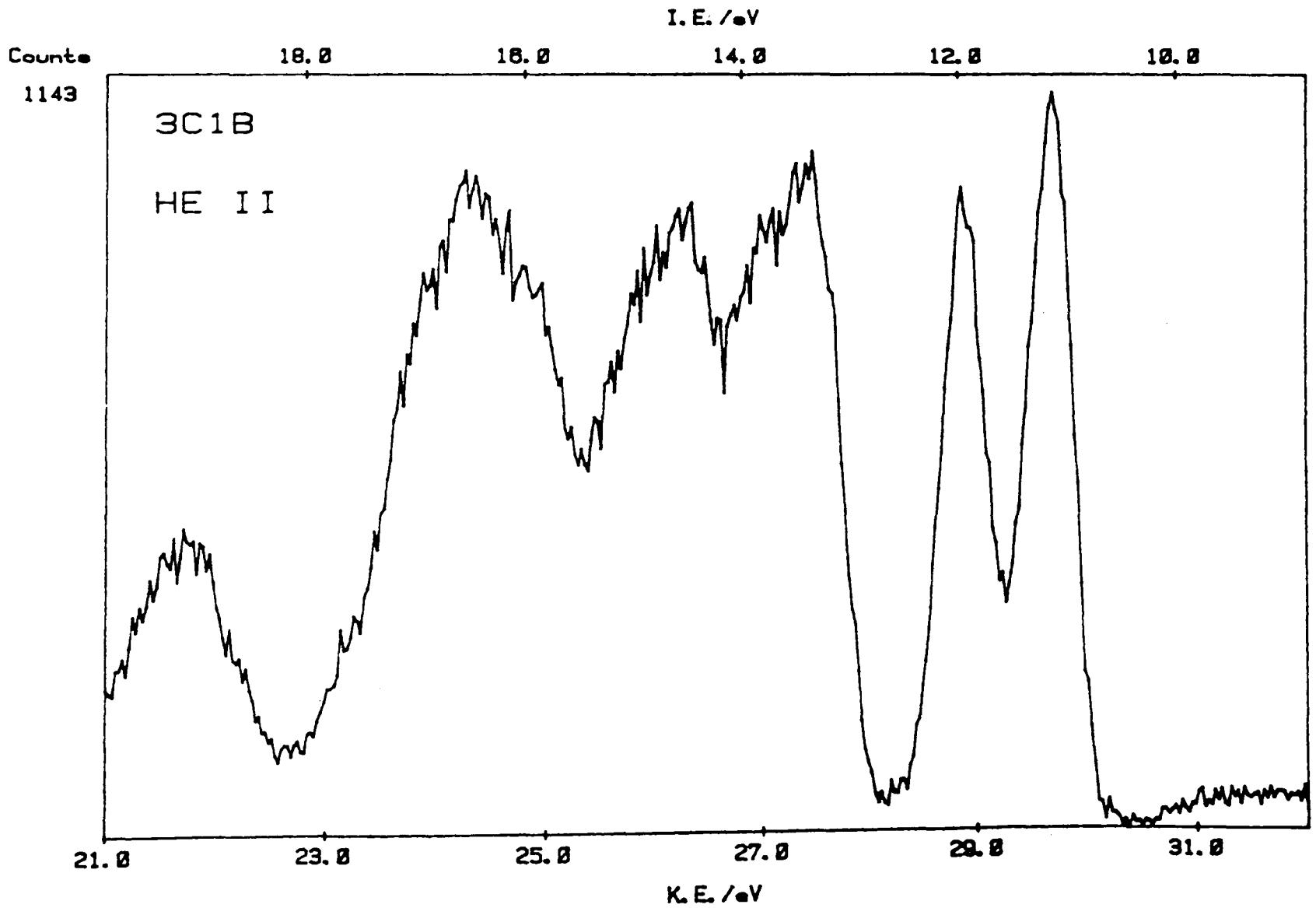
I.E. /eV
Counts
1143
18.0
16.0
14.0
12.0
10.0
3C1B
HE II
21.0
23.0
25.0
27.0
29.0
31.0
K.E. /eV

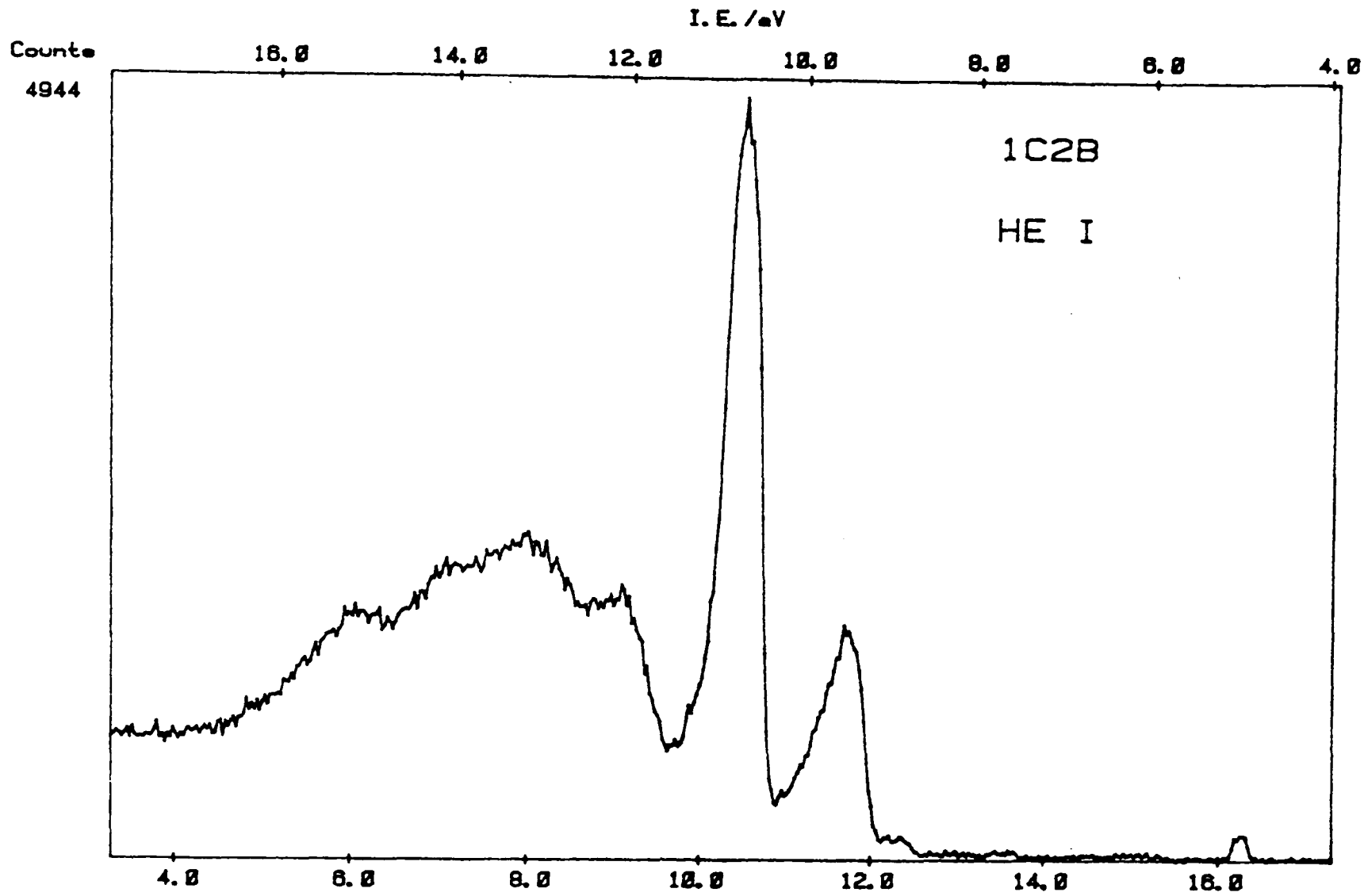
I. E. /eV
Counts
4944
16.0
14.0
12.0
10.0
8.0
6.0
4.0
1C2B
HE I
4.0
6.0
8.0
10.0
12.0
14.0
16.0

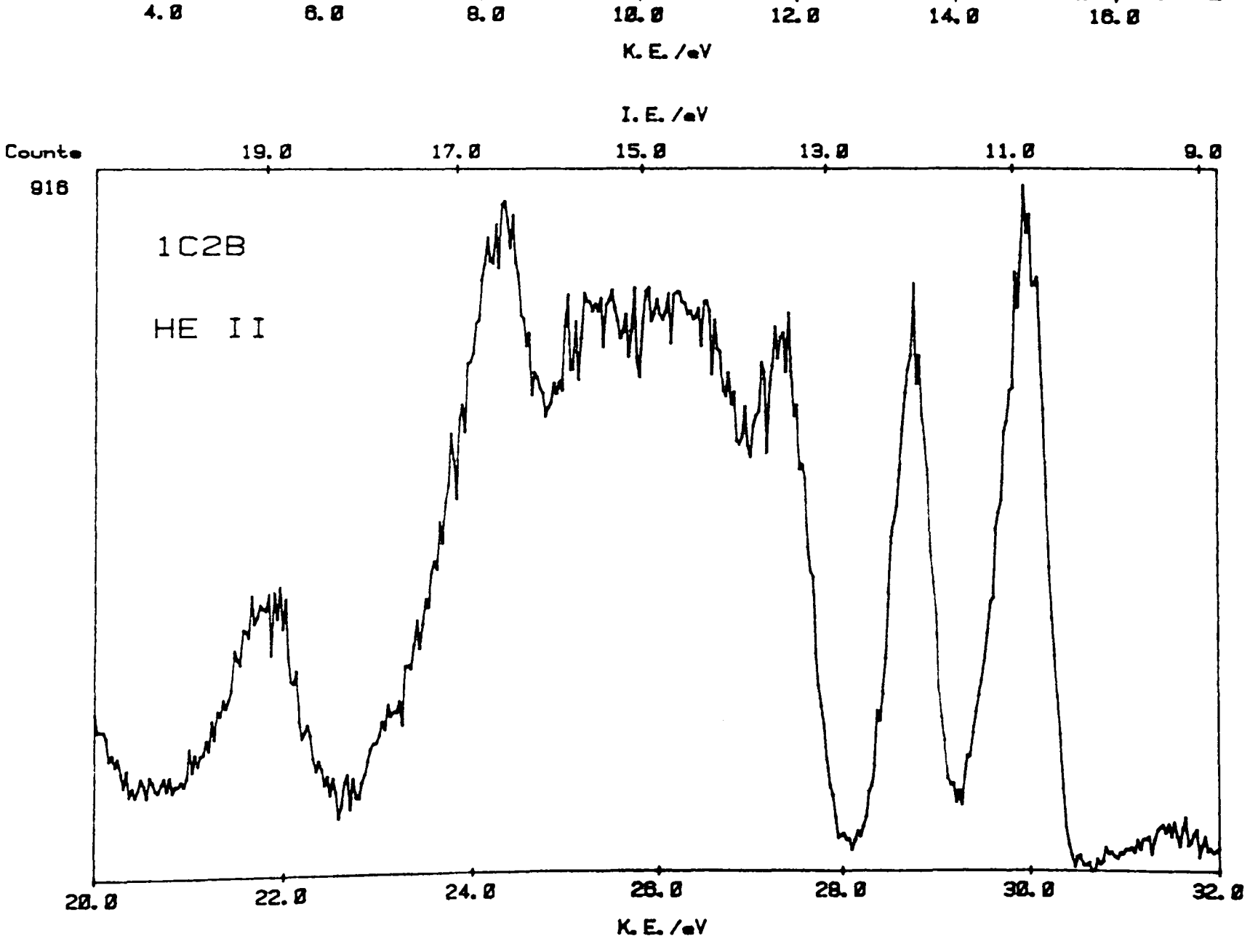
K. E. /eV
I. E. /eV
Counts
916
19.0
17.0
15.0
13.0
11.0
9.0
1C2B
HE II
20.0
22.0
24.0
26.0
28.0
30.0
32.0
K. E. /eV

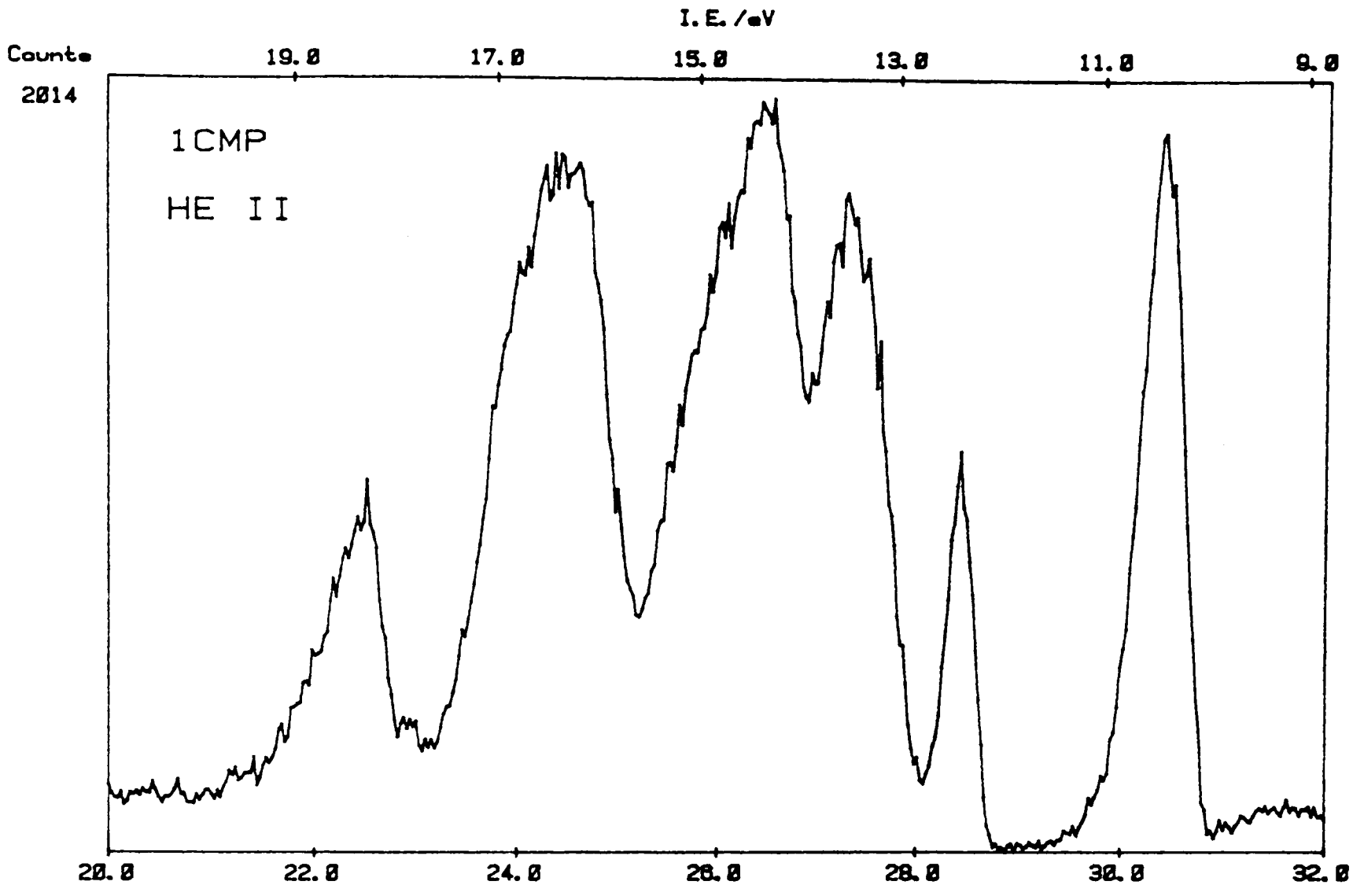
I.E. /eV
Counts
2014
19.0
17.0
15.0
13.0
11.0
9.0
1CMP
HE II
20.0
22.0
24.0
26.0
28.0
30.0
32.0
K.E. /eV

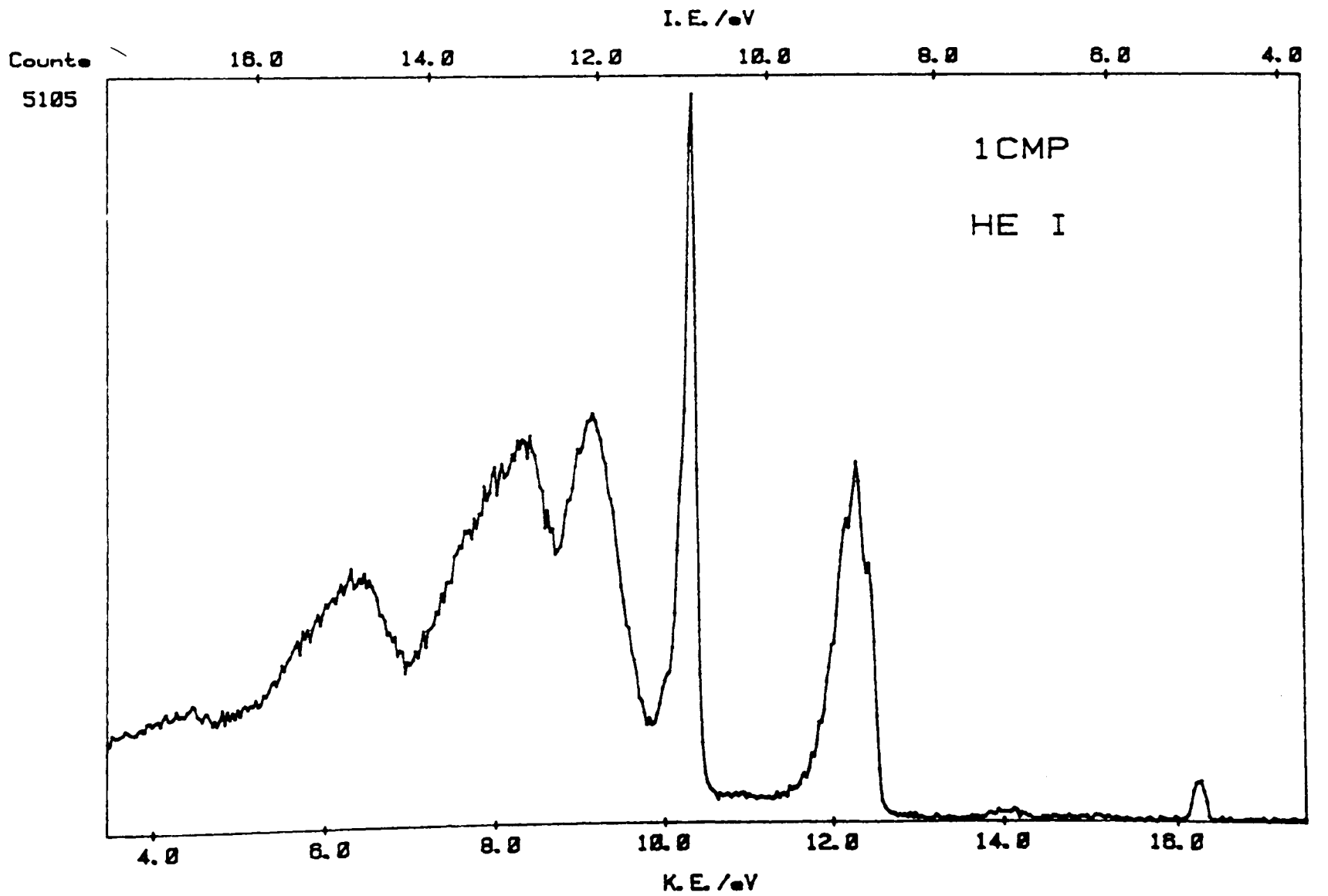
I.E. /eV
Counts
5105
16.0
14.0
12.0
10.0
8.0
6.0
4.0
1CMP
HE I
4.0
6.0
8.0
10.0
12.0
14.0
16.0
K.E. /eV

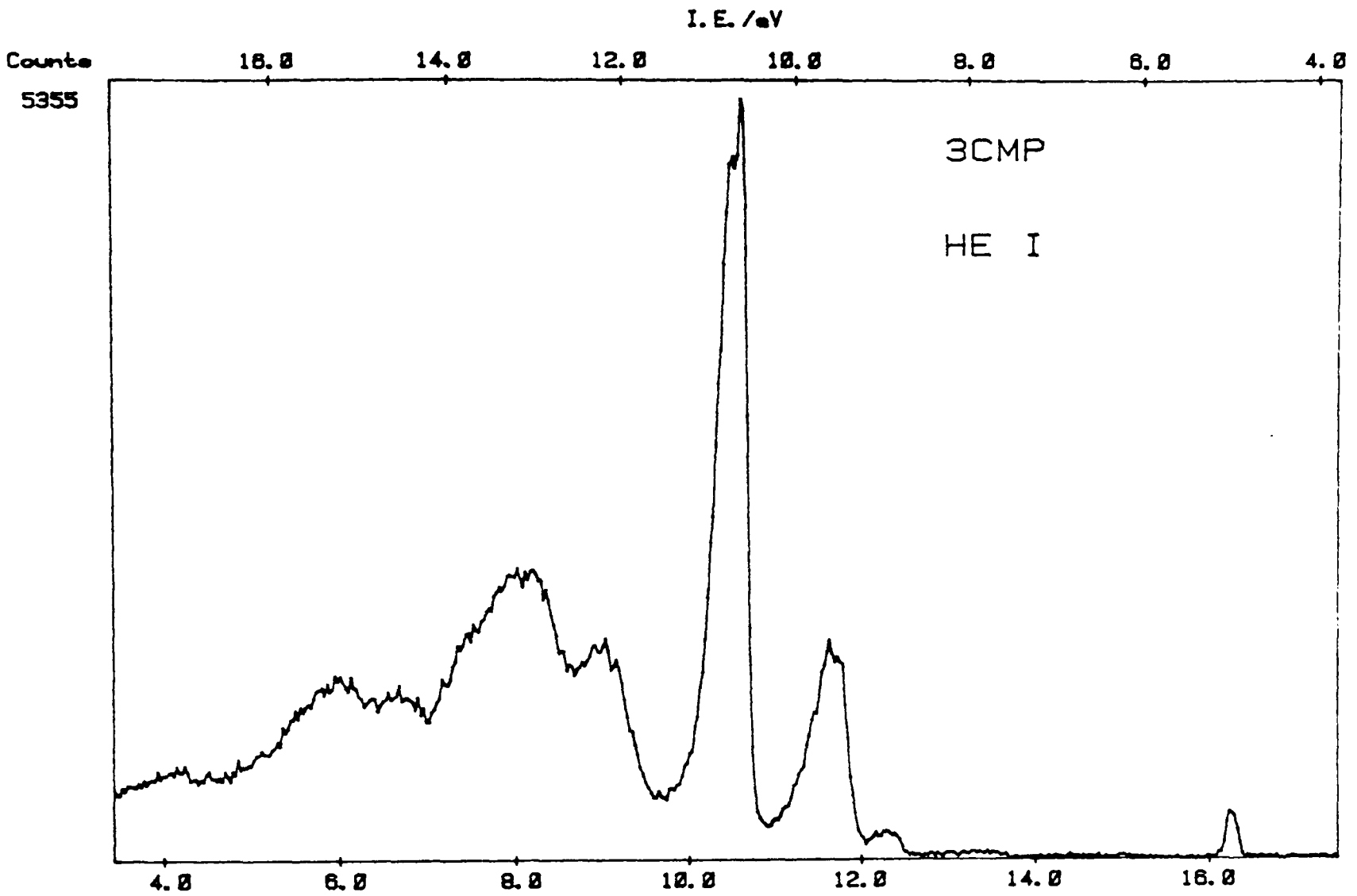
I. E. /eV
Counts
5355
16.0
14.0
12.0
10.0
8.0
6.0
4.0
3CMP
HE I
4.0
6.0
8.0
10.0
12.0
14.0
16.0

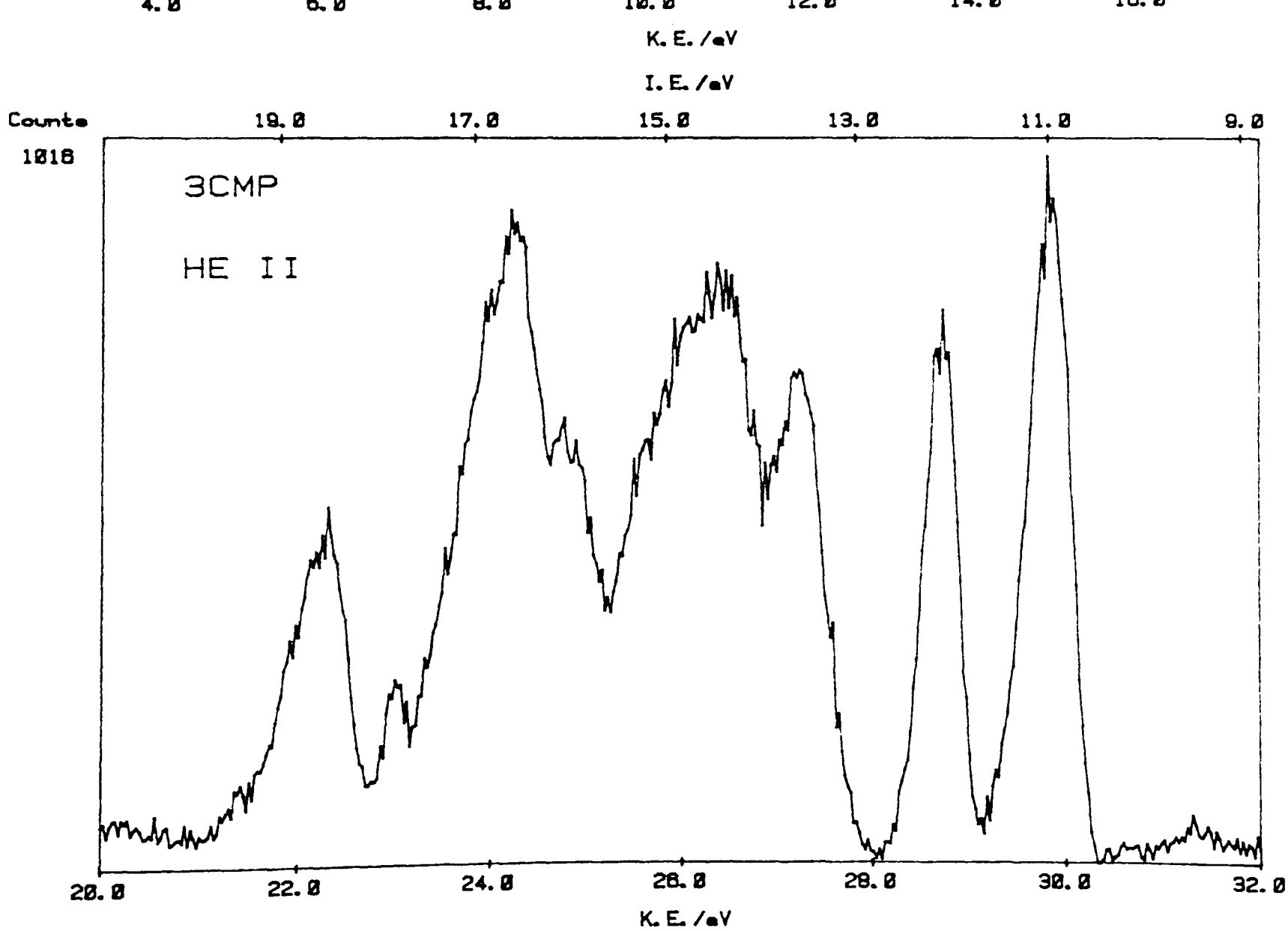
K. E. /eV
I. E. /eV
Counts
1018
19.0
17.0
15.0
13.0
11.0
9.0
3CMP
HE II
20.0
22.0
24.0
26.0
28.0
30.0
32.0
K. E. /eV

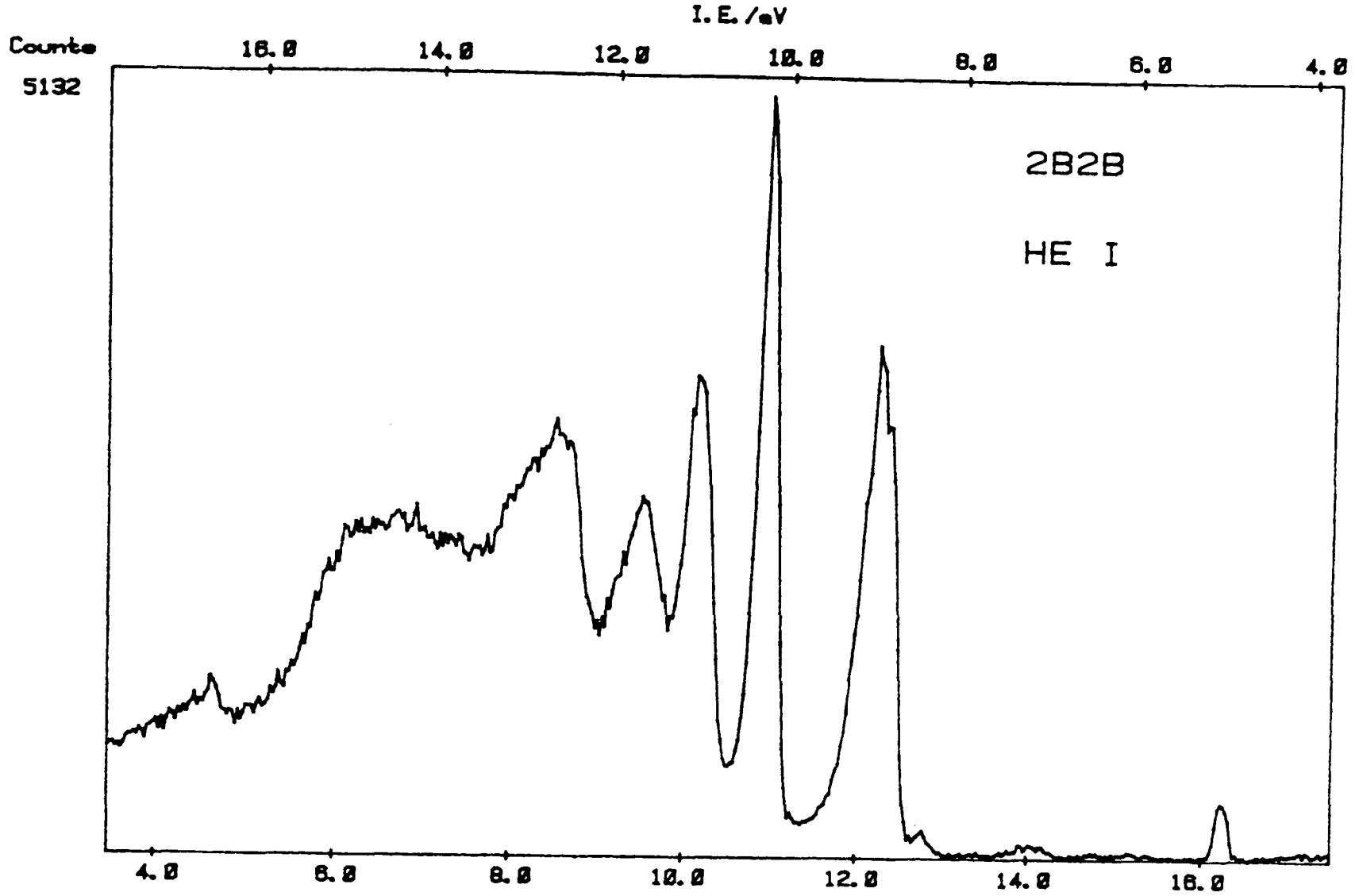
I. E. /eV
Counts
5132
16.0
14.0
12.0
10.0
8.0
6.0
4.0
2B2B
HE I
4.0
6.0
8.0
10.0
12.0
14.0
16.0

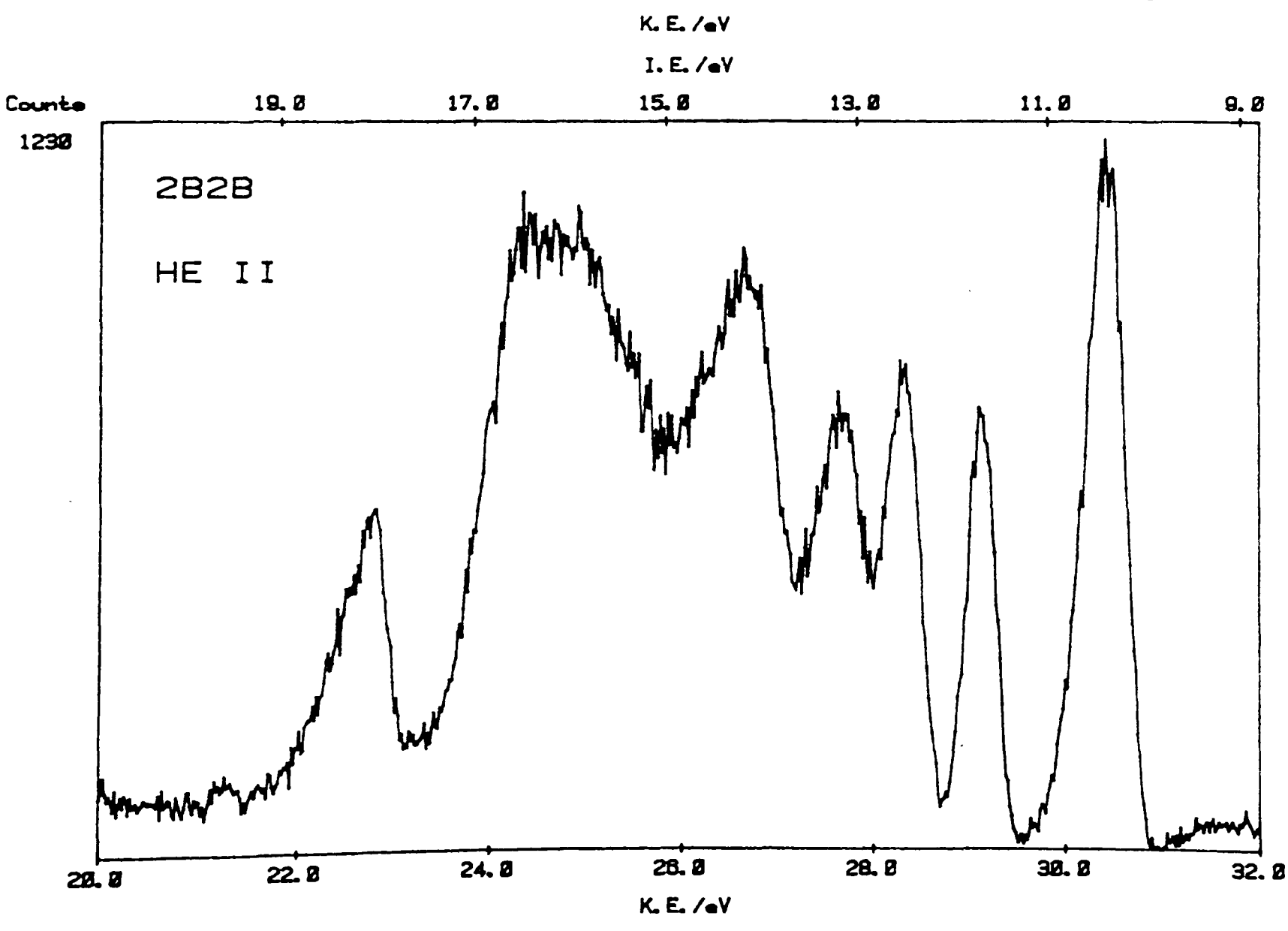
K. E. /eV
I. E. /eV
Counts
1230
18.0
17.0
15.0
13.0
11.0
9.0
2B2B
HE II
20.0
22.0
24.0
26.0
28.0
30.0
32.0
K. E. /eV

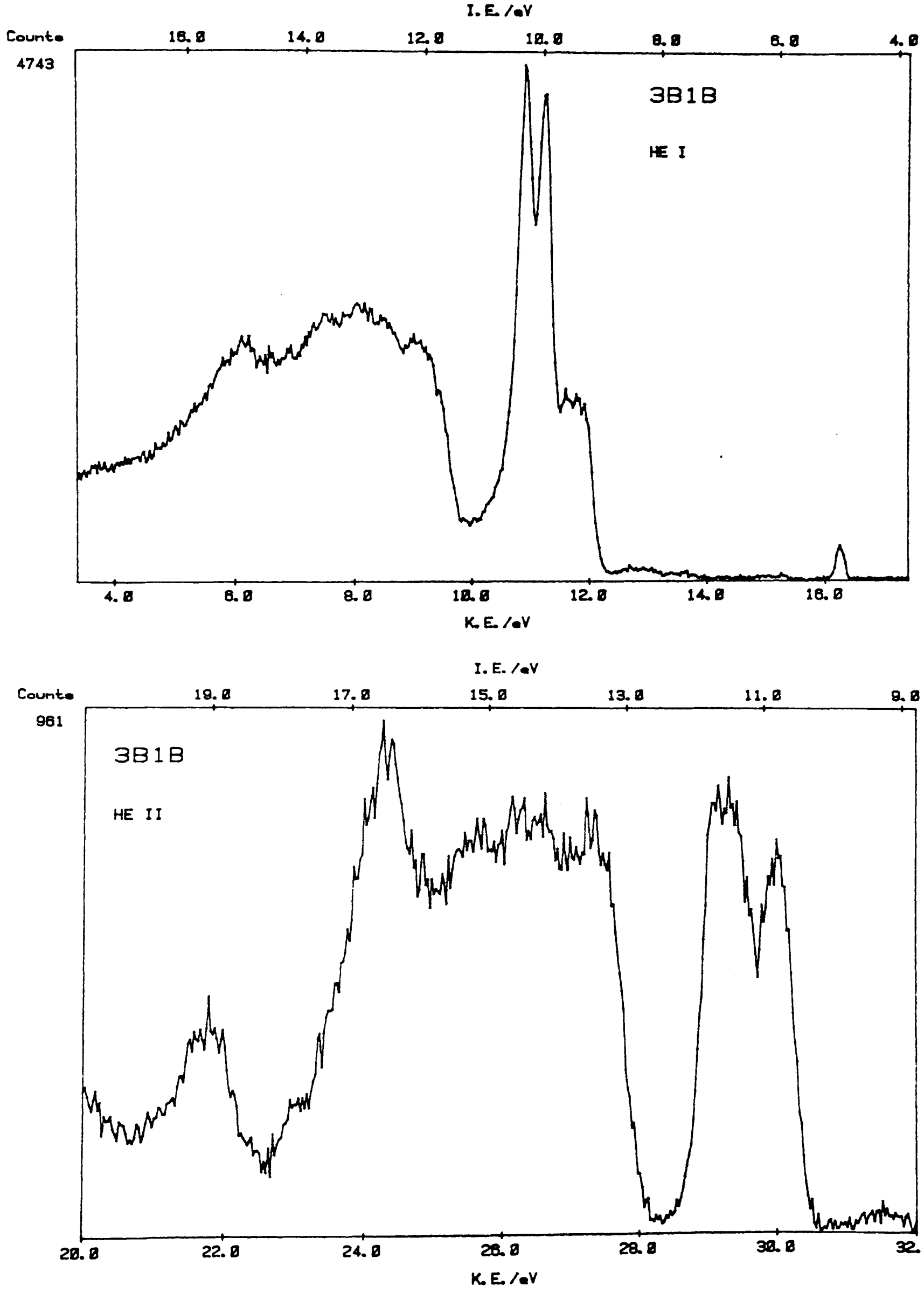
I.E./eV
Counts
4743
18.0
14.0
12.0
10.0
8.0
6.0
4.0
3B1B
HE I
4.0
6.0
8.0
10.0
12.0
14.0
16.0
K.E./eV
I.E./eV
Counts
961
19.0
17.0
15.0
13.0
11.0
9.0
3B1B
HE II
20.0
22.0
24.0
26.0
28.0
30.0
32.0
K.E./eV

Appendix II

The program for producing NO_3 time-concentration profiles from flash-photolysis data

This program uses the UNIRAS graphics library for displaying traces.

```
C*********************************************
C*      FLASH plot  PROGRAM                  *
C*      PSM July(1990)/Nov (1990)          *
C*      Adpt. DEC.FOR                    *
C*********************************************
C
C This version of the program v3.1, is the one
C that uses cursors for selecting the data.
C
C  (Wayne et al., 1991) cross-section for NO3 used.
C
C
C SET-PARAMETERS
C
C
        INTEGER CO,N,ZEROC
        INTEGER SM,NB,AD
        REAL BAS,BAF
        DIMENSION X(5000),Y(5000),XX(5000),YY(5000)
        DIMENSION XXT(5000),YYT(5000),YSM(5000)
        CHARACTER*20 FLNM,DRIVER1,DRIVER2
        CHARACTER*5 ANS
        REAL XX,YY,PA
        REAL X,Y,YMAX,XMAX,YMIN
C
C [NO3] Parameters
C
        REAL SIGMA,PLN,IOBS,NOC,IO
        REAL XA,YA
C Absorption cross section (SIGMA)
        SIGMA=224.0E-20
C Geometric path length (PLN)
        PLN=259
C No. of points to be averaged during smoothing (PA)
        PA=40.0
C Drivers for UNIGRAPH
        DRIVER1='SELECT vt4010;EXIT'
        DRIVER2='SELECT HPOSTA4;EXIT'
C
C   To ensure no interruptions during plotting
C
        CALL LIB$SPAWN('SET TERM /NOBROADCAST')
C
5       WRITE(6,100)
        WRITE(6,*)'       FLASH PLOT PROGRAM'
     WRITE(6,*)'       ================='
        WRITE(6,100)
```

```
      WRITE(6,*)' N.B.  PLN, SIGMA, PA'
      WRITE(6,*)PLN,SIGMA,PA
      WRITE(6,100)
      WRITE(6,*)' .DAT files in current directory'
      CALL LIB$SPAWN('DIR *.DAT') !VAX SPECIFIC COMMAND!
      WRITE(6,100)
      WRITE(6,*)' INPUT FLASH DATA FILE NAME (.DAT)'
      READ(5,107)FLNM
      WRITE(6,*)'  Reading data from file '
      OPEN(UNIT=7,FILE=FLNM,STATUS='OLD')
      CO=1
      YMAX=0.1
      XMAX=10.0
      YMIN=0
11    CO=CO-1
10    CO=CO+1
C
C Read data, find graph scaling factors
C
            READ(7,160,END=15)X(CO),Y(CO)
            IF (Y(CO).EQ.0) GOTO 11
            IF (Y(CO).GE.YMAX) YMAX=Y(CO)
            IF (X(CO).LE.XMIN.AND.Y(CO).GE.YMIN) XMIN=X(CO)
            IF (X(CO).GE.XMAX) XMAX=X(CO)
            IF (Y(CO).LE.YMIN) YMIN=Y(CO)
      GOTO 10
15    WRITE(6,100)
      WRITE(6,*)'  Data read complete OK'
      WRITE(6,105)CO
      CLOSE(7)
C
C Remove Computer Generated Baseline
C
      CO=CO-150
C
C Set offset for data plotting
C
      XMAX=XMAX+10
      YMAX=YMAX+0.3
C
C GRAPHICS ROUTINE FOR PLOTTING TRACE (1)
C
      CALL GROUTE(DRIVER1)
            CALL GSHMES('SUP','DIS')
            CALL GOPEN
            CALL BGRAF(25.0,35.0,150.,100.)
            CALL BTICKM(6)
            CALL BTICKJ(0)
            CALL BAXIS(1,XMIN,0.0,XMAX,'Time (arb.)$')
            CALL BAXIS(2,YMIN,0.0,YMAX,'Absorption (V)$')
            CALL BLINE (X,Y,CO)
         CALL BFRAME(2)
            CALL BGRID(0,0)
            CALL BTITLE('Run :$',5.0,1)
            CALL GSCALE
```

```
                CALL GCURSR(BAF,SHF)
        CALL GCLOSE
C
C FIND BASELINE AVG. REMOVE THEN OFFSET DATA TO 0
C ALSO FIND REFERENCE POINTS
C Correct to baseline 0
C
C The data (start/stop) is taken from the screen cursors (GCURSR)
C
        DO 56 N=BAF,CO
                Y(N)=Y(N)+ABS(SHF)
C               IF (Y(N).LE.0) Y(N)=0.1
56      CONTINUE
        YMAX=YMAX+ABS(SHF)
C Xmark plot
        DO 57 N=1,CO
                IF (X(N).GE.BAF) GOTO 59
57      CONTINUE
59      XMARK=N
        AD=0
        DO 58 N=XMARK,CO
                AD=AD+1
                XX(AD)=X(N)
                YY(AD)=Y(N)
                IF (XX(AD).LE.0) THEN ZEROC=ZEROC+1
58      CONTINUE
C
C GRAPHICS ROUTINE FOR PLOTTING TRACE (2)
C
        CALL GROUTE(DRIVER1)
                CALL GSHMES('SUP','DIS')
                CALL GOPEN
                CALL BGRAF(25.0,35.0,150.,100.)
                CALL BTICKM(6)
                CALL BTICKJ(0)
                CALL BAXIS(1,BAF,0.0,XMAX,'Time (arb.)$')
                CALL BAXIS(2,-0.2,0.0,YMAX,'Absorption (V)$')
                CALL BLINE (XX,YY,AD)
            CALL BFRAME(2)
                CALL BGRID(0,0)
                CALL BTITLE('Run :$',5.0,1)
        CALL GCLOSE
C
C [] Conversion
C
        WRITE(6,140)ZEROC
        WRITE(6,*)'Input I0'
        READ(5,*)IO
        WRITE(6,*)'Input max peak height in V'
        READ(5,*)IOBS
C Convert profile to []
        DO 60 N=1,AD
                IOBS=YY(N)
                IF (IOBS.LE.0) IOBS=0
                NOC=((1/(SIGMA*PLN))*LOG(IO/(IO-IOBS)))
```

```
                YY(N)=NOC
                IF (YMAX.LT.NOC) YMAX=NOC
60      CONTINUE
C
C Graphics routine for plotting profiles (3)
C
        CALL GROUTE(DRIVER1)
                CALL GSHMES('SUP','DIS')
                CALL GOPEN
                CALL BGRAF(25.0,35.0,150.,100.)
                CALL BTICKM(6)
                CALL BTICKJ(0)
                CALL BAXIS(1,BAF,0.0,XMAX,'Time (arb.)$')
                CALL BAXIS(2,-0.2,0.0,YMAX,'[NO3] cm3 molecule-1$')
                CALL BLINE (XX,YY,AD)
            CALL BFRAME(2)
                CALL BGRID(0,0)
                CALL BTITLE('Run :$',5.0,1)
                CALL GSCALE
                CALL GCURSR(XA,YA)
        CALL GCLOSE
C
C       Time conversion (mark t=0)
C
        ZTIME=XA
        DO 200 CO=1,AD
                IF (XX(CO).LE.ZTIME) MARK=CO
200     CONTINUE
        N=0
        DO 201 CO=MARK,AD
                N=N+1
                XXT(N)=XX(CO)
                XXT(N)=XXT(N)-ZTIME
                YYT(N)=YY(CO)
                XMAX=XXT(N)
                YSM(N)=YYT(N)
201     CONTINUE
C
C Smothing of the final curve (PA-defines no of points to average)
C
        CALL SMOOFT (YYT,N,PA)
C
C Graphics routine for plotting profiles (4)
C
        CALL GROUTE(DRIVER1)
                CALL GSHMES('SUP','DIS')
                CALL GOPEN
                CALL BGRAF(30.0,35.0,150.,100.)
                CALL BTICKM(6)
                CALL BTICKJ(0)
                CALL BAXIS(1,XXT(1),0.0,XMAX,'Time (s)$')
                CALL BAXIS(2,-0.2,0.0,YMAX,'[NO3] cm3 molecule-1 NO$')
                CALL BLINE(XXT,YSM,N)
                CALL BLICOL(4)
                CALL BLINE (XXT,YYT,N)
```

```
            CALL BFRAME(2)
               CALL BGRID(0,0)
               CALL BTITLE('Run :$',5.0,1)
         CALL GCLOSE
         WRITE(6,*)' Time v [] output start'
         WRITE(6,*)' NO3TC.DAT = NO3 TIME V [] SMOOTHED'
         WRITE(6,*)' NO3TCRW.DAT = NO3 TIME V [] RAW DATA'
         OPEN(UNIT=7,FILE='NO3TC.DAT',STATUS='NEW')
               DO 202 CO=1,N
                     WRITE(7,*)XXT(CO),YYT(CO)
202            CONTINUE
         CLOSE(7)
         OPEN(UNIT=7,FILE='NO3TCRW.DAT',STATUS='NEW')
               DO 203 CO=1,N
                     WRITE(7,*)XXT(CO),YSM(CO)
203            CONTINUE
         CLOSE(7)
         WRITE(6,*)' Output finished'
         CALL LIB$SPAWN ('SET TERM /BROADCAST')
         WRITE(6,100)
         WRITE(6,*)' ******************************'
         WRITE(6,*)' *    PROGRAM TERMINATED      *'
         WRITE(6,*)' ******************************'
C
C  FORMATS
C
100      FORMAT(/)
105       FORMAT('   No. of data points = ',I4)
106      FORMAT(3X,2F12.5)
107       FORMAT(A15)
140       FORMAT(' Zero count= ',I4)
150       FORMAT(A/F20.10/F20.10)
160       FORMAT(1X,2F9.7)
170    FORMAT('    File saved as ',A)
180       FORMAT(A)
190       FORMAT('    Max. [NO3]',F20.10)
195       FORMAT(' Calculated baseline offset =',1f10.5)
          STOP
          END

C
C SUBROUTINE FOR SMOOTHING THE DATA
C
      SUBROUTINE SMOOFT(Y,N,PTS)
      PARAMETER(MMAX=5000)
      DIMENSION Y(MMAX)
      M=2
      NMIN=N+2.*PTS
1     IF(M.LT.NMIN)THEN
        M=2*M
      GO TO 1
      ENDIF
      IF(M.GT.MMAX) PAUSE 'MMAX too small'
      CONST=(PTS/M)**2
      Y1=Y(1)
```

```
      YN=Y(N)
      RN1=1./(N-1.)
      DO 11 J=1,N
        Y(J)=Y(J)-RN1*(Y1*(N-J)+YN*(J-1))
11    CONTINUE
      IF(N+1.LE.M)THEN
        DO 12 J=N+1,M
          Y(J)=0.
12      CONTINUE
      ENDIF
      MO2=M/2
      CALL REALFT(Y,MO2,1)
      Y(1)=Y(1)/MO2
      FAC=1.
      DO 13 J=1,MO2-1
        K=2*J+1
        IF(FAC.NE.0.)THEN
          FAC=AMAX1(0.,(1.-CONST*J**2)/MO2)
          Y(K)=FAC*Y(K)
          Y(K+1)=FAC*Y(K+1)
        ELSE
          Y(K)=0.
          Y(K+1)=0.
        ENDIF
13    CONTINUE
      FAC=AMAX1(0.,(1.-0.25*PTS**2)/MO2)
      Y(2)=FAC*Y(2)
      CALL REALFT(Y,MO2,-1)
      DO 14 J=1,N
        Y(J)=RN1*(Y1*(N-J)+YN*(J-1))+Y(J)
14    CONTINUE
      RETURN
      END
C
C FT-Routine
C
      SUBROUTINE REALFT(DATA,N,ISIGN)
      REAL*8 WR,WI,WPR,WPI,WTEMP,THETA
      DIMENSION DATA(*)
      THETA=6.28318530717959D0/2.0D0/DBLE(N)
      C1=0.5
      IF (ISIGN.EQ.1) THEN
        C2=-0.5
        CALL FOUR1(DATA,N,+1)
      ELSE
        C2=0.5
        THETA=-THETA
      ENDIF
      WPR=-2.0D0*DSIN(0.5D0*THETA)**2
      WPI=DSIN(THETA)
      WR=1.0D0+WPR
      WI=WPI
      N2P3=2*N+3
      DO 11 I=2,N/2+1
        I1=2*I-1
```

```
      I2=I1+1
      I3=N2P3-I2
      I4=I3+1
      WRS=SNGL(WR)
      WIS=SNGL(WI)
      H1R=C1*(DATA(I1)+DATA(I3))
      H1I=C1*(DATA(I2)-DATA(I4))
      H2R=-C2*(DATA(I2)+DATA(I4))
      H2I=C2*(DATA(I1)-DATA(I3))
      DATA(I1)=H1R+WRS*H2R-WIS*H2I
      DATA(I2)=H1I+WRS*H2I+WIS*H2R
      DATA(I3)=H1R-WRS*H2R+WIS*H2I
      DATA(I4)=-H1I+WRS*H2I+WIS*H2R
      WTEMP=WR
      WR=WR*WPR-WI*WPI+WR
      WI=WI*WPR+WTEMP*WPI+WI
11    CONTINUE
      IF (ISIGN.EQ.1) THEN
        H1R=DATA(1)
        DATA(1)=H1R+DATA(2)
        DATA(2)=H1R-DATA(2)
      ELSE
        H1R=DATA(1)
        DATA(1)=C1*(H1R+DATA(2))
        DATA(2)=C1*(H1R-DATA(2))
        CALL FOUR1(DATA,N,-1)
      ENDIF
      RETURN
      END

C
C Routine required for for FT
C
      SUBROUTINE FOUR1(DATA,NN,ISIGN)
      REAL*8 WR,WI,WPR,WPI,WTEMP,THETA
      DIMENSION DATA(*)
      N=2*NN
      J=1
      DO 11 I=1,N,2
        IF(J.GT.I)THEN
          TEMPR=DATA(J)
          TEMPI=DATA(J+1)
          DATA(J)=DATA(I)
          DATA(J+1)=DATA(I+1)
          DATA(I)=TEMPR
          DATA(I+1)=TEMPI
        ENDIF
        M=N/2
1       IF ((M.GE.2).AND.(J.GT.M)) THEN
          J=J-M
          M=M/2
        GO TO 1
        ENDIF
        J=J+M
11    CONTINUE
```

```
      MMAX=2
2     IF (N.GT.MMAX) THEN
        ISTEP=2*MMAX
        THETA=6.28318530717959D0/(ISIGN*MMAX)
        WPR=-2.D0*DSIN(0.5D0*THETA)**2
        WPI=DSIN(THETA)
        WR=1.D0
        WI=0.D0
        DO 13 M=1,MMAX,2
          DO 12 I=M,N,ISTEP
            J=I+MMAX
            TEMPR=SNGL(WR)*DATA(J)-SNGL(WI)*DATA(J+1)
            TEMPI=SNGL(WR)*DATA(J+1)+SNGL(WI)*DATA(J)
            DATA(J)=DATA(I)-TEMPR
            DATA(J+1)=DATA(I+1)-TEMPI
            DATA(I)=DATA(I)+TEMPR
            DATA(I+1)=DATA(I+1)+TEMPI
12        CONTINUE
          WTEMP=WR
          WR=WR*WPR-WI*WPI+WR
          WI=WI*WPR+WTEMP*WPI+WI
13      CONTINUE
        MMAX=ISTEP
      GO TO 2
      ENDIF
      RETURN
      END
```

References

J.P.D. Abbatt, K.L. Demerjian and J.G. Anderson, *J.Phys.Chem.*, **94**, 1990, 4566.

J.P.D. Abbatt and J.G. Anderson, *J.Phys.Chem.*, **95**, 1991, 2382.

J.D.W. Abernathy, '*Wireless World*', 1970, December issue 1.

C. Anastasi, P.P. Bemand and I.W.M. Smith, *Chem.Phys.Lett.*, **37**, 1976, 370.

Y. Andersson and E. Ljungström, *Atmos.Environ.*, **23**, 1989, 1153.

M.O. Andreae, *Oceanus*, **29**, 1986, 27.

R. Arnaud, *New J.Chem.*, **15**, 1991, 615.

R. Atkinson, *Chem.Rev.*, **86**, 1986, 69.

R. Atkinson, *IntJ.Chem.Kin*, **19**, 1987,799.

R. Atkinson, *J.Phys.Chem.Ref.Data*, Monograph 1, 1989.

R. Atkinson, *Atmos.Env.*, **24A**, 1990, 1.

R. Atkinson, *J.Phys.Chem.Ref.Data*, **20**, 1991, 459.

R. Atkinson, S.M.A. Aschmann and M.A. Goodman, *Int. J.Chem.Kin.*, **19**, 1987, 299.

R. Atkinson, S.M.A. Aschmann and J.N. Pitts Jr., *J.Phys.Chem.*, **92**, 1988, 3454.

R. Atkinson, D.L. Baulch, R.A. Cox, R.F. Hampson Jr., J.A. Kerr and J. Troe, *J.Phys.Chem.Ref.Data*, **18**, 1989, 881.

A. Auty, Private Communication, 1990.

A.D. Baker and D. Betteridge '*Photoelectron spectrscopy; Chemical and Analytical Aspects*', Pergamon Press, Oxford, 1972.

C.H. Bamford and C.F.H. Tipper Ed.,' *Comprehensive Chemical Kinetics*', Vol.2, Elsevier, Amsterdam, 1969.

I. Barnes, V. Bastian, K.H. Becker and T. Zhu, *J.Phys.Chem.*, **94**, 1990, 2413.

S.W. Benson, "*Thermochemical Kinetics*", J.Wiley, New York, 2nd edition, 1976.

T. Benter, E. Becker, U. Wille, R.N. Schindler, C.E. Canosa-Mas, S.J. Smith, S.J. Waygood and R.P. Wayne, J.Chem.Soc. Faraday Trans., **87**, 1991, 2141.

R. Beringer and J.G. Castle Jr., *Phys.Rev.*, **75**, 1949, 1963.

F. Bernardi, A. Bottoni and N.D. Epiotis, *J.Am.Chem.Soc.*, **100**, 1978, 7207.

P.R. Bevington, " *Data reduction and Error analysis for the Physiscal Sciences*", McGraw-Hill, New York, 1969.

P. Biggs, Private Communication, 1990.

P.Biggs, A.A. Boyd, C.E. Canosa-Mas, D.M. Joseph and R.P. Wayne, *Meas.Sci.Technol.*, **2**, 1991, 675.

P. Biggs, C.E. Canosa-Mas, R.P. Wayne, I. Barnes and H. Sidebottom, Atmospheric oxidation processes, Air pollution research report 33, Ed. K.H. Becker, CEC, Brussels, 1991, 212.

M. Bodenstein, *Z.Physik.Chem.*, **100**, 1922, 68.

K.F. Bonhoeffer, *Z.Phys.Chem.*, **113**, 1924, 199.

R.B. Boodaghians, C.E. Canosa-Mas, P.J. Carpenter and R.P. Wayne, *J.Chem.Soc. Faraday Trans. II*, **84**, 1988, 931.

P. Borrell, C.J. Cobos and K. Luther, *J.Phys.Chem.*, **92**, 1988, 4377.

A.A. Boyd, C.E. Canosa-Mas, A.D. King, R.P. Wayne and M.R. Wilson, *J.Chem.Soc. Faraday Trans.*, **87**, 1991, 2913.

J.C.D. Brand and A.R. Hoy, *J.Molec.Spectrosc.*, **65**, 1977, 55.

C.G. Broyden, *J.Inst.Math.App.*, **6**, 1970, 222.

J. Brunning, M.J. Frost and I.W.M. Smith, *Int.J.Chem.Kin.*, **20**, 1988, 957.

I.M. Campbell, '*Energy and the atmosphere*', 2nd Edn., John Wiley and Sons, Chichester, 1986.

E. Canadell, O. Eisenstein, G. Ohanessian and J.M. Poblet, *J.Phys.Chem.*, **89**, 1985, 4856.

P.H. Cannington and N.S. Ham, *J.Electron Spectrosc.Relat.Phenom.*, **31**, 1983, 175.

C.E. Canosa-Mas, M. Fowles, P.J. Houghton and R.P. Wayne, *J.Chem.Soc.Faraday Trans.* II, **83**, 1987, 1465.

C.E. Canosa-Mas, S.J. Smith, S. Toby and R.P. Wayne, *J.Chem.Soc.Faraday Trans. II*, **84**, 1988, 263.

C.E. Canosa-Mas, S.J. Smith, S. Waygood and R.P. Wayne, *J.Chem.Soc.Faraday Trans.*, **87**, 1991, 3473.

C.A. Cantrell, J.A. Davidson, R.E. Shetter, B.A. Anderson and J.G. Calvert, *J.Phys.Chem.*, **91**, 1987, 5858.

C.A. Cantrell, J.A. Davidson, A.H. McDaniel, R.E. Shetter and J.G. Calvert, *J.Phys.Chem.*, **88**, 1988, 4997.

W.P.L. Carter, *Atmos.Env.*, **24A**, 1990, 481.

A.R. Chance, A.R. Curtis, I.P. Jones and C.R. Kirby; Report L8775, United Kingdom Atomic Energy Authority, Harwell, 1977.

S. Chapman, *Mem.Roy.Meteorol.Soc.*, **3**, 1930, 103.

M.A.A. Clyne, '*Physical chemistry of fast reactions*', Vol. 1, Ed. B.P. Levitt, Plenum Press, New York, N.Y., 245, 1973.

G. Cooper, Pt.II Thesis, Oxford, 1984.

J.W. Cooper, *Phys.Rev.Lett.*, **41**, 1976, 73.

J.D. Coyle, R.R. Hill, D.R. Roberts ed., '*Light, Chemical Change and Life*', Oxford University Press, 1982.

R.A. Cox, *J.Photochem.Photobiol.A*, **51**, 1990, 29.

A.E. Croce de Cobos, H. Hippler and J. Troe, *J.Phys.Chem.*, **88**, 1984, 5083.

D.R. Crosley, *High Temp. Mat.Proc.*, **7**, 1986, 41.

J.N. Crowley, J.P. Burrows, G.K. Moortgat, G. Poulet and G. LeBras, *Int.J.Chem.Kinet.*, **22**, 1990, 673.

A.R. Curtis, '*Technical Report AERE R9352*', Harwell, 1979.

D.D. Davis and W. Braun, 1968, *App. Opt.*, **7**, 1968, 2701.

W.B. DeMore, S.P. Sander, D.M. Golden, M.J. Molina, R.F. Hampson, M.J. Kurylo, C.J. Howard and A.R. Ravishankara,' *Chemical Kinetics and photochemical data for use in stratospheric modeling*', Evaluation no. 9, JPL 90-1, Pasadena, 1990.

W. Demtröder, '*Laser spectroscopy*', Spinger-Verlag, Berlin, 1982.

M.J.S. Dewar, '*The molecular-orbital theory of organic chemistry*', McGraw-Hill, New York, 1969.

M.J.S. Dewar, *J.Phys.Chem.*, **89**, 1985, 2145.

M.J.S. Dewar and R.C. Dougherty, '*The PMO theory of organic chemistry*', Plenum Press, New York, 1975.

M.J.S. Dewar and J.J.P. Stewart, *Chem.Phys.Lett.*, **111**, 1984, 416.

M.J.S. Dewar and D.M. Storch, *J.Am.Chem.Soc.*, **107**, 1985, 3898.

M.J.S. Dewar, E.A. Zoebisen, C.F. Healy and J.J.P. Stewart, *J.Am.Chem.Soc.*, **107**, 1985, 3902.

G.H. Dieke, '*Biographical Memoirs of Fellows of the Royal Society*', **2**, Royal Society, London, 1956, 327.

E.J. Dlugokencky and C.J. Howard, *J.Phys.Chem.*, **92**, 1988, 1188.

E.J. Dlugokencky and C.J. Howard, *J.Phys.Chem.*, **93**, 1989, 1091.

L. Dogliotti and E. Hayon, *J.Chem.Phys.*, **71**, 1967, 3802.

J.H.D. Eland, '*Photoelectron spectroscopy*', Butterworths, London, 1974.

M.G. Evans and M. Polanyi, *Trans. Faraday Soc.*, **34**, 1938, 11.

F. Ewig, A. Hoffmann and R. Zellner, *Xth International Symposium on Gas Kinetics*, Swansea, U.K., 24-29 July, 1988.

W.M. Fairbanks, T.W. Hänsch, A.L. Schawlow, *J.Opt.Soc.Am.*, **65**, 1975, 199.

J.C. Farman, B.G. Gardiner and J.D. Shanklin, *Nature*, **315**, 1985, 217.

D.M. Fasano and N.S. Nogar, *J.Chem.Phys.*, **78**, 1983, 6688.

F.F. Fenter and J.G. Anderson, *J.Phys.Chem.*, **95**, 1991, 3172.

B.J. Finlayson-Pitts and J.N. Pitts Jr., *Adv.Environ.Sci.Technol.*, **7**, 1977, 75.

B.J. Finlayson-Pitts, J.N. Pitts Jr. and A. Winer, *Adv.Environ.Sci.Technol.*, **11**, 1977, 568.

B.J. Finlayson-Pitts and J.N. Pitts Jr., '*Atmospheric Chemistry*', John Willey & Sons, New York, 1986.

G.R. Fleming, *Ann.Rev.Phys.Chem.*, **37**, 1986, 81.

I. Flemming, ' *Frontier Orbitals and Organic Chemical Reactions*', John Wiley and Sons, New York, 1976.

R. Fletcher, *Comp. J.*, **13**, 1970, 317.

A. Fontijn and W. Felder, *J.Phys.Chem.*, **83**, 1979, 10.

R.R. Friedl and S.P. Sander, *J.Phys.Chem.*, **91**, 1987, 2721.

K. Fukui, T. Yonezawa and H. Shingu, *J.Chem.Phys.*, **20**, 1952, 722.

C.W. Gear, *Commun. Association for Computing Machninery*, **14**, 1971, 176.

B. Giese, *Agnew.Chem.Int.Ed.(Engl.)*, **22**, 1970, 830.

D. Goldfarb, *Math. Comput.*, **24**, 1970, 23.

R.A. Graham and H.S. Johnston, *J.Phys.Chem.*, **82**, 1978, 254.

T.J. Graedel and P.J. Crutzen, *Scientific American*, **261**, 1989, 28.

H. Güsten and L. Klasinc, *Naturwissenschaften*, **73**, 1986, 129.

H. Güsten, L. Klasinc and D. Marić, *J.Atmos.Chem.*, **2**, 1984, 83.

G. Hall and J.M. Watt,' *Modern numerical methods for ordinary differential equations*', O.U. Press, Oxford, 1976.

P.D. Hammer, E.J. Dlugocencky and C.J. Howard, *J.Phys.Chem.*, **90**, 1986, 2491.

G. Hancock, *J.Chem.Soc. Faraday Trans. II*, **84**, 1988, 429.

P. Harteck, *Z.Phys.Chem.*, **A139**, 1928, 98.

P. Hautefeuille and P.J. Chapuis, *C.R. Acad.Sci.Paris*, **92**, 1881, 80.

P. Hautefeuille and P.J. Chapuis, *C.R. Acad.Sci.Paris*, **94**, 1882a, 1111.

P. Hautefeuille and P.J. Chapuis, *Ann. de l'Ecole Norm. Sup. série 2*, **11**, 1882b, 137.

J.A. Hipple and D.P. Stevenson, *Phys. Rev.*, **63**, 1943, 121.

E. Hirota, K. Kawaguchi, T. Ishiwata, I. Tanaka, *J.Chem.Phys.*, **95**, 1991, 771.

H.D. Holland, '*The chemistry of the atmosphere and oceans*', John Wiley, Chichester, 1978.

J.M. Hollis, '*Modern spectroscopy*', J.Wiley and Sons, Chichester, 1987.

J.T. Houghton, '*The Physics of Atmospheres*', 2nd edn., Cambridge University Press, Cambridge, 1986.

C.J. Howard, *J.Phys.Chem.*, **83**, 1979, 3.

D. Hussain and R.G.W. Norrish, *Proc.Roy.Soc.Ser.A*, **273**, 1963, 165.

T. Ishiwata, I. Fujiwara, Y. Naruge, K. Obe and I. Tanaka, *J.Phys.Chem.*, **87**, 1983, 1349.

D.J. Jacob, E.W. Gottlieb and M.J. Prather, *J.Geophys.Res.*, **94**, 1989, 12.975.

S.M. Japar and H. Niki, *J.Phys.Chem.*, **79**, 1975, 1629.

N.R. Jensen, J. Hjorth, J. Lohse, C. Skov and G. Restelli, *Atmos. Env.*, 1991, Submitted for publication.

H.S. Johnston, C.A. Cantrell and J.G. Calvert, *J.Geophys.Res.*, **91**, 1986, 5159.

H.S. Judeikis, *J.Phys.Chem.*, **84**, 1980, 2481.

J.M. Kay and R.M. Nedderman, '*Fluid mechanics and transfer processes*', Cambridge University Press, Cambridge, 1985.

F. Kaufman, *Proc.R.Soc.London Ser.A*, **247**, 1958, 123.

F. Kaufman, *J.Phys.Chem.*, **88**, 1984, 4909.

M.C. Kelley, '*The earth's ionosphere*', Academic Press, San Diego, 1989.

L.F. Keyser, *J.Phys.Chem.*, **88**, 1984, 4750.

L.F. Keyser, *J.Phys.Chem.*, **95**, 1991, 5496.

K. Kimura, S. Katsumata, Y. Achiba, T. Yamazaki and S. Iwata,' *Handbook of He I photoelectron spectra of fundamental organic molecules.*', Japan Scientific Societies Press, Tokyo, and Halsted Press, New York, 1981.

C.C. Kircher, J.J. Margitan, S.P. Sander, *J.Phys.Chem.*, **88**, 1984, 4370.

K. Kleinermans and A.C. Luntz, *J.Chem.Phys.*, **77**, 1982, 3533.

G. Klopman, *J.Amer.Chem.Soc.*, **90**, 1968, 223.

J.B. Koffend, J.S. Holloway, M.A. Kwok and R.F. Heidner II, *J.Quant.Spectrosc.Radiat. Transfer*, **37**, 1987, 449.

T. Koopmans, *Physica*, **1**, 1934, 104.

R.H. Krech, G.J. Diebold and D.L. McFadden, *J.Am.Chem.Soc.*, **19**, 1977a, 4605.

R.H. Krech and D.L. McFadden, *J.Am.Chem.Soc.*, **99**, 1977b, 8402.

K.J Laidler, '*Chemical Kinetics*', Harper and Row, New York, 1987.

Landolt-Bornstein " *Zahlenwerte und Funktionen*", Vol.1 " *Atom und Molekular Physik*", Part 3, 1951, 509, Springer-Verlag, West Berlin, 1951.

P.A. Leighton, ' *Photochemistry of air pollution*', Academic Press, New York, 1961.

K.K. Lehmann and S.L. Coy, *Ber.Bunsenges. Physik.Chem.*, **92**, 1988, 306.

R.D. Levin and S.G. Lias, ' *Ionisation potentials and appearence potential measurement, 1971-1981*', Natl.Stand.Ref.Data.Ser., Nat.Bur.Stand., **71**, 1982, Cat.No. C13.98:71.

A.R. Lloyd, *J.Phys.E Sci.Inst.*, **3**, 1970, 629.

L.M. Loewenstein and J.G. Anderson, *J.Phys.Chem.*, **91**, 1987, 2993.

J.A. Logan, *J.Geophys.Res.*, **88**, 1983, 10785.

F. Magnotta, Ph.D. Thesis, 1979, University of California, Berkley, CA.

F. Magnotta and H.S. Johnston, *Geophys.Res.Lett.*, **7**, 1980,769.

M.W. Malko and J.Troe, *Int.J.Chem.Kinet.*, **14**, 1982, 399.

E. Marason, *Opt.Commun.*, **37**, 1981, 56.

Matheson Company Inc., '*Matheson Gas Data Book*', 5th edn., Hesrt Litho Inc. N.Y., New York, 1981.

A. Mellouki, G. Le Bras and G. Poulet, *J.Geophys.Res.*, **92**, 1987, 4217.

T.R. Merroro and A.E. Mason, *J.Phys.Chem.Ref.Data*, **1**, 1972, 3.

D. Mihelcic, P. Müsgen and D.H. Enhalt, *J.Atmos.Chem.*, **3**, 1985, 341.

D.N. Mitchell, R.P. Wayne, P.J. Allen, R.P. Harrison and R.J. Twin, *J.Chem.Soc. Faraday Trans. II*, **76**, 1980, 785.

J.H. Moore, C.C. Davies and A. Coplan, '*Building scientific apparatus*', 2nd edn., Addison-Wesley publishing, 1989.

H.H. Nelson, L. Pasternack and J.R. MacDonald, *J.Chem.Phys.*, **79**, 1983a, 4279.

H.H. Nelson, L. Pasternack and J.R. MacDonald, *J.Phys.Chem.*, **87**, 1983b, 1286.

D.C. Nonhebel, G.M. Tedder and J.C. Walton, '*Radicals*', Cambridge University Press, Cambridge, 1979.

R.G.W. Norrish and B.A. Thrush, *Q.Rev.Chem.Soc.*, **10**, 1956, 149.

J.F. Noxon, R.B. Norton, and W.R. Henderson, *J.Geophys.Res.Lett.*, **5**, 1978, 675.

M. Ogawa, *J.Chem.Phys.*, **54**, 1971, 2550.

H. Okabe, '*Photochemistry of small molecules*', John Wiley and sons, New York, 1978.

L. Pauling, *J.Am.Chem.Soc.*, **54**, 1932, 3570.

D. Perner, J. Greenberg, J.F. Noxon, A. Schmeltekopf, P. Winkler and P. Zimmerman, *J.Atmos.Chem.*, 1991, Submitted for publication.

J. Perry, ' *Chemical engineers handbook*', **19**, McGraw-Hill, 782, 1941.

G. Persch, E. Mehdizadeh, W. Demtröder, Th. Zimmermann, H. Köppel and L.S. Cederbaum, *Ber. Bunsenges. Physik. Chem.*, **92**, 1988, 312.

M. Pilling and I.W.M. Smith (eds), ' *Modern gas kinetics theory, experiment and application*', Blackwell Scientific Publications, Oxford, 1987.

Ch. Plass, F.J. Johnan, R. Koppmann and J. Rudolph, Fifth European Symposium on Physico-Chemical Behaviour of Atmospheric Pollutants, Varese, Italy, 25-27 Sept., 1989.

U. Platt, G. LeBras, G. Poulet, J.P. Burrows and G. Moortgat, *Nature*, **348**, 1990, 147.

U. Platt, D. Perner, A.M. Winer, G.W. Harris and J.N. Pitts Jr., *Geophys.Res.Lett.*, **7**, 1980, 89.

U. Platt, A.M. Winer, H. Bierman, R. Atkinson and J.N. Pitts Jr., *Env. Sci. Technol.*, **18**, 1984, 365.

J.M. Poblet, E. Canadell and T. Sordo, *CanJ.Chem*, **61**, 1983, 2068.

G. Poulet, J.L. Jourdain and G. Le Bras, *C.R. Acad.Sci.Paris série II*, **293**, 1981, 899.

W.H. Press, B.P. Flannery, S.A. Teukolsky, W.T. Vettering, ' *Numerical recipes*', Cambridge University Press, Cambridge, 1986.

W.C. Price, A.E. Potts and D.G. Streets in D.A. Shirley (Ed.), '*Electron spectroscopy*', North Holland, Amsterdam, 187, 1972.

J.M. Prospero and D.L. Savoie, *Nature*, **339**, 1989, 687.

M. Protić and A. Sablić, *Aquat. Toxicol.*, **14**, 1989, 47.

J.G. Pruett and R.N. Zare, *J.Chem.Phys.*, **64**, 1976, 1774.

J.F. Rabek, '*Experimental methods in photochemistry and photophysics*', J.Wiley and Sons, New York, 1982.

M.M. Rahman, E. Becker, Th. Benter and R.N. Schindler, *Ber.Bunsenges.Phys.Chem.*, **92**, 1988, 91.

D.A. Ramsay, '*Optical spectra of gaseous free radicals*', Proc. Xth Colloquium Spectroscopium Internationale (1962), Ed. E.R. Lippincoat and M. Margoshes, Spartan books, Washington D.C., 1963.

A.R. Ravishankara, *Ann.Rev.Phys.Chem.*, **39**, 1988, 367.

A.R. Ravishankara, F.L. Eisele and P.H. Wine, *J.Phys.Chem.*, **86**, 1982, 1854.

A.R. Ravishankara and R.L. Mauldin II, *J.Phys.Chem.*, **89**, 1985, 3144.

A.R. Ravishankara and R.L. Mauldin II, *J.Geophys.Res*, **94**, 1986, 8709.

G.W. Ray and R.T. Watson, *J.Phys.Chem*, **85**, 1981, 2955.

R.C. Reid, J.M. Prausnitz and T.K. Sherwood, *'The properties of gases and liquids'*, 3rd Edition, McGraw-Hill, New York, 1977.

W.G. Richards and D.L. Cooper, *'Ab-initio molecular orbital calculations for chemists'*, 2nd Edn., Clarendon Press, Oxford, 1983.

C.P. Rinsland, J.S. Levine and T. Miles, *Nature*, **318**, 1085, 245.

C. Rüchardt, *Agnew.Chem.Int.Ed.(Engl.)*, **9**, 1970, 830.

A.G. Russell, G.R. Cass and J.H. Seinfeld, *Environ.Sci.Technol.*, **20**, 1986, 1167.

A. Sablić, *Environ. Sci. Technol.*, **21**, 1987, 358.

A. Sablić, In '*Physical property prediction Organic Chemistry*', Ed. J.C. Jochum, M.G. Hicks and J. Sunkel, Springer Verlag, Heidelberg, 1988, 336.

A. Sablić and H. Güsten, *Atmos.Env.*, **24A**, 1990, 73.

J. Sadlej, ' *Semi-empirical methods of quantum chemistry*', Ellis-Horwood ltd., Chichester, 1985.

L. Salem, *J.Amer.Chem.Soc.*, **90**, 1968a, 543.

L. Salem, *J.Amer.Chem.Soc.*, **90**, 1968b, 553.

S.P. Sander, *J.Phys. Chem*, **90**, 1986, 1435.

F.P. Schäfer, *Appl.Phys.B*, **46**, 1988, 199.

G. Schönle, M.M. Rahman and R.N. Schindler, *Ber.Bunsenges Phys.Chem.*, **91**, 1987, 66.

G. Schott and N. Davidson, *J.Am.Chem.Soc.*, **80**, 1958, 1851.

S.E. Schwartz, *Science*, **243**, 1989, 753.

A. Schweig and W. Thiel, *J. Electron Spectrosc.Relat.Phenom.*, **3**, 1974, 27.

R.L. Seila and W.A. Lonneman, 81st Annual meeting of the air pollution control association, Dallas, Texas, 1988.

J.H. Seinfeld, *'Atmospheric Chemistry and Physics of Air Pollution'*, John Wiley and Sons, New York, 1986.

J.H. Seinfeld, *Science*, **243**, 1989, 745.

S.S. Shaik and E. Canadell, *J.Am.Chem.Soc.*, **112**, 1990, 1446.

D.F. Shanno, *Math. Comput.*, **24**, 1970, 647.

A.E. Siegman, *'Lasers'*, Oxford University Press, Oxford, 1986.

J. Simmons, *J.Phys.Chem.*, **95**, 1991, 1017.

H.J. Singh, L.J. Salas and W.Viezee, *Nature*, **321**, 1986, 588.

I.R. Slagle, D. Gutman, J.W. Davies and M.J. Pilling, *J.Phys.Chem.*, **92**, 1988, 2455.

H.M. Smallwood, *J.Am.Chem.Soc.*, **51**, 1929, 1985.

C.A. Smith, A.R. Ravishankara and P.H. Wine, *J.Phys.Chem.*, **81**, 1985, 1423.

I.W.M. Smith, *J.Chem.Soc. Faraday Trans.*, **87**, 1991, 2271.

I.W.M. Smith and R. Zellner, *J.Chem.Soc. Faraday Trans.II*, **69**, 1973, 1617.

B. Stauffer, G. Fischer, A.G.Nefal and A. Oeschger, *Science*, **229**, 1985, 1386.

J.J.P. Stewart, MOPAC, *' A semi-empirical molecular orbital program'*, QCPE, 1983, 455.

J.J.P. Stewart, *J.Comp.Chem.*, **10**, 1989a, 202.

J.J.P. Stewart, *J.Comp.Chem.*, **10**, 1989b, 221.

W.R. Stockwell and J.G. Calvert, *J.Photochem.*, **8**, 1978, 193.

J.M. Tedder and J.C. Walton, *Tet.Let.*, **36**, 1980, 701.

R.S. Timonen, E. Ratajczaak and D. Gutman, *J.Phys.Chem.*, **92**, 1987a, 653.

R.S. Timonen, J.J. Russell, D. Sarynski and D. Gutman, *J.Phys.Chem.*, **91**, 1987b, 1873.

D.W. Turner, *Adv.Phys.Org.Chem.*, **4**, 1966, 31.

D.W. Turner and M.I. Al-Jobourg, *J.Chem.Soc.*, 1963, 5141.

D.W. Turner and M.I. Al-Jobourg, *J.Chem.Phys.*, 1962, 3007.

D.W. Turner, A.D. Baker, C. Baker and C.R. Brundle, *Molecular Photoelectron Spectrscopy*, Wiley, New York, 1970.

F.I. Vilesov, B.L. Kurbatov and A.N. Terennin, *Sov.Phys.Dokl.*, **6**, 1961, 490.

Gg.H. Wagner, C. Zetzsch and J. Warnatz, *Ber.Bunsenges.Phys.Chem.*, **76**, 1972, 526.

T.J. Wallington, R. Atkinson, A.M. Winer and J.M. Pitts Jnr., *J.Phys.Chem.*, **90**, 1986, 4640.

I. Wangberg, E. Ljungström, J. Hjorth and G. Ottobrini, *J.Phys.Chem.*, **94**, 1990, 8036.

S.J. Waygood, Pt.II Thesis, Oxford, 1988.

R.P. Wayne, *J.Phys.E Sci.Inst.*, **14**, 1981, 306.

R.P. Wayne, '*Principles and applications of photochemistry*', Oxford University Press, Oxford, 1988.

R.P. Wayne, '*Chemistry of Atmospheres*', 2nd Edn., Oxford University Press, Oxford, 1991.

R.P. Wayne, I. Barnes, P. Biggs, J.P. Burrows, C.E. Canosa-Mas, J. Hjorth, G. le Bras, G.K. Moortgat, D. Perner, G. Poulet, G. Restelli and H. Sidebottom., *Atmos. Environ.*, **25A**, 1991, and references therein.

A.A. Westenberg and N. de Haas, *J.Chem.Phys.*, **46**, 1967, 490.

J.U. White, *J.Opt.Soc.Am.*, **32**, 1942, 285.

E.T. Wilkins, *J.R. Sanitary Inst.*, **14**, 1954, 1.

U. Wille, E. Becker, R.N.Shindler, I.T. Lançar, G. Poulet and G.Le Bras, *J.Atmos.Chem.*, submitted.

J. Wolfrum, *Laser Chem.*, **9**, 1988, 171.

R.W. Wood, *Phil. Mag.*, **6**, 1905, 513.

R.W. Wood and F.L. Mohler, *Phys. Rev.*, **11**, 1918, 70.

World Meteorological Organisation (W.M.O.), Global Ozone Research and Monitoring Project - report No. 16, '*Atmospheric Ozone*', 1985.

E. Wrede, *Z.Phys.*, **54**, 1929, 53.

R. Zellner and A. Weibrig, *Nature*, 1991, Paper Submitted.

X.Z. Zhao, T.X. Lu and Z.F. Cui, in: '*Third International conference - Trends in quantum electronics*', Ed. I. Ursu and A.M. Prokhorov, Bucharest, 442, 1988.

X.Z. Zhao, T.X. Lu and Z.F. Cui, *Chem.Phys.Lett.*, **162**, 1989, 140.

H.S. Johnston, S.G. Cheng and G. Whitten, *J.Phys.Chem.*, **78**, 1, 1974.

O. Ratigan, Private Communication, 1991.